

Studies on design of spindle-tool system and their effects on overall milling process stability

*Dissertation submitted to the
National Institute of Technology Rourkela
in partial fulfilment of the requirements*

of the degree of

Doctor of Philosophy

in

Mechanical Engineering

by

Jakeer Hussain Shaik

(Roll Number: 512ME129)

under the supervision of

Prof. J Srinivas



January 2017

Department of Mechanical Engineering
National Institute of Technology Rourkela



Mechanical Engineering
National Institute of Technology Rourkela

January 11, 2017

Certificate of Examination

Roll Number: 512ME129

Name: Jakeer Hussain Shaik

Title of Dissertation: Studies on design of spindle-tool system and their effects on overall
milling process stability

We the below signed, after checking the dissertation mentioned above and the official record book (s) of the student, hereby state our approval of the dissertation submitted in partial fulfilment of the requirements of the degree of Doctor of Philosophy in Mechanical Engineering at National Institute of Technology Rourkela. We are satisfied with the volume, quality, correctness, and originality of the work.

J Srinivas
Principal Supervisor

D.R.K.Parhi
Member (DSC)

H.P.Roy
Member (DSC)

H.B. Sahu
Member (DSC)

Name
Examiner

B.B. Biswal
Chairman (DSC)



Mechanical Engineering

National Institute of Technology Rourkela

Prof. /Dr. Jonnalagadda Srinivas

Associate Professor

January 11, 2017

Supervisor's Certificate

This is to certify that the work presented in this dissertation entitled "*Studies on design of spindle-tool system and their effects on overall milling process stability*" by "Mr. Jakeer Hussain Shaik ", Roll Number 512ME129, is a record of original research carried out by her under my supervision and guidance in partial fulfilment of the requirements of the degree of *Doctor of Philosophy in Mechanical Engineering*. Neither this dissertation nor any part of it has been submitted for any degree or diploma to any institute or university in India or abroad.

J Srinivas

This dissertation is dedicated to

My family members

&

*The lord almighty **ALLAH***

Declaration of Originality

I Jakeer Hussain Shaik, Roll Number 512ME129 hereby declare that this dissertation entitled "*Studies on design of spindle-tool system and their effects on overall milling process stability*" is my original work carried out as a doctoral student of NIT Rourkela and, to the best of my knowledge, it contains no material previously published or written by another person, nor any material presented for the award of any other degree or diploma of NIT Rourkela or any other institution. Any contribution made to this research by others, with whom I have worked at NIT Rourkela or elsewhere, is explicitly acknowledged in the dissertation. Works of other authors cited in this dissertation have been duly acknowledged under the section "Bibliography". I have also submitted my original research records to the scrutiny committee for evaluation of my dissertation. I am fully aware that in case of any non-compliance detected in future, the Senate of NIT Rourkela may withdraw the degree awarded to me on the basis of the present dissertation.

January 11, 2017
NIT Rourkela

Jakeer Hussain Shaik

Acknowledgment

I would like to thank my supervisor Prof. J Srinivas for all his support, enthusiasm, guidance wealth of ideas, the time and effort he put for me in completing this work. I have selected the problem and known the developments in this area from time to time by constantly getting in touch with literature from him. I thank for his encouragement in making me to understand the complete details relating to manipulators.

I am thankful to our director Prof. Sunil Kumar Sarangi, and very much obliged to the Head of Department of Mechanical Engineering Prof. S.S. Mohapatra, NIT Rourkela for providing all the support and concern regarding my academic requirements.

I would like to thank to all my DSC members, Prof. B.B. Biswal, Prof. D.R.K. Parhi, Prof. H.P. Roy, and Prof. H.B. Sahu for their valuable suggestions and comments during this research work and other faculty members of the institute for their co-operation and help.

I would also like to thank my wife for her continued encouragement and support throughout the work. I am thankful to my daughter and son for bringing laughter and joy to my life. Finally, I would like to thank my father, mother and brother for their endless encouragement and motivation in completing this research work.

Specially, I extend my deep sense of indebtedness and gratefulness to all my colleagues M Rajasekhar, K.V Varalakshmi, Puneet Kumar, Prabhu L, M Rajasekhar Reddy, S Madhusmitha, N Khayyum, and many other M.Tech scholars who helped me to complete the project directly and indirectly. I am thankful to all the teaching & non-teaching staff of Mechanical Engineering Department for their kind cooperation.

January 11, 2017
NIT Rourkela

Jakeer Hussain Shaik
Roll Number: 512ME129

Abstract

High speed machining using vertical CNC milling centres continues to be a popular approach in a variety of industries including aerospace, automobile, mould and die casting etc. Chatter oscillations have significant influence in restricting the metal removal rates of the machining process. The cutting process instability or chatter is assessed by prediction of frequency response at the tool tip. Present work aims at evaluating the combined effect of a spindle-housing and tool holder on the dynamics of cutting tool by considering the flexibility of spindle unit supported on bearings. The spindle-tool is analysed by using finite element modeling using Timoshenko beam theory. The dynamic characteristics and tool-tip frequency responses are obtained without considering the cutting forces. The results are compared with receptance coupling approach and using 3D modeling in ANSYS. Further experimental modal analysis on the machining spindle of same dimensions has revealed the same dynamic modes. Using the validated FE model of the system, the effects of nonlinear bearing contact forces, spindle-tool holder interface stiffness, bearing span and axial preload, tool overhang and diameter on the frequency response and cutting process stability are studied. Optimal spindle-tool system is designed for achieving maximum dynamic stiffness.

The analytically stability lobe diagrams are obtained from the real and imaginary terms of these frequency responses at the tool tip. Dynamic stability issues in helical end-milling using the two and three dimensional cutting force models are considered for the analysis. The stability boundaries are experimentally verified using the cutting tests on both CNC milling spindle and modified drilling tool spindle systems while machining Al-alloy work pieces. Vibration and sound pressure levels are also employed to assure the stability of cutting operations, while surface images are used to identify the chatter marks at various combinations of cutting parameters. Dynamic milling model is employed with the flexible spindle-tool system by considering several effects including variable tool pitch, tool run-out, nonlinear feed forces and process damping. Design and stability studies on the modified drill spindle with a custom-designed work table for milling operations allowed in understanding several interesting facts about spindle-tool systems. Some control strategies including semi-active and active methods are implemented using finite element model of the spindle-tool system to minimize the chatter vibration levels/maximize the stable depth of cut during cutting operations.

Keywords: Frequency response; Spindle machine receptances; 3D stability model; variable pitch effect; run out effect; semi-active and active control strategies.

Contents

Certificate of Examination	i
Supervisor's Certificate	ii
Dedication	iii
Declaration of Originality	iv
Acknowledgment	v
Abstract	vi
Contents	vii
List of Figures	xii
List of Tables	xviii
Nomenclature	xix
Chapter 1	1
Introduction	1
1.1 Overview	1
1.2 Vibrations in machine tool	2
1.3 Stability issues in machining	4
1.4 Aim and objectives	5
1.5 Organization of the Thesis	6
Chapter 2	8
Literature Review	8
2.1 Bearing characteristics on the dynamic stability	8
2.2 Spindle design and optimization issues	11

2.3 Cutting force modeling and stability issues	17
2.4 Milling process control issues	27
2.5 Summary	30
Chapter 3	31
Dynamic Modeling of spindle-tool unit	31
3.1 Analytical modeling of spindle system	32
3.1.1 Modeling of spindle shaft	32
3.1.2 Bearing system	34
3.2 Coupled spindle tool system	36
3.2.1 Distributed parameter modeling	37
3.2.2 Finite element modeling	38
3.2.3 Effect of joint stiffness in spindle-holder-tool assemblies	40
3.2.4 Modified Receptance coupling theory	41
3.3 Numerical Results	49
3.3.1 Frequency response studies	50
3.3.1.a Full-order finite element modeling approach	50
3.3.1.b Receptance coupling sub-substructuring	51
3.3.1.c Three-dimensional finite element modelling	55
3.3.1.d Experimental Modal Analysis	58
3.3.1.e Studies on spindle-tool system interfaces with interface stiffness	60
3.3.1.f Non-linear bearing force effects	64
3.3.2 Parametric studies of spindle variables	69

3.3.2.a Optimum Design of Experiments	73
3.3.3 Optimal design of spindle-tool system	79
3.3.4 Dynamic modelling of drilling-spindle for milling-A case study	91
3.4 Concluding remarks	98
Chapter 4	100
Cutting dynamics and stability analysis	100
4.1 Classical cutting force model	101
4.1.1 Effects of process damping	112
4.1.2 Cutting force simulation with tool run-out	118
4.1.3 Cutting force simulation with variable pitch effect	120
4.2 Three-dimensional cutting force model	123
4.2.1 Time-domain simulations	131
4.2.2 Nonlinear force feed model	135
4.3 Effects of spindle-tool system parameters on stability	138
4.4 Cutting dynamics with nonlinear bearing forces	140
4.5 Stability analysis of a practical drill spindle for milling	143
4.5.1 Sound spectrum analysis using LabVIEW	146
4.5.2 Stability charts for modified drill spindle	151
4.6 Conclusions	152
Chapter 5	154
Control strategies in end milling process	154
5.1 Methods for Chatter Mitigation	155

5.2 Semi-active control using secondary system	156
5.3 Active vibration control	163
5.4 Conclusions	170
Chapter 6	171
Conclusions	171
6.1 Summary	171
6.2 Future Scope	173
References	174
APPENDIX -A Finite element matrices	187
A.1 Shape functions	187
APPENDIX-B Fourth order Runge-Kutta time integration method	192
APPENDIX-C Static condensation techniques	193
APPENDIX -D Training algorithm for MLP neural network	195
D.1 Neuron model	195
D.2 Learning in Multi-Layer Perceptron	196
APPENDIX -E LabVIEW programs for sound spectrum analysis	197
E.1 Read the sound spectrum data	197
E.2 Save the sound spectrum data	197
E.3 Power spectral density of cutting signals	198
APPENDIX-F Computer programs	199
F.1 Finite element method to obtain the matrices	199
F.2 Program for receptance coupling approach	200

F.3 Programs for Stability Computations	201
F.4 Programs for time domain computations	202
F.5 Programs FFT and amplitude spectrum	203
F.6 Programs for process damping	204
Dissemination	205
Curriculum Vitae	207

List of Figures

Figure no.	Caption	Page no.
2.1	Jones' elastic model of the bearing	10
2.2	Schematic view of the integrated spindle-tool unit	14
2.3	Geometry of a helical end mill	19
2.4	Tool deflection due to milling forces	21
2.5	Variable pitch angle of the helical end mill	23
2.6	Geometry of milling tool with damper	28
3.1	Integrated spindle tool unit	31
3.2	Section of the beam	33
3.3	Ball bearing schematic	35
3.4	Simplified spindle-tool unit	37
3.5	Equivalent model of spindle-tool device	40
3.6	Equivalent line model of spindle tool unit	41
3.7	Overall process chart	42
3.8	Three component receptance coupling model	43
3.9	Finite element model of spindle supported by housing	48
3.10	Tool tip frequency responses using the Full-order FEM	51
3.11	Configuration of spindle tool system	52
3.12	Present receptance coupling concept	52
3.13	Receptance T_{11} of the Tool-Holder sub assembly	53

3.14	Spindle machine receptances (Y_{3b3b}) obtained from finite element analysis	54
3.15	Tool tip frequency response of the assembly	55
3.16	Individual solid work components of MTAB MAXMILL realistic spindle system	56
3.17	Meshed model of spindle-bearing system	56
3.18	First six mode shapes of spindle tool unit	57
3.19	Harmonic response of spindle bearing system	58
3.20	First modal frequency of spindle-tool assembly	58
3.21	Experimental set up employed	59
3.22	Frequency response of the integral tool-spindle unit	60
3.23	Equivalent model of the spindle-tool interfaces with distributed contact springs	61
3.24	Tool tip frequency response at different stiffness values	62
3.25	Tool tip FRF with rigid and flexible interfaces	62
3.26	Tool tip FRF plots for different structural damping factors	63
3.27	Element degrees of freedom for spindle discretization	64
3.28	Tool-tip node displacements at $r_0=10\mu\text{m}$	65
3.29	Effect of small negative clearance at the two bearings	66
3.30	FFT plots for negative radial clearance of $-10\mu\text{m}$	66
3.31	FFT plots for different preload values ($r_0=10\mu\text{m}$)	68
3.32	FFT at tool-tip node in two lateral directions	69
3.33	Effect of bearing span on spindle-tool dynamics	70
3.34	Effect of tool overhang on spindle-tool dynamics	71

3.35	Effect of bearing preload on spindle-tool dynamics	72
3.36	Variation of fundamental frequency with other parameters	73
3.37	Data normality testing for natural frequency	76
3.38	Signal to noise ratios plots for the control factors on natural frequency (Hz)	76
3.39	Data normality testing for dynamic stiffness	78
3.40	S/N plots for control factors on dynamic stiffness	78
3.41	Imaginary part of FRF of spindle	80
3.42	Block diagram of the proposed Neuro-Genetic system	80
3.43	Typical 3-layer neural network	81
3.44	Neural network model in present case	82
3.45	Convergence trends for various hidden neuron structures	83
3.46	Correlation between the predicted values and test data	84
3.47	Error plot rate of HS algorithm	87
3.48	Flowchart for genetic algorithm	89
3.49	Error plot rate of GA algorithm	89
3.50	Tool-tip FRF for the spindle-tool unit with optimal dimensions	91
3.51	Drill-spindle modification procedure	88
3.52	Original component modeling of drilling spindle	92
3.53	Spindle-tool unit of the in-house drilling machine	93
3.54	Instrumentation for modal analysis	93
3.55	Experimental response for original drill spindle	95
3.56	Experimental measured FRF in modified drill spindle	96

3.57	Tool tip FRF of drill and modified spindle	97
3.58	Meshed assembly of the model in ANSYS Workbench	97
3.59	Comparison chart for the first mode of vibration	98
4.1	Two-degree of freedom milling model	101
4.2	Stability lobe plots for different percentages of radial immersion	107
4.3	Experimental set-up employed	108
4.4	Machining areas of workpiece at different depths of cut	109
4.5	Time history and FFT plots for different axial depths of cut	110
4.6	Amplitude and FFT plots for different axial depths of cut	111
4.7	Predicted SLD with experimental validation	111
4.8	Geometry for up-milling using average tooth angle approach	113
4.9	Geometry for down-milling using average tooth angle approach	114
4.10	Analytical stability lobe diagrams	116
4.11	Cutting tool vibrations at $\Omega = 3000rpm$ at 1mm depth of cut	117
4.12	Tool displacement levels with run-out correction	119
4.13	Force variations with tooth-to-tooth run-out	120
4.14	Angular position of edges for end mill on cutter circumference	121
4.15	Time domain simulation with variable pitch at 25% radial immersion	122
4.16	Tool vibration levels at 1mm depth of cut	122
4.17	Three-degree of freedom cutting force model	123
4.18	Stability lobe diagrams with 40% depth of immersion	128
4.19	Stability lobe plots for two different damping ratios	129

4.20	Experimental response and FFT plots at differnt axial depths of cut	130
4.21	Optical microscope images of workpiece	131
4.22	Predicted SLD with experimetal validation	131
4.23	Three directional cutting force histories	132
4.24	Time history plots for an axial depth of cut of 1mm	133
4.25	Time history plots for an axial depth of cut of 2 mm	134
4.26	Phase plane plots at 1850 rpm	135
4.27	Time domain simulation at a depth of 4mm	135
4.28	Effect of non-linear feed rate forces	137
4.29	Prediction of average stable depth of cut	138
4.30	Variation of average depth of cut as a function of spindle tool parameters	140
4.31	Stability lobe diagram at the critical bearing span=180mm	140
4.32	Transient response with bearing and cutting forces	141
4.33	Experimental set-up employed	142
4.34	Experimental FFT plot	143
4.35	Experimental set-up employed for the modified drilling machine	144
4.36	Time histories and FFT plots at 1030 rpm	145
4.37	Time histories and FFT plots at 1300 rpm	145
4.38	Time history and FFT plots at 1650 rpm	146
4.39	Amplitude and FFT plots for different depths of cut at 1030 rpm	148
4.40	Amplitude and FFT plots for different depths of cut at 1300 rpm	149

4.41	Amplitude and FFT plots for different depths of cut at 1650 rpm	150
4.42	Testing of stability boundaries with surface images	151
4.43	Stability lobe diagrams for modified spindle	152
5.1	Classification of the methods for chatter mitigation	156
5.2	Finite element discretization of spindle-tool system with vibration absorber	157
5.3	Tool tip FRF of the spindle-tool unit	159
5.4	Stability lobe plots with and without absorber	159
5.5	Flowchart of PSO algorithm	161
5.6	Convergence trend corresponding to population size=30	162
5.7	Tool tip FRF with optimal vibration absorber parameters	162
5.8	Stability lobe diagrams from tool-tip FRF	163
5.9	Block diagram of a single-input single-output system closed loop system	164
5.10	Block diagram of control scheme	165
5.11	Electro-magnetic actuator for the spindle	166
5.12	Tool tip vibration levels at a depth of 1mm	167
5.13	Tool tip vibration levels at a depth of 3mm	168
5.14	Time domain simulation at a depth of 1mm and 3mm	169
5.15	FFT plots at different depths of cut	170

List of Tables

Table no.	Caption	Page no.
3.1	Parameters of the finite element model	50
3.2	Convergence result of natural frequencies of spindle tool unit	51
3.3	Parameters of the tool-holder and spindle machine unit	51
3.4	Detailed simulated experimental data using Taguchi L27 (3**5) array	70
3.5	Analysis of Variance for natural frequency (Hz)	71
3.6	Response table for signal to noise ratio (Larger is better)	73
3.7	Analysis of Variance for dynamic stiffness (N/m)	74
3.8	Response table for signal to noise ratio (Larger is better)	75
3.9	The weight structure for 5 hidden node skeleton	80
3.10	Optimal data from HSO and GA	86
3.11	Modal frequencies (Hz)	94
4.1	Modal and cutting coefficients for the system	102
4.2	Summary of directional orientation factors	110
4.3	Directional dynamic parameters for simulation	123

Nomenclature

α_j	Angular location of the j^{th} ball
β	Helix angle, Learning rate
γ	Non-linear feed power constant
δ_j	Radial deformation of the j^{th} ball
η	Solid damping factor
λ	Run cut angle
ρ	Run-out of cutting edge
τ	Tooth period
ϕ_j	Instantaneous angular immersion of the tooth (j)
Ω	Angular spindle speed (rad/s)
ϕ_p	Tooth pitch
Θ	Contact angle of static angular-contact ball bearing
ω_c	Chatter frequency
μ_x and μ_y	Directional orientation factors in x and y directions
N_t^*	Average number of teeth in the cut,
$h(\phi_j)$	Instantaneous variable total chip thickness
h_{ro}^j	Variation of the chip thickness due to run-out
$[A(t)]$	Directional coefficient matrix in time domain
$[A_0]$	Immersion dependent directional cutting coefficient matrix
$[H(i\omega_c)]$	Frequency response function at tool tip in frequency domain
$\{F\}$	Force vector
b	Axial depth of cut
b_{lim}	Average stable depth of cut obtained from the stability lobe
C	Process damping coefficient
c_1, c_2	Absorber damping

C_b	Interface stiffness of balls and radii of curvature
$C_{new, x}, C_{new, y}$	Damping for the process stability calculations
D_b	Ball diameter
E	Elastic modulus
E_s	Material dependent damping
F_a	Bearing preload
F_d	Process damping force
f_t	Feed per revolution
$F_{t,k}, F_{r,k}, F_{a,k}$	Tangential radial and axial force components
$f_{t,mean}$	Mean feed per tooth
$H(.)$	Heavy-side function
H_{or}	Oriented frequency response function
k_1, k_2	Absorber stiffness coefficients in two directions
K_P, K_D	Parameters of the proportional and derivative gains
K_t, K_r, K_a	Tangential, radial and axial cutting coefficients
k_{xx}, k_{yy}	Static radial stiffness of the bearings
K_{xx}, K_{yy}, K_{zz}	Cutting stiffness coefficients in X, Y and Z directions
m_1, m_2	Masses of the damper in two directions
N	Number of teeth of the cutter
n	Spindle speed in rev/min calculated through tooth passing period
N_b	Number of balls
n_{j-1}, n_j	Present and previous tooth periods
r, R	Radii of inner race and outer race
r_0	Radial clearance
$U(t)$	Control force
Z_{loc}	Location of the absorber placement
ω_{cage}	Angular velocity of the cage

Chapter-1

Introduction

1.1 Overview

Modern industries focus on high quality machining and automation technology. Quality of products and productivity are improved by continuous monitoring of machine tools and process. The competitive economic environment has brought new challenges to the machining industry. Significantly reductions in machining time, production cost, and improvement in overall productivity have become an ultimate requirement. Especially, in machining industries, the main objective is to select chatter free cutting conditions with lower cutting forces while maintaining the power and torque limits of machine tools and other practical constraints of the system. Therefore, right and optimal selection of cutting conditions is of great concern for machining industry. In order to satisfy the needs, a system must be developed to ensure the optimal selection of cutting conditions as well as the design of spindle-tool system with various physical phenomena occurring during machining.

The condition monitoring strategies have importance in assessing the quality of the machining process for improving the overall efficiency of the system. Cutting forces, workpiece surface quality, tool vibration levels, sound pressure intensities are some of the important process indicators which determine the limits on the cutting conditions, accuracy of products, machine tool failures and other information useful for monitoring and controlling the machining process. It is well known that productivity reduces due to onset of regenerative chatter phenomenon associated with instabilities in cutting operations.

In machining operations like milling and boring, regenerative chatter instabilities hamper the machining continuity and such conditions need to be identified at the beginning itself. Out of various factors, spindle design is one of the important issues dictating the process stability. For example, a rigid spindle permits higher depths of cuts without violent oscillations during machining. However, spindle works in combination with tool and holder system, whose flexibility plays an important role in cutting operations.

1.2 Vibrations in machine-tool

Vibration analysis in metal cutting has significance since vibrations may cause loss of surface finish of work pieces, shortens tool life, degrades machine tool components and produces noise contamination. In addition, the mechanics of the cutting process is also affected by the vibrations, changing the contact conditions between the tool and the material. During the machining processes, three different types of mechanical vibrations can occur due to the lack of dynamic stiffness of one or several elements of the system composed by the machine tool, tool holder, cutting tool and the workpiece material [1]. These are (i) Free or transient vibrations (ii) Forced vibrations and (iii) Self-excited vibrations. In the first case, the vibrations are initiated by an external energy source momentarily and thereafter removed. In the absence of non-conservative forces, free vibrations sustain themselves and are periodic. The structure will vibrate in its natural modes until the damping causes the motion to die out. Forced vibrations occur due to external harmonic excitations. The principle source of forced vibrations in milling processes is when the cutting edge enters and exits the workpiece. However, forced vibrations are also associated with unbalanced bearings or cutting tools, or it can be transmitted by other machine tools through the workshop floor. Self-excited vibrations also known as chatter, extract the energy to start and grow continuously, as a result of the interaction between the cutting tool and the workpiece during the machining process. Such a chatter phenomenon is further classified into regenerative and non-regenerative types. The regenerative effect is caused by the undulation of successive cuts, where the tool removes a wavy surface generated in the previous pass. Non regenerative vibration is maintained by the cutting force fluctuations that are induced by the tool-workpiece relative displacement of a periodic nature.

Free and forced vibrations can be avoided or reduced if the causes of the vibration are identified. In this field, a variety of methods and techniques have been developed to mitigate their occurrence. However, self-excited vibrations as a result of an unstable interaction between the machining forces and the structural deflections cannot be avoided. The forces generated when the cutting tool and part come into contact produce significant structural deflections. These structural deflections modulate the chip thickness that, in turn, changes the machining forces. Regenerative chatter may result in excessive machining forces and tool wear, tool failure, and unacceptable surface finish, thus severely decreasing operation productivity and part quality, loss of contact and mode coupling effects. When chatter occurs, the vibration amplitude will increase continuously until the relative displacement between the cutter and workpiece is so large that the cutter will leave the workpiece for part of the time. This becomes a nonlinear behavior, which limits the vibration amplitude to a finite value. The magnitude of vibration depends on the cutting

force characteristics, such as the magnitude and direction of the cutting forces, and the tooth passing frequency at which a cutting flute comes in contact with the workpiece. The dynamic characteristics of the entire machining system in terms of the natural frequencies the damping coefficients and the stiffness of the machine tool structure, also affect the vibration magnitudes.

In comparison with other machining processes, the cutting force characteristics of milling process are more complex (see for e.g., [2]). The cutting forces generated during a milling process induce dynamic deflections of the workpiece-tool system, which in turn modulate the cutting forces. Such self-excited vibrations are mostly caused by two well-known mechanisms: regeneration and mode-coupling. As described earlier paragraphs, regeneration occurs when the cut produced at a current time leaves a wavy surface on the material regenerated during subsequent passes of cut. The phase difference between the inner and outer waves and the amplitude gain of the system plays a key role in stability of cutting process. In mode-coupling approach, even when there is no interaction between the undulated surface of workpiece and tool vibration, the tool traces out an elliptic path that varies the depth of cut in such a way to intensify the coupled modes of vibration. Self-excited vibrations may persist in machining operations and require attention.

In traditional low-speed machining processes, the machining dynamics are not considered as a significant issue because spindle speeds and depths of cut are conservatively selected. Therefore, the system vibrations are typically small. However, with the increased use of high-speed machining and requirements for smaller parts with higher tolerances, errors caused by machining dynamics can be significant. The behavior of a dynamic system depends on the force input and its dynamic characteristics. In operations like milling, the force depends on a combination of user defined parameters and the interaction between the tool and the workpiece. Some user defined machining parameters include: the axial depth of cut, the radial depth of cut, the feed rate, and the spindle speed. In addition to this, selection of the cutting tool affects the machining accuracy due to material composition, tool geometry, and coatings all influence the forces that are developed between the tool and workpiece.

In any dynamic system, the time dependent motion, or vibration, is determined by the system's dynamic response and the force input and initial conditions. Especially, in milling, the system dynamics includes that of combined machine-tool-holder-workpiece system model. The system dynamics are generally expressed as the complex valued ratio of the displacement to the input force over a selected frequency range; called frequency response function (FRF) and it can be modeled or measured. The FRF is determined at the point of interest for example at the free end of the cutting tool, which usually represents the most flexible point in the system connecting the tool and workpiece.

1.3 Stability issues in machining

Machining systems involve a machine tool, a cutting tool and holder, and a workpiece and work holding devices as structural elements. Depending on their relative rigidity, one or more components may dominate the total deformation at the tool-workpiece contact point contributing to the form errors and the dynamics of the process which may yield instability. Generally, machining centres are composed of a bed, linear and rotary axes, a column, a spindle etc., the spindle-holder-tool assembly is usually the most flexible part of the whole system due to the slender geometries of these components and multiple interfaces between them. In this case, the cutting process forces are the main cause of the structural deformations.

In machining process, stability depends on the phasing of vibrations on each successive flute engagement. As the cutter engages with the workpiece, forces are generated which cause vibrations. These vibrations, in turn, are imprinted on the workpiece surface. If the vibrations are in phase with (i.e., match up to) the surface left by the previous tooth engagement, then the chip thickness remains relatively the same. When the vibrations satisfy this “in phase” condition, the forces and vibrations in the system persist in a steady state or stable condition. On the other hand, if the vibrations from one tooth engagement to the next do not match up or are “out of phase”, the chip thickness varies and the force amplitude varies. The force variation excites the system dynamics and causes vibrations which lead to subsequent changes in the chip thickness. This system is described by using a set of time delayed differential equations (one for each force direction in consideration) where the time between tooth engagements is the amount of the delay. The phase difference between engagements depends on the spindle speed and axial depth of cut acts as the feedback system gain. Stability information can be presented in terms of input parameters (axial depth, spindle speed and radial depth). Generally at a particular radial depth, a stability lobe boundary is predicted in the spindle speed-axial depth domain.

The stability lobes diagram is a plot that separates stable and unstable machining operations for different spindle speeds. Stable cuts occur in the region below the stability boundary, while unstable cuts (chatter) occur above the stability boundary. The user can select optimum operating conditions for spindle speed and axial depth of cut based on this diagram. Stability lobes are functions of the dynamic stiffness at the tool center point (TCP), the tool geometry, the radial immersion of tool into material, as well as of the material to be machined. Machining operators usually, distinguish between two types of chatter (i) structural chatter or machine chatter: which is low frequency chatter, recognizable for a low-pitched sound and the chatter is associated with the structural modes of the machine. (ii) tool chatter: which appears at higher frequencies and is recognizable

for a high-pitched sound, the chatter is associated with the modes of the tool or spindle. The type of chatter depends on the cutting frequencies; low cutting frequencies excite structural modes and high cutting frequencies excite spindle- tool holder-tool modes. The mechanical modeling of the spindle-tool system is a key to estimate the static and dynamic behavior of a machine tool. An accurate modeling of this system is very important part in predicting stability of cutting process. Detailed description of chatter stability can be found in open literature (e.g., [3]).

1.4 Aim and objectives

From the last two decades, chatter phenomenon has been extensively studied to predict the appropriate machining conditions. In parallel, different methods to counteract tool chatter have been developed and are being used in the machining industries. The operations such as milling may require a special attention even at normal operating conditions with flexible/rigid tool work combinations. In applications such as utilizing a drilling machine for milling operations, the spindle design modifications are very important to machine the components smoothly.

The main focus of present work is to design the spindle-tool unit by considering various factors affecting the tool-tip frequency response along with stability studies during cutting with the use of optimally designed spindle-tool system.

- The combined dynamics of a spindle-tool unit on the process effectiveness is to be presented by considering the flexibility of spindle unit supported on bearings.
- Frequency response functions at the tool-tip are to be obtained for the spindle-tool model using various approaches such as direct finite element method, receptance coupling approach and experimental modal analysis.
- Optimal spindle-tool system parameters are to be obtained for achieving the maximum dynamic stiffness and improving the cutting process stability.
- Cutting process stability is to be validated with the designed spindle by considering the practical conditions with the help of time-domain and frequency-domain (stability lobe diagrams).
- Case studies are to be conducted by modifying the design of drill spindle to improve the cutting stability while it is used for slot cutting operations as in a three axes milling machine.
- Detailed experimental cutting tests are to be conducted for stability testing by measurement of vibration levels, sound pressure intensities and surface images using the designed spindles.

- In improving the stability boundaries, some semi-active and active control strategies are to be implemented without changing the major operating variables significantly.
- **To develop semi and active control methods for maximizing the stable depth of cut and reduction of chatter in online fashion.**

Some of the contributions in the present work are as follows:

- (i) Development of a generalized approach for dynamic model for the spindle-tool unit by accounting practical considerations including joint interface effects, non-linear bearing forces etc.
- (ii) Optimal design of spindle-tool unit for maximizing the dynamic stiffness and improving the average stable depth of cut
- (iii) Design and modifications of drill spindle for milling operations.
- (iv) Improve the stability limits by using semi-active and active control techniques.

Various experimental and numerical studies support the concepts provided in the work.

1.5 Organization of the thesis

Thesis is organized into six chapters. In the present chapter, the spindle-tool system and its importance in assessment of machining stability has been introduced.

Chapter-2 deals with the comprehensive literature review related to the current work. The various works related to design analysis and control of spindle-tool systems as well as their influence on machining process performance are reported.

Chapter-3 presents the results of theoretical modeling such as finite element analysis using Timoshenko beam theory. Further one of most popular coupling techniques such as receptance-coupling substructure analysis (RCSA) are highlighted in this section. Three dimensional analyses are conducted on the prototype spindle-tool unit in ANSYS Workbench. Later parametric studies are carried for the spindle and tool design variables. Since one of the purposes of modeling the spindle system is to avoid chatter vibrations during machining process, the maximum dynamic stiffness has to be improved. Meta-heuristic optimization studies are presented in order to show the importance of these techniques in the effective design of spindle-tool unit. Further, a modified design approach for drilling spindles is illustrated economically for milling operations.

Chapter-4 describes the role of the dynamic interaction between the spindle system and the work piece on the overall performances and presents the generalized dynamics of 3-axis milling operations. The chatter stability of the milling operations are solved both in

frequency and time domains. A detailed comparison of various stability models is also presented. Moreover, the analytical zero-order solution available in literature is generalized to model stability of end mills with complex geometries. Time domain simulations are carried out for different cases of process parameters that affect the cutting force dynamics.

Chapter-5 deals with the study of active structural methods dedicated to the suppression of chatter. A block diagram of the control system is developed. The frequency-response characteristics are determined from mathematical modeling for the closed-loop vibration control system is presented.

Moreover, chapter-6 summarize the major findings from the research and make the recommendations for the future research.

Chapter-2

Literature review

Enormous literature is available on various issues relating to milling operation. Especially, for predicting the role of spindle during the milling operation in-terms of stability, and subsequent effects including work piece surface finish and tool wear, several research articles appeared over last one decade. Literature in the present work is classified under the following headings.

2.1 Bearing characteristics on the dynamic stability

The spindle-bearing system is one of the most critical components of the high speed spindles, must able to provide high rotational speed and reasonable load capacity. The types of bearings that are available for high speed spindles are angular-contact ball bearings, roller bearings and taper roller bearings. Angular contact ball bearings are most commonly used today in high-speed spindles. This is because angular contact ball bearings can provide the required precision, load carrying capacity, and spindle speeds. In addition, the costs are low compared to hydrostatic, aerostatic or magnetic bearings.

Angular contact ball bearings are designed to provide the capabilities to withstand external loads from both axial and radial directions when they are properly preloaded. In some cases, taper roller bearings are also used because they can offer larger load-carrying capacity and higher stiffness than ball bearings. However, taper roller bearings do not allow the high speeds required by high speed spindles. In this thesis, angular contact ball bearings are studied.

The dynamics of spindle systems mainly depends on the characteristics of the bearings, tool-holder interface, spindle shaft and housing. This review gives an overview of previous research findings of the spindle design analysis and their effects of the cutting dynamics. The simplest model for angular contact ball bearings is the conventional two-degrees-of-freedom proposed by Palmgren [4]. This model considers only the axial and radial translations of the inner ring relative to the outer ring, which is usually suitable for most applications where misalignment and shaft bending effects are insignificant. The pioneering work on mathematical models for angular contact ball bearings was proposed by Jones [5], who developed a general theory for load-deflection analysis of bearings that considered centrifugal force and gyroscopic loading of the rolling elements under high-speed operation.

Demul et al. [6] established the dynamic equations in a matrix form that considered the centrifugal force but neglected the gyroscopic moment in the bearing. This method provides an advantage that the Jacobian matrix of the bearing is derived analytically, producing the bearing stiffness. Filiz and Gorur [7] conducted a load-deflection analysis of bearings under combined axial and radial loads. This analysis produced a simplified model for determining the incremental stiffness in axial and radial directions.

Houper [8] and Hernot et al. [9] presented a stiffness matrix form with five degrees of freedom. Their model enables using the finite element method for solving the coupled problem of the spindle-bearing system, but the centrifugal forces and gyroscopic moments are not included. Harris [10] conducted a comprehensive analysis of different aspects of bearings, but his model is independent of the spindle and shaft.

Walford and Stone [11-12] measured stiffness and damping for bearings under oscillating conditions. They used two degrees of freedom mathematical model to extract a representative stiffness value and found that the levels of damping obtained were considerably higher than expected. They concluded that this result was due to interaction among the races, housing and shaft.

Tiwari and Vyas [13] developed a technique for estimating nonlinear stiffness parameters for rolling in rotor systems, based on an analysis of the random response signals picked up from the bearing caps. The analysis uses a stochastic characteristic of the bearing excitation in conjunction with a single degree of freedom model to estimate a representative stiffness. Marsh and Yantek [14] presented an experimental method for estimating the dynamic stiffness of precision bearings, based on measurements of the frequency response functions.

Aini et al. [15] carried out experiments to investigate the frequency responses of grinding machine tool spindle supported by angular contact ball bearings. Several works [16-19] proposed the fundamental theory of bearings for the high speed spindles and proposed the recent trends in design of spindles. The main lubrication systems for bearings are grease and oil air lubrication. The advantage of grease lubrication is that the rotation speed can be quite high without high cost and maintenance.

However, for advanced high speed spindles, the oil air lubrication system is required because of its low viscosity and exhaust system [20-21]. The preload for the bearings is also an important issue for high speed spindles. The preload tends to increase with the increase of the rotation speed of the spindle, and the over preload causes the bearings to break. Therefore, the preload must be applied and adjusted properly, with a suitable preload system depending on the spindle specifications. Angular contact ball bearings have been widely used in machine tool spindles, and the bearing preload plays an

important role on the performance of the spindle. With the development of high speed machining, especially for high speed milling, heavy cutting at a low speed and light cutting at a high speed are often performed on a single machine tool spindle, thus, high stiffness at low speed and low temperature rise at high speed are required.

Lin et al. [22] presented an integrated model with experimental validation and sensitivity analysis for studying various thermo-mechanical-dynamic spindle behaviours at high speeds. The bearing preload effects on bearing stiffness, high-speed rotational effects, including centrifugal forces and gyroscopic moments on the spindle shaft and, subsequently, on overall spindle dynamics are investigated.

Jiang and Mao [23] investigated the variable preload technology was systematically applied to the high-speed spindles. At high-speed range, FEM method was used to analyze the temperature distribution of the spindle, and the variable spindle preload was determined according to the constraint of temperature rise of bearings.

Ozturk et al. [24] predicted the spindle speed-dependent dynamic properties at the tool tip and errors in-process stability predictions. Effects of bearing preload on the stability limits were demonstrated via simulations and cutting tests. Cao et al. [25] compared two main types of bearing preloads such as constant and rigid mechanisms using a mathematical model as well as with experiments. Timoshenko beam element theory coupled with a non-linear model of angular contact ball bearings, the dynamics of the spindle shaft, housing, and bearings system was modelled as a non-linear function of preload mechanism and amplitude, spindle speed, and external cutting loads. Figure. 2.1 shows the bearing model employed in this work.

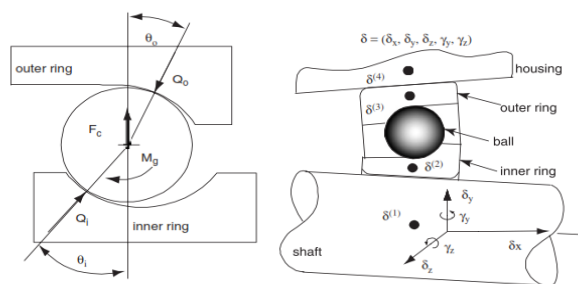


Figure 2.1: Jones' elastic model of the bearing [25]

Kim et al. [26] developed statistical models and software's to numerically simulate the rotational precision of spindles running on ball bearings. It was identified that the rotational accuracy of the spindle can differ significantly with spinning speed. The impact of the bearing preload has an extra significance.

Zahedi and Movahhedy [27] extended a widespread model of high speed spindles that includes viable models for the mechanical and thermal behaviour of its major components such as bearings, shaft and housing. The spindle housing and shaft were treated as six-degree-of-freedom Timoshenko beam elements.

Zivkovic et al. [28] presented the thermo-mechanical model of the spindle with angular contact ball bearings. The non-linear change of spindle stiffness under the influence of temperature is studied and it is experimentally verified.

2.2 Spindle design and optimization issues

A schematic of the spindle-drawbar-bearing assembly of a high-speed milling motorized spindle unit is shown in Figure 2.1. The rotor of the spindle is supported by two pairs of angular contact ball bearings. To drive this spindle bearing system, an integral induction motor is located between the front and rear bearings. A drawbar is mounted inside the hollow shaft to change tools. The hollow shaft, the drawbar and the bearings constitute a typical double-rotor dynamic system. Labels (1, 5) represents the front and rear bearings and (2, 3, 4) represents the spindle, motor rotor and drawbar.

In an effort to choose the factors that avoid chatter and to attain the better surface finish, accurate dynamic models of tool-holder-spindle assembly are required. Such a dynamics reflected at tool tip can be acquired by modal testing, but entails a huge number of tool-holder arrangements in a manufacturing facility. The measurements are time taking and at times, problematic as in the case of micro-end mills. Few studies are reported in view of analytical and experimental works related to modelling of the spindle.

Yang [29] conducted an in-depth analysis of the radial stiffness of machine-tool spindles. He concluded that shortening the overhang, and increasing the area moment of inertia of the spindle and the stiffness of the front bearing, can enhance the static stiffness of spindle systems. The addition of the third bearing may change the dynamics of the spindle, depending on the forces and moments exerted on it.

Ruhl and Booker [30] is one of the earliest researchers to use the finite element method for modelling of rotor systems. His model includes translational inertia and bending stiffness but neglects rotational inertia, gyroscopic moments, shear deformation, and axial load. Nelson [31-32] used the Timoshenko beam theory to establish shape functions and formulate system matrices, including the effects of rotary inertia, gyroscopic moments, shear deformation, and axial load.

Jorgensen and Shin [33] used DeMul's bearing model and the Timoshenko beam to develop a model for a spindle supported by a pair of angular contact bearings, including cutting-load effects. The cutting load is divided into static and dynamic components. The

dynamic loads are assumed to provide system excitation due to the dynamic motion of the cutting tool. Bossmanns et al. [34] and Lin et al. [35] proposed an integrated thermo-mechanical dynamic model for a motorized machine-tool spindle, using an empirical formula to calculate the stiffness of bearings. However, some constants need to be identified in order to use this model.

Li and Shin [36-37] presented a spindle-bearing model that includes thermal effects to predict the bearing stiffness and natural frequencies of the spindle system, using DeMul's bearing model. The bearing configuration, however, is limited to several cases and the gyroscopic effect is not included. Only the natural frequencies are compared in these papers, not the FRF, which is most crucial in predicting the dynamic performance of the spindle during cutting.

Cao and Altintas [38-39] updated the FE model to assist the industrial engineers in achieving a reliable model that can accurately represent the dynamic characteristics of machine-tool spindle systems. Suzuki et al. [40] presented a new technique of determining the transfer function(TF) by utilize inverse research of the self-excited vibrations calculated during an end mill. In their technique a TF could be identified to reduce mistakes between numerical analysis and trial results.

Gagnol et al. [41] outlined the spindle's modal modifications using a finite element model of the high-speed spindle-bearing system, considering the rotor dynamic effects. The reliance of these models were then examined and determined with precision. Tandon and Rajik khan [42] described the technique to design the geometry for a flat end mill in their three-dimensional aspects with regards to surface areas, flutes as helicoidally surfaces and the shank as a surface of revolution.

Rantatalo et al. [43] proposed a method to analyze the lateral vibrations in a milling machine spindle by including finite-element modeling magnetic excitation and inductive displacement measurements of the spindle response. Cao et al. [44] adapted the finite element model to update system dynamic characteristics and achieved the reliable dynamic model for the system.

Tanga and Song [45] designed a new technique which opinions the consequences of multiple-mode features of an application, at high excitation frequencies and wider ranges of spindle speed. These studies are employed to obtain the stability limits to increase the enhanced metal removal rate without chatter.

Gagnola and Bouzgarrou [46] formulated a highly effective design of high-speed spindle-bearing model and it is analyzed with the basic applications of rotor dynamics and its design is remodified with the help of experimentation. It is identified that lobe diagrams

were altered as of the non-rotational frequency response function (FRF) predictions due to changes in dynamic stiffness.

Bravo et al. [47] analyzed a means for obtaining both the uncertainty zones and stability zones in the lobe diagrams, relevant for both the machine tool structure and work piece possess the same dynamic behaviour. For machining the thin walls of work piece at all the intermediary stages, depend on virtual movement of the cutter and work piece a conventional 3-D lobes are employed.

Wang and Chang [48] employed finite element method for analysis of a spindle bearing unit using Rayleigh's formulation, with exclusive considerations of high speed effects in the system.

Lin and Tu [49] designed a flowchart to signify all the general spindle design problems. Sensitivity analysis is carried out for the major eight design factors with the help of finite element analysis to examine their control on the frequencies of the system. Jiang and Zheng [50] established a coupling model for the power-driven high-speed machine tool spindles rests over the bearings using the conventional transfer matrix technique. The bearing model was studied by Jones-Harris theory by incorporating both the effects centrifugal force and gyroscopic.

Hung et al. [51] illustrated the effect of interaction on spindle and machine frame on the machining stability using finite element modelling. Belforte [52] presented the rotor air bearing system for high speed machining process. Various parametric studies are conducted such as clearance and port diameter etc. and are further experimentally verified. Chao et al. [53] considered the joint characteristics for modelling the spindle, tool holder, bearing system to predict the dynamic behaviour. Further these models are experimentally verified. Movahhedy and Mosaddegh [54] included the effect of the gyroscopic moment on the spindle dynamics are illustrated.

Jiang and Zheng [55] considered the drawbar effect on the high speed milling motorized was investigated. The centrifugal and gyroscopic moments were established by the whole transfer matrix method. Figure 2.2 shows the schematic view of the integrated motorized high spindle with multiple bearings at different positions of the spindle.

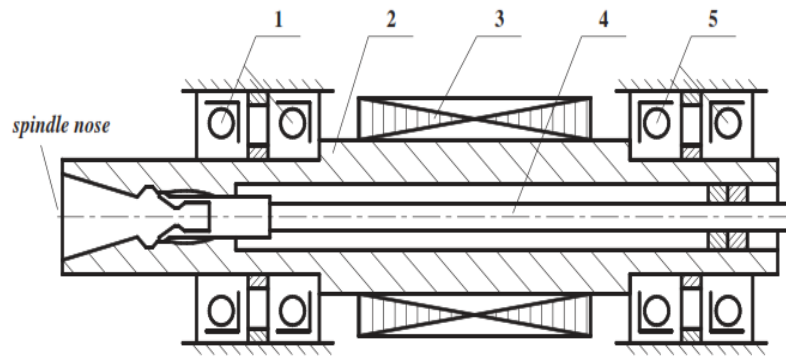


Figure 2.2: Schematic view of the integrated spindle-tool unit [55]

Ahmed and Atsushi [56] used the displacement sensors to measure the spindle stiffness in the radial direction for the precision machining process. A case study was investigated for both the small and medium assemblies.

Wang et al. [57] obtained the optimum process parameters in milling of the titanium alloys using the various algorithms. Chi et al. [58] performed the transient thermal analysis for the high speed spindle. Thermal models are proposed to investigate the thermal contact resistance of the solid joints and bearings.

In this thesis, a general method has been developed for systematically modelling the bearings, spindle shaft, and housing by including the effects of preload and spindle speeds. This method can predict the bearing stiffness, frequency response functions, and time history of responses under cutting forces. It can also simulate the milling operation to predict the cutting performance and contact forces on bearings. Both centrifugal force and gyroscopic effect is included in modelling the spindle shaft. The bearings and spindle shaft are systematically coupled. The contact forces on bearing balls and the time response of the spindle-bearing system under dynamic cutting forces have been studied.

Computational memory and time involved in modelling and analysis of integrated spindle-tool system can be considerably reduced with the use of sub-structural techniques such as Component Mode Synthesis (CMS), Receptance-Coupling Substructure Analysis (RCSA) etc. Especially, RCSA has several convenient stages for handling the systems such as spindle-tool-holder in a modular fashion. In this line, several authors reported the use of RCSA for prediction of dynamic characteristics of machine tool-spindle system.

Park et al. [59] presented a method of assembling known dynamics of the spindle-tool holder with an analytically modeled end mill using the receptance coupling technique. The classical receptance technique is enhanced by proposing a method of identifying the

end mill–spindle/tool holder joint dynamics, which include both translational and rotational degrees of freedom.

Schmitz and Duncan [60] proposed the second generation receptance coupling substructure analysis (RCSA) method, which was used to predict the tool point response for high-speed machining applications. This method divides the spindle-holder-tool assembly into three substructures: the spindle-holder base; the extended holder; and the tool. The tool and extended holder receptances are modeled, while the spindle-holder base subassembly receptances are measured using a “standard” test holder and finite difference calculations.

Movahhedy and Gerami [61] proposed a simple joint model that accounts for rotational degrees of freedom (RDOFs) at joints by considering the bending modes. An optimization method based on genetic algorithm is employed to find parameters of the joint model which shows good agreement and confirmed that the joint model has been successful in predicting the tool bending modes.

Erturk et al. [62] presented an analytical method that used Timoshenko beam theory for calculating the tool point FRF of a given combination by using the receptance coupling and structural modification methods. The model studied the effects of individual bearing and contact parameters on tool point FRF so that better approaches can be found in predicting contact parameters from experimental measurements.

Schmitz et al. [63-65] presented a finite element modeling approach to determine the stiffness and damping behavior between the tool and holder in thermal shrink fit connections. Once the holder and inserted tool section are connected using the finite element analysis-based stiffness and damping values, this subassembly is then rigidly coupled to the (measured) spindle–holder base and (modeled) tool. Namazi et al. [66] introduced the flexible coupling between the tool-holder-spindle interfaces during the coupling. Analytical procedures are adapted to reduce the errors between experimental and theoretical approaches.

Jun et al. [67] measured the receptance of machine-spindle by Impact testing, the Timoshenko beam model was employed to analyze the dynamics of holder and tool shank, and the finite element method (FEM) was used to calculate the receptance of the tool’s fluted portion. Schmitz [68] described the application of receptance coupling substructure analysis (RCSA) to the prediction of torsional and axial, as well as bending, receptances. Kumar and

Schmitz [69] determined spindle-machine dynamics using two different approaches such as synthesis and Euler–Bernoulli beam approach. In the former case, a direct frequency response measurement of a standard artifact inserted in the test spindle

was combined with a cross frequency response measurement to calculate the required rotational receptances. In the later one, a new approach where the direct frequency response measurement is fit using an assumed (fixed-free) form of each mode within the measurement bandwidth.

Zhongqun et al. [70] employed a two -section step beam vibration model was used to calculate the direct and cross response of the tool at free-free status. A RCSA method was employed to identify the joint properties and couple the tool point FRF of the assembly. Ghanatim et al. [71] combined the analytical-experimental sub-structuring procedure was proposed to determine the tool point FRFs usable for different holder-tool configurations. This approach introduced the contact stiffness and damping in more detail with taking into consideration the variations of normal pressure in the tool–holder and holder-spindle joints.

Filiz et al. [72] presented a tool–holder model that incorporates a spectral-Tchebychev technique with the Timoshenko beam equation to obtain a completely parameterized solution. Comparison of the tool–holder model to a three-dimensional finite elements solution showed that the dynamic behavior was captured with sufficient accuracy.

Zhang et al. [73] utilized the Timoshenko beam model to analyze the dynamics at various interfaces of the tool, holder and spindle. The predicted response is verified experimentally with various tool overhang lengths. Mehrpouya [74] measured overall dynamics at the joints for the rigidly coupled substructures by the numerical FE simulation. The inverse receptance coupling (IRC) method and the point-mass joint model were applied at the joints to evaluate the modal properties.

Ganguly and Schmitz [75] applied the particle swarm optimization technique for fitting the spindle-machine measurement using a fixed-free Euler–Bernoulli beam model for each mode. The performance of the optimization process and RCSA in predicting the tool tip frequency response is evaluated at each mode.

Recently, Albertelli et al. [76] presented an approach which avoids the estimates of rotational and moment receptances in order to provide more accuracy to RCSA. Mancisidor et al. [77] proposed an approach based on calculation of fixed boundary-dynamic behaviour of tool to improvise RCSA outcomes.

Design of spindles using RCSA is still an open problem leading to improvisations with additional considerations. The basic formulation considers the spindle-machine as fixed-free beam, while tool and holder are considered as free-free beams. Even though a rigid machine member is holding the spindle, the dynamics of spindle with reference to the housing has considerable effect on the tool tip FRF. In the present thesis, initially the spindle system is supported on the angular contact ball bearings and it is analyzed using 1-

D finite element analysis using Timoshenko beam elements to find the spindle end frequency receptances. Tool and holder receptances are obtained analytically and the coupled receptances give the frequency response at the tool-tip. The methodology is different from conventional fixed-free spindle housing systems analyzed often analytically.

2.3 Cutting force modelling and stability issues

Milling forces predicted by analytical and semi-analytical methods had been extensively used in the past to avoid empirical techniques, which require an abundant amount of experimental data.

In late 1920s, Salomon [80] expressed the specific cutting pressure as an exponential function of chip thickness based on the work done with a straight tooth cutter. Sabberwal [81] and Koenigsberger [82] used similar exponential specific cutting pressures to model milling forces analytically. This model is known as mechanistic model and instantaneous force acting at right angles to the chip area is calculated by the product of the chip area and the specific cutting pressure (K)

$$F_{cuttingforce} = K \times a \times h$$

Where $K=C \cdot h^m$ is the specific cutting pressure, C and m are constants depending on the work-piece material and the milling cutter, $(a \cdot h)$ is the chip area, a is the depth of cut and h is the instantaneous uncut chip thickness. This approach has been adopted by many researchers in the analysis of milling forces.

Armarego [83] defined an alternative form of mechanistic modelling by separating shear deformation (cutting) from the edge effect (rubbing). Cutting coefficients were defined based on the classical oblique model, whereas edge forces were related to rubbing of the work material on the flank face of the cutting edge. The linear edge force model expresses the cutting force as a function of cutting coefficients, axial depth of cut and chip thickness as:

$$F_{cuttingforce} = K_e \times a + K_c \times a \times h$$

where K_e and K_c are the edge and cutting force coefficients, respectively. In order to calculate cutting forces, cutting force coefficients need to be identified for the work material. One of the most widely studied models to determine cutting force coefficients is the mechanistic approach. In this model, cutting forces are measured while keeping immersion constant and varying feed rates. Then, linear regression is applied to fit an approximate line to the average of measured cutting forces, which leads to identification of the unknown cutting force coefficients. Since geometric properties of a milling cutter

such as helix angle, rake angle, relief angle; workpiece material and other variables are all embedded in cutting coefficients, identified cutting coefficients become valid only for a specific cutter and a workpiece material.

In an overview study, Smith and Tlusty [84] classified various models of the milling process into five groups:

(1) The Average Rigid Force Static Deflection Model: This model takes material removal rate as a basis for calculation of process outputs. Cutting force, static tool deflection, torque and power are assumed to be linearly dependant on material removal rate. This model is the simplest and the least accurate as there is no simple relationship between material removal rate and process out-puts.

(2) The Instantaneous Rigid Force Model: Force is computed on incremental sections of the helical cutting edge and the resultant force is calculated using vectorial sum of all incremental forces. In this model, cutter deflection in response to force does not cause any change in force. Sabberwal and Koenigsberger [81, 82] presented the first model in this group.

(3) The Instantaneous Rigid Force, Static Deflection Model: This is similar to the previous model but static deflection of the tool is also considered under static loading. In this model, deflection of the cutter does not influence the uncut chip thickness; hence it does not affect the cutting forces. Form errors can be predicted at points where the helical flutes generate the finished surface.

(4) The Instantaneous Force with Static Deflection Feedback Model: The deflection of the cutter is computed and its influence on the chip thickness and the force is considered by Armarego et al. [86].

(5) The Regenerative Force, Dynamic Deflection Model: This is the most accurate and complex model of the milling process. The equations of motion are solved in the time domain in order to calculate the vibration of the tool. These vibration terms are then used to calculate instantaneous dynamic chip thickness, which results in dynamic cutting forces. Term "regeneration" is used to emphasize that the effect of previous time steps are taken into account.

Tlusty and Ismail [85] presented the time domain simulation of helical end mills by including the structural dynamics of the system. Sutherland and DeVor [86] utilized the regeneration model and improved their static model by considering dynamic cutting force as a feedback.

Montgomery and Montgomery [87] and Altintas [88] contributed significantly to the prediction of chip formation using the exact kinematics of milling. In their model, surface

and cutter locations were divided into small elements so that exact chip thickness was calculated by intersecting the tool and the current surface at each time step. Surface and cutter locations were calculated using dynamics of workpiece and cutter; therefore, nonlinearities such as the tool jumping out of cut and the influence of vibrations could be easily incorporated into their general dynamic model. By integrating the process along each cutting edge in contact with the workpiece, cutting forces, vibrations, and dimensional surface finish were predicted. The geometry of the end-mill cutter employed was shown in Figure 2.3. Where D denotes the diameter of the end mill, β is the helix angle of the cutting flutes, ϕ_p is the pitch angle.

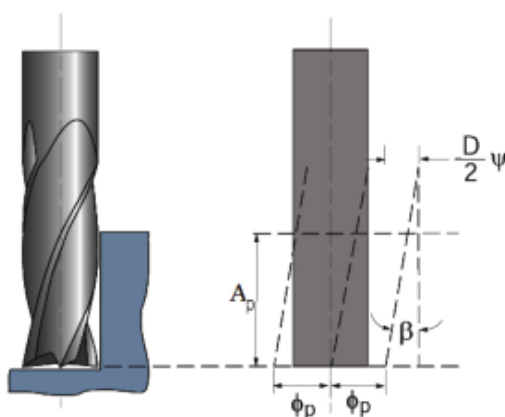


Figure 2.3: Geometry of a helical end mill [88]

Smith and Tlustý [89] used time domain simulation to obtain peak-to-peak force ratios, which were later used as a criterion in identification of stability limits. Several authors [90-92] simulated the dynamic modelling of milling processes using the regeneration technique. Li et al. [93] developed a theoretical model for forces in milling based on a predictive machining theory and the mechanics of milling have been developed. In the model, the action of a milling cutter is considered as the simultaneous work of a number of single-point cutting tools, and milling forces are predicted from input data of the workpiece material properties, the cutter parameters and tooth geometry, the cutting condition, and the types of milling.

Li and Liu [94] accounted the instantaneous undeformed chip thickness was modeled to include the dynamic modulation caused by the tool vibration. Simulated the chatter stability lobes in time-domain and the influences of different spindle speeds on the vibration amplitudes of the tool under a fixed chip-load condition was analyzed. Khachan and Ismail [95] developed a computer graphics approach for time-domain simulation of

chatter in multi-axis milling. The dynamic characteristics at the tool tip as well as the regeneration mechanism were accounted for the graphical chatter simulation.

Altintas et al. [96] presented the frequency and discrete time domain chatter stability laws for milling operations in a unified manner. The time periodic dynamics of the milling process were modelled by averaging time varying directional factors at cutter pitch intervals, the stability lobes were solved directly and analytically.

Lacerda and Lima [97] analytical method was applied in which the time-varying directional dynamic milling forces coefficients were expanded in Fourier series and integrated in the width of cut bound by entry and exit angles. The forces in the contact zone between cutter and workpiece during the cut are evaluated by an algorithm using a mathematical model derived from several experimental tests with a dynamometer located between the workpiece and machine table.

Li and Li [98] developed a predictive milling force model, which represents the action of milling cutter by the simultaneous operations of a number of single-point cutting tools and predicts the milling forces from the fundamental work piece material properties, tool geometry and cutting conditions.

Li et al [99] considered the cutting action of each slices was modelled as an oblique cutting process. The first slice of each tooth, is modelled as oblique cutting with end cutting edge effect and tool nose radius effect, whereas the cutting actions of other slices are modelled as oblique cutting without end cutting edge effect and tool nose radius effect. A windows-based simulation system for the cutting forces in helical end milling was developed using the model.

Chiou et al [100] investigated the influence of the helix angle on the shear stress, friction and shear angle. The helix angle effect on the cutting force model was experimentally determined and it was shown that the cutting force model could be applied for a wide range of cutter helix angles.

Wan and Zhang [101] systematically studied the cutting force modelling methods in peripheral milling process in the presence of cutter run-out. Emphasis was put on how to efficiently calibrate the cutting force coefficients and cutter run-out. Mathematical derivations and implementation procedures were carried out based on the measured cutting force or its harmonics from Fourier transformation.

Wan et al. [102] proposed a new and simplified method for the calibration of cutting force coefficients and cutter run-out parameters for cylindrical end milling using the instantaneous cutting forces measured instead of average ones. The calibration procedure was derived for a mechanistic cutting force model in which the cutting force coefficients

are expressed as the power functions of instantaneous uncut chip thickness (IUCT). Dang et al. [103] proposed a novel mechanistic cutting force model for flat end milling. The prominent feature of this model lies in that the overall cutting forces contributed by both the flank edge and the bottom edge cuttings are simultaneously taken into consideration.

Run out is differences or variations in the diameter of a cutting tool at certain points along the outside edge while the tool is rotating. When an end mill is in rotation it is important that each tooth hits at the exact same spot along the work piece. If one tooth is hitting the work piece more than the others then that tooth is doing the bulk of the work. This will cause the end mill to wear and breakdown more quickly. Therefore, tool run-out and its effects is an important area of research within modelling, simulation, and control of milling forces. Tool run-out causes tool cutting edges to experience uneven forces during milling. Several authors have worked to minimize this effect.

Li and Li [104] developed the theoretical cutting force model for helical end milling with cutter run-out using a predictive machining theory, which predicts cutting forces from the input data of workpiece material properties, tool geometry and cutting conditions. Cifuentes et al. [105] adapted a procedure based on chip thickness modification by means of the fast correction of the tool feed rate. Dynamic feed rate modification was provided by superposing the design of a fast feed system driven by a piezo-electric actuator to the conventional feed drive of the CNC machine tool. The tool deflection due to run-out effect was shown in Figure 2.4.

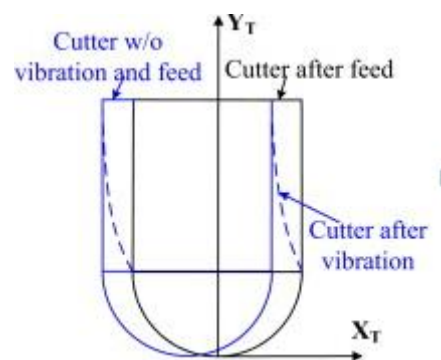


Figure 2.4: Tool deflection due to milling forces [105]

Schmitz et al. [106] investigated the effect of milling cutter teeth run out on surface topography, surface location error, and stability in end milling. The effect of run out on cutting force and surface finish for proportional and non- proportional tooth spacing was isolated by completing experiments on a precision milling machine with 0.1 mm positioning repeatability and 0.02 mm spindle error motion.

Wang et al. [107] proposed a cutting force prediction algorithm considering the influence of cutter vibrations and cutter run-out. The effect of cutter run-out was modelled as an extra feed for machining, which produces a cyclic change on the uncut chip thickness. Sun and Guo [108] presented a new method to effectively model and predict the instantaneous cutting forces in 5-axis milling processes with radial cutter run-out based on tool motion analysis. Identified the run-out parameters from the measured cutting forces were proposed, and then the mechanistic method applied to predict the cutting force.

Taner et al. [109] proposed a generalized cutting force model for the multi-axis milling operation. The cutting kinematics are simulated to determine the exact chip thickness. Sheng et al. [110] predicted the cutting force coefficients by computing the dynamic chip thickness. Taylor's series was adapted for the simulation to improve the efficiency of the solution.

Olufayo and Hossein [111] accessed the quality of the machined surface by monitoring the tool life. Machining parameters are identified online by monitoring using the acoustic emission sensor. Sims et al. [112] presented the fuzzy techniques to acquire the chatter stability regions. The problem of milling chatter uncertainty is then considered within the framework of Ben-Haim's information-gap theory.

Ming et al. [113] investigated the critical lobe curve of the milling process by fuzzy stability theory. Sigmoid functions are developed to model the fuzzy stability lobe diagram. Wan et al. [114] selected the multiple modes for constructing the stability lobe diagrams. The lowest envelop method was considered to predict the overall dynamic compliance of the system.

For milling problems, the mechanism of regenerative chatter could not be worked by using milling cutters with variable pitch. In case of variable pitch cutters, the phase between two waves is not constant for all teeth, thus disturbing the regeneration mechanism. Such disturbance reduces the modulation in chip thickness and slows down vibrations, which consequently increasing the stability of cutting.

In this line several authors had studied the impact of variable pitch effect on the cutting stability. Altintas et al. [115] formulated the stability of the system, by transforming time varying directional cutting constants into time-invariant constants. Constant regenerative time delay in uniform cutters was transformed into non-uniform multiple regenerative time delay for variable pitch cutters.

Budak [116-117] improved the stability against chatter by considering the milling cutters with non-constant pitch angles. An explicit relation was obtained between the stability limit and the pitch variation which leads to a simple equation for determination of optimal pitch angles. Jin et al. [118] improved the semi discretization algorithm to predict

the stability lobes for variable pitch cutters. The shape of the weight distribution function was presented and discussed for non-uniform and harmonically varied helix angles. Song and Zhao [119] presented the design of structural geometry of variable pitch end mills in detail. Based on the analysis of tooth engagement factor, and was expressed to design variable pitch end mill with high milling stability.

Huang [120] predicted the forced vibration in end milling could be reduced by using the variable pitches and variable helix angle of the end mill cutter. Further, experimental study had conducted on the titanium alloys using different cutters with these geometries in both up and down milling process. The different pitch angles of the helical end mill cutter was shown in Figure 2.5.

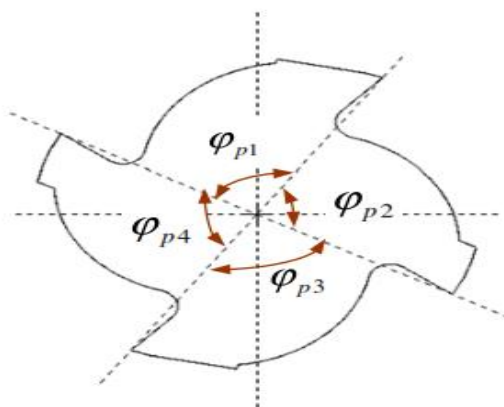


Figure 2.5: Variable pitch angle of the helical end mill [120]

Sellmeier and Denkena [121] investigated both the experimentally and theoretically the process stability of an unequally pitched end mill. This influence was studied theoretically for a simple one DOF system with respect to the number of teeth, different types of alternating and linear tooth pitch variations and the helix angle.

In this work, a detailed time domain simulation based on the regenerative force - dynamic deflection model is used to analyze a milling process with variable cutting conditions (spindle speed, feed rate and depth of cut). Using this time domain simulation, the effect of tool tip run-out and variable pitch was studied for different cases to identify the allowable permissible limits for the system.

Material nonlinearity, structural nonlinearities and high order nonlinear terms in cutting forces are the primary sources of nonlinearity included in cutting models. Several authors were worked to find the effects of nonlinearity on the cutting forces were studied. Hanna and Tobias [122] developed a mathematical theory of nonlinear chatter. In this, the structure is represented by an equivalent single degree of freedom system with

nonlinear stiffness characteristics and the cutting force by a third degree polynomial of the chip thickness. The equivalent model leads to a second order differential equation with nonlinear stiffness and nonlinear time delay terms from which the conditions of steady state chatter are derived.

Martínez et al [123] provided the nonlinear techniques to understand phenomenon of chatter. Considered a weakly nonlinear model with square and cubic terms in both structural stiffness and regenerative terms, to represent self-excited vibrations in machining. An approximate solution was derived by using the method of multiple scales. Gradisek et al [124] presented the expressions for semi-empirical mechanistic identification of specific cutting and edge force coefficients for a general helical end mill from milling tests at an arbitrary radial immersion. The expressions were derived for a mechanistic force model in which the total cutting force was described as a sum of the cutting and edge forces.

Tsai [125] presented the geometrical analysis of a new three-dimensional force model of end milling. The analysis includes description of the relative relationships among undeformed chip thickness, rake angle, cutting velocity, shear plane area and chip flow angle during peripheral and face milling processes.

Landers and Ulsoy [126] accounted the force-feed nonlinearity into the model by extending the regular chatter analysis technique proposed by Budak and Altintas. The analysis provides insight into the feed effect on chatter in machining operations by directly including the force-feed nonlinearity in the chatter analysis. The analysis was developed for turning and face-milling operations and validated via time domain simulations for both operations and by experiments for a face-milling operation.

Moradi et al [127] considered the nonlinear cutting forces of milling process as a function of chip thickness with a complete third order polynomial. An optimal control strategy is developed for chatter suppression of the system described through non-linear delay differential equations. Khaled et al. [128] presented the mechanistic cutting force coefficients for the linear and nonlinear force models of the end milling process. By using both the average force and the optimization technique method, the cutting force coefficients are determined for the end-milling process.

During the milling process, chatter can occur at specific combinations of axial depth-of-cut and spindle speed. Several studies have been performed since the late 1950s regarding regenerative chatter, for example by Altintas and Budak [129] proposed an alternative technique to transform the dynamic milling equations into a time-invariant but radial immersion dependent system. Time-varying dynamic cutting force coefficients were approximated by their Fourier series components, and the chatter-free axial depth of cuts

and spindle speeds are calculated. Gao and Meng [130] examined the chatter isolated islands and non-linear responses of a spindle milling system supported by ball bearings. The stability trends were then examined for several up-milling and down-milling machining processes respectively, with varying machine tool radial immersions.

Tanga and Song [131] developed a new method which considers the effects of multi-mode dynamics of system, at higher excited frequency (i.e. tooth passing frequency) and wider spindle speed ranges, and these stability limits in high-speed milling helps in selection of milling parameters for maximum metal removal rate without chatter. Bravo et al. [132] studied a method for obtaining the instability or stability lobes, applicable when both the machine structure and the machined work piece have similar dynamic behaviours. Three dimensional lobe diagrams have been developed based on the relative movement of both systems, to cover all the intermediate stages of the machining.

Mane et al. [133] considered an integrated spindle–work piece model by coupling with a rotor-dynamics-based spindle FEM model. They showed that the dynamic behaviour of the coupled system to be greatly dependent on two variables, respectively the spindle–work piece relative position and the spindle rotation speed based on this 3D stability lobe diagrams are plotted and examined that the specific speed rules which optimize the maximum material removal rate without chatter during the machining of the flexible workpiece are elaborated.

Solis et al. [134] a new chatter’s analytical prediction method was combined with experimental multi degree-of-freedom systems modal analysis to achieve the objective of generating a new method to obtain the stability lobes information for some vibration modes that can be used to graph the stability lobes for high-speed milling, and these to help in the selection of parameters for chatter free operations.

Quintana et al. [135] conducted experimental analysis to construct stability lobe diagram in which the feed per tooth was maintained as constant. Milling sound analyses of frequencies and amplitudes, through FFT of the time-based audio signal, produced good results and allowed to obtain an accurate approach to understand milling process incidences through vibration occurrence.

Surmann and Biermann [136] described a geometric model for predicting the surface formation resulting from peripheral milling processes when tool vibrations are present. They consider a simple geometric algorithm which converts tool vibration trajectories into a model of the flank surface and this model can be analyzed to the real workpiece.

Seguy et al. [137] consider the effect of spindle speed variation and it is analyzed in the high-speed domain for spindle speeds corresponding to the first flip (period

doubling) and to the first Hopf lobes. The optimal amplitudes and frequencies of the speed modulations are computed using the semi discretization method. They show that stability properties can always be improved by spindle speed variation within the unstable domain of the first flip lobe and amplitude also has a greater effect on the stability of the process than frequency. Raphael et al. [138] improved the precision of stability lobes and examined the importance of the spindle electronic location and speed to organize the precision of the stability lobe diagram (SLD).

Penga et al. [139] studied the influences of the bearing clearance related to the chatter stability of milling process were examined by using numerical simulation method. The results revealed that the presence of bearing clearance could make the milling process easier to enter the status of chatter instability and can shift the chatter frequency. Munoa et al. [140] proposed the bifurcation techniques to improve the stability lobe diagram by using the multiple modes of chatter frequency. This frequency domain method showed that the lobes related to flip bifurcation are a special case of the interaction between modes.

Liu and Chen [141] presented an integrated model to study the electro-thermo-mechanical dynamic behavior of motorized spindles. The model accurately predicted the dynamic characteristics of motorized spindles, and the sensitivities of the six design parameters to the natural frequencies of the spindle system. Kecik et al. [142] developed a nonlinear model of high-speed down milling by taking into account the regeneration and frictional chatter. Model includes friction force produced between an edge of a tool and a workpiece, modeled by nonlinear and non-smooth function and also the time delay effect, which was responsible for vibration regeneration.

Fonga et al. [143] employed an optimal high-speed CNC milling process with high-dimensional quality, to increase the process versatility, flexibility, and robustness. Taguchi dynamic approach coupled with a proposed ideal function model was developed to improve the optimal conditions during the machining process.

Modelling and optimization of cutting process can be effectively achieved by means of intelligent design techniques. In order to achieve a global optimum solution, various meta-heuristic algorithms such as genetic algorithms, ant/bee colonies, particle swarm simulating approaches are often employed in practice. Optimization studies in milling process have been carried-out earlier by several researchers considering various process parameters.

Mounayri et al. [144-145] applied the Radial basis neural network (RBN) for the modeling the cutting forces in ball end milling operation. Experiments were conducted to train as well as to validate and assessed the performance of the proposed network. Zuperl et al. [146] and Briceno et al. [147] applied the neural adaptive control strategy to estimate

the cutting forces in end milling process. Simulations and experiments were conducted to estimate the efficiency of the neural architecture.

Palanisamy and Kalidass [148] predicted the surface roughness by using the artificial neural networks and regression mathematical methods. Zain et al. [149] utilized simulated annealing and genetic algorithms to set the optimal cutting conditions for better machining performance. The two techniques were integrated, and validated by the experimental studies. Saffar and Razfar [150] presented a model to predict the cutting forces in end milling operation and optimized the cutting forces using genetic algorithms (GA). Palanisamy et al. [151] developed a mathematical model relating the dynamics of machining with material behaviour, and adopted GA to optimize the machining time with cutting process parameters and vibration levels of tool.

Hsieh and Chu [152] developed an optimized tool path in five axis milling machine using another heuristic called particle swarm optimization (PSO). Advance and fully informed PSO's are employed to enhance the search capability. Jaberipour and Khorram [153] described two New Harmony search (HS) meta-heuristic algorithms for engineering optimization problems with continuous design variables. First algorithm, proposed harmony search (PHS), introduced a new definition of bandwidth (bw). Second algorithm, improving proposed harmony search (IPHS) employed to enhance accuracy and convergence rate of PHS algorithm.

Zareia et al. [154] presented the harmony search (HS) algorithm to figure out the possible parameters for face-milling. The best possible value of machining parameters for various number of passes for depth of cut, feed and speed was obtained to reduce overall fabrication cost.

In the present work, the parametric data is employed to relate the stable depth of cut with geometric parameters using a feed-forward neural network model. The trained model generating the average stable depth of cut is employed in conjunction with harmonic search optimization scheme to achieve optimum spindle-tool data.

2.4 Milling process control issues

The presence of vibrations in machining processes has a negative effect on the quality of the machined surfaces. As formerly described these vibrations are sources of machine fatigue, tool damage, high cutting edge wear, machine tool damage, wear of machine tool components and annoying high noise levels. Spindle is considered one of the most crucial machine-tool components especially in high speed machining and its performance is often strictly related to the quality and the surface finishing of the machined work pieces.

Albrecht et al. [155] measured the cutting forces from the displacements of rotating spindle shafts. A capacitance displacement sensor is integrated into the spindle and measures static and dynamic variations of the gap between the sensor head and the rotating spindle shaft under cutting load. Park and Altintas [156] presented a dynamically compensated Spindle Integrated Force Sensor (SIFS) system to measure cutting forces. Piezo-electric force sensors were integrated into the stationary spindle housing. The structural dynamic model between the cutting forces acting on the tool tip and the measured forces at the spindle housing was identified.

Jang and Tarn [157] used a piezoelectric actuator for the active vibration damper of cutting tool. The actuator resonance tuned over a wide frequency range by adjusting the size of the inertial mass, so that the actuator could provide an extremely large damping force to suppress undesired vibration of the cutting tool at the resonance frequency of the actuator. Duncan et al. [158] applied the receptance coupling substructure analysis (RCSA) to develop the models for a stacked flexure setup and a spindle-holder-tool assembly. Dynamic absorber effect was introduced into the model to improve the system dynamic stiffness and, therefore, increase the critical stability limit in machining.

Madoliat et al. [159] proposed a frictional damper so as to enhance structural damping leading to the chatter suppression in the slender end-mill tool. Parametric study was conducted to find optimum parameters of the damper for the increase of the stability limit. Figure 2.6 shows the frictional damper used in the end-mill tool.

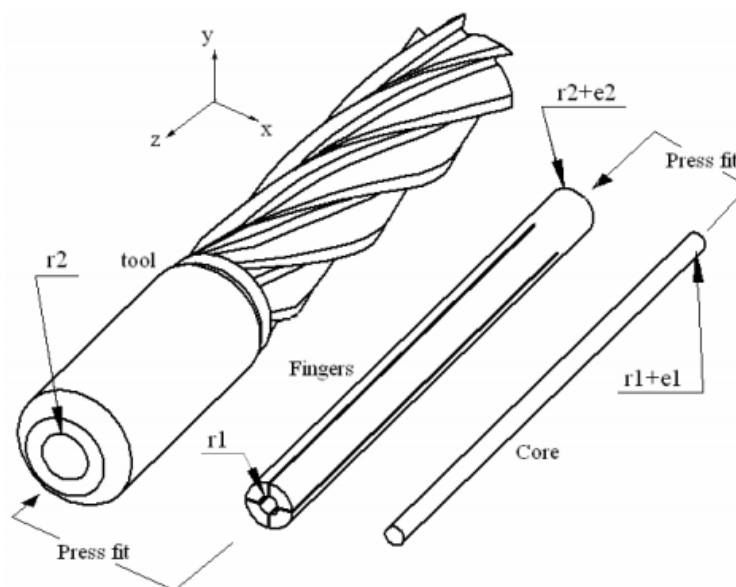


Figure 2.6: Geometry of milling tool with damper [159]

Parus et al. [160] presented an active control system that counteracts the development of chatter vibration. The proposed active control system employed a Linear

Quadratic Gaussian (LQG) algorithm and piezoelectric actuator to suppress vibration during cutting.

Madoliat et al. [161] proposed a frictional damper for suppression of chatter in slender end mill tool. An analytical model including accurate modeling of friction in sliding and pre-sliding regions was developed for this damper. Regib et al. [162] presented a method for programming spindle speed variation for machine tool chatter suppression and it was based on varying the spindle speed for minimum energy input by the cutting process. Sulaiman et al. [163] presented an approach to chatter control during end milling of titanium alloy Ti-6Al-4V using ferrite permanent magnets to reduce the unwanted vibrations. A special fixture was fabricated and mounted on a vertical machining centre spindle for holding the permanent magnet bars, used in suppressing the vibration amplitudes.

Monnin et al. [164-165] presented an active system integrated into a spindle unit with two different optimal control strategies. In the first strategy, dynamics of the machine structure in the controller design was considered which minimizes the influence of cutting forces on tool tip deviations. While the other, takes explicitly the process interaction into account and attempts to guarantee the stability of the overall closed-loop system for specific machining conditions. Graham et al. [166] utilized the edge theorem and the zero exclusion condition, a robust chatter stability model, based on the analytical chatter stability milling model, was developed. compared to the projected pseudo single degree of freedom model the reliability was improved.

Moradi et al. [167] designed a tunable vibration absorber (TVA) to suppress regenerative chatter in milling of cantilever plates. Under regenerative chatter conditions, optimum values of the absorber position and its spring stiffness were found such that the plate vibration was minimized. Zhang et al. [168] developed an active model predictive control (MPC) method for the milling process such that the chatter-free domain of stable operation was substantially enlarged and achieve a higher efficiency.

Rafal et al. [169] investigated stability of the milling process of titanium alloy Ti6242 on the basis of experimental time series of cutting forces. In order to obtain the initial point of chatter vibrations, the recurrence quantification analysis and the Hilbert–Huang transform (HHT) were employed. Wu et al. [170] included the various machine tasks like thread milling, weld cutting, and boring operations using the robots. Different vibration reduction models are incorporated to improve the stability of the machining process.

2.5 Summary

This chapter provides an intensive review on the various integrated spindle-tool design variables related to the machining instability. Various numerical modelling techniques for the spindle design issues that made progress in the past decades have been studied and discussed. Further, the literature review focuses on previous research in the area of machining stability, outlining work in the implementation of analytical and time-domain simulations for stability predictions.

The following issues are found to be the open areas:

- (a) Design of spindle for stable cutting conditions by selecting several secondary parameters including bearing dynamics, interface dynamics, tool effects etc.
- (b) Improving the stability using new cost-effective control methods which are applied to generalized rotor dynamic systems.
- (c) Development of improvised spindle designs for using a machine tool for different machining operations.

The next chapter discusses about the various mathematical models to arrive the tool tip response of spindle-tool unit.

Chapter-3

Dynamic Modeling of spindle-tool unit

The conventional milling spindle system normally has spindle housing carrying spindle shaft over the front and rear bearings, a tool holder and tool. The machine tool frame affects the dynamic properties of the tool and spindle by improving its stiffness and damping [17]. The frame represents a structure with limited stiffness which supports the spindle system. Interaction of the machine frame and spindle causes a shift in the spindle natural frequencies and frequency responses. The machine frame structure contributes also to an increased level of structural damping at the tool end point of the spindle. In practice, the frame (housing) is considered as a rigid member and spindle unit dynamics drastically influences the cutting process stability. Therefore, design of spindles is of paramount importance in the structure. This chapter describes dynamic modeling of spindle-tool unit of a standard CNC milling centre using finite element modelling and receptance coupling methodology. Various considerations including bearing dynamics, the spindle-tool coupling stiffness effects as well as the geometry of the tool on the tool-tip frequency responses are explained.

A typical spindle system consists of tool, tool-holder, spindle shaft, housing, bearings, pulleys, sleeves and nuts, and the motor. Figure. 3.1 shows the schematic of a vertical milling tool spindle system.

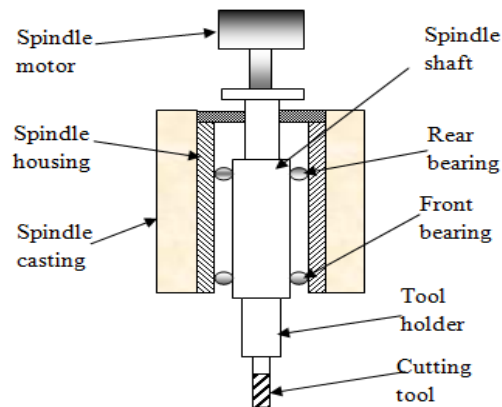


Figure 3.1: Integrated spindle tool unit

The dynamic stiffness at the tool tip, where the cutting forces are acting, is the sum of the stiffness of all the elements of the system, i.e., the tool, the tool-holder, the shaft, the bearings, the housing and the mechanical joints between them. Here, the machine part is

not included because of its lower natural frequencies. On the other hand, the spindle rotation introduces forces that change the stiffness of both the bearings and the shaft, thus modifying the dynamic response at the tool tip. The front and rear bearings are often of rolling contact type. Ball bearings usually have initial preload. When the spindle does not rotate, the contact angle of balls with the inner and outer raceways is defined by the geometry and kinematics of the bearing [18]. When the spindle starts rotating, additional radial load due to contact of balls with races comes into picture. The centrifugal force reduces the initial preload and slightly changes the kinematics of the bearing, varying the contact angles and thus decreasing the bearing and spindle stiffness. On the other hand, the contact force in the ball-raceway interface varies due to the cutting forces and the thermal gradient between the inner and outer raceways of the bearing at high speeds. At the same time, a gyroscopic moment acts on the shaft due to the high rotating speed, which splits the modal frequencies into forward and backward whirling modes and changes the tool tip frequency response [21]. The experimental measurement of the real FRF at the tool tip when the spindle runs at high speeds becomes therefore very complex.

To avoid lengthy experimental approaches, often modelling of the spindle-tool holder-tool system using finite element modelling is preferred. Another way is to employ the substructure coupling techniques which allows the dynamics of the spindle and the tool to be studied separately and then combined to obtain the system global response. Consequently, once the spindle dynamics have been studied theoretically or experimentally, it is possible to estimate the response at the tool tip for different tools.

The dimensions of the spindle shaft- tool holder-tool are taken approximately of the original machine tool. The length of the spindle shaft is taken as 248mm, tool-holder as 80mm and tool as 60mm.

3.1 Analytical modeling of spindle system

Often the tool, tool-holder, spindle shaft and housing are modeled as beams. Pulley and nut as treated as rigid disks and the sleeve is considered as a bar. The motor is modelled as a rigid mass.

3.1.1 Modeling of spindle shaft

A segment of shaft treated as a Timoshenko beam, is shown in Figure 3.2. A Cartesian coordinate system named $O - xyz$ is defined on the beam where the x -axis is coinciding with the centroidal axis before the beam gets deformed [25].

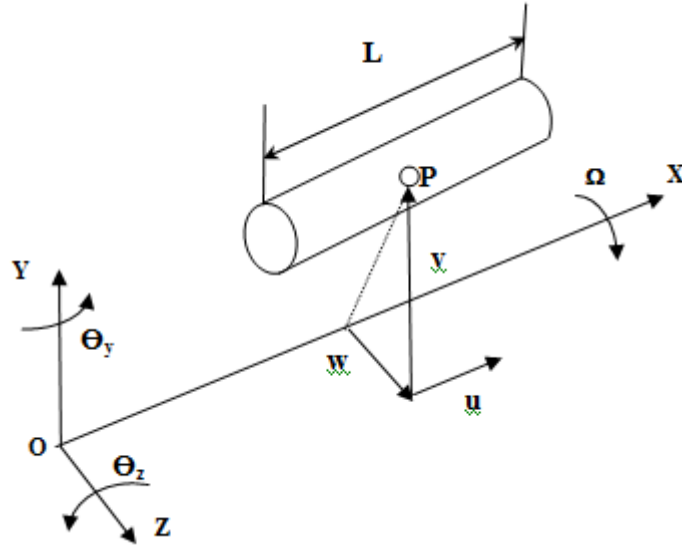


Figure 3.2: Section of the beam

Kinetic energy for a section of beam of length L is [28]:

$$T = \int_0^L \frac{1}{2} J \rho \Omega^2 dx + \int_0^L \frac{1}{2} \rho A (\dot{u}^2 + \dot{v}^2 + \dot{w}^2) dx + \int_0^L \frac{1}{2} I \rho (\dot{\theta}_y^2 + \dot{\theta}_z^2) dx + \int_0^L \frac{1}{2} J \rho \Omega (\dot{\theta}_y \theta_z - \theta_y \dot{\theta}_z) dx \quad (3.1)$$

where $I = (1/4)\pi R^4$, $J = (1/2)\pi R^4$ are respectively the cross-sectional and polar moments of inertia of circular shaft element, R is the radius of the beam section, A is the cross-sectional area, ρ is the density of the material and Ω is the rotational speed of the beam. The first term is the energy of rotation about the axis x . The second term is the energy of translational movement. The third term is the energy of rotation about the axis y and z . The last term is the energy contribution from the gyroscopic moment.

Similarly the potential energy of spindle (shaft) element is given as:

$$V = \int_0^L \frac{1}{2} EA \left(\frac{\partial u}{\partial x} \right)^2 dx + \int_0^L \frac{1}{2} EI \left[\left(\frac{\partial \theta_y}{\partial x} \right)^2 + \left(\frac{\partial \theta_z}{\partial x} \right)^2 \right] dx + \int_0^L \frac{1}{2} k_s AG \left[\left(\theta_y + \frac{\partial w}{\partial x} \right)^2 + \left(\theta_z - \frac{\partial v}{\partial x} \right)^2 \right] dx + \int_0^L \frac{1}{2} EA \left[\left(\frac{1}{2} \left(\frac{\partial v}{\partial x} \right)^2 \right)^2 + \left(\frac{1}{2} \left(\frac{\partial w}{\partial x} \right)^2 \right)^2 \right] dx \quad (3.2)$$

where k_s is shear correction factor.

The work done by external forces is given by:

$$W = \int_0^L (q_x u + q_y v + q_z w + m_y \theta_y + m_z \theta_z) dx + \int_0^L \frac{1}{2} \Omega^2 v^2 \rho A dx + \int_0^L \frac{1}{2} \Omega^2 w^2 \rho A dx \quad (3.3)$$

where q_x , q_y and q_z are distributed load per unit length in directions x , y , and z , respectively. and m_y and m_z are distributed moment per unit length about axis y and z , respectively.

By using Hamilton's principle [38],

$$\delta I = \delta \int_{t_1}^{t_2} (T - V + W) dt = 0 \quad (3.4)$$

(Where δ is variational operator), the following equations of motion for the beam are obtained

$$\rho A \frac{d^2 v}{dt^2} - EA \frac{\partial^2 u}{\partial x^2} - q_x = 0 \quad (3.5)$$

$$\rho A \frac{d^2 v}{dt^2} - \frac{\partial}{\partial x} \left[k_s AG \left(\frac{\partial v}{\partial x} - \theta_z \right) - P_a \frac{\partial v}{\partial x} \right] - q_y - \Omega^2 \rho A v = 0 \quad (3.6)$$

$$\rho A \frac{d^2 w}{dt^2} - \frac{\partial}{\partial x} \left[k_s AG \left(\frac{\partial w}{\partial x} + \theta_y \right) - P_a \frac{\partial w}{\partial x} \right] - q_z - \Omega^2 \rho A w = 0 \quad (3.7)$$

$$\rho I \frac{d^2 \theta_y}{dt^2} + \Omega \rho J \frac{d \theta_z}{dt} - EI \frac{\partial^2 \theta_y}{\partial x^2} + k_s AG \left(\frac{\partial w}{\partial x} + \theta_y \right) - m_y = 0 \quad (3.8)$$

$$\rho I \frac{d^2 \theta_z}{dt^2} - \Omega \rho J \frac{d \theta_y}{dt} - EI \frac{\partial^2 \theta_z}{\partial x^2} - k_s AG \left(\frac{\partial v}{\partial x} - \theta_z \right) - m_z = 0 \quad (3.9)$$

where the first equation is the force equilibrium along axis x . The second and third equations are the force equilibrium along axis y and z . The fourth and fifth equations are the moment equilibrium about axis y and z . $P_a = \frac{1}{2} EA \left(\frac{\partial v}{\partial x} \right)^2$ or $\frac{1}{2} EA \left(\frac{\partial w}{\partial x} \right)^2$ is the axial force contributing to the bending deformation.

3.1.2 Bearing system

Bearing flexibility plays an important role in the dynamics of spindle-tool unit. A major source of nonlinear behavior in a bearing is attributed to the Hertzian contact. The analysis of vibrations caused by rolling element bearing gives important information to analyse the rotor dynamics of the system. The following assumptions are made in bearing force considerations [8]:

- 1) The motion of rolling elements, races and the rotor is in the plane of the bearing only.
- 2) Hertzian theory of elasticity is used for calculating the deformations in the contact. The effect of elasto-hydrodynamic lubricated contact is neglected.

- 3) The cage is considered as rigid and there is constant angular separation between the rolling elements and hence no contact between them. The angular velocity of cage and rolling element can change at the same rate over time.
- 4) Only structural damping is assumed to be present in the model and damping of ball bearings is neglected.
- 5) There is no slipping of balls as they roll on the surface of races.
- 6) Effects due to temperature change such as change in viscosity of lubricant, deformation of balls and races are neglected.
- 7) The lateral moments at the bearing are ignored in comparison with three forces.

Figure 3.3 shows a simplified ball-bearing model considered for analysis. The contact forces arise between balls and race during rotation of the spindle and can be expressed in terms of the radial deformation δ_j of j^{th} ball according to [25]:

$$F_{zb} = \sum_{j=1}^{N_b} \left(-C_b (\delta_j)^n H \right) \cos \alpha_j \cos \theta_j \quad (3.10a)$$

$$F_{yb} = \sum_{j=1}^{N_b} \left(-C_b (\delta_j)^n H \right) \sin \alpha_j \cos \theta_j \quad (3.10b)$$

$$F_{xb} = \sum_{j=1}^{N_b} \left(-C_b (\delta_j)^n H \right) \sin \theta_j + F_a \quad (3.10c)$$

where $n = \frac{3}{2}$ for ball bearing; $n = \frac{10}{3}$ for roller bearing

Here, F_a is axial preload, θ_j is the ball contact angle with outer race and the radial deformation of the j^{th} ball is expressed as $\delta_j = \sqrt{w_0^2 + v_0^2} - R$. Also, N_b , r and R are respectively indicate the number of balls, radii of inner race and outer race and r_0 is radial clearance.

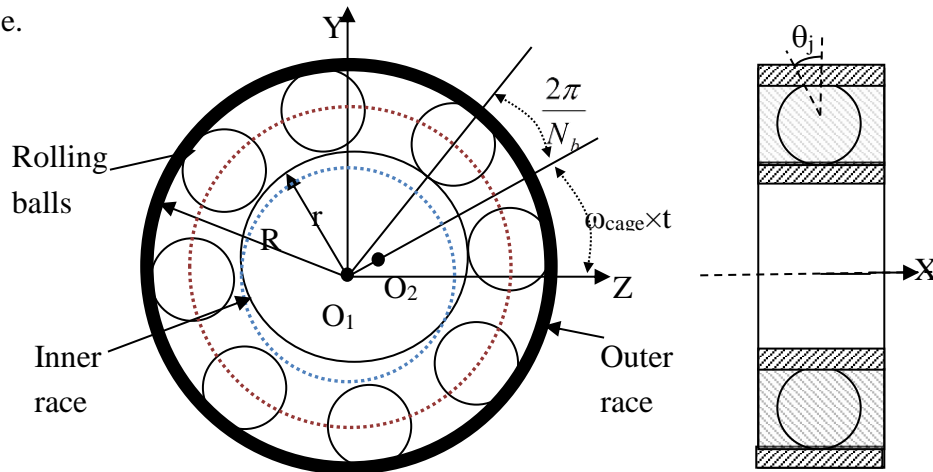


Figure 3.3: Ball Bearing schematic

Further, C_b is interface stiffness which depends on material and radii of curvatures of contacting surfaces. The components of radial deformations of the circumferential points on balls are given as:

$$w_o = w + (r + 2r_b) \cos \alpha_j ; v_o = v + (r + 2r_b) \sin \alpha_j \quad (3.11)$$

with $r_b = \left[\frac{R - (r + r_0)}{2} \right]$ is ball radius in terms of radial clearance r_0 and u and v are time-varying bending displacement at the bearing node (shaft). The heavy-side function H used in eq.(3.10) is defined as

$$H = \begin{cases} 1, & \text{if } \delta_j > 0 \\ 0, & \text{if } \delta_j \leq 0 \end{cases} \quad (3.12)$$

Also α_j is angular location of the j^{th} ball, which is given by

$$\alpha_j = \omega_{\text{cage}} \times t + \frac{2\pi}{N_b} (j-1), j=1, 2, \dots, N_b \quad (3.13)$$

Here, ω_{cage} is the angular velocity of the cage given in terms of speed of rotation Ω as:

$$\omega_{\text{cage}} = \frac{\Omega \times r}{(R + r)} \quad (3.14)$$

The stiffness behaviour of the spindle supported over the angular contact ball bearings rely about the practical loading and the positions of bearing arrangement. Many different empirical formulae are available in literature to estimate the static radial stiffness of the bearings in terms of number of balls(N), ball diameter(D), axial preload (F_a) and contact angle of ball bearing(θ) and one such useful expression frequently employed is given by [48]

$$k_{xx} = k_{yy} = 1.77236 \times 10^7 \times (N_b^2 \cdot D_b)^{1/3} \frac{\cos^2 \theta}{\sin^{1/3} \theta} F_a^{1/3} \text{ N/m} \quad (3.15)$$

3.2 Coupled spindle tool system

The dynamic behavior of the spindle-holder-tool assembly plays a significant role in cutting process stability. The quality of machined surface depends on the frequency response function of the spindle system at the tool tip. Flexible connections at the spindle-holder and holder-tool interfaces also influence the dynamic of spindle unit. The interaction between these three components affects the overall dynamic behavior of the assembly.

3.2.1 Distributed parameter modeling

The spindle shaft provides motion to the cutting tool. In milling operation, the tool and spindle are coupled by a holder (adapter) as shown in Figure 3.4.

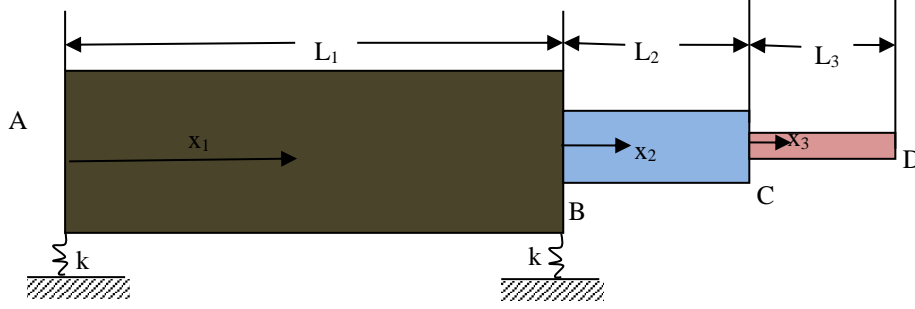


Figure 3.4: Simplified spindle-tool unit

The frequency response function at the tool tip is predicted by the three step continuous beam model. The equation of motions for the individual portions of the beam elements based on the Timoshenko beam theory is written as follows:

For the portion CD (tool) ($0 \leq x_3 \leq L_3$)

$$EI_1 \frac{\partial^4 y_1}{\partial x_1^4} + \rho A_1 \frac{\partial^2 y_1}{\partial t^2} - \rho A_1 r_{o1}^2 \frac{\partial^4 y_1}{\partial x_1^2 \partial t^2} - \frac{EI_1 \rho}{\kappa G} \frac{\partial^4 y_1}{\partial x_1^2 \partial t^2} + \frac{\rho^2 A_1 r_{o1}^2}{\kappa G} \frac{\partial^4 y_1}{\partial t^4} = 0 \quad (3.16)$$

For the portion BC (tool-holder) ($0 \leq x_2 \leq L_2$)

$$EI_2 \frac{\partial^4 y_2}{\partial x_2^4} + \rho A_2 \frac{\partial^2 y_2}{\partial t^2} - \rho A_2 r_{o2}^2 \frac{\partial^4 y_2}{\partial x_2^2 \partial t^2} - \frac{EI_2 \rho}{\kappa G} \frac{\partial^4 y_2}{\partial x_2^2 \partial t^2} + \frac{\rho^2 A_2 r_{o2}^2}{\kappa G} \frac{\partial^4 y_2}{\partial t^4} = 0 \quad (3.17)$$

For the portion AB (spindle shaft) ($0 \leq x_1 \leq L_1$)

$$EI_3 \frac{\partial^4 y_3}{\partial x_3^4} + \rho A_3 \frac{\partial^2 y_3}{\partial t^2} - \rho A_3 r_{o3}^2 \frac{\partial^4 y_3}{\partial x_3^2 \partial t^2} - \frac{EI_3 \rho}{\kappa G} \frac{\partial^4 y_3}{\partial x_3^2 \partial t^2} + \frac{\rho^2 A_3 r_{o3}^2}{\kappa G} \frac{\partial^4 y_3}{\partial t^4} = 0 \quad (3.18)$$

were $y_1(x_1, t)$, $y_2(x_2, t)$ and $y_3(x_3, t)$ are the transverse displacements for the elemental portions CD, BC and AB respectively. Similarly, E , I , ρ , G and κ represents the Young's modulus, moment of inertia for the corresponding beam sections, density of the beam material, shear modulus and Timoshenko shear coefficient respectively. The approximate solution is obtained from the method of separation of variables as: $y_1 = Y_1(x_1)e^{i\omega t}$, $y_2 = Y_2(x_2)e^{i\omega t}$, $y_3 = Y_3(x_3)e^{i\omega t}$. Further, at each connecting point, the following boundary conditions are applicable [57].

1. For the point D (Free end):

$$\kappa A_3 G \left[\frac{\partial y_3}{\partial x_3} - \phi_3 \right]_{x_3=L_3} = 0; \left[EI_3 \left[\frac{\partial \phi_3}{\partial x_3} \right] \right]_{x_3=L_3} = 0 \quad (3.19)$$

2. For the point C:

$$\begin{aligned} \kappa A_2 G \left[\frac{\partial y_2}{\partial x_2} - \phi_2 \right]_{x_2=L_2} &= \kappa A_3 G \left[\frac{\partial y_3}{\partial x_3} - \phi_3 \right]_{x_3=0} \\ \left[EI_2 \left[\frac{\partial \phi_2}{\partial x_2} \right] \right]_{x_2=L_2} &= \left[EI_3 \left[\frac{\partial \phi_3}{\partial x_3} \right] \right]_{x_3=0} \quad [\phi_2]_{x_2=L_2} = [\phi_3]_{x_3=0} \\ [y_2]_{x_2=L_2} &= [y_3]_{x_3=0} \end{aligned} \quad (3.20)$$

3. For the point B (supported by bearing of stiffness $k=k_{xx}$)

$$\begin{aligned} \kappa A_1 G \left[\frac{\partial y_1}{\partial x_1} - \phi_1 \right]_{x_1=L_1} - \kappa A_2 G \left[\frac{\partial y_2}{\partial x_2} - \phi_2 \right]_{x_2=0} &= k y_2 \Big|_{x_2=0} \\ \left[EI_1 \left[\frac{\partial \phi_1}{\partial x_1} \right] \right]_{x_1=L_1} &= \left[EI_2 \left[\frac{\partial \phi_2}{\partial x_2} \right] \right]_{x_2=0} \quad [\phi_1]_{x_1=L_1} = [\phi_2]_{x_2=0} \\ [y_1]_{x_1=L_1} &= [y_2]_{x_2=0} \end{aligned} \quad (3.21)$$

4. For the point A (supported by bearing of stiffness $k=k_{xx}$)

$$\begin{aligned} \kappa A_1 G \left[\frac{\partial y_1}{\partial x_1} - \phi_1 \right]_{x_1=0} &= k y_1 \Big|_{x_1=0} \\ \left[EI_1 \left[\frac{\partial \phi_1}{\partial x_1} \right] \right]_{x_1=0} &= 0 \end{aligned} \quad (3.22)$$

The solution obtained by the means of continuous beam model for the spindle-tool structure is very ambiguous and takes more time in calculation. Because of these, sub-structural coupling techniques and finite element modelling are often employed which gives tool point FRF with less computational time and desired accuracy.

3.2.2 Finite element modeling

The finite element modeling is one of the most effective approaches for reasonably provide the relationship between the displacements and forces at a finite number of discrete points (called nodes) of a continuous structure [44].

By considering the shape functions [N] and [D] according to the following equations.

$$\begin{Bmatrix} v \\ w \end{Bmatrix} = [N][q_e] \quad (3.23)$$

$$\begin{Bmatrix} \theta_y \\ \theta_z \end{Bmatrix} = [D][q_e] \quad (3.24)$$

$$\text{Where } [N] = \begin{bmatrix} N_{r1} & 0 & 0 & N_{r2} & N_{r3} & 0 & 0 & N_{r4} \\ 0 & N_{r1} & -N_{r2} & 0 & 0 & N_{r3} & -N_{r4} & 0 \end{bmatrix}$$

$$[D] = \begin{bmatrix} 0 & -N_{\theta1} & N_{\theta2} & 0 & 0 & -N_{\theta3} & N_{\theta4} & 0 \\ N_{\theta1} & 0 & 0 & N_{\theta2} & N_{\theta3} & 0 & 0 & N_{\theta4} \end{bmatrix}$$

Where, [N] and [D] are translational and rotational shape function matrices and are given in the appendix-A. By introducing the above equations into the kinetic and potential energy expressions and carrying out the integrations over the element length and applying the Hamilton's principle, the following matrix equations of motion for the beam are generated

$$[M_b] = \int_0^L \rho A [N]^T [N] ds + \int_0^L \rho I [D]^T [D] ds \quad (3.25)$$

$$[G_b] = \int_0^L \rho I_p [D]^T \begin{bmatrix} 0 & 1 \\ -1 & 0 \end{bmatrix} [D] ds \quad (3.26)$$

$$[K_b] = \int_0^L EI [D']^T [D'] ds + \kappa GA \int_0^L \left\{ [N]^T [N] + [D]^T [D] + 2[N]^T \begin{bmatrix} 0 & -1 \\ 1 & 0 \end{bmatrix} [D] \right\} ds \quad (3.27)$$

The following equations of the beam in matrix forms can be obtained by using the finite element method for the whole spindle-tool system is written as:

$$[M_b]\{\ddot{q}\} - \Omega [G_b]\{\dot{q}\} + \left([K_b] + [K_b]_p - \Omega^2 [M_b]_c \right) \{q\} = \{F_b\} \quad (3.28)$$

Where [M_b] is the mass matrix, [M_b]_c is the mass matrix used for computing the centrifugal forces, [G_b] is the gyroscopic matrix which is skew-symmetric, [K_b] is the stiffness matrix, [K_b]_p is the stiffness matrix due to the axial force, and {F_b} is the force vector, including the distributed and concentrated forces. The sub-script b represents the beam. The details of the matrices are also shown in Appendix-A. The vibration performance of the spindle-tool device can be effectively recognized using confined spindle assembly model shown in Figure 3.5.

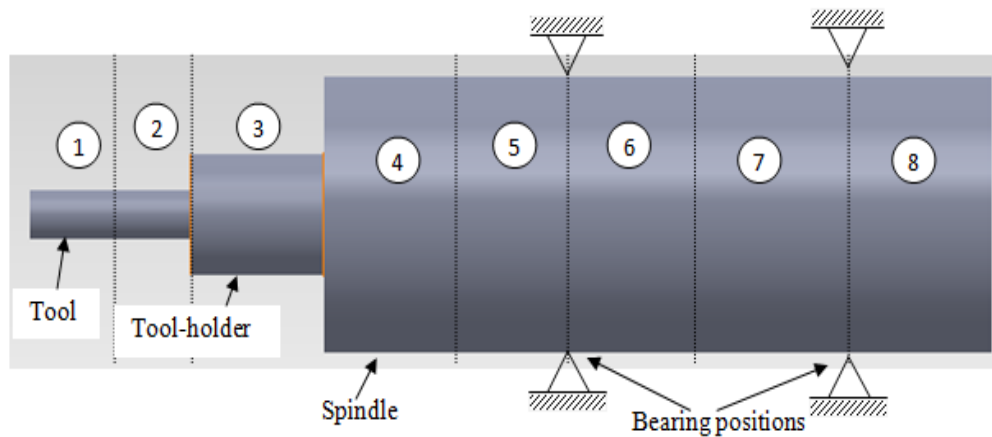
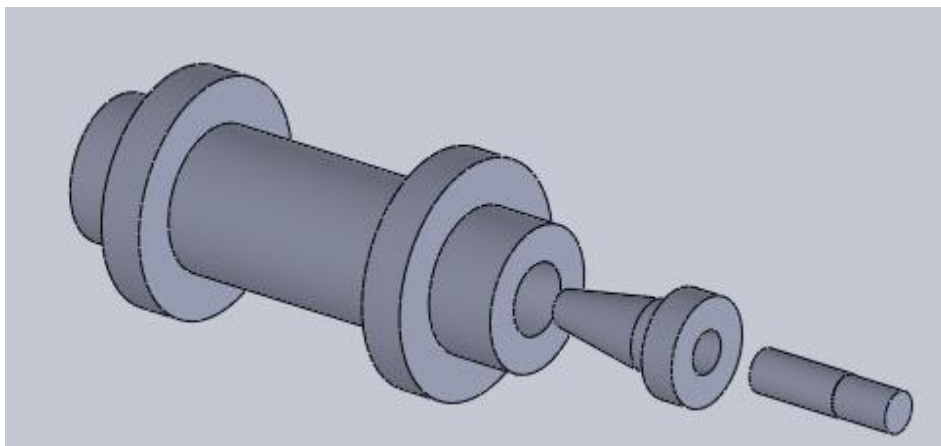


Figure 3.5: Equivalent model of spindle-tool device

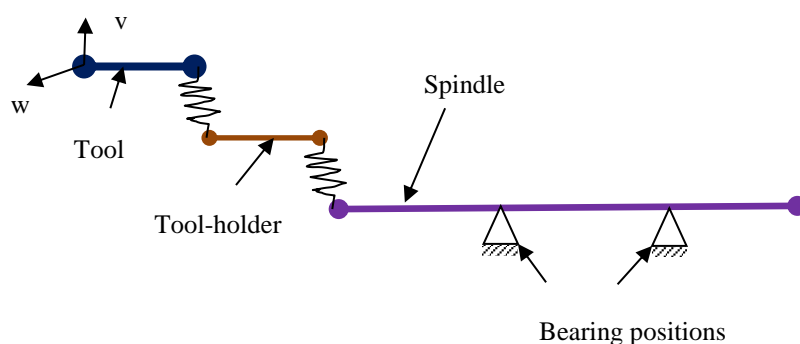
All the segments of the spindle-holder-tool can be discretized with Timoshenko beam elements incorporating shear deformation and rotary inertia effects. In the present analysis, eight elements are considered and each node has two translations (x , y) and two rotational (θ_x , θ_y) degrees of freedom. The spindle is supported between two bearings at the front and rear positions.

3.2.3 Effect of Joint stiffness in spindle-holder-tool assemblies

In the spindle-holder assemblies, often the joints cannot be considered as perfectly rigid. The joints are primarily responsible for the major part of the energy dissipation in assembled structures during cutting process [46]. The dissipated work in a joint depends on the excitation force. Figure 3.6 shows the segments of the spindle-holder-tool joined by spring elements at interfaces along with a Solid Works assembly model.



(a) CAD model in Solid Works



(b) Line diagram with interfaces

Figure 3.6: Equivalent line model of spindle tool unit

Flexible joints at tool-holder and spindle-holder locations are represented by two springs having equivalent stiffness in y and z (bending) directions. The stiffness behavior of angular contact bearings rely on the applied loads and the bearing layout.

3.2.4 Modified Receptance coupling theory

In the full-order finite element modelling described above, as the number of elements increases so as to account the spindle shaft non-uniformities in cross-section, the compellability in handling the matrices rises enormously. The computational time increases and if the simulations are required for several tool-holder combinations, it takes huge computational memory. In this regard, receptance coupling substructure analysis procedure as a reduction scheme often employed in practice. In conventional methodology, often spindle machine fixed to the machine tool is tested experimentally using impact testing, while tool-holder are examined using beam theories analytically.

In the present work, unlike use of the experimental data of the spindle unit, a FE model of spindle alone is employed to obtain spindle-tip receptances. While the tool and holder receptances are computed analytically in an independent way. These spindle-device receptances are then systematically combined to the beam designs of tool and tool-holder to visualize the tool end point receptances for grouping of tool-holders and tools. The tool and the tool-holder are described using Bishop and Johnson theory with free-free boundary conditions, while the receptances of the spindle-machine are difficult to model based on first principles, primarily due to the difficulty in estimating damping at interfaces and the actual supporting conditions [64]. The overall principle is depicted in Figure 3.7.

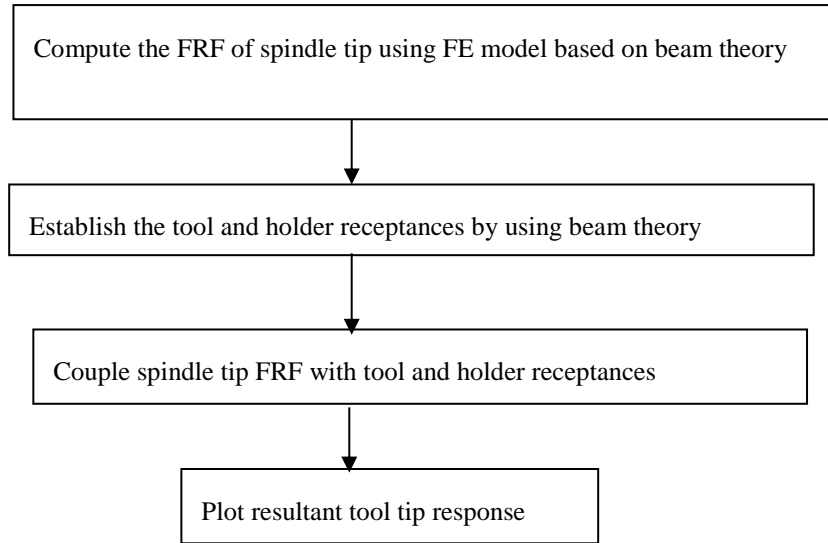


Figure 3.7: Overall process chart

The four bending receptances primarily used to describe each component.

These are presented below:

displacement to force, $u_{ij}=x_i/f_j$

displacement to couple, $v_{ij}=x_i/m_j$

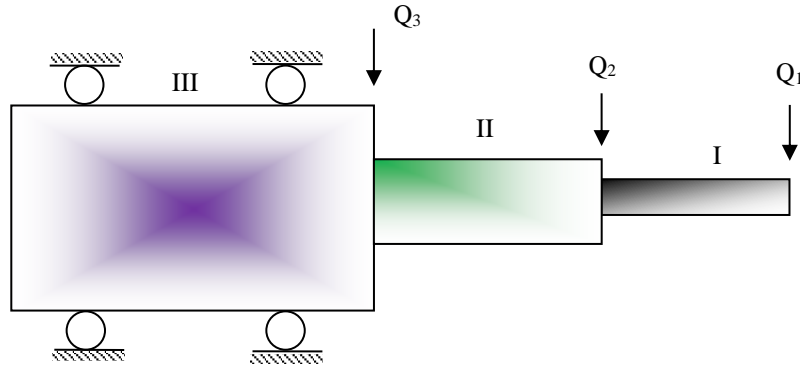
rotation to force, $w_{ij}=\theta_i/f_j$

rotation to couple, $z_{ij}=\theta_i/m_j$

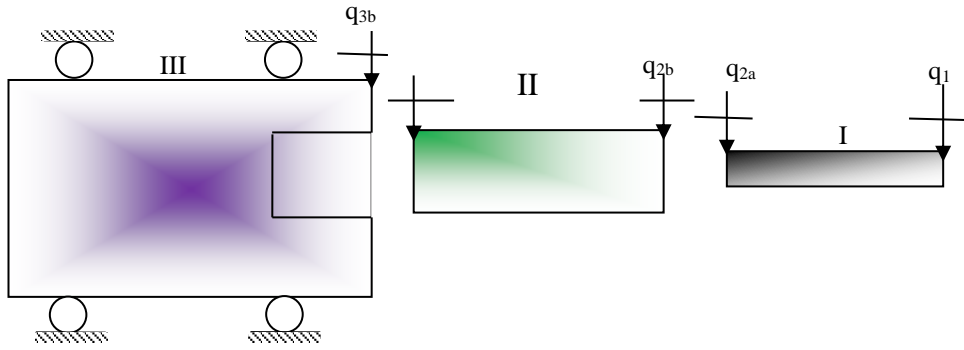
where i and j are the measurement and force/moment application coordinate locations, respectively. If i and j are equal, the receptances are referred to as direct-receptances; otherwise, they are called cross-receptances [63]. The individual component, or substructure-receptances, $Y_{ij}(\omega)$, are organized in matrix form given by the equation

$$Y_{ij}(\omega) = \begin{bmatrix} \frac{x_i}{f_j} & \frac{x_i}{m_j} \\ \frac{\theta_i}{f_j} & \frac{\theta_i}{m_j} \end{bmatrix} = \begin{bmatrix} u_{ij} & v_{ij} \\ w_{ij} & z_{ij} \end{bmatrix} \quad (3.29)$$

where x_i is the substructure displacement at the coordinate location i , θ_i is the substructure rotation at the coordinate location i , f_j is the force employed to the substructure at location j and m_j is the couple employed to the substructure at location j . The direct and cross receptances for the components I and II (tool and holder) at the coordinate locations as shown in Figure 3.8 are first obtained.



(a) Component assembly



(b) Individual components

Figure 3.8: Three component receptance coupling model

For component-I, the tool receptances are described as:

$$Y_{11} = \begin{bmatrix} \frac{x_1}{f_1} & \frac{x_1}{m_1} \\ \frac{\theta_1}{f_1} & \frac{\theta_1}{m_1} \end{bmatrix} = \begin{bmatrix} u_{11} & v_{11} \\ w_{11} & z_{11} \end{bmatrix} \quad (3.30)$$

$$Y_{2a2a} = \begin{bmatrix} \frac{x_{2a}}{f_{2a}} & \frac{x_{2a}}{m_{2a}} \\ \frac{\theta_{2a}}{f_{2a}} & \frac{\theta_{2a}}{m_{2a}} \end{bmatrix} = \begin{bmatrix} u_{2a2a} & v_{2a2a} \\ w_{2a2a} & z_{2a2a} \end{bmatrix} \quad (3.31)$$

$$Y_{12a} = \begin{bmatrix} \frac{x_1}{f_{2a}} & \frac{x_1}{m_{2a}} \\ \frac{\theta_1}{f_{2a}} & \frac{\theta_1}{m_{2a}} \end{bmatrix} = \begin{bmatrix} u_{12a} & v_{12a} \\ w_{12a} & z_{12a} \end{bmatrix} \quad (3.32)$$

$$Y_{2a1} = \begin{bmatrix} \frac{x_{2a}}{f_1} & \frac{x_{2a}}{m_1} \\ \frac{\theta_{2a}}{f_1} & \frac{\theta_{2a}}{m_1} \end{bmatrix} = \begin{bmatrix} u_{2a1} & v_{2a1} \\ w_{2a1} & z_{2a1} \end{bmatrix} \quad (3.33)$$

Similarly, for the component-II (the holder), the receptances are described by the following equations:

$$Y_{2b2b} = \begin{bmatrix} \frac{x_{2b}}{f_{2b}} & \frac{x_{2b}}{m_{2b}} \\ \frac{\theta_{2b}}{f_{2b}} & \frac{\theta_{2b}}{m_{2b}} \end{bmatrix} = \begin{bmatrix} u_{2b2b} & v_{2b2b} \\ w_{2b2b} & z_{2b2b} \end{bmatrix} \quad (3.34)$$

$$Y_{2b3a} = \begin{bmatrix} \frac{x_{2b}}{f_{3a}} & \frac{x_{2b}}{m_{3a}} \\ \frac{\theta_{2b}}{f_{3a}} & \frac{\theta_{2b}}{m_{3a}} \end{bmatrix} = \begin{bmatrix} u_{2b3a} & v_{2b3a} \\ w_{2b3a} & z_{2b3a} \end{bmatrix} \quad (3.35)$$

$$Y_{3a3a} = \begin{bmatrix} \frac{x_{3a}}{f_{3a}} & \frac{x_{3a}}{m_{3a}} \\ \frac{\theta_{3a}}{f_{3a}} & \frac{\theta_{3a}}{m_{3a}} \end{bmatrix} = \begin{bmatrix} u_{3a3a} & v_{3a3a} \\ w_{3a3a} & z_{3a3a} \end{bmatrix} \quad (3.36)$$

$$Y_{3a2b} = \begin{bmatrix} \frac{x_{3a}}{f_{2b}} & \frac{x_{3a}}{m_{2b}} \\ \frac{\theta_{3a}}{f_{2b}} & \frac{\theta_{3a}}{m_{2b}} \end{bmatrix} = \begin{bmatrix} u_{3a2b} & v_{3a2b} \\ w_{3a2b} & z_{3a2b} \end{bmatrix} \quad (3.37)$$

The relationships between displacements/rotations and forces/couples can be written using the matrix form.

$$\begin{Bmatrix} x_1 \\ \theta_1 \end{Bmatrix} = \begin{bmatrix} u_{11} & v_{11} \\ w_{11} & z_{11} \end{bmatrix} \begin{Bmatrix} f_1 \\ m_1 \end{Bmatrix} \text{ or } \{k_1\} = [Y_{11}]\{q_1\} \quad (3.38)$$

$$\{k_1\} = [Y_{12a}]\{q_{2a}\} \quad (3.39)$$

$$\{k_{2a}\} = [Y_{2a2a}]\{q_{2a}\} \quad (3.40)$$

$$\{k_{2a}\} = [Y_{2a1}]\{q_1\} \quad (3.41)$$

$$\{k_{2b}\} = [Y_{2a2b}]\{q_{2b}\} \quad (3.42)$$

$$\{k_{2b}\} = [Y_{2a3a}]\{q_{3a}\} \quad (3.43)$$

$$\{k_{3a}\} = [Y_{3a3a}]\{q_{3a}\} \quad (3.44)$$

$$\{k_{3a}\} = [Y_{3a2b}]\{q_{2b}\} \quad (3.45)$$

where k and q the generalized displacement/rotation and the force/couple vectors, respectively.

Rigid coupling for free-free receptances

The free-free tool and holder models are coupled to form the subassembly I-II identified in Fig 3-7. In order to calculate the subassembly receptances, T_{11} (direct) and T_{3a1} (cross), a generalized force Q_1 (representing both the externally applied force and couple) is applied at coordinate location 1.

$$T_{11} = \begin{bmatrix} \frac{X_1}{F_1} & \frac{X_1}{M_1} \\ \frac{\Theta_1}{F_1} & \frac{\Theta_1}{M_1} \end{bmatrix} = \begin{bmatrix} U_{11} & V_{11} \\ W_{11} & Z_{11} \end{bmatrix} \quad (3.46)$$

$$T_{3a1} = \begin{bmatrix} \frac{X_{3a}}{F_1} & \frac{X_{3a}}{M_1} \\ \frac{\Theta_{3a}}{F_1} & \frac{\Theta_{3a}}{M_1} \end{bmatrix} = \begin{bmatrix} U_{3a1} & V_{3a1} \\ W_{3a1} & Z_{3a1} \end{bmatrix} \quad (3.47)$$

The displacement equations for the substructures can be described as follows:

$$k_1 = Y_{11}q_1 + Y_{12a}q_{2a} \quad (3.48)$$

$$k_{2a} = Y_{2a2a}q_{2a} + Y_{2a1}q_1 \quad (3.49)$$

$$k_{2b} = Y_{2b2b}q_{2b} \quad (3.50)$$

$$k_{3a} = Y_{3a2b}q_{2b} \quad (3.51)$$

If rigid coupling between the two components is assumed, the compatibility and equilibrium condition that describes the connection between the two components is expressed as:

$$k_{2b} - k_{2a} = 0 \quad (3.52)$$

$$q_{2b} + q_{2a} = 0 \quad (3.53)$$

At coordinate location 1, the external force/couple is applied, which gives the following set of equations:

$$q_1 = Q_1 \quad (3.54)$$

$$k_{2b} - k_{2a} = Y_{2b2b}q_{2b} - Y_{2a2a}q_{2a} - Y_{2a1}q_1 = 0 \quad (3.55)$$

$$(Y_{2b2b} + Y_{2a2a})q_{2b} - Y_{2a1}Q_1 = 0 \quad (3.56)$$

In order to determine the subassembly receptances, T_{11} (direct) and T_{3a1} (cross), a generalized force Q_1 (representing both the externally applied force and couple) is employed at location-1 as shown in Fig. 3.7(a). The displacement equations and compatibility conditions for the substructures I and II are written individually and then sub-assembly receptances can be expressed as a function of the component receptances by rigidly coupling them [67]. The following equations give the receptances for sub-assembly of I-II.

$$q_{2b} = (Y_{2b2b} + Y_{2a2a})^{-1} Y_{2a1} Q_1 \quad (3.57)$$

$$T_{11} = \frac{K_1}{Q_1} = \frac{k_1}{Q_1} = \frac{Y_{11}q_1 + Y_{12a}q_{2a}}{Q_1} \quad (3.58)$$

$$T_{11} = \frac{Y_{11}Q_1 - Y_{12a}(Y_{2b2b} + Y_{2a2a})^{-1}Y_{2a1}Q_1}{Q_1} \quad (3.59)$$

$$T_{11} = Y_{11} - Y_{12a}(Y_{2b2b} + Y_{2a2a})^{-1}Y_{2a1} = \begin{bmatrix} U_{11} & V_{11} \\ W_{11} & Z_{11} \end{bmatrix} \quad (3.60)$$

Similarly, the cross receptances between coordinates 3a and 1 are given by:

$$T_{3a1} = \frac{K_{3a}}{Q_1} = \frac{k_{3a}}{Q_1} = \frac{Y_{3a2b}q_{2b}}{Q_1} = \frac{Y_{3a2b}(Y_{2b2b} + Y_{2a2a})^{-1}Y_{2a1}Q_1}{Q_1} \quad (3.61)$$

$$T_{3a1} = Y_{3a2b}(Y_{2b2b} + Y_{2a2a})^{-1}Y_{2a1} = \begin{bmatrix} U_{3a1} & V_{3a1} \\ W_{3a1} & Z_{3a1} \end{bmatrix} \quad (3.62)$$

To establish the direct (T_{3a3a}) and cross receptances (T_{13a}) of the spindle-device (III) with respect to the sub-assembly (I-II), a generalized force Q_{3a} is applied to the spindle at the position 3 as shown in Fig. 3.7(a) which gives the following set of equations.

$$T_{3a3a} = \begin{bmatrix} \frac{X_{3a}}{F_{3a}} & \frac{X_{3a}}{M_{3a}} \\ \frac{\Theta_{3a}}{F_{3a}} & \frac{\Theta_{3a}}{M_{3a}} \end{bmatrix} = \begin{bmatrix} U_{3a3a} & V_{3a3a} \\ W_{3a3a} & Z_{3a3a} \end{bmatrix} \quad (3.63)$$

$$T_{13a} = \begin{bmatrix} \frac{X_1}{F_{3a}} & \frac{X_1}{M_{3a}} \\ \frac{\Theta_1}{F_{3a}} & \frac{\Theta_1}{M_{3a}} \end{bmatrix} = \begin{bmatrix} U_{13a} & V_{13a} \\ W_{13a} & Z_{13a} \end{bmatrix} \quad (3.64)$$

The component displacement/rotation equations and compatibility and equilibrium conditions are applied in the similar manner which gives the subsequent equations as:

$$k_1 = Y_{12a} q_{2a} \quad (3.65)$$

$$k_{2a} = Y_{2a2a} q_{2a} \quad (3.66)$$

$$k_{2b} = Y_{2b2b} q_{2b} + Y_{2b3a} q_{3a} \quad (3.67)$$

$$k_{3a} = Y_{3a3a} q_{3a} + Y_{3a2b} q_{2b} \quad (3.68)$$

$$k_{2a} - k_{2b} = 0 \quad (3.69)$$

$$q_{2a} + q_{2b} = 0 \quad (3.70)$$

$$q_{3a} = Q_{3a} \quad (3.71)$$

$$k_{2a} - k_{2b} = Y_{2a2a} q_{2a} - Y_{2b2b} q_{2b} - Y_{2b3a} q_{3a} = 0 \quad (3.72)$$

$$(Y_{2b2b} + Y_{2a2a}) q_{2a} - Y_{2b3a} Q_{3a} = 0 \quad (3.73)$$

$$q_{2a} = (Y_{2b2b} + Y_{2a2a})^{-1} Y_{2b3a} Q_{3a} \quad (3.74)$$

$$T_{3a3a} = \frac{K_{3a}}{Q_{3a}} = \frac{k_{3a}}{Q_{3a}} = \frac{Y_{3a3a} q_{3a} + Y_{3a2b} q_{2b}}{Q_{3a}} \quad (3.75)$$

$$T_{3a3a} = \frac{Y_{3a3a} Q_{3a} - Y_{3a2b} (Y_{2b2b} + Y_{2a2a})^{-1} Y_{2b3a} Q_{3a}}{Q_{3a}} \quad (3.76)$$

$$T_{3a3a} = Y_{3a3a} - Y_{3a2b} (Y_{2b2b} + Y_{2a2a})^{-1} Y_{2b3a} = \begin{bmatrix} U_{3a3a} & V_{3a3a} \\ W_{3a3a} & Z_{3a3a} \end{bmatrix} \quad (3.77)$$

$$T_{3a3a} = \frac{K_1}{Q_{3a}} = \frac{k_1}{Q_{3a}} = \frac{Y_{12a} q_{2a}}{Q_{3a}} = \frac{Y_{12a} (Y_{2b2b} + Y_{2a2a})^{-1} Y_{2b3a} Q_{3a}}{Q_{3a}} \quad (3.78)$$

$$T_{3a3a} = Y_{3a3a} - Y_{3a2b} (Y_{2b2b} + Y_{2a2a})^{-1} Y_{2b3a} = \begin{bmatrix} U_{3a3a} & V_{3a3a} \\ W_{3a3a} & Z_{3a3a} \end{bmatrix} \quad (3.79)$$

$$T_{13a} = Y_{12a} (Y_{2b2b} + Y_{2a2a})^{-1} Y_{2b3a} = \begin{bmatrix} U_{13a} & V_{13a} \\ W_{13a} & Z_{13a} \end{bmatrix} \quad (3.80)$$

The free-free component receptances of I (tool) and II (tool-holder) are connected to obtain the sub assemblage I-II, it might be firmly connected towards the spindle-device (component-III) to obtain the final assembled tool end point receptances, T_{11} . The possible connection is employed by means of equation given below

$$T'_{11} = T_{11} - T_{13a}(T_{3a3a} + Y_{3b3b})^{-1}T_{3a1} = \begin{bmatrix} U_{11} & V_{11} \\ W_{11} & Z_{11} \end{bmatrix} \quad (3.81)$$

where the T_{ij} are the individual subassembly matrices. The remaining unknown in the equation is the spindle-device receptance matrix: Y_{3b3b} . The receptances of the spindle-machine (component-III) are difficult to obtain due to operating speed and interference coupling. This receptance matrix can also be obtained using dynamic modelling of spindle machine. In present case, the four bending component receptances are arrived for the spindle using finite element analysis.

Spindle-housing Receptances

It has been noticed that finite element models have the potential to provide more precise design model predictions for the spindle machine receptances. The spindle-housing receptances are acquired by finite element modelling with Timoshenko beam theory, where the spindle-device unit supported over the rear and front bearings as shown in Figure 3.9. Housing of the spindle goes into the machine and the outer races of rolling-contact ball bearings are mounted on the housing [67]. During the analysis of spindle unit through finite element approach, both gyroscopic and shear deformation effects are taken into consideration. The degrees of freedom at each node include: two bending displacements and the corresponding slopes. Axial preload at the bearings is considered as 1500N.

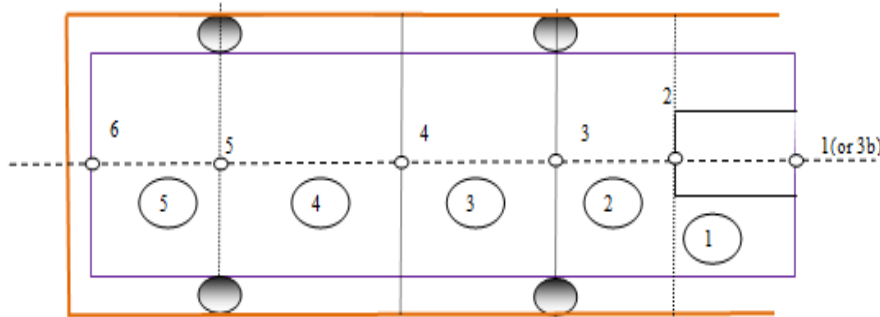


Figure 3.9: Finite element model of spindle supported by housing

The assembled stiffness (K_a), mass (M_a) and gyroscopic matrices (G_a) are formulated and the boundary conditions (spring stiffness) at the bearings are applied. The frequency response function of the spindle system is given by

$$[H(i\omega_c)] = [\text{Re}(\omega_c)] + i[\text{Im}(\omega_c)] = [-[M_b]\omega_c^2 + i\omega_c[-\Omega[G_b]] + ([K_b] - \Omega^2[M_b]_c)]^{-1} \quad (3.82)$$

where Im and Re are the imaginary and real elements of the frequency response function of the spindle portion. This gives the four bending component receptances at position (node)-3b.

In modelling of continuous beam, the material dependent damping is conveniently introduced in the elastic modulus as given by the term $E_s = E(1 + i\eta)$, where η is the solid damping factor and E is the elastic modulus. In this line, the free-free beam boundary conditions are applied for the tool and tool-holder components to get the direct and cross receptances and are given by the following equations [171]:

$$u_{ii} = \frac{-k_1}{\alpha^3 k_7}; v_{ii} = \frac{k_2}{\alpha^2 k_7}; w_{ii} = v_{ii}; z_{ii} = \frac{k_5}{\alpha k_7} \quad (3.83)$$

$$u_{ij} = \frac{k_3}{\alpha^3 k_7}; v_{ij} = \frac{-k_4}{\alpha^2 k_7}; w_{ij} = \frac{k_4}{\alpha^2 k_7}; z_{ij} = \frac{k_6}{\alpha k_7} \quad (3.84)$$

where

$$\alpha^4 = \omega^2 \frac{\rho A_s}{EI(1 + i\eta)} \quad (3.85)$$

$$k_1 = \cos(\alpha l) \sinh(\alpha l) - \sin(\alpha l) \cosh(\alpha l) \quad (3.86)$$

$$k_2 = \sin(\alpha l) \sinh(\alpha l) \quad (3.87)$$

$$k_3 = \sin(\alpha l) - \sinh(\alpha l) \quad (3.88)$$

$$k_4 = \cos(\alpha l) - \cosh(\alpha l) \quad (3.89)$$

$$k_5 = \cos(\alpha l) \sinh(\alpha l) + \sin(\alpha l) \cosh(\alpha l) \quad (3.90)$$

$$k_6 = \sin(\alpha l) + \sinh(\alpha l) \quad (3.91)$$

$$k_7 = E_s I (\cos(\alpha l) \cosh(\alpha l) - 1) \quad (3.92)$$

$$k_8 = E_s I (\cos(\alpha l) \cosh(\alpha l) + 1) \quad (3.93)$$

Here, ω is frequency in rad/sec, A_s is beam cross-section, ρ is the density, and l is the component length.

3.3 Numerical Results

This section describes the spindle-tool dynamic analysis results under four headings: (i) tool-tip frequency response analysis (ii) Parametric studies of spindle-tool variables on overall dynamics (c) Optimization of spindle parameters (d) Dynamic studies of a drilling spindle.

3.3.1 Frequency response studies

When the energy input exceeds the energy dissipated, the amplitude of vibration of the system will increase and it results-in an undesired relative vibration between the workpiece and the tool. To illustrate the methodology, materials and geometric properties of the individual components are selected from the manual of vertical CNC end milling machine: (make MTAB-MAXMILL).

3.3.1.a Full-order finite element modeling approach

The integrated tool-spindle dimensions as a finite element model data (referring to Figure 3.4) is illustrated in Table 3.1.

Table 3.1: Parameters of the finite element model

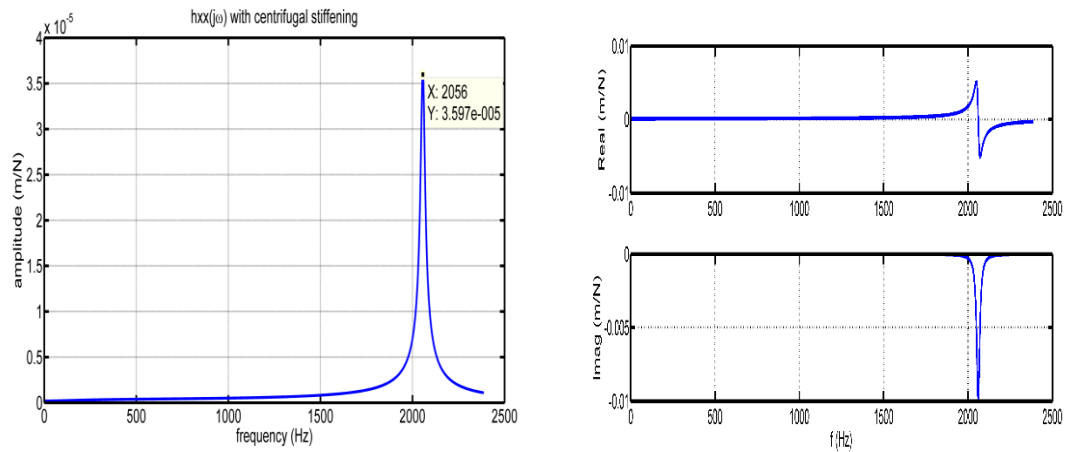
Parameter s	Elements of the spindle tool unit							
	#1	#2	#3	#4	#5	#6	#7	#8
Length (mm)	30	30	85	51	60	45	45	47
Outer diameter (mm)	12	12	40	75	75	75	75	75
Inner diameter (mm)	0	0	0	40	0	0	0	0
E (Pa)	2.8×10^{11}	2.1×10^{11}	2.1×10^{11}	2.1×10^{11}	2.1×10^{11}	2.1×10^{11}	2.1×10^{11}	2.1×10^{11}
Density(K g/m ³)	7972	7850	7850	7850	7850	7850	7850	7850

The tool is rigidly connected to the tool holder whose lengths are adjustable and the spindle shaft is axially supported between the angular contact ball bearings. The ball bearings data considered for finding the equivalent stiffness is: $N_b=20$, $D_b=9\text{mm}$, $F_a=1500\text{ N}$, and $\theta=25^\circ$. An interactive computer program is developed in MATLAB software to analyse the dynamics of spindle system. Convergence tests are carried out on the present finite element modeling to minimize discretization errors by increasing the number of degrees of freedom (DOF). It is observed from Table 3.2, that after eight elements, it maintains the same frequency value.

Table 3.2: Convergence result of natural frequencies of spindle tool unit

S No	Natural frequency(Hz)
3 elements	2055.8
5 elements	2057.65
8 elements	2056.45
10 elements	2056.45
15 elements	2056.45

The eight element model considers 36 degrees of freedom and the rotational degrees of freedom were eliminated by using Guyan reduction technique. Figure 3.10 presents absolute part of tool tip FRF. It is observed that the first dominant modal frequency occurs at 2056 Hz.



(a) Absolute FRF

(b) Real and Imaginary FRF

Figure 3.10: Tool tip frequency responses using the Full-order FEM

Considering the bearing dynamics and centrifugal stiffening effect, the direct frequency response function at the tool tip $h_{xx}(j\omega)$ is obtained at a particular spindle speed (Ω) of 3000 rpm.

3.3.1.b Receptance coupling sub-sub structuring

Using RCSA approach for analyzing the tool-tip FRF, data for tool, holder and spindle considered is depicted in Table 3.3.

Table 3.3: Parameters of the tool-holder and spindle machine unit

	Component	Outer Lengths (mm)	Outer diameter (mm)	Inner diameter (mm)	Young's modulus E, (Pa)
1	Tool	60	12	0	2.8×10^{11}
2	Holder	80	40	12	2.1×10^{11}
3	Spindle	248	75	40	2.1×10^{11}

Here, 20mm length portion of the tool is inserted into the tool holder and remaining outer length is 60mm. Similarly, for the tool holder, 30mm is inserted into the spindle nose region as shown in Figure 3.11.

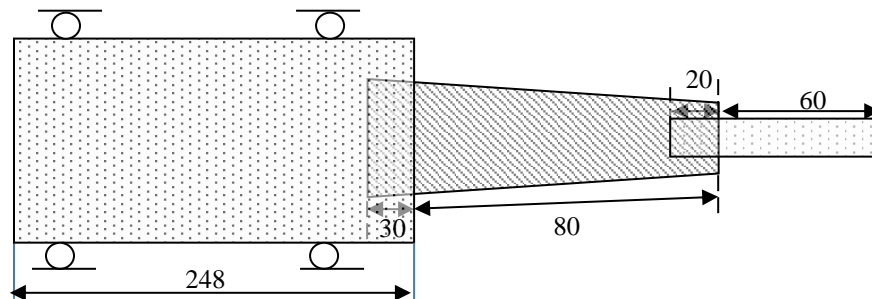


Figure 3.11: Configuration of spindle tool system

Figure 3.12 shows the methodology employed during receptance coupling.

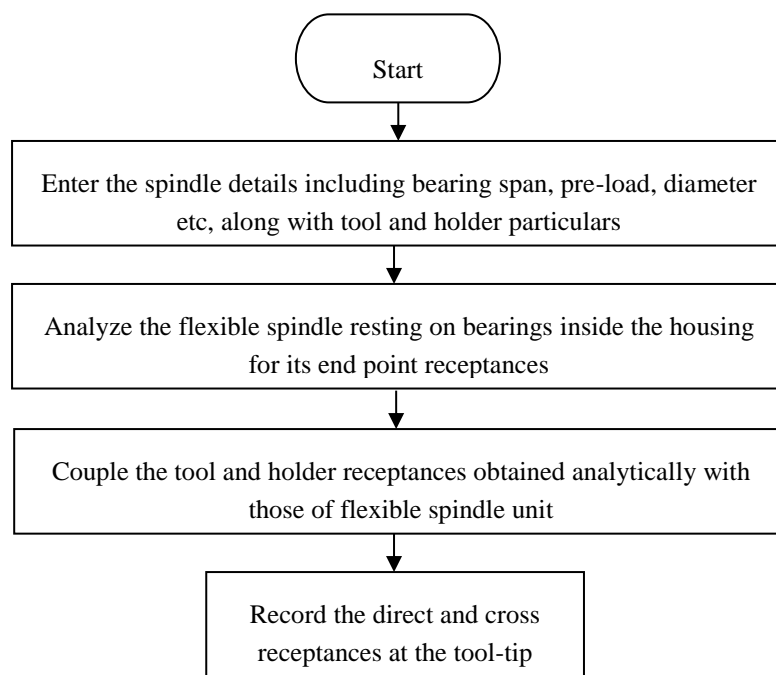
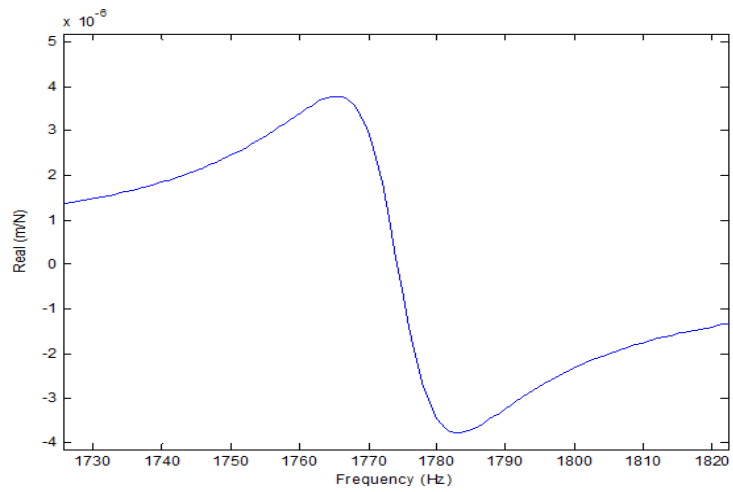
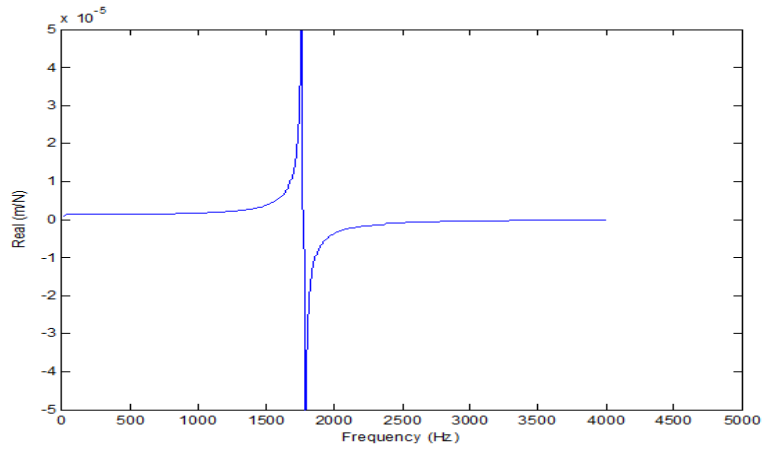


Figure 3.12: Present receptance coupling concept

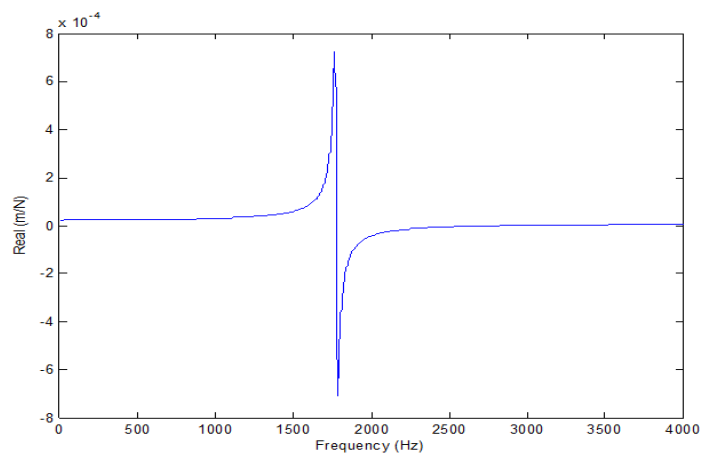
Figure 3.13 shows the four predicted receptances in T_{11} of the tool-holder component subassembly independently at the holder-tip (where spindle would be joined) using Euler's beam theory and it is in the frequency range of 1500 Hz to 2000 Hz. These receptances are further used to couple with the spindle- machine receptances.



(a) Real part of U_{11}



(b) Real part of V_{11} and W_{11}



(c) Real part of Z_{11}

Figure 3.13: Receptance T_{11} of the Tool-Holder sub assembly

The component receptances at joint node corresponding to spindle-machine supported on ball-bearings are obtained from finite element model by discretizing it with five beam elements accounting the shear deformation and rotary inertia effects. Figure 3.14 shows the four component receptance at joint node. It is observed that the spindle possess two bending modes at around 650 Hz and 750 Hz in all the receptance curves.

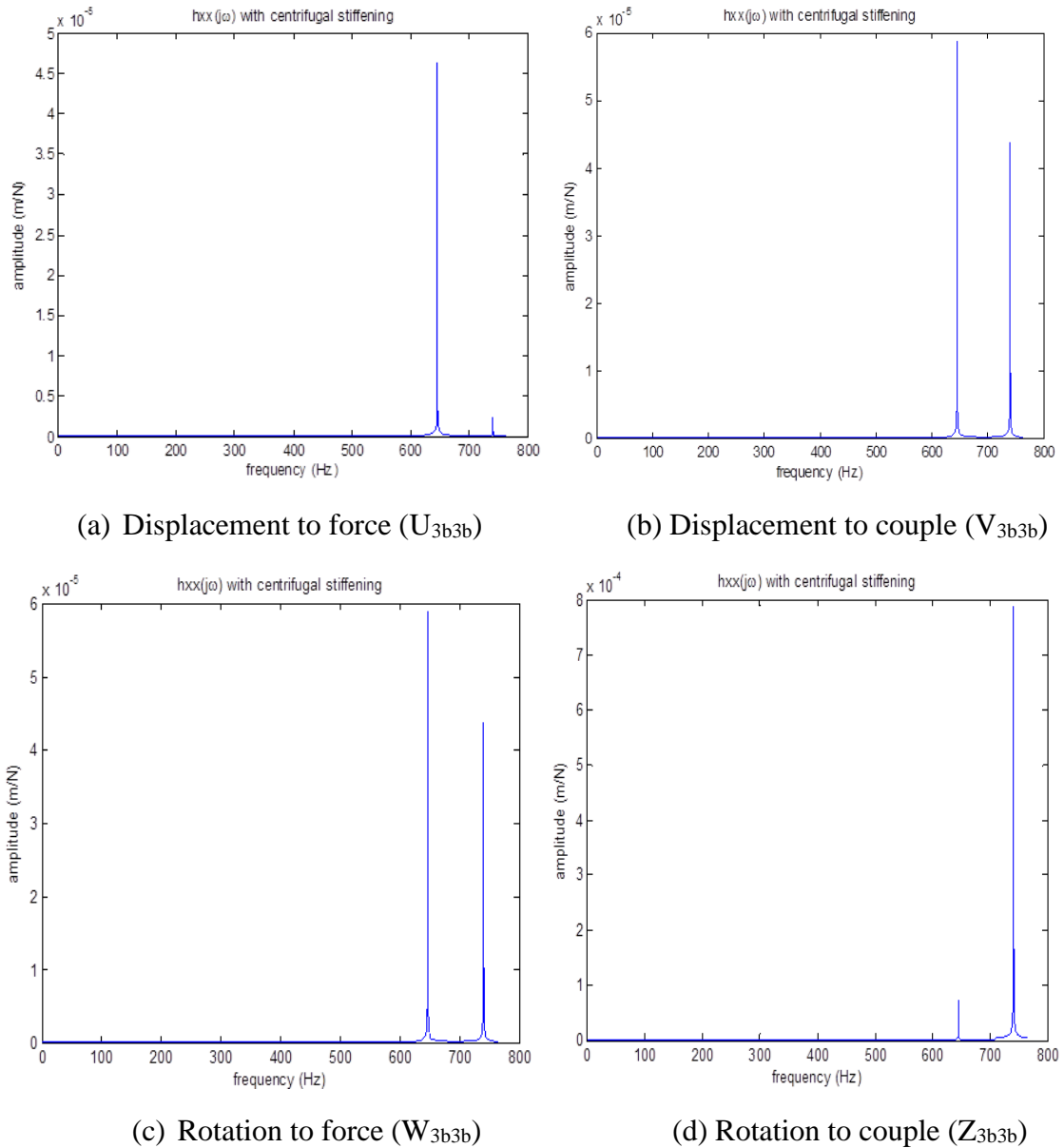
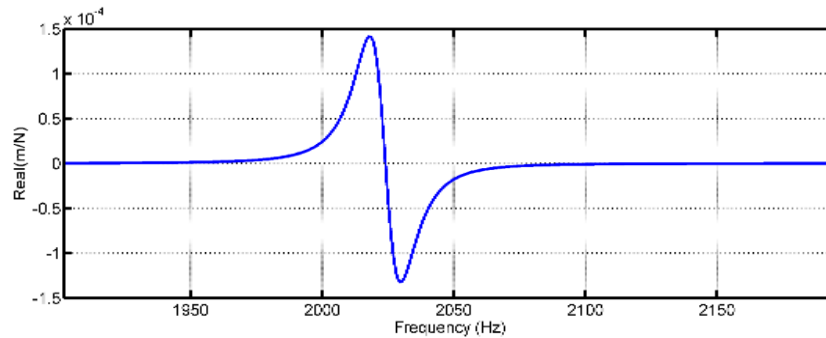


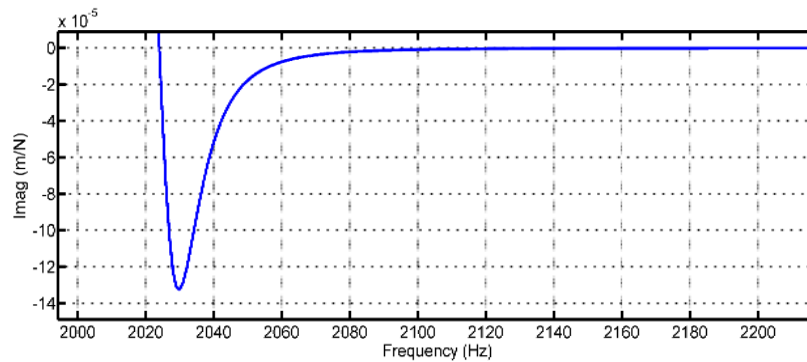
Figure 3.14: Spindle machine receptances (Y_{3b3b}) obtained from finite element analysis

Further, these receptances are added to the previously obtained tool-holder receptances to arrive the assembled receptances. A program is written for obtaining tool- tip frequency response by considering all individual receptances and their coupling. Figure 3.15 shows the resultant tool-tip response as displacement to force receptance $U_{11}=G(j\omega)$ in the form of real,

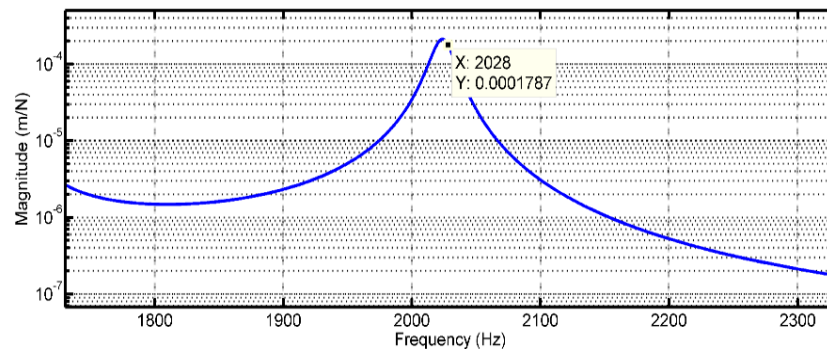
imaginary and absolute graphs. It is observed that the first bending mode of the assembly occurs at 2028 Hz.



(a) Real Part of U_{11}



(b) Imaginary part of U_{11}



(c) Semi-log magnitude plot

Figure 3.15: Tool tip frequency response of the assembly

3.3.1.c Three-dimensional finite element modelling

In order to further validate the natural frequency results, a three-dimensional finite element analysis of the entire spindle tool unit is carried in ANSYS workbench. Figure 3.16 shows the initial solid model of spindle-bearing assembly developed in SolidWorks software as per the available dimensions of CNC spindle unit available at central workshop.

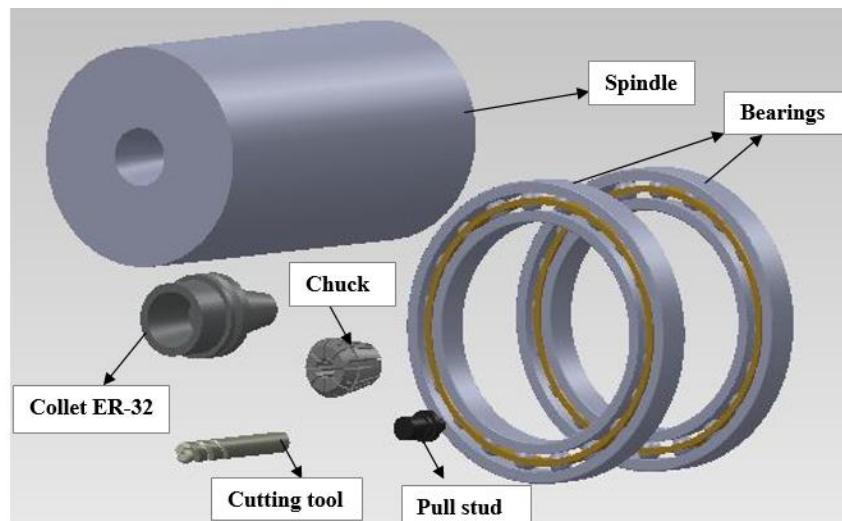


Figure 3.16: Individual solid work components of MTAB MAXMILL realistic spindle system

The model is imported into ANSYS V14 for dynamic analysis. Eight-node SOLID 187 elements with 3 translational (u_x , u_y and u_z) degrees of freedom are used to mesh the spindle shaft, tool holder, collet as well as the cutting tool with the material properties as considered for one-dimensional model. As boundary conditions, all the outer race nodes of the front and rear bearings are arrested. The meshed assembly is shown in Figure 3.17.

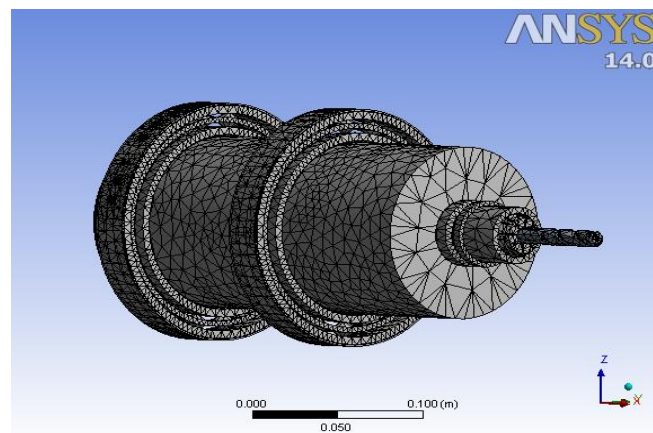


Figure 3.17: Meshed model of spindle-bearing system

The modal analysis of static spindle system revealed the first eight natural frequencies as 2.0473 kHz, 2.0546 kHz, 2.6654 kHz, 2.6857 kHz, 2.7629 kHz, 4.4816 kHz, 4.7111 kHz, 4.7143 kHz. The first six mode shapes are illustrated in Figure 3.18.

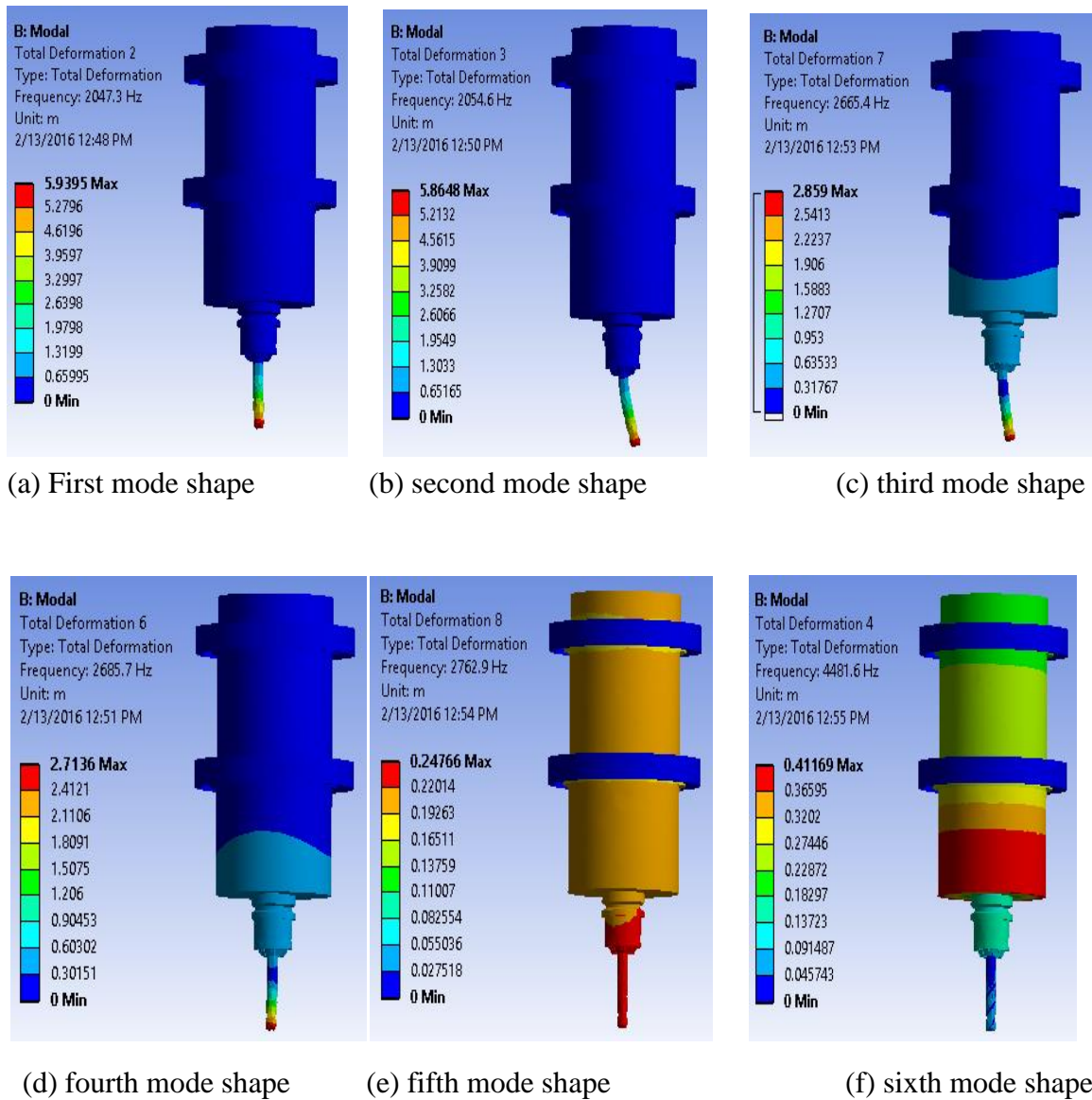


Figure 3.18: First six mode shapes of spindle tool unit

The first four modes have low deformation rates and are due to bending in two directions. Harmonic response analysis is also carried-out to predict the sustained dynamic behavior of spindle-bearing system. Figure 3.19 shows the harmonic response (displacement at tool tip due to harmonic load applied at a random node on the model) obtained from ANSYS workbench. The first peak is coming at approximately 2050Hz without considering any damping in the system. As the 3-D finite element model considers a mesh made-up of tetrahedral elements, it results in certain extra modes in axial direction.

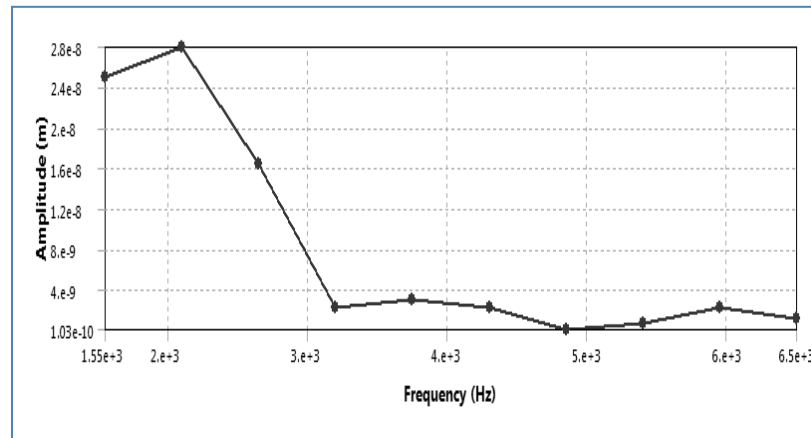


Figure 3.19: Harmonic response of spindle bearing system

Figure 3.20 shows a comparative chart of the natural frequencies obtained from the three approaches. It is seen that RCSA approach gives a lower approximation due to consideration of both Euler and Timoshenko beam theories for modelling of different components.

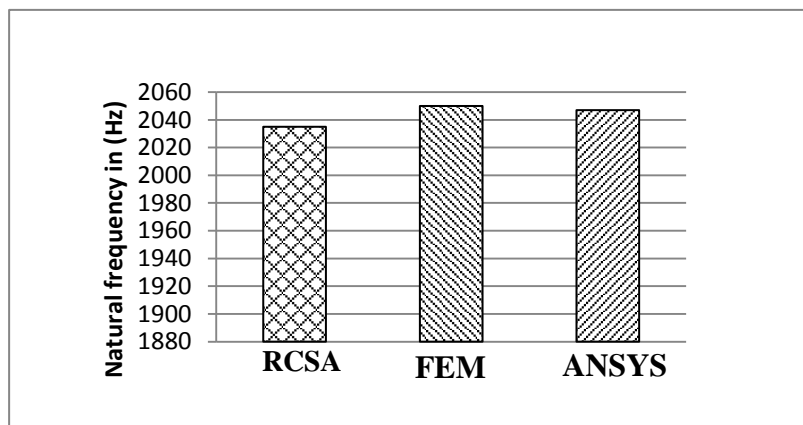
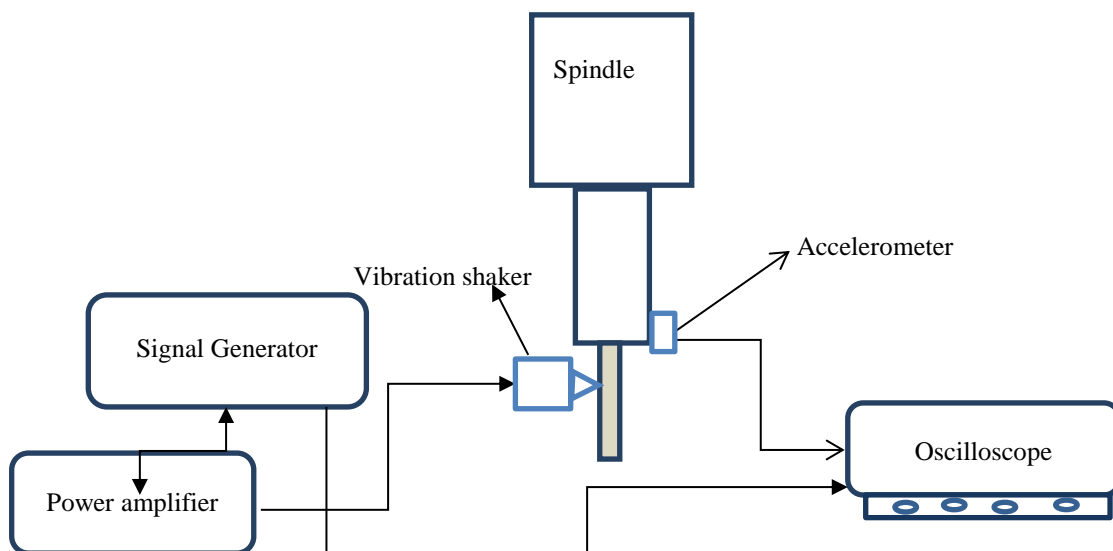


Figure 3.20: First modal frequency of spindle-tool assembly

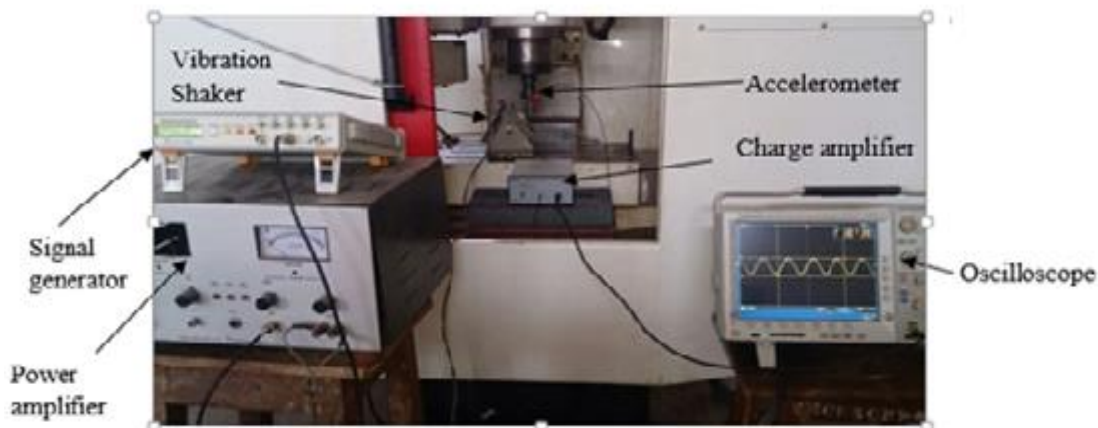
3.3.1.d Experimental Modal Analysis

An experimental modal analysis is conducted for the spindle -tool holder system of CNC milling centre (make: MTAB-Maxmill) available at NIT central workshop. The three axis machine tool has a single phase AC synchronous motor driving the spindle at variable speeds. The cutting tool is a 4-fluted HSS milling cutter (12 mm diameter) purchased from local market. In order to obtain the modal information of spindle-tool unit, the following instrumentation is employed: (i) 4-channel digital oscilloscope(model-DPO 43034 for recording time histories), (ii) a power amplifier (model- SI-28), (iii) an accelerometer (PG 109 M0, frequency range 1 to 10,000 Hz), (iv) a charge amplifier (Model: CA 201 A0,

maximum output voltage- $\pm 5V$, frequency range- 0.2 Hz to 15 kHz), (v) a signal generator and (vi) vibration shaker (Type:V-6-27050). Figure 3.21 shows the schematic of experimental set-up arranged on the milling machine for modal testing along with a photograph.



(a) Schematic diagram of the experimental set-up



(a) Photograph of the experimental set-up

Figure 3.21: Experimental set up employed

Sine-sweep testing is conducted by varying the frequency of the signal keeping the amplitudes constant (frequency modulation) with the help of a power amplifier. The vibration shaker excites the spindle-tool and the corresponding accelerometer readings are

recorded at every frequency using the oscilloscope. Amplitudes of response from the time-domain at each frequency case are tabulated and plotted as a function of frequency as shown in Figure 3.22.

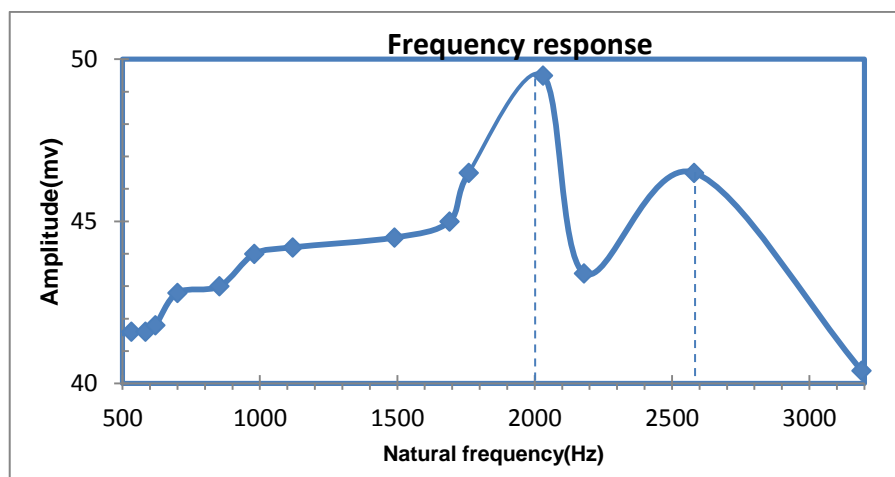


Figure 3.22: Frequency response of the integral tool-spindle unit

It can be seen that the first two peaks are found at 1998Hz and 2590Hz respectively within the sweeping range, which are in agreement with the earlier result obtained from numerical model.

3.3.1.e Studies on spindle-tool system interfaces with interface stiffness

As described in section 3.3.2, the spindle-holder coupling in machine tools plays a prominent role in the performance of the spindle. The taper portion of this coupled joint determines the machining capacity in terms of their stability. The spindle-holder joint is one of the most flexible connections in spindle systems and about 25–50% deformation at the tool tip is derived from the joint [74]. It is necessary to investigate the dynamic response of the spindle-holder joint to ensure the precision and stability in the machining process. The conical tapered connections are used as the interface between the spindle and the tool holder. The friction between the holder and spindle taper interfaces determine the translational and rotational stiffness of the connection. The connection between the tapered surfaces is modelled by springs in the y and z directions to prevent the holder from rotating and translating inside the spindle taper.

In present task, along with four-degree-of-freedom Timoshenko beam finite element model elements for discretization of spindle assembly, the spindle-holder joint is modelled with three springs representing three tapered portion in the assembly. Similarly, holder-tool interface is modelled by two springs in both the bending directions as shown in the Figure 3.23. The spindle-holder taper portion is modelled by two elements with three nodes and

for the tool portion inserted in the holder is assumed to be connected with two springs instead of rigid connection.

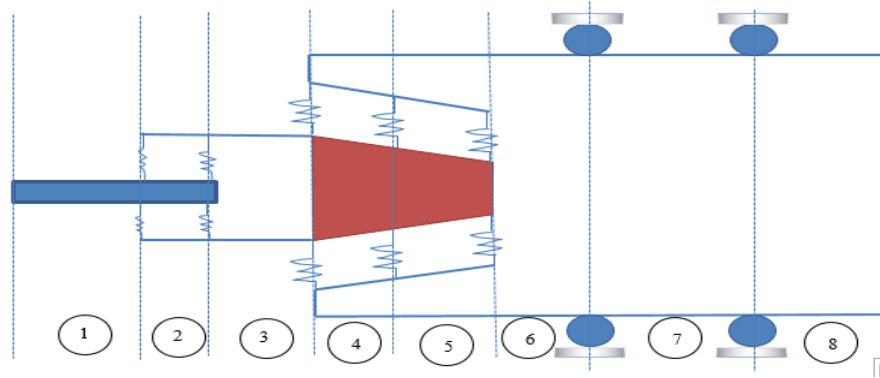
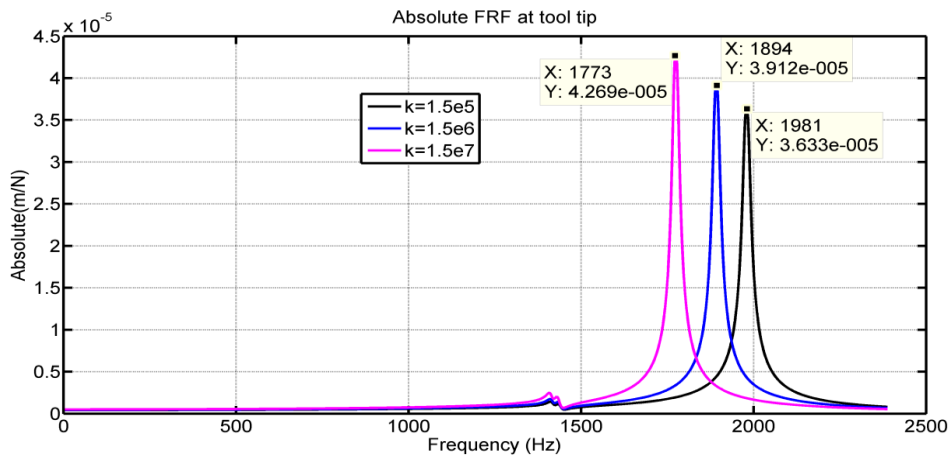


Figure 3.23: Equivalent model of the spindle-tool interfaces with distributed contact springs

The magnitudes of simulated FRF's at tool tip with different interface stiffness are shown in the Figure 3.24. As the tool and holder assembly is relatively rigid, its inter-phase stiffness is selected to higher ($k_{t-h}=1e9$ N/m), while studies are carried out for the variation in interface stiffness between the holder and spindle region. The stiffness is considered both in the bending directions. Figure 3.24(a) shows the absolute part of the tool tip FRF and it is observed that for the stiffness value of 1.5×10^5 N/m, the fundamental mode of natural frequency as 1981Hz. Comparatively, this is close to the natural frequency obtained earlier from the experimental modal testing. As the stiffness of the contact springs has increased, the amplitude of the tool-tip displacement levels (y-axis) raise with a decrease in the corresponding natural frequencies (x-axis). The corresponding real and imaginary parts of the tool-tip frequency responses for all three cases are shown in Figure 3.24(b) &(c).



(a) Absolute part

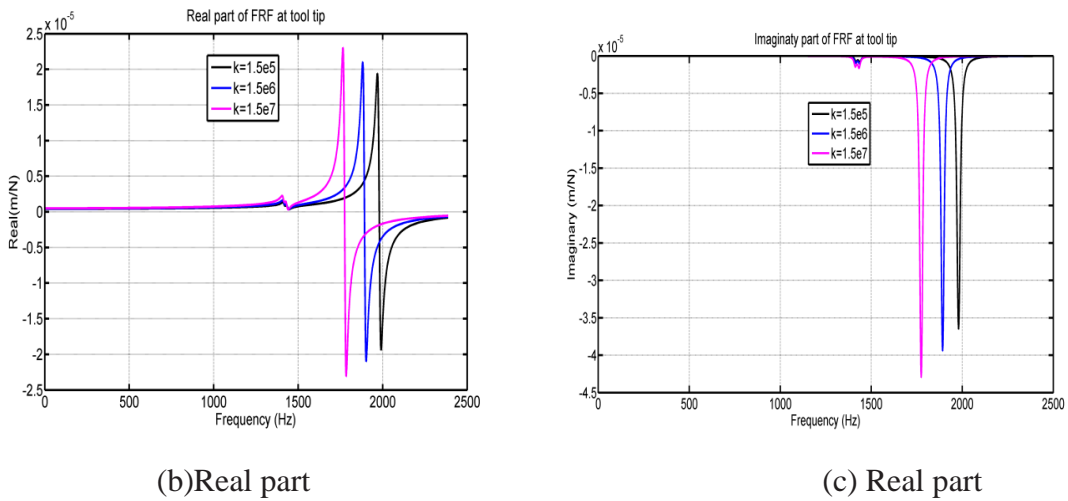


Figure 3.24: Tool tip frequency response at different stiffness values

Figure 3.25 shows the FRF plot of the system with and without considering the joint stiffness effects.

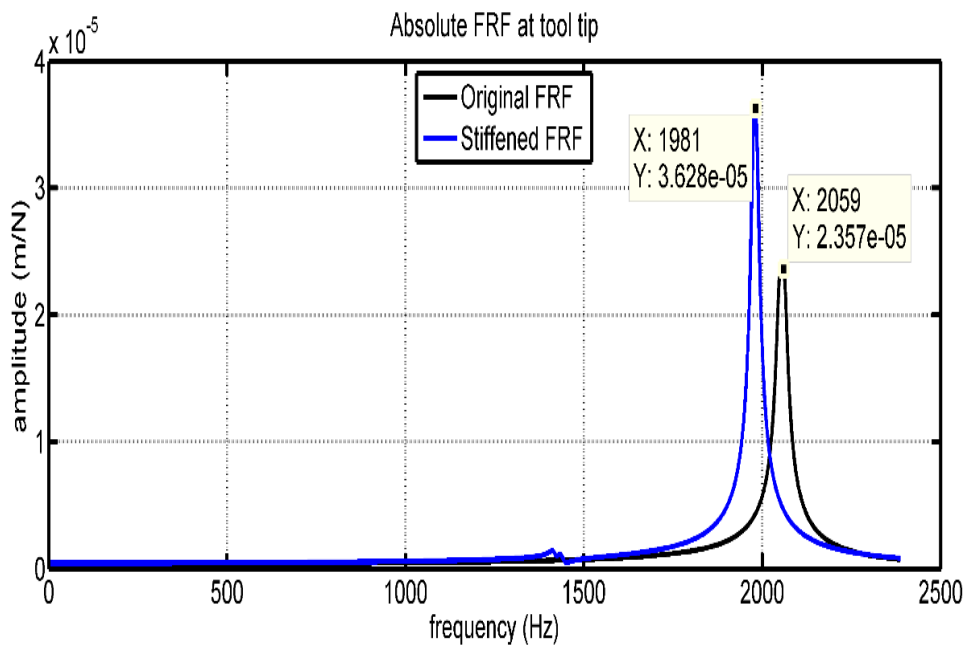
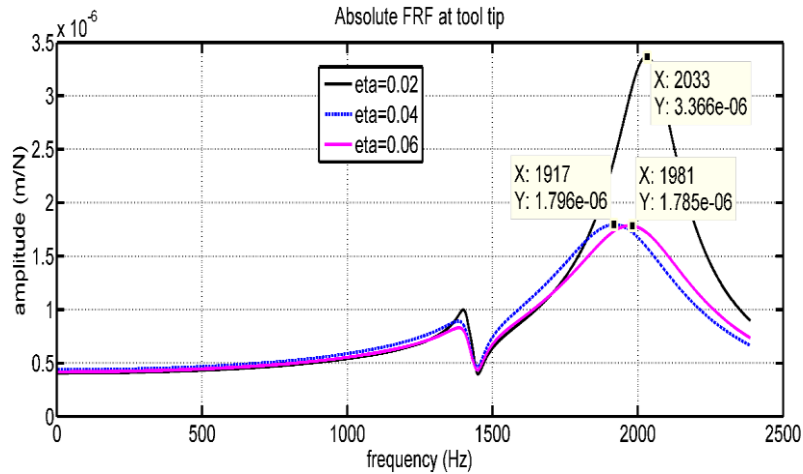


Figure 3.25: Tool tip FRF with rigid and flexible interfaces

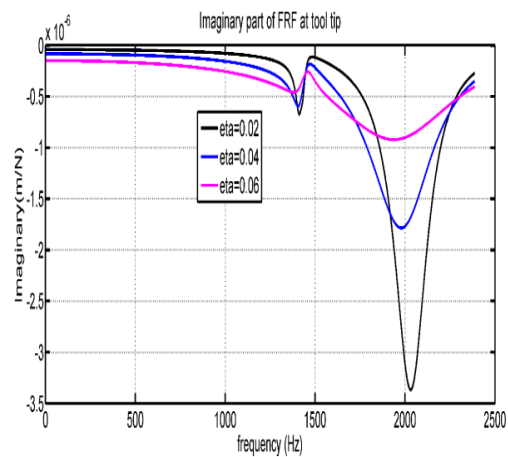
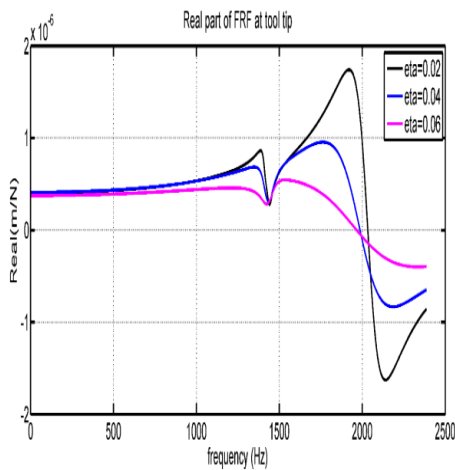
In the next case, the stiffness of the spindle-holder connection is assumed to be varied along the interface layer instead of considering the individual stiffness at the connecting nodes. Toward this, an elastic interface layer stiffness coefficient $K^i(x)$ is considered and it is assumed that there is no slip between these two parts during machining operations and stiffness coefficient remains constant. The stiffness of elastic interface layer is proportional to the normal pressure, therefore a parametric stiffness distribution based on the joint type (shrink fit, etc.) is selected and the stiffness parameters can be identified. These coefficients

are assumed to be complex valued to include a displacement-dependent energy dissipation mechanism in the joint interface $K(x) = k(x)(1 + i\eta)$ where $k(x)$ and η are the joint interface stiffness and its structural damping factor.

Initially, a case study has been carried out for different structural damping factors (η). Proper selection of the structural damping factor produces a more representative model of damping compared to the viscous damping model commonly adopted in other machine tool dynamic models. Figure 3.26 shows the absolute magnitude of the FRF at the tool tip. It is observed that for the structural damping of 0.06 the fundamental mode is 1981 Hz which is closer to the value obtained for the experimental modal test. Similarly, for the structural damping factor of 0.02, the first mode frequency is 2033 Hz, this value is closer to the finite element modeling with rigid coupling. This shows the marked effect of damping on dynamic response behaviour.



(a) Absolute FRF at $k(x) = 1.5 \times 10^5$ N/m



(b) Real part of FRF at $k(x) = 1.5 \times 10^5$ N/m (c) Imaginary part of FRF at $k(x) = 1.5 \times 10^5$ N/m

Figure 3.26: Tool tip FRF plots for different structural damping factors

The significance of this study is that one can identify the interface stiffness from the experimentally measured frequency response using finite element modelling.

3.3.1.f Non-linear bearing forces effects

For studying the effect of flexible bearing dynamic contact forces, the frequency responses are obtained by solving the finite element formulation with nonlinear bearing forces in time-domain. Using an additional degree of freedom at each node in the axial direction for earlier finite element model, the bearing contact forces are expressed in terms of the corresponding nodal degrees of freedom and the combined set of equations are formulated with two bending deflections, corresponding slopes and an axial deflection at every node as shown in Figure 3.27.

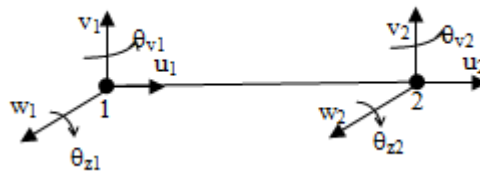
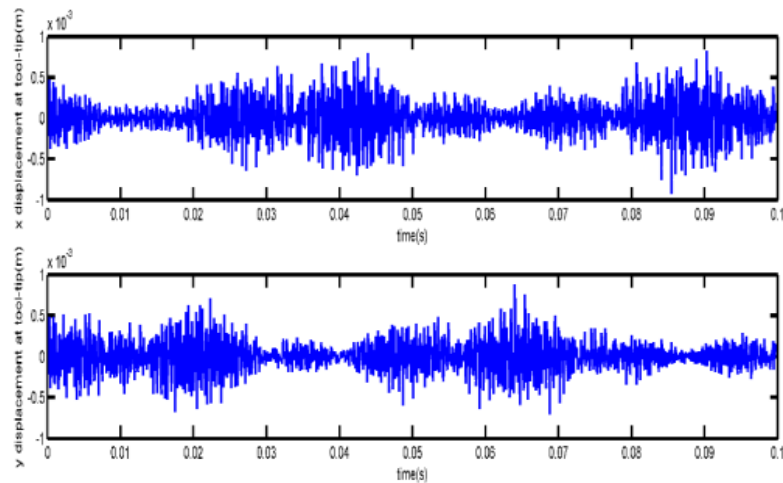
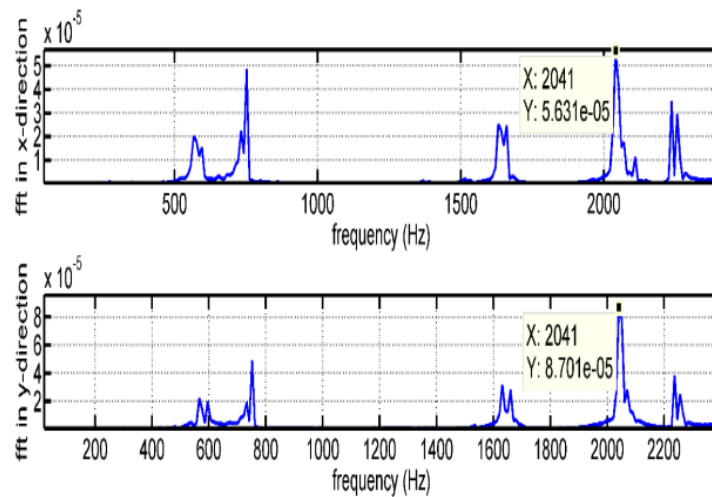


Figure 3.27: Element degrees of freedom for spindle discretization

The reduced coupled set of differential equations is solved explicitly, by using Runge-Kutta time-integration scheme [71]. The following bearing parameters are considered to arrive the time histories at different nodes: Inner radius (r)=75mm, outer radius(R)=110 mm, number of ball (N_b)=20, $C_b=13.34 \times 10^9$ N/m^{3/2}, diametral clearance(d_0)=5.5 μ m. Initially, the dynamic behavior of the rotor bearing system is analyzed with changes in the radial clearance. Figure 3.28 shows the time histories and FFT plots at the tool-tip node in two lateral directions at 5000 rpm corresponding to a radial clearance of 10 μ m. As is observed from FFT plots that there are several sub-harmonics existing before the overall system frequency of 2041 Hz, (which is obtained earlier). The smaller peaks are due to ball-passing excitations. An axial load $F_a=1500$ N is maintained through-out.



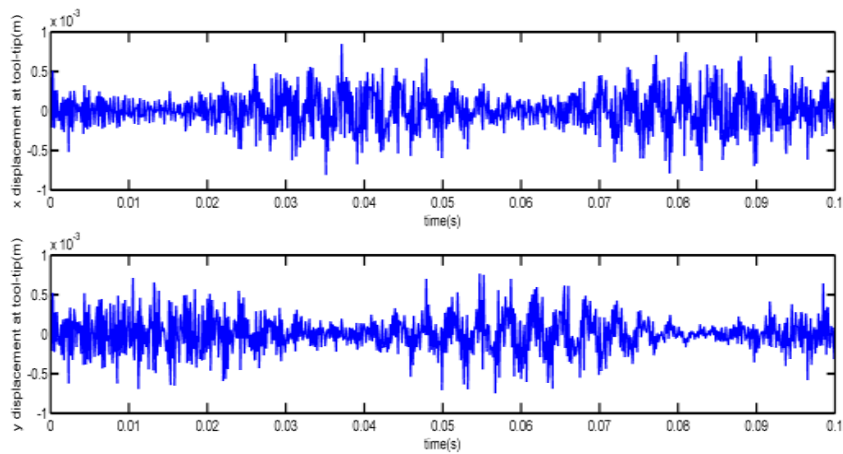
(a) Time-responses



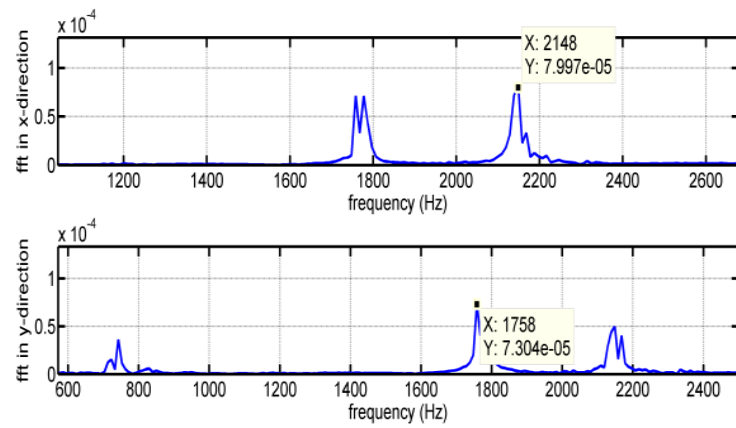
(b) FFT diagrams

Figure 3.28: Tool-tip node displacements at $r_0=10\mu\text{m}$

In high speed applications, spindle bearings possess negative clearances as reported earlier. In such a low negative clearance, the Hertzian contact force model reduces to a linear spring model, which was used previously. A case of negative clearance is also therefore considered for illustration. Figure 3.29 shows the time histories and FFT plot simulations corresponding to $r_0 = -0.5\mu\text{m}$.



(a) Time response



(b) FFT diagrams

Figure 3.29: Effect of small negative clearance at the two bearings

Figure 3.30 shows the FFT plots at tool-tip node for $r_0 = -10\mu\text{m}$

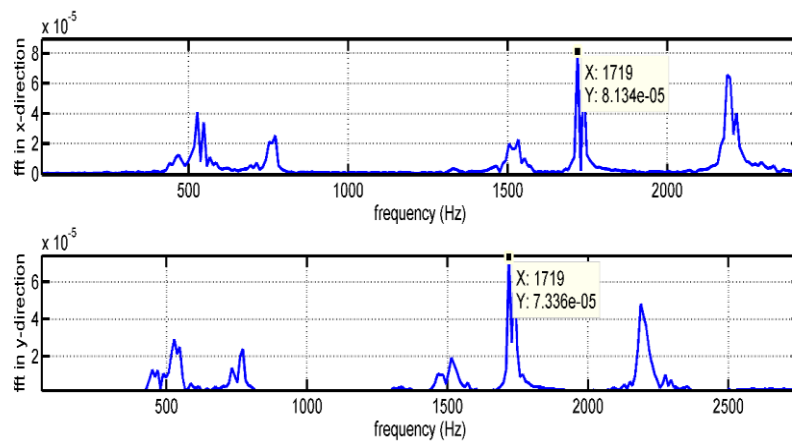
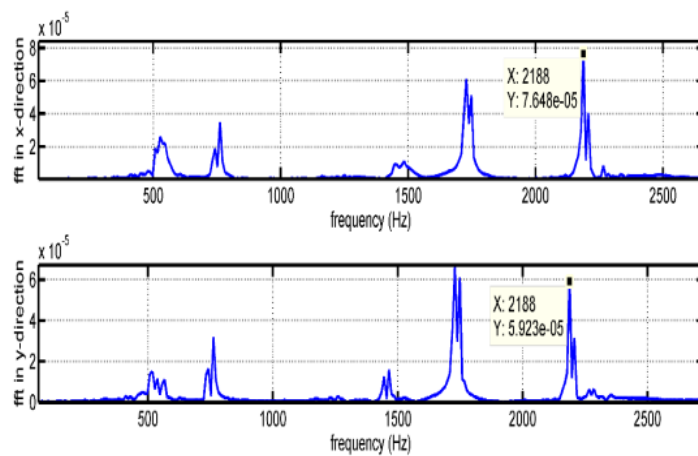


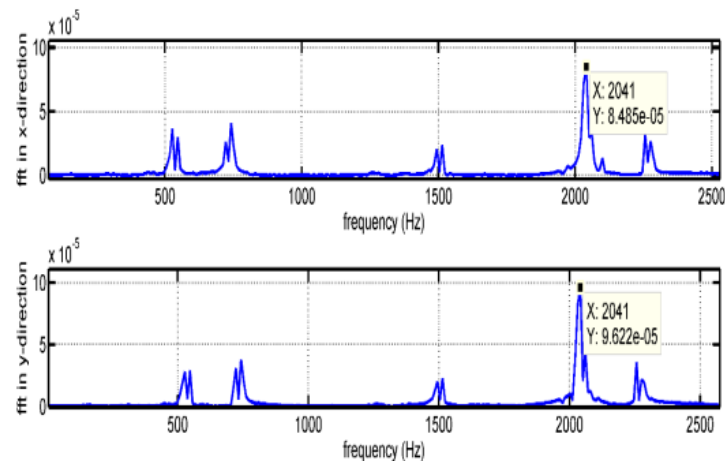
Figure 3.30: FFT plots for negative radial clearance of $-10\mu\text{m}$

It is evident that the amplitude of the tool vibration level decreases for higher negative values of radial clearance and in turn produces the change in the peak values closer to around 1719 Hz, which is less than the previously predicted first natural frequency.

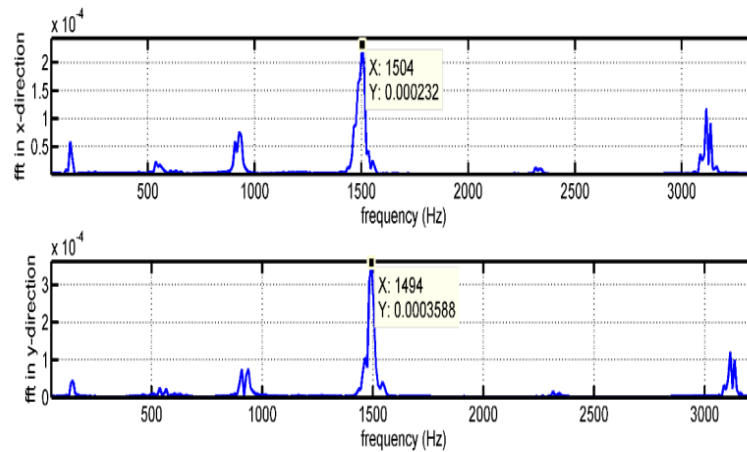
Next, it is planned to study the effect of axial preload on the dynamic response. Figure 3.31 shows the FFT plots at various preload values applied at the front and rear bearings. It is observed from all these plots, for the preload value of 1500N the peak frequency value is 2041Hz, which merely equal to the value obtained from the finite element methods and experimental approach. As the axial preload value increases, the amplitude of the tool displacement levels are also raises, reducing the resonant frequencies.



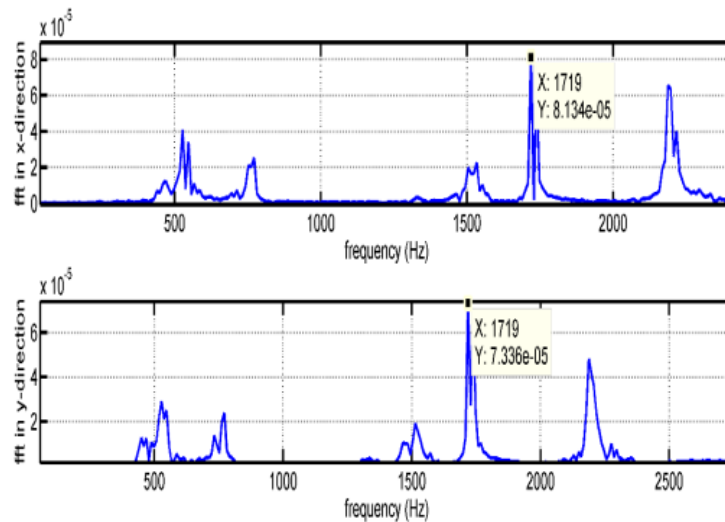
(a) FFT at $F_a=1000\text{N}$



(b) FFT at $F_a=1500\text{N}$

(c) FFT at $F_a=2000\text{N}$ Figure 3.31: FFT plots for different preload values ($r_0=10\mu\text{m}$)

In general, the contact angle (θ) of the ball with races influences the dynamic load capacity of the bearing. This contact angle constantly varies when there is a difference of velocity exists between the balls and races of the bearing. In the present work, the constant change in the value of contact angle is investigated with a constant axial preload $F_a=1500\text{N}$ and radial clearance of $10\mu\text{m}$. Figure 3.32(a) shows the FFT diagram at tool-tip node for $\theta=10^\circ$. It is observed that from FFT plot that the magnitude of the highest peak is at around 1719Hz in both the bending directions. Figure 3.32(b) shows the corresponding diagram at $\theta=35^\circ$. As the contact angle increases, the amplitudes in both the bending directions have slightly increased.

(a) $\theta=10^\circ$

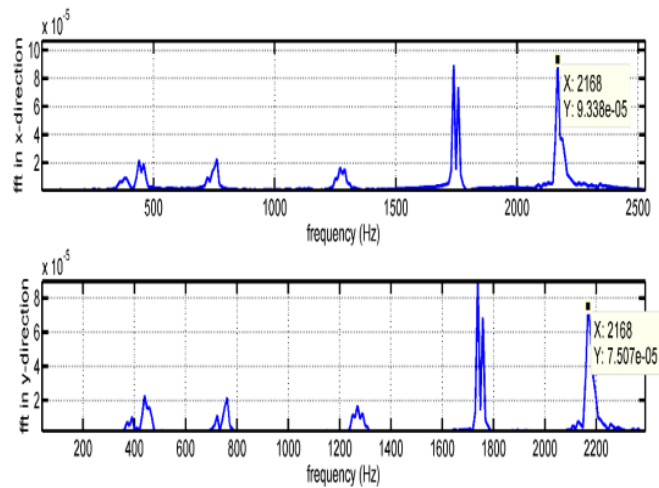
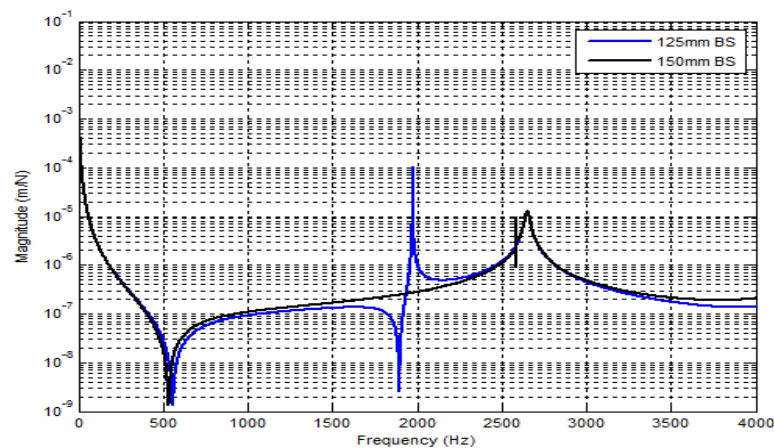
(b) $\theta=35^{\circ}$

Figure 3.32: FFT at tool-tip node in two lateral directions

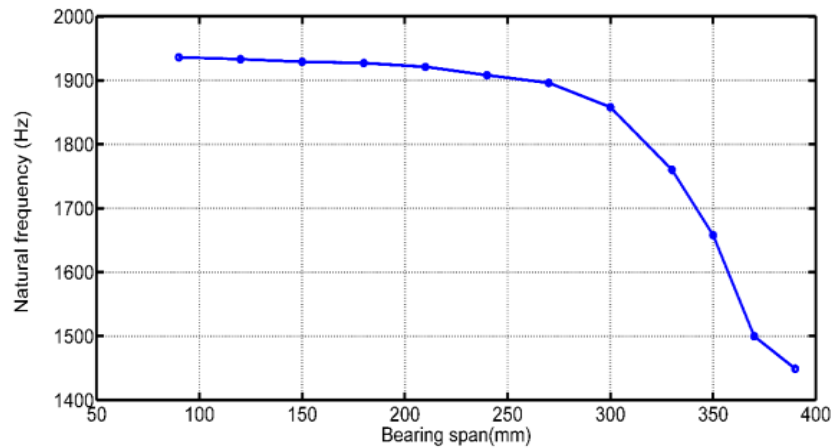
In conclusion, this study revealed the effect of various ball bearing parameters including radial clearance, axial preload and contact angle on the overall dynamic behavior of the spindle-tool integral system.

3.3.2 Parametric studies of spindle variables

In order to select the optimal spindle configuration, initially it requires identification of variables influencing the dynamic response behavior of integral spindle-tool unit. Effects of bearing span (axial distance between rear and front bearings), axial-preload and tool-overhang on tool-tip dynamic response are considered with constant bearing stiffness values using RCSA methodology. Figure 3.33(a) shows tool-tip FRF at two different bearing spans on the spindle system. In Figure 3.33(b), the variation of fundamental mode with different values of bearing span is shown using full-order FEM approach.



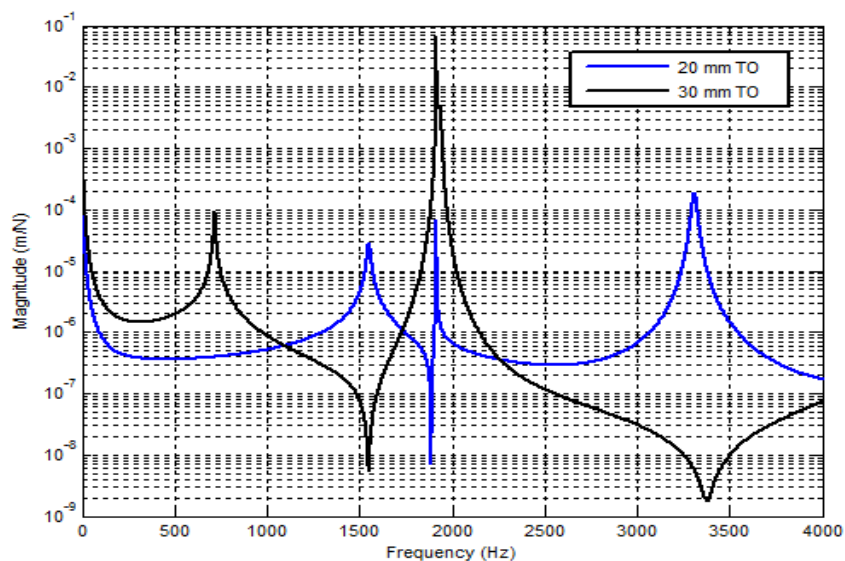
(a) FRF at tool-tip (RCSA)



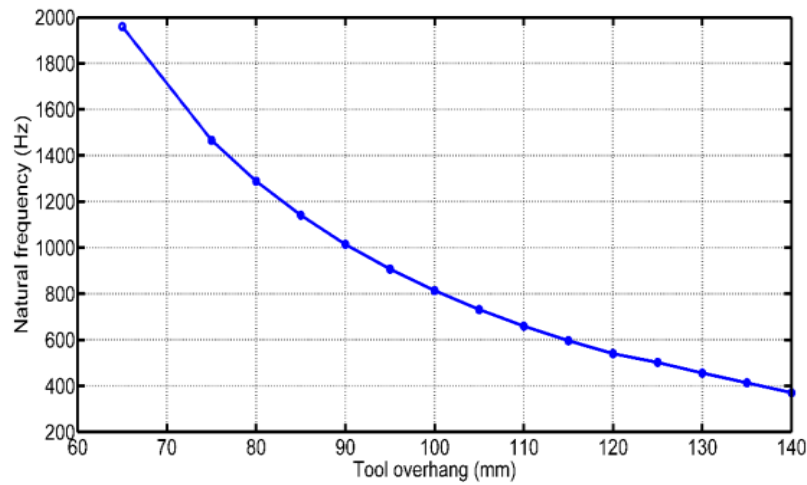
(b) Variation of natural frequencies

Figure 3.33: Effect of bearing span on spindle-tool dynamics

It is observed that the first mode has shifted from 1975Hz to 2658Hz as bearing span increases. Figure 3.34(a) shows the effect of tool overhang. It indicates that, as the overhang increases, the first mode has shifted from 1550Hz to 716Hz. But the maximum vibration frequency response of the system is mainly dominated by the second mode as the amplitude of vibration level is high. The remaining higher vibration modes have lesser effect on dynamic rigidity of the system. Thus, the second mode produces the most flexible vibration instabilities during machining process as the tool overhang length increases. Smaller tool-overhang is preferred as the amplitude of the vibration levels is comparatively less. Using FEM, the corresponding fundamental modes are obtained by varying the tool-overhang lengths and are shown in Figure 3.34(b).



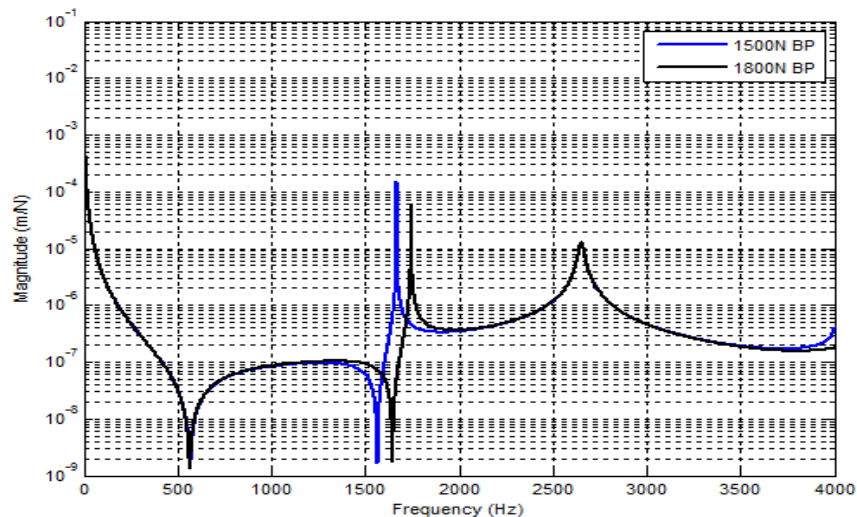
(a)FRF at tool-tip (RCSA)



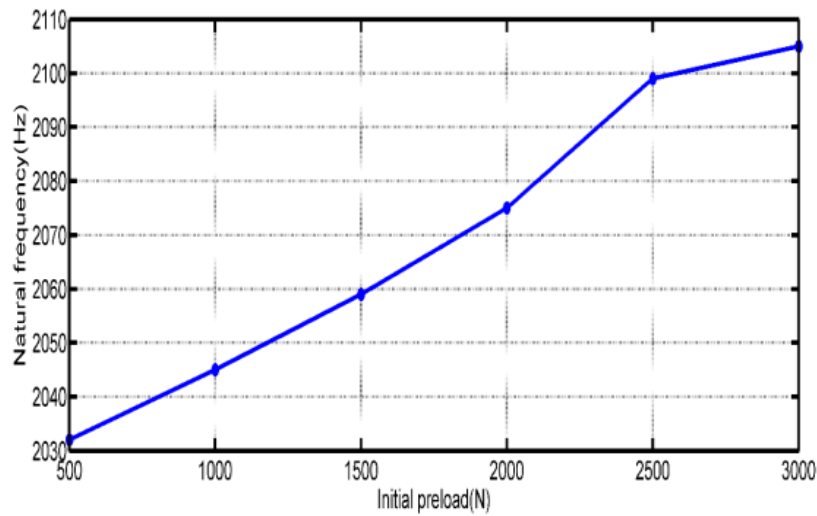
(b) Variation of natural frequencies

Figure 3.34: Effect of tool overhang on spindle-tool dynamics

Similarly, the analysis is carried out for two different values of bearing preloads as shown in Figure 3.35(a). As the preload increases from 1800N to 2000N, it is observed that the curves match each other except during the first mode range (1300-2000 Hz). The first mode frequency increases from 1660Hz to 1750Hz. Figure 3.35 (b) shows corresponding fundamental frequencies of the system for different preload values using full-order FEM. Obviously, the frequencies increase with the bearing preload. In all above studies, the constant stiffness model (i.e., small negative clearance criterion) is employed.



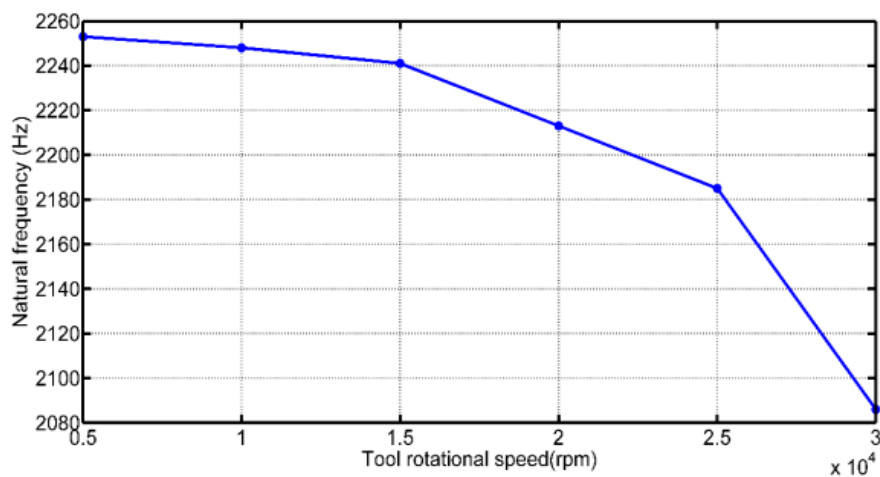
(a)FRF at tool-tip (RCSA)



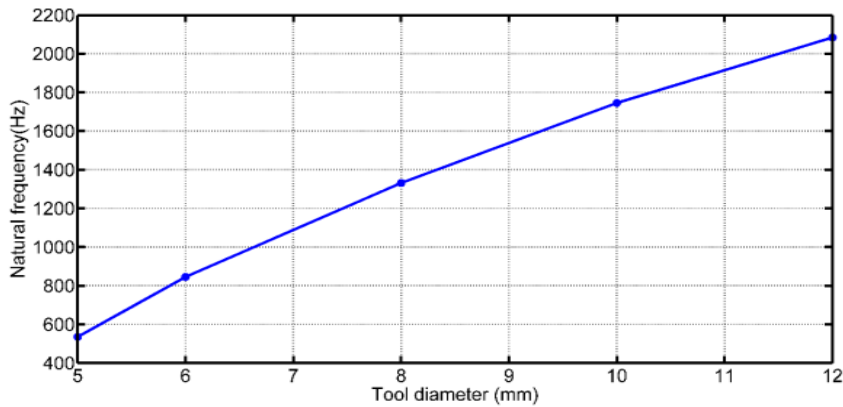
(b) Variation of natural frequencies

Figure 3.35: Effect of bearing preload on spindle-tool dynamics

Further, to study the effect of multiple parameters on the tool-tip FRF simultaneously, full-order FE model is employed. This approach gives reasonable results at relatively lower computational time. Effects of additional parameters like tool diameter and spindle speed are also considered on the first mode frequency as shown in Figure 3.36.



(a) spindle speed



(b) tool diameter

Figure 3.36: Variation of fundamental frequency with other parameters

3.3.2.a Optimum Design of Experiments

In order to reduce the numbers of experiments and maintain the resolution of the results, a three-level factorial design with five factors is implemented. Table 3.4 shows the process parameters and their levels for the experiments. Taguchi $L_{27}(3^{*5})$ orthogonal array is used for the experimental design in order to predict the influence of controlled factors such as bearing span (BS), tool overhang length (TO), interface stiffness k_c (N/m), tool diameter (d_t) and axial preload (F_a) on the natural frequencies and dynamic stiffness of the spindle-tool unit.

In this table, the first variable tool overhang (X_1) is selected between practical values between 55 to 75 mm based on the available flute and shank lengths of commercial cutting tools. Bearing span (X_2) likewise is an internal spindle parameter which can be varied within the feasible region. In present task $X_2 \in [120, 240]$ mm in three levels depending on the total length of the spindle shaft of 280 mm. The tool diameter (X_3) is varied between 8 to 12 mm as per the commercially available end-mill tools. The fourth parameter interface stiffness $X_4 \in [1.5 \times 10^5, 1.5 \times 10^7]$ N/m is varied in three levels chosen based on the shaft stiffness. The final parameter axial preload (X_5) is selected in three levels: 1000 N, 1500 N and 2000 N.

Table 3.4: Detailed simulated experimental data using Taguchi L₂₇ (3**5) array

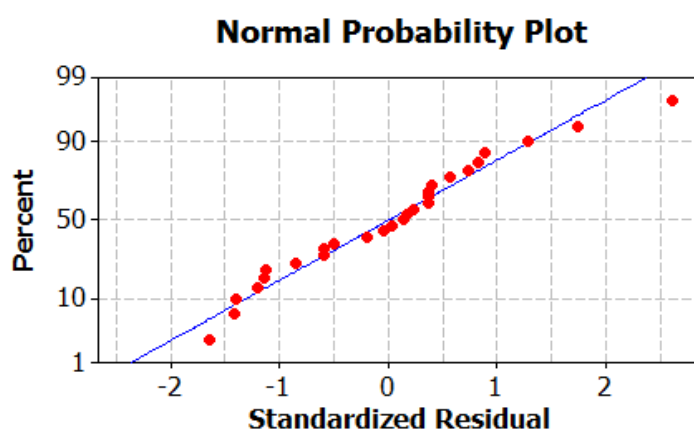
Exp No	Tool overhang (TO) in mm	Bearing span(BS) in mm	Tool diameter (mm)	Interface stiffness (N/m)	Axial preload (N)	Natural frequency (Hz)	Dynamic stiffness (N/m)
1	55	120	8	1.5×10^5	1000	827	2170
2	55	120	8	1.5×10^5	1500	805	2070
3	55	120	8	1.5×10^5	2000	799	2060
4	55	180	10	1.5×10^6	1000	1292	5500
5	55	180	10	1.5×10^6	1500	1285	5400
6	55	180	10	1.5×10^6	2000	1274	5200
7	55	240	12	1.5×10^7	1000	2386	111480
8	55	240	12	1.5×10^7	1500	2374	110910
9	55	240	12	1.5×10^7	2000	2369	110630
10	65	120	10	1.5×10^7	1000	2286	343600
11	65	120	10	1.5×10^7	1500	2149	321800
12	65	120	10	1.5×10^7	2000	2121	320100
13	65	180	12	1.5×10^5	1000	920	7930
14	65	180	12	1.5×10^5	1500	914	7810
15	65	180	12	1.5×10^5	2000	901	7340
16	65	240	8	1.5×10^6	1000	1265	1690
17	65	240	8	1.5×10^8	1500	1242	1340
18	65	240	8	1.5×10^6	2000	1231	1290
19	75	120	12	1.5×10^8	1000	1038	23090
20	75	120	12	1.5×10^6	1500	1021	22460
21	75	120	12	1.5×10^8	2000	1011	21630
22	75	180	8	1.5×10^7	1000	2379	808400
23	75	180	8	1.5×10^7	1500	2269	794100
24	75	180	8	1.5×10^7	2000	2232	769500
25	75	240	10	1.5×10^5	1000	663	2850
26	75	240	10	1.5×10^5	1500	641	2690
27	75	240	10	1.5×10^5	2000	629	2540

The data was statistically analysed by Analysis of variance (ANOVA) to check the capability of the parameters. Table 3.5 shows the ANOVA outputs using MINITAB (V15) software.

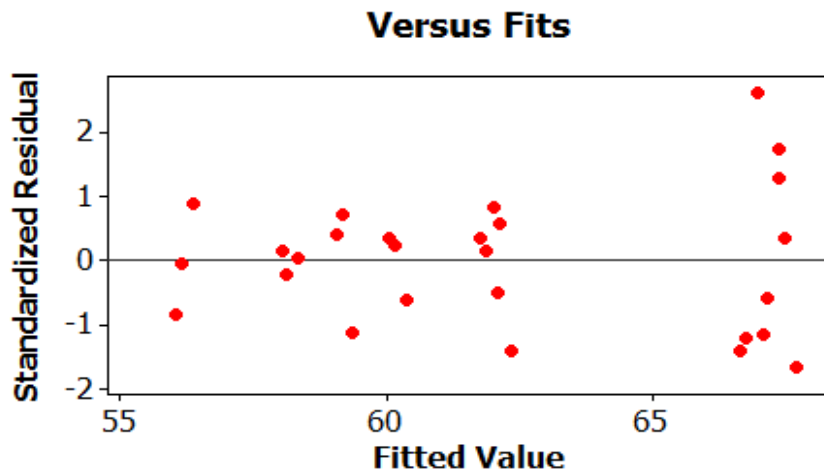
Table 3.5: Analysis of Variance for Natural frequency (Hz)

Factors	DOF	Sum of squares	Mean square	F-value	P-value	Percentage of contribution
Tool overhang(TO)in mm	2	12.267	6.133	509.45	0.000	2.917
Bearing span(BS) in mm	2	6.879	3.440	285.69	0.000	1.636
Tool diameter(mm)	2	2.648	1.324	109.98	0.000	0.629
Interface stiffness(N/m)	2	397.957	198.978	16527.38	0.000	94.662
Axial preload(N)	2	0.454	0.227	18.85	0.000	0.107
Residual error	16	0.193	0.012	---	---	0.045
Total	26	420.397	---	---	---	---

It is observed that, all the input factors are statistically significant on response parameter as the P value is less than 0.05. Compared to other factors, interface stiffness is the most dominant process parameter. The interface stiffness is having more influence on the natural frequency, as its F value is very high and the corresponding percentage of contribution is high. The adequacy of the model has also been investigated by the examination of residuals. The residuals are examined using the normal probability plots of the residuals and the plot of the residuals versus the fitted response for the natural frequencies. Figure 3.37(a) revealed that the residuals generally fall on a straight line implying that the errors are distributed normally. Also Figure 3.37(b) revealed that they have no obvious pattern and unusual structure. This implies that the model proposed is adequate and there is no reason to suspect any violation of the independence or constant variance assumptions.



(a) Normal probability plot



(b) Residual plot

Figure 3.37: Data normality testing for natural frequency

The combination of bearing span, tool overhang, interface stiffness, tool diameter and axial preload are applied to get the maximum natural frequency. The S/N rate helps to recognize the best possible stage of process parameters. The grouping of parameters with the biggest S/N rate is definitely the best possible setting of process parameters. The formula for

determining S/N percentages for “larger is better” is given as $(S/N) = -10 \log \left[\frac{1}{n} \sum_{i=1}^n \left(\frac{1}{y_i^2} \right) \right]$

, where, y_i = trial value in the i^{th} test, y_o =objective value and n = number of reproductions. It is also observed from the main effects plot for S/N ratios as seen from Figure 3.38, the optimized parameters could be taken as $X_1=180\text{mm}$, $X_2=55\text{mm}$, $X_3=8\text{mm}$, $X_4=1.5 \times 10^7 \text{ N/m}$ and $X_5=1000\text{N}$.

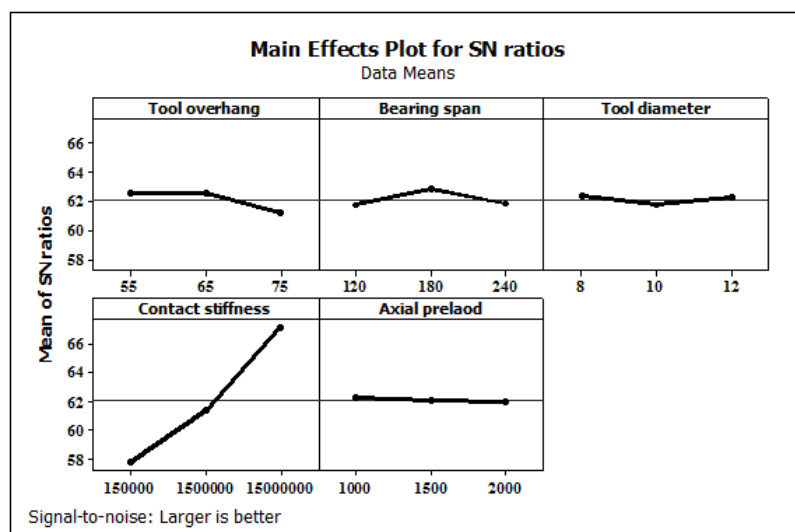


Figure 3.38: Signal to noise ratios plots for the control factors on natural frequency (Hz)

It is also observed from Table 3.6, the levels and ranks are given for the control factors. Interface stiffness is the most dominant process parameter followed by the tool overhang, influences the dynamics of the spindle-tool system.

Table 3.6: Response table for signal to noise ratio (Larger is better)

level	Tool overhang(TO) in mm	Bearing span(BS) in mm	Tool diameter (mm)	Interface stiffness(N/m)	Axial preload (N)
1	62.62	61.72	62.43	57.85	62.32
2	62.63	62.86	61.71	61.43	62.11
3	61.20	61.87	62.30	67.17	62.01
Delta	1.44	1.14	0.72	9.32	0.31
Rank	2	3	4	1	5

Similarly, the data was statistically analysed to check the influence of dynamic stiffness on the input process parameters. Table 3.7 shows the ANOVA outputs for the dynamic stiffness.

Table 3.7: Analysis of Variance for dynamic stiffness (N/m)

Factors	DOF	Sum of squares	Mean square	F-value	P-value	Percentage of contribution
Tool overhang(TO)in mm	2	528.72	264.36	1911.12	0.000	5.439
Bearing span(BS) in mm	2	810.50	405.25	2929.64	0.000	8.337
Tool diameter(mm)	2	170.36	85.18	615.79	0.000	1.752
Interface stiffness(N/m)	2	8206.42	4103.21	29662.80	0.000	84.421
Axial preload(N)	2	2.51	1.25	9.06	0.002	0.025
Residual error	16	2.21	0.14			0.022
Total	26	9720.73				

It is observed that, all the input factors are statistically significant on response parameter as the P value is less than 0.05. Compared to other factors, interface stiffness is the most dominant process parameter. The interface stiffness is having more influence on the

dynamic stiffness, as its F value is very high and the corresponding percentage of contribution is high. The normal probability plot, given in Figure 3.39(a) shows a clear pattern (as the points are almost in a straight line) indicating that all the factors are affecting the dynamic stiffness. Also the errors are normally distributed and the regression model is well fitted with the observed values. Figure 3.39(b) indicates that the maximum variation of -2 to 4, which shows the high correlation that exists between fitted values and observed values.

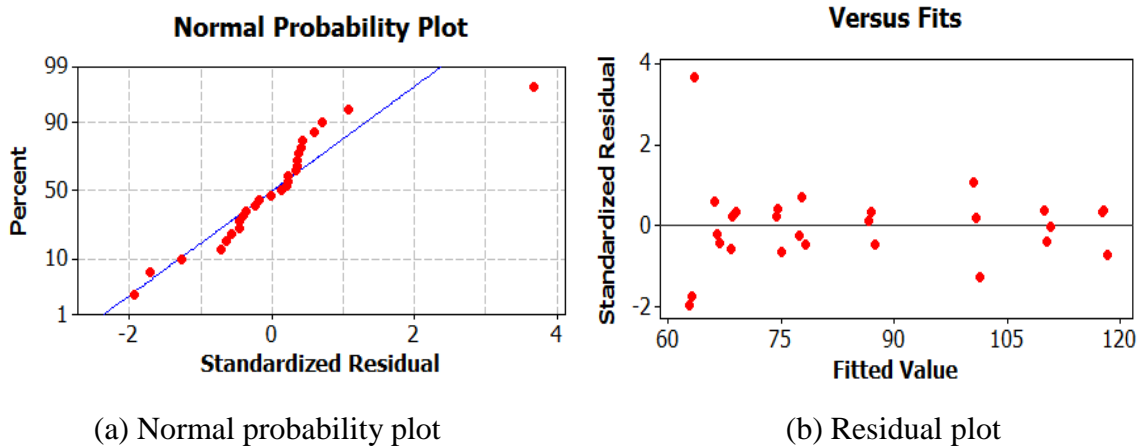


Figure 3.39: Data normality testing for dynamic stiffness

The signal to noise (S/N) ratio plots are taken for the combination of same input design parameters on the dynamic stiffness. From Figure 3.40, the optimized parameters could be taken as $X_1=75$ mm, $X_2=180$ mm, $X_3=12$ mm, $X_4=1.5 \times 10^7$ N/m and $X_5=1000$ N.

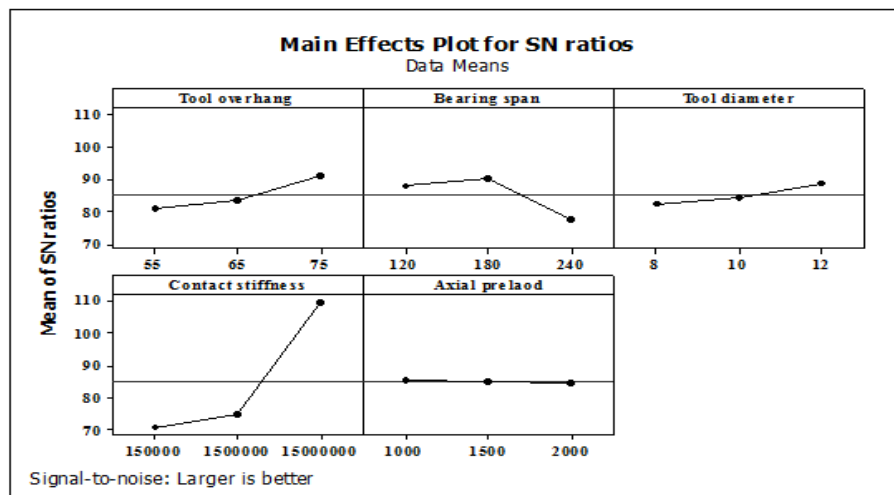


Figure 3.40: S/N plots for control factors on dynamic stiffness

From Table 3.8, it is seen that the delta values and ranks are given for the control factors. Interface stiffness is the most dominant process parameter followed by the bearing span influences the dynamic stiffness of the spindle-tool system.

Table 3.8: Response table for signal to noise ratio (Larger is better)

level	Tool overhang(TO) in mm	Bearing span(BS) in mm	Tool diameter (mm)	Interface stiffness(N/m)	Initial preload (N)
1	80.65	87.92	82.50	70.92	85.58
2	83.72	90.09	84.50	74.90	85.11
3	91.18	77.54	88.54	109.73	84.85
Delta	10.54	12.55	6.04	38.81	0.74
Rank	3	2	4	1	5

Based on the above studies, it observed that the dynamic stiffness of the system has been greatly affected by these spindle-tool parameters. So, as a next study, it is planned to obtain the optimal dimensions of spindle-tool system.

3.3.3 Optimal design of spindle-tool system

The design of spindle-tool system for improving the cutting process stability (increasing stable depth of cut at a speed) over operating process conditions is essentially important. As, the stability directly depends on tool-tip frequency response function, often the focus is on obtaining optimal values of frequency response function-based quantities [35]. Various performance criteria can be selected such as minimum weight, highest basic frequency, maximum dynamic stiffness, depth of cut, and so on. From these objectives, maximum dynamic stiffness and depth of cut are directly related to chatter vibration, which are the utmost important issues in the high-speed machining applications.

In present work, the dynamic stiffness of the spindle-tool system is considered as the main objective function. Various parameters influencing the dynamic stiffness are the bearing span, tool overhang, tool rotational speed, tool diameter and preload which are treated as the design variables (X). The dynamic stiffness(K_{di}) of the spindle-tool system is defined from the frequency response function at the tool tip as shown in Figure 3.41, which is described as:

$$K_{di} = \frac{1}{\left| (H_{imag})_i \right|} \quad (3.94)$$

Here, H_{imag} represents the imaginary part of FRF at the tool tip and 'i' is the mode number which represents that each mode has its own dynamic stiffness.

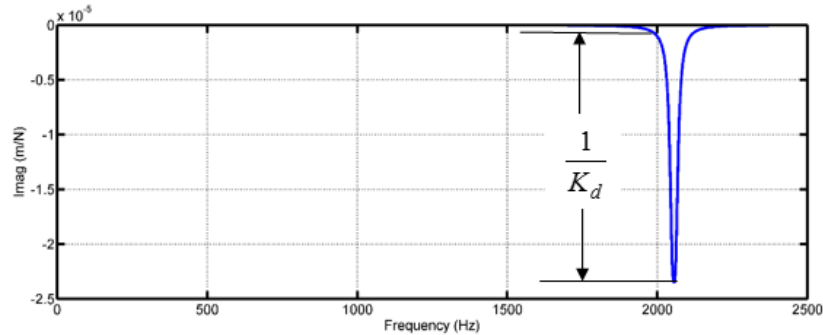


Figure 3.41: Imaginary part of FRF of spindle

In achieving high dynamic stability during the cutting operation, the tool-tip frequency response function is to be optimally designed. As this is a nonlinear function of spindle-tool parameters, a solution is obtained from non-conventional optimization scheme in present work. Figure 3.42 shows the concept of optimization procedure employed in this work, which has four modules: (i) a neural network module, (ii) de-normalization module (iii) fitness function definition and (iv) optimization module. First and last modules are explained in detail

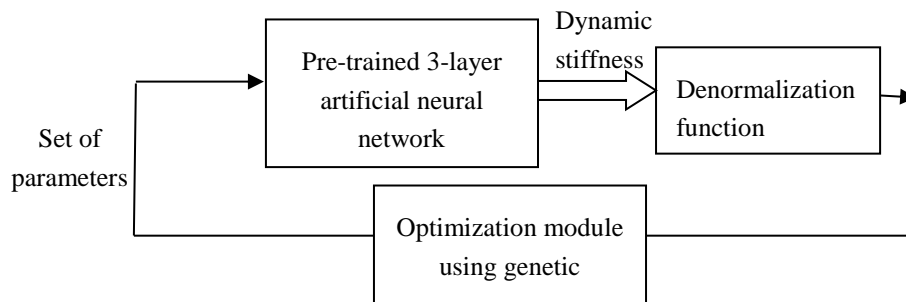


Figure 3.42: Block diagram of the proposed Neuro-Genetic system

(i) Neural network Module

The first module is based on the trained neural network, which acts in function approximation of dynamic stiffness in terms of the input parameters considered. The famous neural network model is multi-layer perceptron (MLP) trained with back-propagation learning algorithm [141]. MLP neural network consists of an input and output layer along with one or multiple intermediate (hidden) layers of neurons. It requires a set of input and output (target) patterns initially. Such a data is generated from a reliable computational procedure or experimental analysis. Entire data is grouped into training

(75%) and testing (25%) samples. During the training phase, the training samples (both inputs and corresponding targets) are presented one by one. As inputs are supplied to the input layer, hidden layers process them to output layer through a sequence of operations. The input at every layer (Y) is the sum of products of the outputs at previous layer (X) and the corresponding weights (strength of synapse) connecting the current node with all other nodes of previous layer (W^j). That is $Y = \sum W^j X$. The output at each of the hidden layers ($O = f(Y)$) and output layer are computed using a threshold function (often sigmoidal function). Once, outputs at output layer are estimated from threshold function, they are compared against the target values corresponding to that sample. Then an error (e) or square error is estimated.

Training in neural network concept refers to the adjustment of connection weights in each layer such that the mean square error at the output layer gets minimized. For such an adjustment, error is back-propagated and the initially chosen random weight matrices between the layers are updated.

All the input-output data is initially normalized before it is supplied to neural network. The purpose of the normalization is to minimize issues arising out of different ranges between the variables of interest and to adjust the values of the attributes to the same interval [144]. The weight adjustment law or learning law is called back-propagation rule.

Figure 3.43 shows typical architecture of 3-layer error back-propagation neural network.

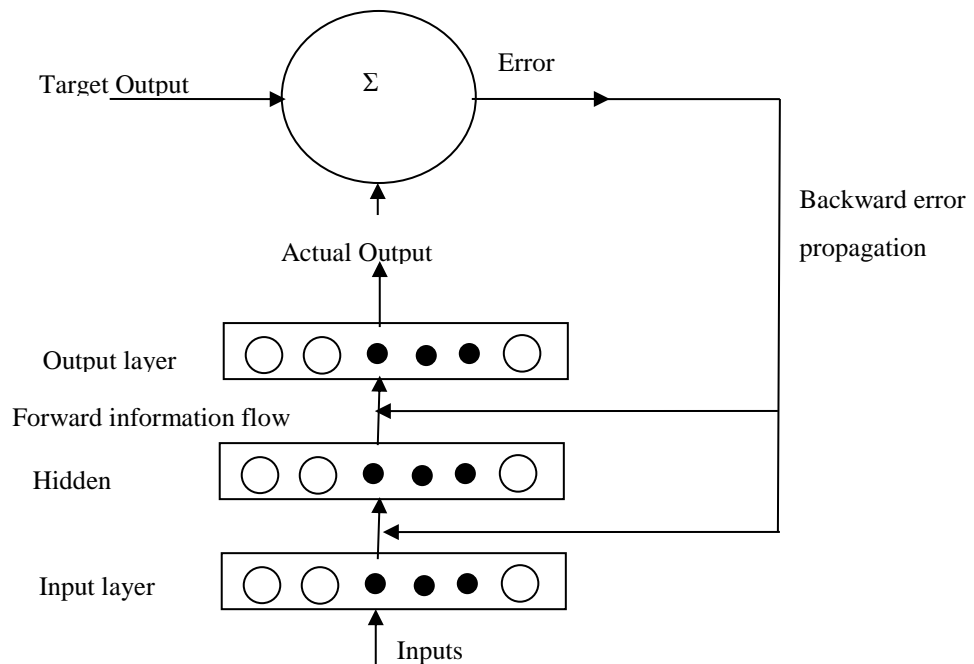


Figure 3.43: Typical 3-layer neural network

Here, the computations are passed forward from input to output layer and resulting errors are propagated back in other direction to change the weights. The connection weights are initially chosen randomly. In each subsequent training step, the initial set of weight vectors is adjusted to minimize the square error E as follows:

$$W_{new} = W_{old} - \lambda \nabla E, \quad (3.95)$$

Where, $\nabla E = \left[\frac{dE}{dW_1}, \frac{dE}{dW_2}, \dots, \frac{dE}{dW_n} \right]$ and λ is learning parameter. While computing the

gradient, the selection of the output function is important. There are different output functions such as linear function, step function and sigmoid functions. One useful property of sigmoid function is that the differential (gradient) of the function can be expressed in terms of the function itself. i.e., $f'(x) = g(f(x))$. This property simplifies the computation of new weights from initial random values. When the number of layers and the number of variables and data points increase, the learning tends to be slow during training. Also, as it is a gradient based algorithm, it may reach a local minimum in weight space. By adding momentum/modifying the error optimization rule according to other schemes including Newton/Marquardt methods, it is possible to overcome the difficulty. At the end of the training phase, the associated trained weights of the neurons are stored in the memory. In the next phase (testing), the trained network is fed with a new set of input data. The network predictions (using the trained weight) are compared to the target output values to assess the ability of the network to produce (generalize) correct responses for the testing. Once the training and testing phases are found to be successful, the corresponding network can be put to use in practical application. Details of the training algorithm is given in Appendix-D. In the present work, dynamic stiffness is taken as a function in terms of spindle-tool system variables. It is approximated using a single hidden layer feed-forward neural network model trained and tested with 27 sets of data derived earlier. Figure 3.44 shows the neural network architecture.

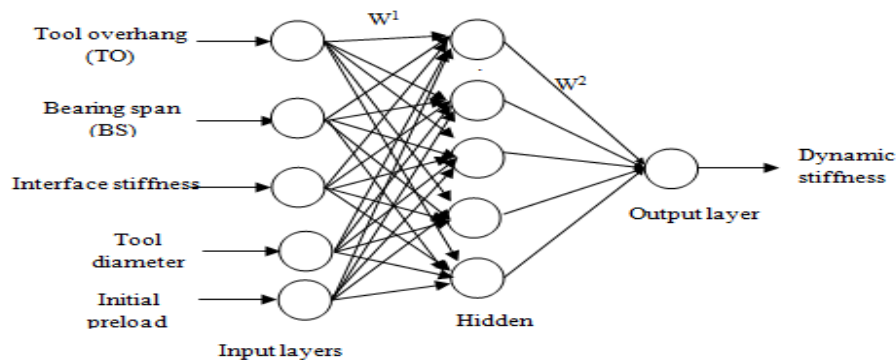
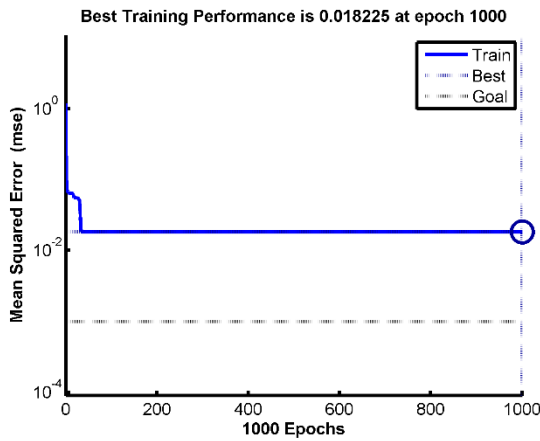
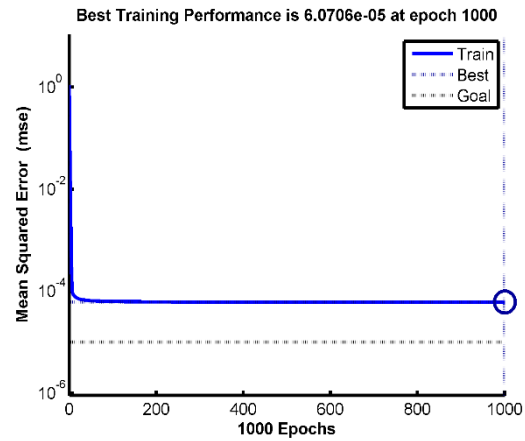


Figure 3.44: Neural network model in present case

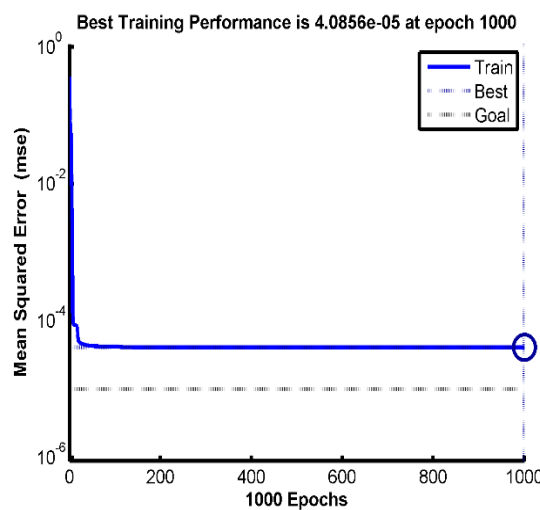
Twenty-two sets of input-output data are used for training and remaining five sets are employed for testing. Number of neurons in the hidden layer is varied and in each case the mean square error at the end of one thousand cycles is computed. Figure 3.45 shows the convergence plots of the neural network training with different number of hidden neurons.



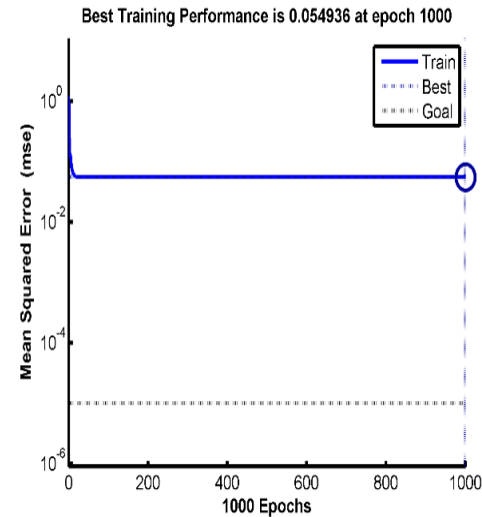
(a) 3 Hidden neurons



(b) 4 Hidden neurons



(c) 5 Hidden neurons



(d) 6 Hidden neurons

Figure 3.45: Convergence trends for various hidden neuron structures

MATLAB neural network tool box is employed for training the data. A learning rate of 0.4 is employed through-out. It is observed that the five hidden neuron structure gives smallest mean square error. The final weight structure between the input-hidden layer; and between hidden-output layer are shown in Table 3.9.

Table 3.9: The weight structure for 5 hidden node skeleton

No. of neurons	W^1					W^2
	1	0.040334	-0.07013	0.007651	-1.41E-06	0.004007
2	-0.04021	0.00154	-0.63537	4.66E-07	-3.91E-05	0.64129
3	0.00274	-0.08291	-0.61247	0.000238	-0.01637	0.004103
4	0.222607	0.038745	0.835961	-3.35E-07	-0.01066	0.006297
5	0.079119	-0.00345	-0.63072	0.000446	-0.00861	-0.21506

Logarithmic sigmoidal activation function is used in the hidden and output layers. The performance of the developed network is examined on the basis of correlation coefficient (R value) between the output (predicted) values and the target (experimental) values for the test data set (5) and training data set (22). Figure 3.46 shows the variation of R value as a measure of variation in output with respect to targets. It lies in between 0 and 1. If it is 1 then it indicates the perfect correlation between the target values and output. Correlation coefficient of 0.999 was obtained between the test data set and model predicted values which indicate good correlation.

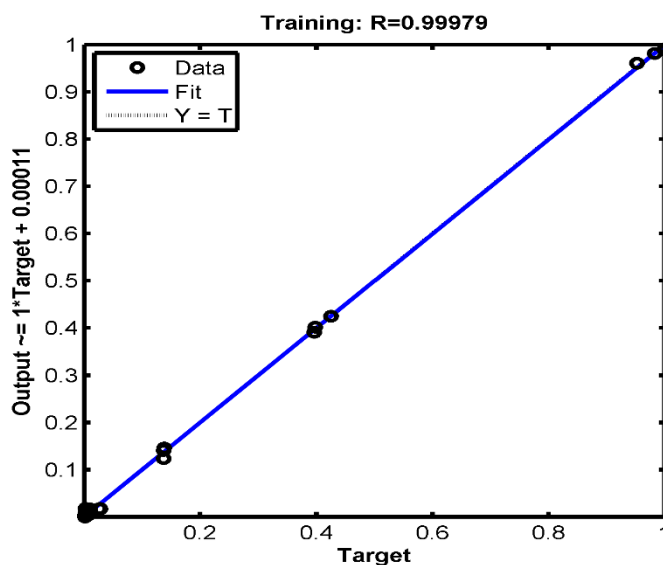


Figure 3.46: Correlation between the predicted values and test data

(ii) Intelligent optimization scheme

(a) Harmony search optimization

Additional optimal studies are carried out related to the cutting dynamics using the harmony search algorithm. Here, the maximum dynamic stiffness function in terms of spindle design variables is approximated using a feed-forward neural network model developed with the

help of training data arrived for different combinations of spindle-tool geometry. The error-back propagation algorithm is employed to update the weight structure for a single hidden layer model. In optimizing the average stable depth of cut, it is proposed to employ one of the latest meta-heuristic algorithm namely harmony search optimization (HSO), which is motivated from the behavioural phenomenon of musicians towards improvisation [150]. The HSO presents the following basic advantages compared to other non-conventional optimization schemes: (a) It requires fewer mathematical requirements (b) the derivative information is not necessary due to its stochastic random nature. The essential steps of the basic method are presented below:

Step1: Problem details and initialization of algorithm parameters

$$\text{Min } f(X)$$

$$X = (X_1, X_2, X_3, \dots, X_D) \quad (3.96)$$

$$X_i \in [X_i^L, X_i^U], \quad i=1,2,3,\dots,D$$

where $f(X)$ is the objective function and D is the number of decision variables. The parameters of algorithm are: harmony memory size (HMS), Pitch adjustment rate (PAR), Harmony memory consideration rate (HMCR), bandwidth vector (bw), maximum number of improvisations etc.

Step2: Initialize the harmony memory

The harmony memory (HM) is composed of HMS harmony vectors. Each harmony vector is produced from a consistent distribution in the possible vicinity, as

$$x_i^j = x_i^L + (x_i^U - x_i^L) \times \text{rand}() \quad (3.97)$$

where $i=1,2,\dots,D; j=1,2,\dots,HMS$, $\text{rand}()$ is random values between 0 to 1.

$$HM = \begin{bmatrix} x^1 \\ x^2 \\ \cdot \\ \cdot \\ x^{HMS} \end{bmatrix} = \begin{bmatrix} x_1^1 & x_2^1 & \cdot & \cdot & x_D^1 \\ x_1^2 & x_2^2 & \cdot & \cdot & x_D^2 \\ \cdot & \cdot & \cdot & \cdot & \cdot \\ \cdot & \cdot & \cdot & \cdot & \cdot \\ x_1^{HMS} & x_2^{HMS} & \cdot & \cdot & x_D^{HMS} \end{bmatrix} \quad (3.98)$$

Step3: Develop a new harmony

A New Harmony vector $x^{new} = (x_1^{new}, x_2^{new}, \dots, x_D^{new})$ is designed based mostly on three rules:

(a) Random generation

(b) Memory consideration

(c) Pitch adjustment

In random generation, every individual decision variable of a new harmony vector is randomly selected with a probability rate of (1-HMCR) and it generally lies between 0 to 1.

$$x'_i \leftarrow \begin{cases} x'_i \in \{x_i^1, x_i^2, \dots, x_i^{HMS}\} & \text{with probability HMCR} \\ x'_i \in x_i & \text{with probability (1 - HMCR)} \end{cases} \quad (3.99)$$

Decision variable has to be pitch-adjusted using PAR parameter with a probability ratio of HMCR*PAR. The initial pitch attained in the memory consideration is retained as HMCR*(1-PAR). The following pitch adjustment rule is employed to each decision variable with a bandwidth (bw) and a uniform distribution $u(-1,1)$ between -1 to 1 as follows

$$x'_i \leftarrow \begin{cases} x'_i \pm u(-1,1) \times bw & \text{with probability HMCR} \times PAR, \\ x'_i \in x_i & \text{with probability HMCR} \times (1 - PAR) \end{cases} \quad (3.100)$$

Step4: Revise the harmony memory

Obtain the worst individual x^{worst} from the HM. If x^{new} is improved than x^{worst} then $x^{worst} = x^{new}$.

Step5: If number of cycles exceeds maximum, exit the loop and display optimum design parameters and corresponding objective function.

HMCR, PAR and bw are very important factors and are useful in adjusting convergence rate. Also, these parameters allow the solution to escape from local optima. So, latest techniques focus on the fine adjustment of these parameters. An improvised HSO scheme is adopted in this work.

The function values are estimated using a set of pre-trained neural network weight structure. The dynamic stiffness of the spindle-tool structure is improved by selecting an optimum set of spindle-tool data. The formulation is solved by using harmony search algorithm. The function evaluations are performed by the trained neural network explained above. The pitch adjustment rate (PAR) is set as 0.3, harmony memory size (HMS) =13, harmony memory considering rate (HMCR) =0.8; range of variables considered same as in parametric studies conducted earlier. The design vector is represented by $X=\{X_1, X_2, X_3, X_4, X_5\}$, where X_1 to X_5 respectively represents the tool overhang, bearing span, tool diameter, interface stiffness and axial preload. In present task, $X_1 \in [55, 75]$ mm, $X_2 \in [120, 180]$ mm, $X_3 \in [8, 12]$ mm, $X_4 \in [1.5 \times 10^5, 1.5 \times 10^7]$ N/m $X_5 \in [1000, 2000]$ N. The convergence pattern observed in HSO technique is shown in Figure 3.47.

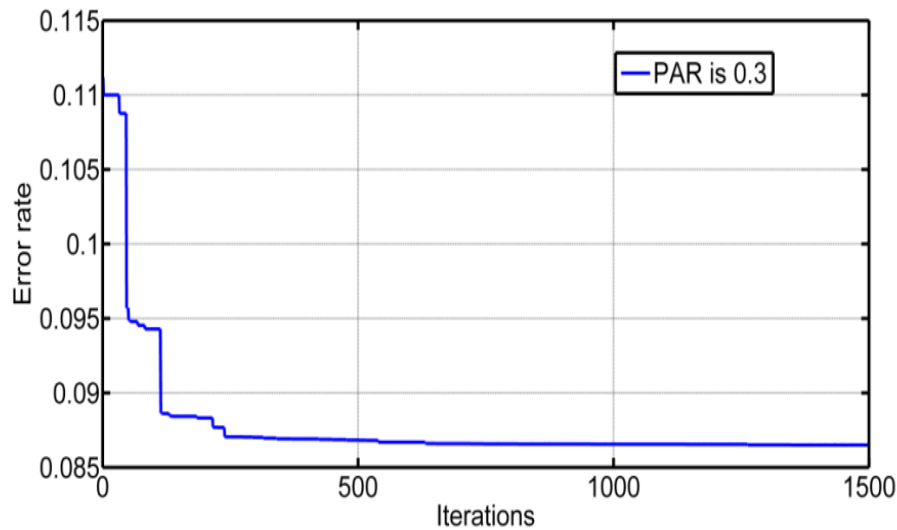


Figure 3.47: Error plot rate of HS algorithm

(b) Genetic algorithms (GA)

In order to validate the results HSO algorithm, the genetic algorithms (GA) approach is used for optimizing the dynamic rigidity of the spindle-tool system. GA procedure is based on the Darwinian principle of survival of the fittest. The data processed by GA includes a set of strings (or chromosomes) each representing a variable with an infinite length in which each bit is called an allele (or a gene). A selected number of strings are called a population and the population at a given time is a generation. The initial population of strings is selected randomly [147]. Since the binary alphabet offers the maximum number of schemata per bit of information of any coding, a binary encoding scheme is traditionally used to represent the chromosomes using either zeros or ones. Thereafter, the fitness value (or objective function value in maximization problems) of each member is computed. The population is then operated by the three main operators, namely, reproduction, crossover, and mutation to create a new population. The new population is further evaluated and tested for determination.

The following steps are implemented in general GA procedure:

(a) Coding: To solve the problem, variables should be first coded in some string structures. Largely binary-coded strings taking ones and zeros are applied. The length of the string is generally defined according to the desired solution accuracy.

(b) Fitness function: Basically the maximization problems are typically altered to minimization problems by means of appropriate transformation. A fitness function $F(x)$ is resulting from the objective function and it is used in consecutive genetic operations. For

maximization problems, fitness function is able to reflect the objective function itself. The fitness function often used in terms of objective function $f(x)$ is

$$F(x) = \frac{1}{1 + f(x)} \quad (3.96)$$

(c) Reproduction: Reproduction is the principal functional operation on a population. Here the particular strings are copied into a distinct string named the ‘mating pool’ giving to their fitness values (the strings with a greater value take a greater probability of contributing one or more offspring in the next generation). To select the mating pools, two famous schemes are employed: (i) roulette wheel selection and (ii) tournament selection. The best possible way is to make a biased roulette wheel where every existing string in the population takes a roulette-wheel-slot-size in part to its fitness. In this way more highly fit strings have higher numbers of offspring in the succeeding generation. Once the string has been selected for reproduction, an exact replica of the string is made. The string is then entered into the mating pool, a tentative new population for further genetic operator action.

(d) Crossover: After reproduction, the population is enriched with good strings from the previous generation but does not have any new string. A crossover operator is applied to the population to hopefully create better strings. The total number of participative strings in crossover is controlled by crossover probability, which is the ratio of total strings selected for mating and the population size. The crossover operator is mainly responsible for the search aspect of GA. Crossover requires a site. Bits on either side of the site will be swapped to generate to new strings. There are both single point and multi-point crossover operations. It is specified by a crossover probability p_c .

(e) Mutation: Mutation, as in the case of simple GA, is the occasional random alteration of the value of a string position. This means changing 0 to 1 or vice versa on a bit by bit basis and with a small mutation probability of 0.001 to 0.05. The need for mutation is to keep diversity in the population. It is specified by mutation probability p_m .

After applying the GA operators, a new set of population is created. Then, they are decoded and objective function values are calculated. This completes one generation of GA. Such iterations are continued till the termination criterion is achieved. The flow of genetic algorithms concepts is shown in Figure 3.48.

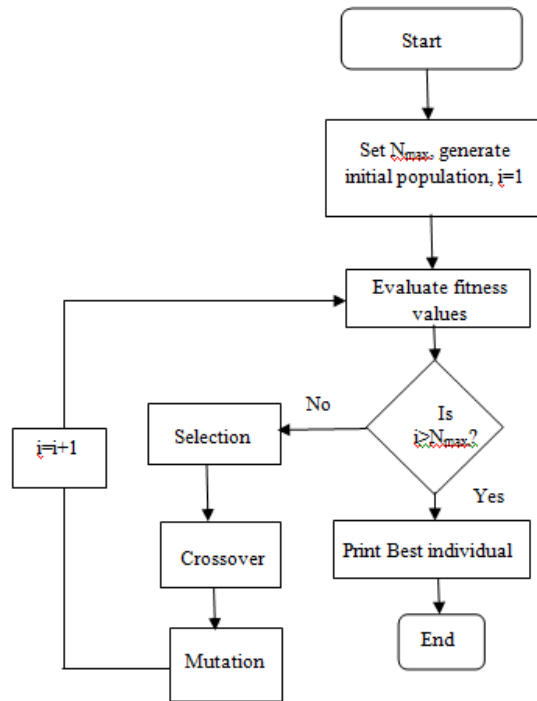


Figure 3.48: Flowchart for genetic algorithms

In present work, the above process is simulated with a population size of 20, iterated for 90 generations and crossover and mutation probability are selected to be 0.9 and 0.001, respectively. MATLAB GA toolbox is used in this work. The convergence pattern observed in GA technique is shown in Figure 3.49. In the present work 50 generations are applied. It can be seen that both of the average value and best fitness value of the GA optimization objective function decrease rapidly at the beginning, but after 25 generations it approaches to a steady value. After 50 generations, the convergent solution value for bestfitness of the objective function is 0.00145086 and the averagevalue is 0.001466.

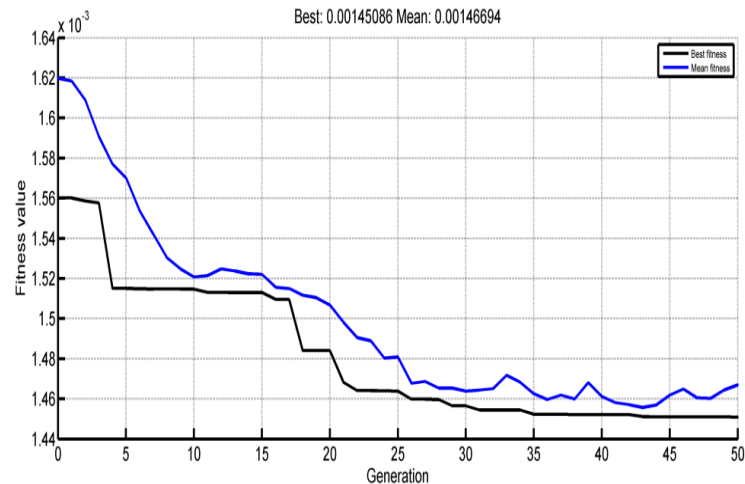


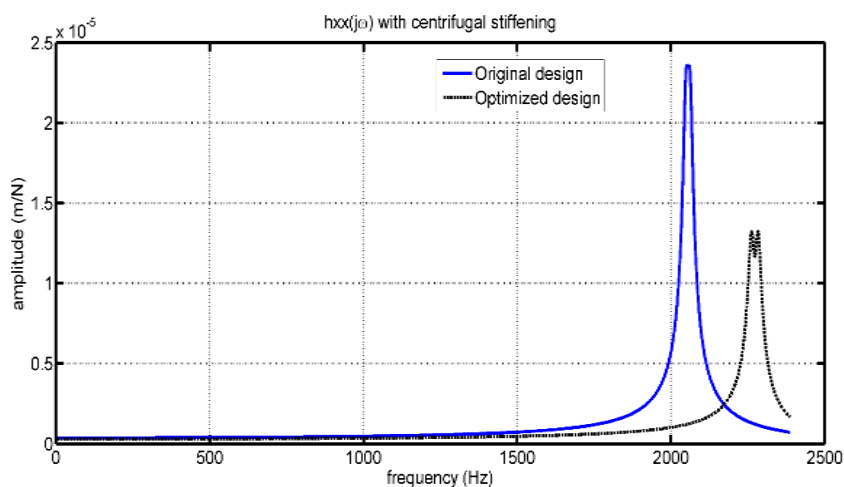
Figure 3.49: Error plot rate of GA algorithm

The best optimal values obtained from these two meta-heuristic algorithms are given in Table 3.10. It is observed that the optimal values obtained from these two algorithms are closely matches.

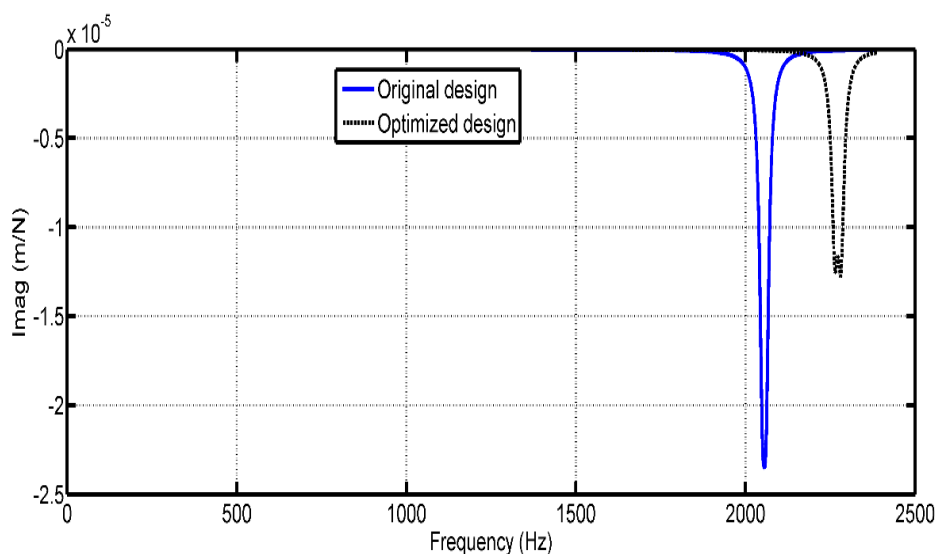
Table 3.10: Optimal data from HSO and GA

S. no	Parameters	Harmony search	Genetic Algorithm
1	Tool overhang(mm)	55.002	55.01
2	Bearing span(mm)	235.37	233.95
3	Tool diameter(mm)	8.9079	8.068
4	Interface stiffness (N/m)	1.43×10^7	1.37×10^7
5	Axial preload (N)	1108.21	1102.87

The best optimal values obtained from the HSO algorithm are used to obtain the frequency response at the tool-tip. In this program the tool diameter is taken as a standard 8mm from available tools. The program takes 25sec on a 2GB RAM, and Core I3 processor system for executing the operation. The frequency responses plotted between the original values and the optimal values obtained from the HSO are shown in Figure 3.50. The optimized values increases the fundamental frequency from 2058 Hz to 2284 Hz. The corresponding imaginary values are also shown in Figure 3.50 (b). It shows that for the optimized dimensions of spindle-tool system, the dynamic stiffness value increases from 0.41×10^5 N/m to 0.99×10^5 N/m.



(a) Absolute FRF



(b) Imaginary part of FRF

Figure 3.50: Tool-tip FRF for the spindle-tool unit with optimal dimensions

3.3.4 Dynamic modelling of drilling-spindle for milling-A case study

High-speed machining using vertical CNC milling centres continues to find widespread applications in a variety of sectors, specifically aerospace, automobile, mould and die-cavity preparation and other processes. During past one decade, several works focussed on fabrication of low-duty machine tools for internal requirements.

Due to economic considerations, sometimes a specific machine tool has to be employed for different machining operations. To carryout vertical milling operations, a drilling machine may be economically employed with appropriate modifications in design by changing the tools and operating parameters etc. However, as the original machine tool is designed for one series of operating conditions, in its original form it cannot be used for other high end machining processes. While machining especially in longitudinal planes, chattering phenomenon becomes significant restricting high metal removal rates as required in typical applications. The spindle is one of the important components in machine tools, which dictates the dynamic stability during cutting operations. It would influence the frequency response at the tool tip which is significant in assessing the vibration levels and cutting forces during the machining.

In present work, a modified design approach for drill-spindles is proposed in economical way for milling operations. To this end, a realistic spindle tool-unit of manual drilling machine is first considered and its modal characteristics are arrived experimentally. The stability lobes are also generated and validated with machining experiments. In order to use the drilling machine for milling operations, a portable X-Y

table of work feed is fabricated as per the existing dimensions of the machine base to ensure a smooth cutting operation. Topology of spindle unit is modified with respect to the existing drill tool spindle to improve its dynamic rigidity. An optimized topology of spindle unit is selected with front and rear bearing supports within the housing. The tool tip frequency response is then arrived by using finite element method. Figure 3.51 shows the design procedure of drilling spindle. The modified spindle unit can operate at higher axial depths of cut without excessive vibrations.

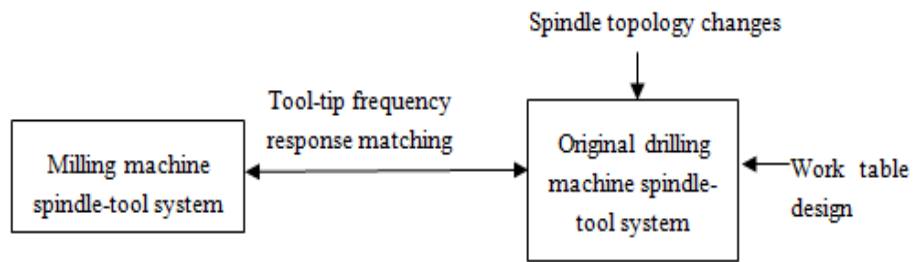


Figure 3.51: Drill-spindle modification procedure

In this section, the dynamic model of topologically modified spindle unit of drilling machine is proposed. Initially, the tool-tip frequency responses are arrived using finite element model of the original drill spindle. The stability lobe diagrams are obtained for conditions of material damping and immersion rates in comparison with original drill spindle unit. Figure 3.52 shows the dimensions of original drill spindle-tool unit.

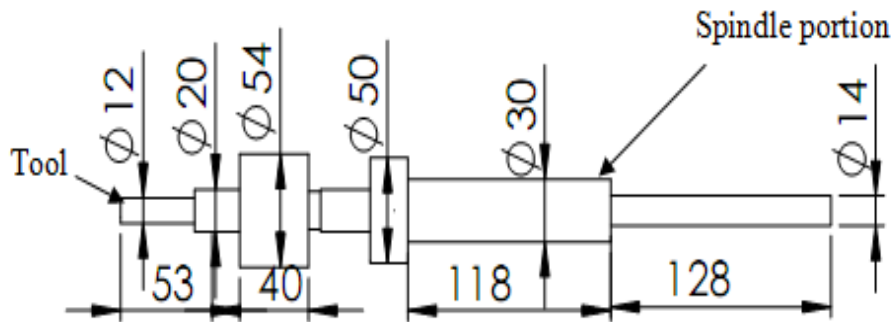
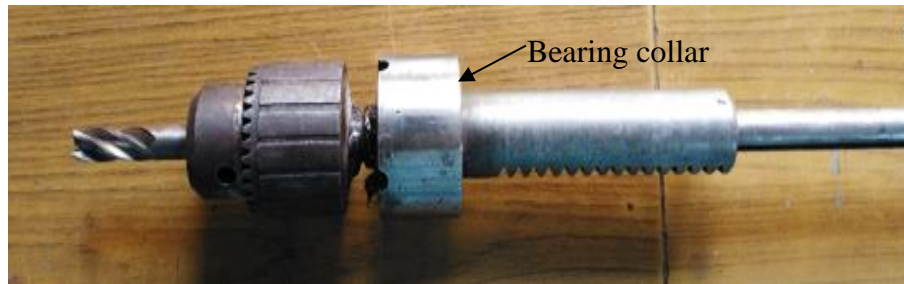


Figure 3.52: Original component modeling of drilling spindle

The drill spindle has a single bearing as shown in the Figure 3.53(a). To improve the dynamic rigidity of this spindle for the machining process an additional bearing is provided with a collar over them as shown in the Figure 3.53(b). This spindle can be utilized for both the drilling as well as for the milling operations.



(a) Original drill spindle with single bearing



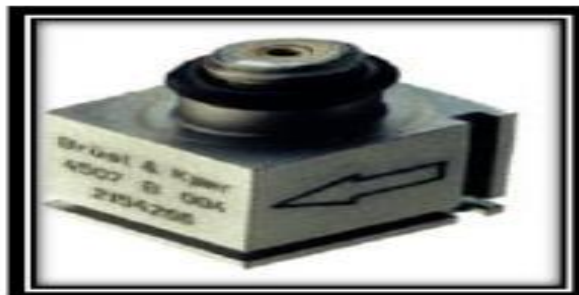
(b) Double bearing spindle with collar

Figure 3.53: Spindle-tool unit of the In-house drilling machine

For experimental modal analysis, an impact hammer (type B&K 2302-5) and accelerometer (type B&K 4507) were employed as shown in Figure 3.54.



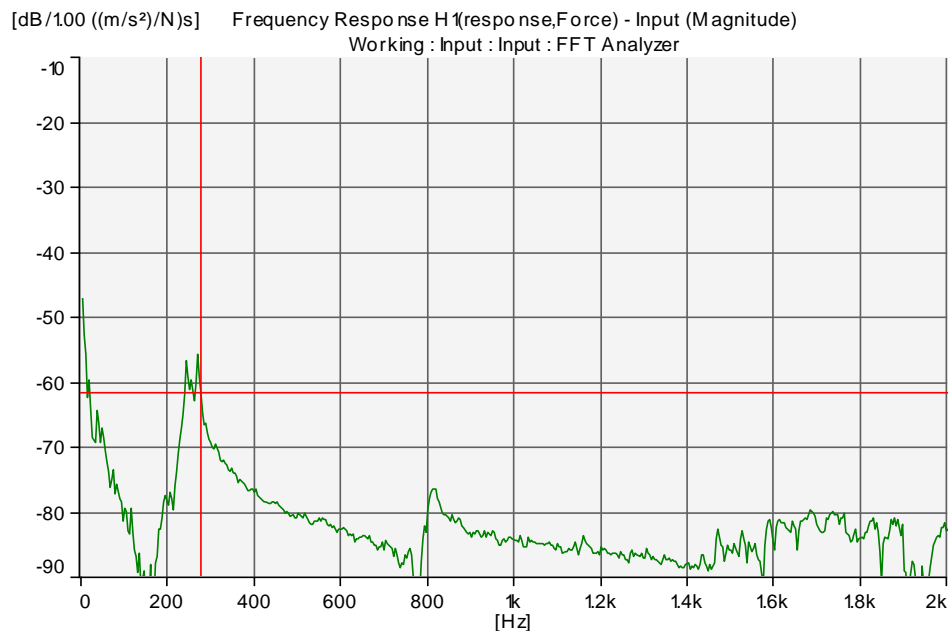
(a) Impact hammer (B&K Type 2302-05)



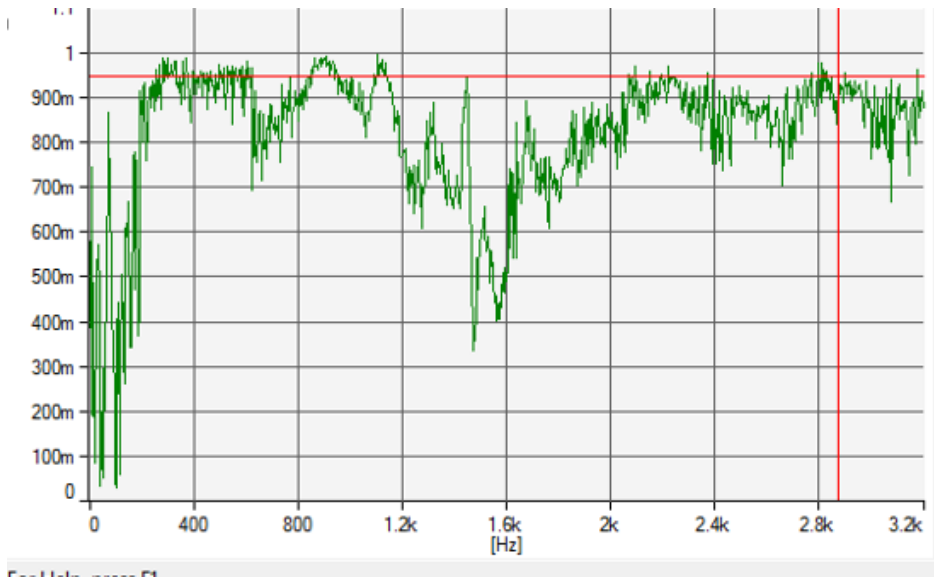
(b) Accelerometer (B&K 4507)

Figure 3.54: Instrumentation for modal analysis

A four channel Bruel & Kjaer pulse analyzer system (type 3560 B) was used to record the frequency response. When the spindle system was excited in a selected point by means of Impact hammer, the signal of resulting vibrations of the specimens were received to the FFT Analyzer with the help of accelerometer mounted on the specimen by means of bees wax. For clamping spindle tool unit, a frame was fabricated which provides the fixed free boundary conditions. The input and output signals are examined through FFT analyzer and the resulting FRF are examined in the laptop screen using the pulse lab software. The peaks of the FRF are taken as the average of the five loadings applied on the tool tip by the hammer along with the coherence plots. When the coherence is straight and equals to one it indicates better FRF. The output from the analyzer was displayed on the display unit in the graphical form which includes graph of force amplitude spectrum, response amplitude spectrum, coherence and frequency response functions. Figure 3.55 shows the FRF and coherence of original spindle, while Figure 3.56 shows that for modified spindle.

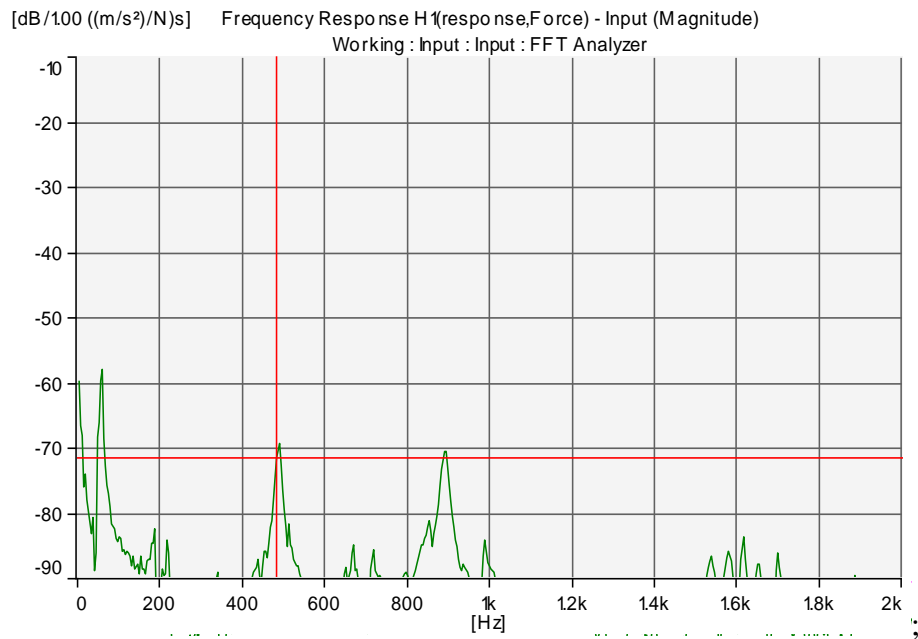


(a) Typical FRF of the drill spindle

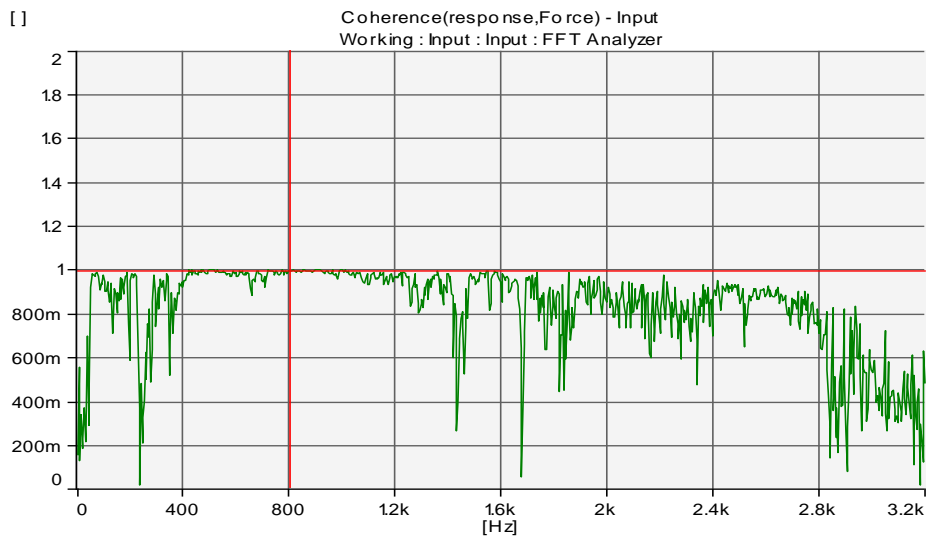


(b) Coherence of the drill spindle

Figure 3.55: Experimental response for original drill spindle



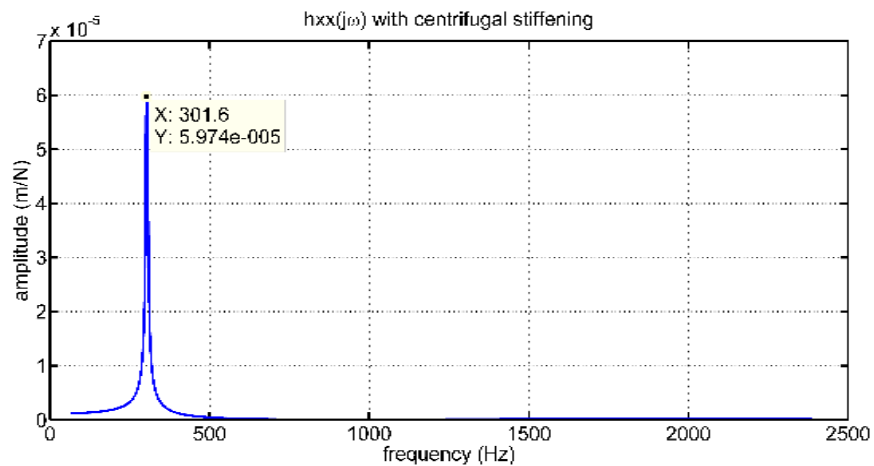
(a) FFT plot of modified spindle



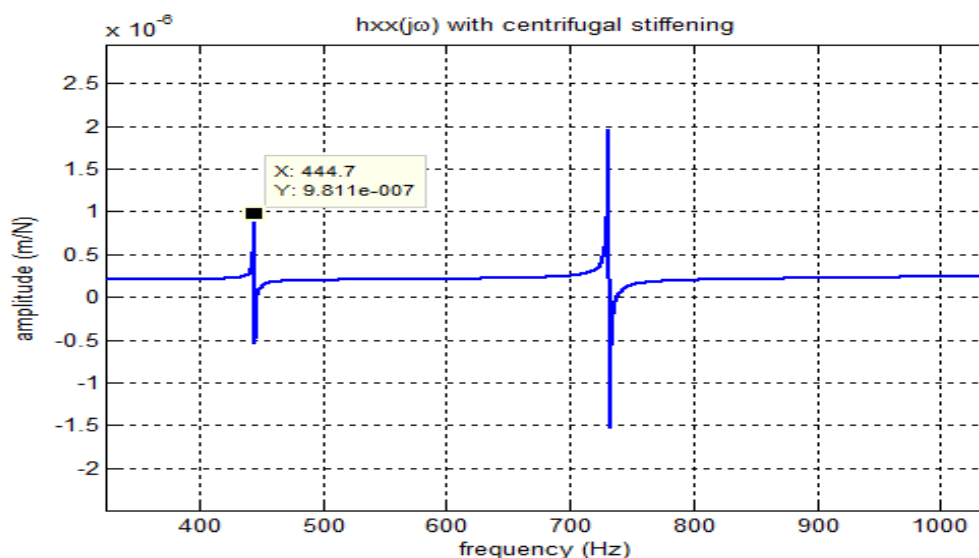
(b) Coherence of the modified spindle

Figure 3.56: Experimental measured FRF in modified drill spindle

In modelling of continuous spindle system using finite element analysis, the material dependent damping is conveniently introduced in the elastic modulus as given by the term $E_s = E(1 + i\eta)$, where η is the solid damping factor and E is the elastic modulus. Figure 3.57 depicts the FRF obtained by considering spindle mounted on bearings at a particular speed. It is observed that, there is a shift in the fundamental frequency of spindle from 301Hz to 444Hz in the modified case.



(a)Original drill spindle



(b) Modified spindle

Figure 3.57: Tool tip FRF of drill and modified spindle

As a further verification, three-dimensional models of the original and modified spindle units are modelled in Solid Works software. The whole assembly is modelled as per the dimensions spindle. In providing boundary conditions, the outer races of the bearings are fixed while the inner races are allowed to rotate with the spindle tool unit. The model was imported into ANSYS workbench and the spindle shaft, tool holder as well as the cutting tool are discretized using eight-node SOLID 187 elements with the uniform material properties as considered for one-dimensional model. Figure 3.58 shows the finite element model of solid.

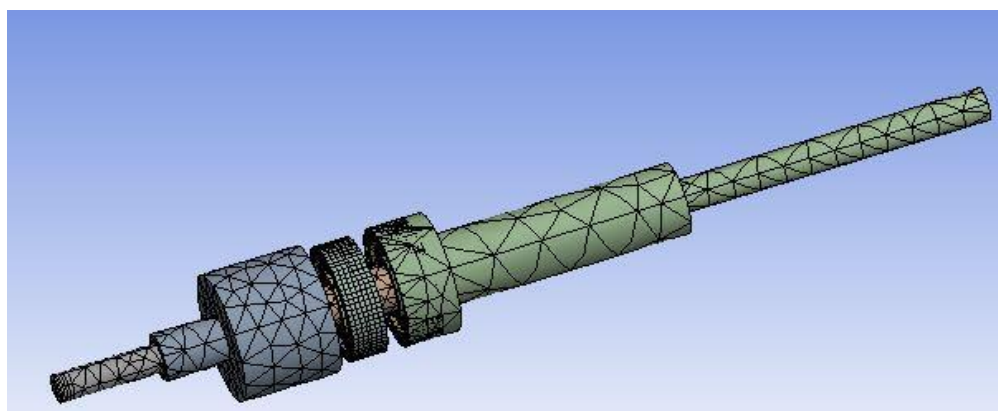


Figure 3.58: Meshed assembly of the model in ANSYS Workbench

Table 3.11 depicts the first few natural frequencies of spindle system with and without modifications of spindle.

Table 3.11: Modal frequencies (Hz)

Mode	With improved topology	Original drill tool spindle
1	464.34	289
2	500.89	350
3	996.75	760
4	1009.75	985
5	1505.5	1025
6	1554.2	1253

Figure 3.59 shows the chart of comparison for the first mode using experimental test along with present FE code and ANSYS solution.

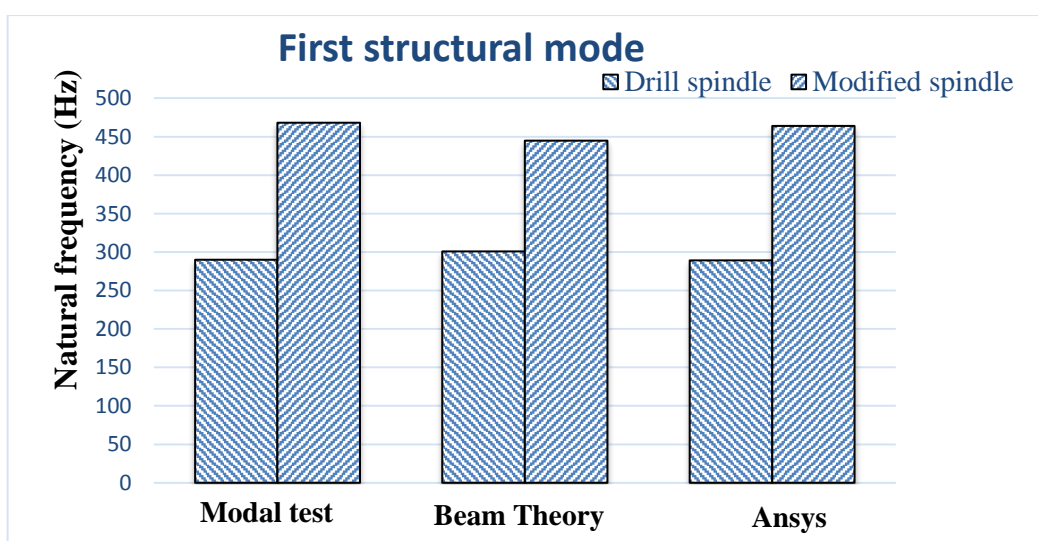


Figure 3.59: Comparison chart for the first mode of vibration

It is observed that there is a considerable agreement between the present finite element model based on Timoshenko beam theory and ANSYS solution. There is a little differences observed between the modal test and theoretical values. This may be due to the fact that real tool has discontinuities like twisted flutes over its length and material and geometric variations.

3.4 Concluding remarks

Present work aims in evaluating the combined effect of a spindle-tool unit on the dynamics of cutting by considering the flexibility of spindle unit supported on bearings. Following are some conclusion from this chapter.

- Dynamic model of the system was analysed by different approaches: (a) integral finite element model (b) three dimensional finite element model (c) receptance coupling model and (d) distributed parameter model.

- A practical spindle dimension of a vertical CNC milling machine was considered for the analysis and simulation task.
- In receptance coupling approach, 1-D finite element model of bearing supported spindle is employed to find the spindle-end frequency receptances. These receptances are combined with the analytical tool-holder receptances and the resultant tool tip FRFs were generated.
- These tool-tip frequency responses were validated with full-order 1-D and 3-D finite element models, where all component flexibilities are included.
- Several parametric studies were conducted for understanding the most influencing spindle-tool parameters on dynamic rigidity of the system.
- Based on the obtained results, a function approximation model was developed with the help of a neural network that works as an estimator for the GA optimization module to optimize the spindle geometry.
- Using the FE modeling, the effects of joint stiffness at spindle-holder-tool connections and nonlinear Hertzian contact ball bearing forces were studied and estimated the dynamics parameters of the spindle-tool structure.
- The modal response of spindle-tool assembly was also obtained experimentally using the sine sweep tests over the integrated spindle-tool system.
- A case study was presented by taking out the spindle-tool unit of an in-house manual drilling machine. The dynamic tests are conducted on the original unit and modified design were proposed and tested to improve the dynamic stiffness.

Chapter-4

Cutting dynamics and stability analysis

Effects of spindle dynamics on the process stability are often studied by using machining simulations. Milling process is an intermittent multi-point cutting operation, in which each tooth is in contact with the workpiece for a fraction of a spindle period. Tooth contact period varies as a function of width of cut, spindle speed and number of flutes. Unlike turning process, where chip thickness remains constant, milling tool follows a trochoidal path due to simultaneous feed and rotation motions leading to a variable chip thickness [84]. Two different methods are observed in planar milling: up (conventional) and down (climb) milling. In up milling, chip thickness increases as the cutter rotates and the direction of the cutter rotation is opposite to the feed motion. In the down milling where the cutter rotation and feed motion are in same phase, the initial chip thickness is at maximum, when the tool enters the workpiece and becomes zero as the tool leaves it. Several terms are often employed in defining the average cutting forces in every time step during cutting operations. Process simulation of milling depends on the kinematics of the spindle dynamics, cutting tool and cutter-workpiece interactions.

The chip thickness is a function of the cutter vibrations, flute-to-flute runout, and the surface undulations left by the previous tooth. Since the tool and workpiece are not rigid, they vibrate as the flutes of the tool move through the workpiece. The vibration results in the tooth leaving a wavy surface behind the workpiece. The variations in the instantaneous chip thickness result from the phasing between the surface left by the previous tooth and the current tooth. The magnitude and phase of the vibration are governed by the tool and workpiece dynamics. Because of phasing, the forces can develop unstable cutting phenomenon called chatter. Chatter is characterized by violent oscillations, changes in the time/frequency domain responses etc. Chatter conditions may occur due to be due to regeneration behaviour or by mode-coupling phenomena. The stability lobe diagram is famous tool based on frequency-domain response for demarking the stable and unstable states during cutting process. The time domain simulation can also be used to determine stability of a process with the selected cutting conditions.

This chapter begins with dynamics of milling process with a well known two-degree of freedom (two mode) cutting model subjected to time-varying forces. The construction of analytical stability-lobe diagram using tool-tip frequency response data is explained by considering various practical issues including process damping, variable

pitch of the tool and tool-tip run-out. Further, a methodology of generating analytical stability lobe diagrams using a three-dimensional cutting force model is presented with and without considering nonlinear force feed terms in the dynamic equations. Frequency and time-domain simulation are conducted. In the later part of the chapter, parametric studies of spindle-tool system on the overall stability of cutting are carried-out and a generalized integrated model of spindle-tool-cutting process is developed. The analytical and computational studies are validated with experimental cutting tests wherever needed.

4.1 Classical cutting force model

Figure 4.1 shows a milling cutter model with two degrees of freedom having N_t number of teeth with a zero helix angle. The tool is assumed to be compliant relative to the rigid work piece. Both tool geometry and machining specifications are important to assess the cutting process stability [86]. The tool geometry includes the number of teeth, helix angle, tooth-to-tooth angle, cutter diameter and the flute-to-flute run-out. The machining specifications needed are the starting and exit angles (a function of radial immersion), spindle speed, axial depth of cut and feed per tooth.

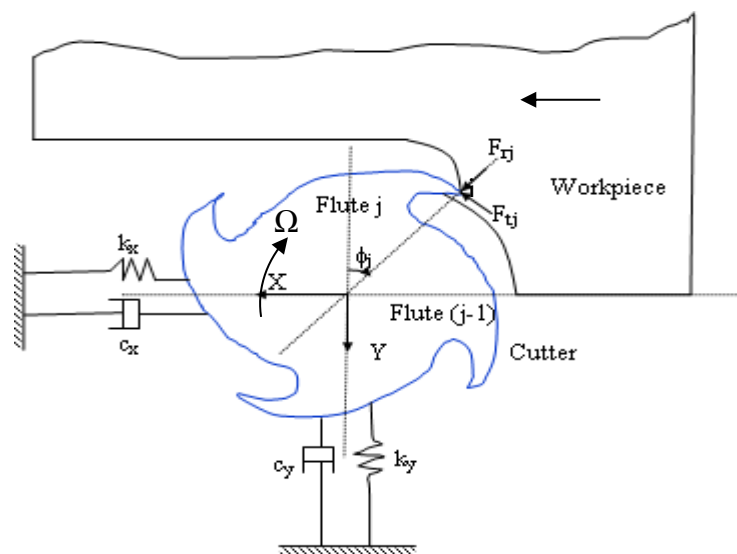


Figure 4.1: Two-degree of freedom milling model

The cutting forces excite the structure in feed and normal directions, causing dynamic displacements x and y , respectively. If the spindle rotates at an angular speed of Ω (rad/s), the immersion angle vary with time as $\phi_j(t) = \Omega t$. The resulting chip thickness consists of a static component $f_t \sin \phi_j$, where f_t is feed per revolution, which is due to rigid body motion of the cutter and a dynamic component $(n_{j-1} - n_j)$ caused by the vibrations

(displacements) of the tool at the present (n_j) and previous (n_{j-1}) tooth periods. Since the chip thickness is measured in radial direction (n), the instantaneous variable total chip thickness is expressed as [171]:

$$h(\phi_j) = (f_t \sin(\phi_j) + (n_{j-1} - n_j))g(\phi_j) \quad (4.1)$$

where the switching function, $g(\phi_j)$, is equal to one when the j^{th} tooth is engaged in the cut (i.e., between the cut start and exit angles) and zero otherwise and is expressed as:

$$g(\phi_j) = \begin{cases} 1, & \text{when } \phi_s \leq \phi_j \leq \phi_e \\ 0, & \text{when } \phi_j < \phi_s, \phi_j > \phi_e \end{cases} \quad (4.2)$$

where ϕ_s and ϕ_e are start and exit immersion angles of the cutter to and from the cut, respectively. As static part of the chip thickness ($f_t \sin \phi_j$) has no effect on the dynamic chip load regeneration mechanism, reduces to

$$h(\phi_j) = (\Delta x \sin(\phi_j) + \Delta y \cos(\phi_j))g(\phi_j) \quad (4.3)$$

where

$$\Delta x = x(t) - x(t-\tau) \quad (4.4a)$$

$$\Delta y = y(t) - y(t-\tau) \quad (4.4b)$$

$$\tau = \frac{2\pi}{N_t \Omega} \quad (4.4c)$$

$[x(t), y(t)]$ and $[x(t-\tau), y(t-\tau)]$ represent dynamic displacements of the cutter at the present and previous tooth periods and τ is the delay time or tooth passing period.

The components of linear cutting force in tangential and radial directions ($F_{t,j}$ and $F_{r,j}$) acting on the tooth j is proportional to the axial depth of cut (b) and chip thickness $h(\phi_j)$

$$F_{t,j}(\phi) = K_t b h(\phi_j) \quad (4.5)$$

$$F_{r,j}(\phi) = K_r F_{t,j}(\phi) = K_r K_t b h(\phi_j) \quad (4.6)$$

where flute coefficients K_t and K_r are contributed by shearing in respectively tangential and normal directions. The projections of the tangential and normal force components onto the fixed (x and y) coordinate frame are

$$F_{x,j} = -F_{t,j} \cos \phi_j - F_{r,j} \sin \phi_j \quad (4.7)$$

$$F_{y,j} = +F_{t,j} \sin \phi_j - F_{r,j} \cos \phi_j \quad (4.8)$$

The closed-form expressions for cutting forces are computed by including the summation over all the teeth (flutes) to obtain the total forces as:

$$F_x(\phi) = \sum_{j=1}^{N_t} F_{x,j} ; F_y(\phi) = \sum_{j=1}^{N_t} F_{y,j} \quad (4.9)$$

The X and Y direction force expressions are arranged in matrix form to obtain:

$$\begin{Bmatrix} F_x \\ F_y \end{Bmatrix} = \frac{1}{2} \mathbf{bK}_t \begin{bmatrix} a_{xx} & a_{xy} \\ a_{yx} & a_{yy} \end{bmatrix} \begin{Bmatrix} \Delta x \\ \Delta y \end{Bmatrix} = \frac{1}{2} \mathbf{bK}_t [A(t)] (\Delta(t)) \quad (4.10)$$

where the elements of matrix [A] are the time varying directional dynamic force coefficients depend on the angular position of the cutter which can be expressed as:

$$a_{xx} = \sum_{j=1}^{N_t} -g(\phi_j) [(\sin(2\phi_j) + K_r(1 - \cos(2\phi_j)))] \quad (4.11)$$

$$a_{xy} = \sum_{j=1}^{N_t} -g(\phi_j) [(1 + \cos(2\phi_j)) + K_r(\sin(2\phi_j))] \quad (4.12)$$

$$a_{yx} = \sum_{j=1}^{N_t} g(\phi_j) [(1 - \cos(2\phi_j)) - K_r(\sin(2\phi_j))] \quad (4.13)$$

$$a_{yy} = \sum_{j=1}^{N_t} g(\phi_j) [(\sin(2\phi_j) - K_r(1 + \cos(2\phi_j)))] \quad (4.14)$$

These expressions are periodic with the tooth pitch: $\phi_p = \frac{2\pi}{N_t}$ (rad) and tooth period

$\tau = \frac{60}{\Omega N_t}$ (s). In general, the Fourier series expansion of the periodic term is used for the

solution of the periodic systems. In stability analysis, the single chatter frequency is usually dominated and the higher harmonics in solution may not be required. Thus, the average

term in Fourier series expansion of $[A(t)]$ is included to reduce the following form:

$$\{F(t)\} = \frac{1}{2} bK_t[A_0]\{\Delta(t)\} \quad (4.15)$$

where $[A_0]$ consists of four directional orientation factors defined as [168] :

$$\alpha_{xx} = \frac{1}{2} \left[(\cos(2\phi) - 2K_r\phi + K_r \sin(2\phi)) \right]_{\phi_s}^{\phi_e} \quad (4.16)$$

$$\alpha_{xy} = \frac{1}{2} \left[(-\sin(2\phi) - 2\phi + K_r \cos(2\phi)) \right]_{\phi_s}^{\phi_e} \quad (4.17)$$

$$\alpha_{yx} = \frac{1}{2} \left[(-\sin(2\phi) + 2\phi + K_r \cos(2\phi)) \right]_{\phi_s}^{\phi_e} \quad (4.18)$$

$$\alpha_{yy} = \frac{1}{2} \left[(-\cos(2\phi) - 2K_r\phi - K_r \sin(2\phi)) \right]_{\phi_s}^{\phi_e} \quad (4.19)$$

By substituting the response and delay terms, the following expression is obtained.

$$\{F\}e^{i\omega_c t} = \frac{1}{2} bK_t[A_0](1 - e^{-i\omega_c \tau})[G(i\omega_c)]\{F\}e^{i\omega_c t} \quad (4.20)$$

where $\{F\}$ represents the amplitude of dynamic milling force vector $\{F(t)\}$ and the transfer function matrix is given as:

$$[G(i\omega_c)] = \begin{bmatrix} G_{xx} & G_{xy} \\ G_{yx} & G_{yy} \end{bmatrix} \quad (4.21)$$

Here, the terms are computed as summation of the cutter and work piece transfer function components. The characteristic equation of the closed loop dynamic milling system is finally expressed as:

$$\det \left([I] - \frac{1}{2} bK_t(1 - e^{-i\omega_c \tau})[A_0][G(i\omega_c)] \right) = 0 \quad (4.22)$$

where the product $[A_0][G(i\omega_c)]$ gives the oriented frequency response function $[G_0]$.

A new variable, Λ is now introduced as

$$\Lambda = \Lambda_{\text{Re}} + i\Lambda_{\text{Im}} = -\frac{N_t}{4\pi} bK_t (1 - e^{-i\omega_c \tau}) \quad (4.23)$$

So that the characteristic equation can be rewritten as

$$\det([I] + \Lambda[FRF_{or}]) = 0 \quad (4.24)$$

The eigenvalue of the above equation can easily be solved for a given chatter frequency ω_c , static cutting factors (K_t , K_r), radial immersion angles (ϕ_s and ϕ_e) and frequency response function at the tool-tip.

By using,

$$\kappa = \frac{\Lambda_{\text{Im}}}{\Lambda_{\text{Re}}} = \frac{\sin \omega_c \tau}{1 - \cos \omega_c \tau} \quad (4.25)$$

the expression for the stability limit is obtained as:

$$b_{\text{lim}} = -\frac{2\pi}{N_t K_t} \Lambda_{\text{Re}} (1 + \kappa^2) \quad (4.26)$$

The corresponding frequency dependent spindle speeds are determined by first by writing the phase shift in the surface undulations between subsequent tooth passages, $\varepsilon = \pi - 2\psi$ where $\psi = \tan^{-1}(\kappa)$. The tooth passing periods are next expressed as $\tau = \frac{1}{\omega_c} (\varepsilon + j2\pi)$, where $j=0, 1, 2, \dots$ refers to the integer number of waves between the teeth and incrementing j leads to the individual lobes. Finally the spindle speeds in rpm are obtained from

$$\Omega = \frac{60}{N_t \tau} \quad (4.27)$$

There are three main graphs employed for stability analysis: (i) the limiting depth-of-cut graph (b_{lim} versus Ω) (ii) the chatter frequency graph (ω_c versus Ω) and (iii) phase shift graph (ε versus Ω). The first plot (called analytical stability lobe diagram) gives the boundary between stable and unstable zones and is often used in most cases.

To illustrate the stability lobe diagram from tool-tip frequency response function in present context, a Matlab program is employed with the variable data given in the Table-4.1.

Table 4.1: Modal and cutting coefficients for the system

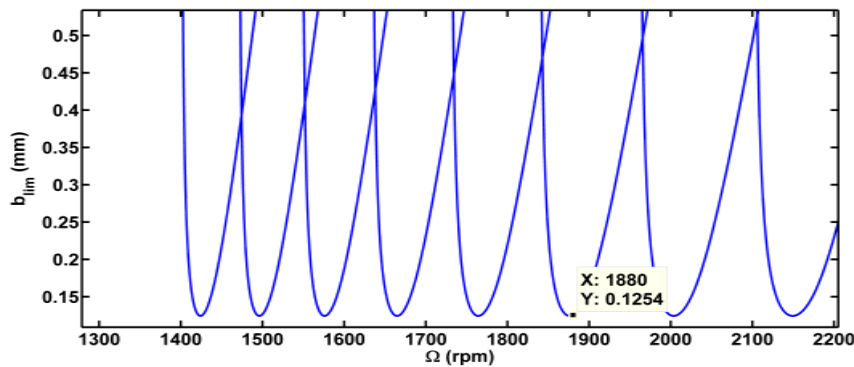
Cutting stiffness in X and Y directions ($K_{xx}=K_{yy}$)	2.1×10^8 N/m
Natural frequencies ($\omega_x=\omega_y$)	2056Hz
Damping ratios ($\xi_x=\xi_y$)	0.01
Tool diameter	12mm
average specific cutting pressure (K_s) (corresponding to Aluminum alloy)	750 N/mm^2
number of teeth (N_t)	4

The starting/exit angle in down/up milling is respectively given as follows

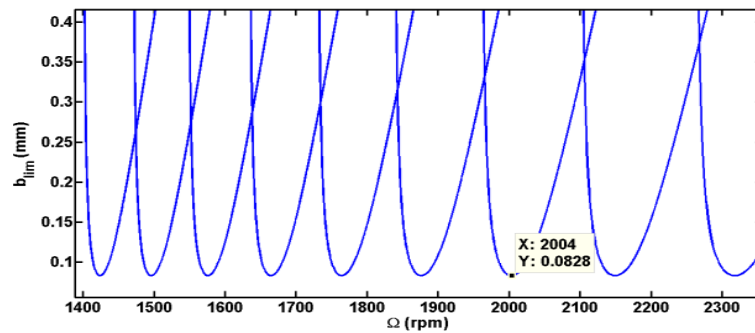
$$\phi_s = 180^\circ - \cos^{-1}\left(\frac{r-a}{r}\right), \quad \phi_s = 180^\circ \text{ for down milling}$$

$$\phi_e = \cos^{-1}\left(\frac{r-a}{r}\right), \quad \phi_s = 0^\circ \text{ for up milling}$$

Here, r is the tool radius, and a is the radial depth of cut defined in terms of percentage if immersion as $a = \% \text{immersion} \times 2r$. The stability regions are plotted for the down-milling process at two different depths of radial immersions as shown in Figure 4.2. This is arrived by using first mode fundamental frequency response data at tool-tip obtained from the finite element analysis earlier.



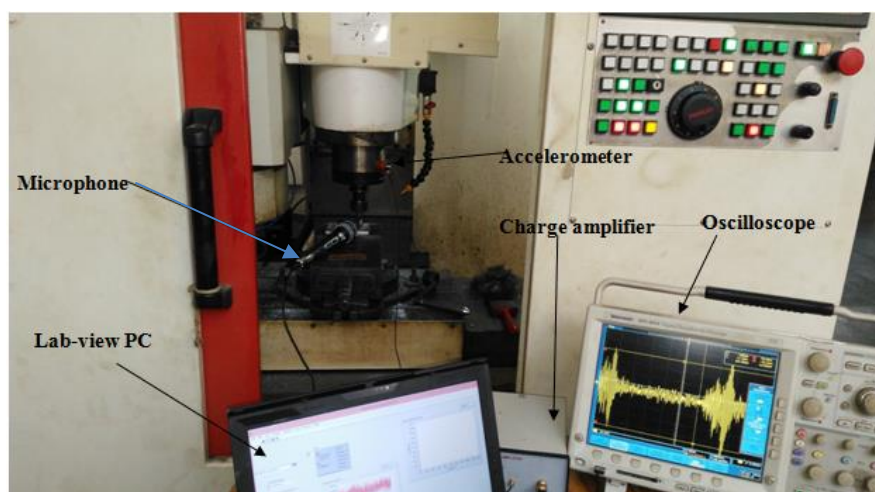
(a) 20% Radial immersion



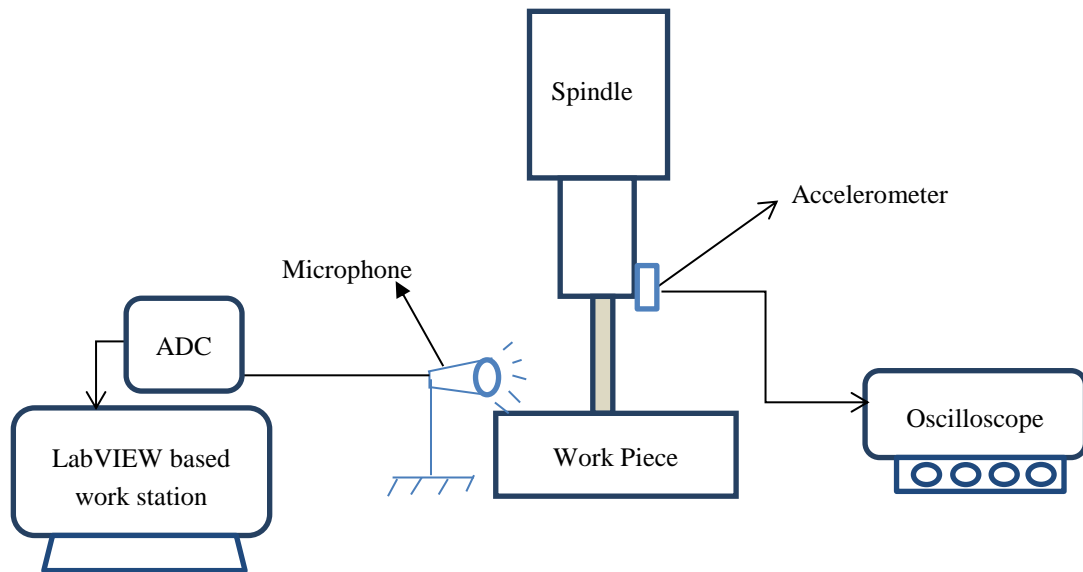
(b) 50% Radial immersion

Figure 4.2: Stability lobe plots for different percentages of radial immersion

It is observed that the average stable depth of cut decreases with the increase of radial immersion as pointed out in earlier literature. To assess the correctness of the stability boundary, cutting tests are conducted on a CNC milling center employing the same spindle as used in finite element modeling. The machine tool has 3-axes with a spindle motor having a maximum speed of 4,000 rpm. A four fluted end mill cutter with 12mm diameter is used for the cutting process. Full-immersion down milling machining is performed on aluminium alloy (Al-6061). The output data of abnormal vibrations occurred during cutting process at specified speeds and depth of cut are recorded using a 4-channel digital oscilloscope (model-DPO 43034), an accelerometer (PG 109 M0, frequency range 1 to 10,000 Hz) and with a charge amplifier (Model: CA 201 A0, maximum output voltage- \pm 5V, frequency range- 0.2 Hz to 15 kHz) as shown in Figure 4.3 (a) along with a schematic diagram shown in Figure 4.3 (b).



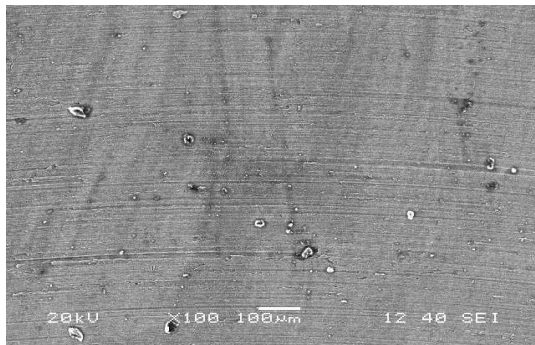
(a) Photograph of the experimental set-up



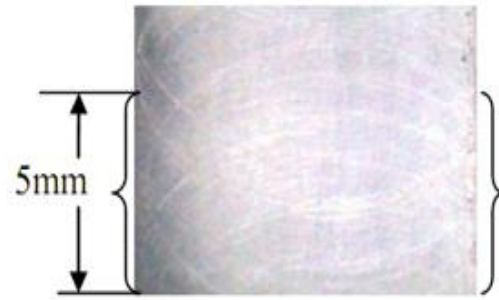
(a) Schematic view of the experimental set-up

Figure 4.3: Experimental set-up employed

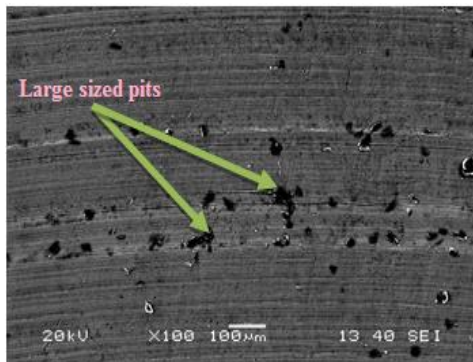
Based on the analytically predicted stability lobe diagrams, a series of cutting tests are conducted at the corresponding spindle speeds and axial depth of cuts. Accelerometer is connected to a non-rotating portion of the spindle with the charge amplifier to measure the vibration response of the cutting tool during machining. The machined surface is photographed by using the scanning electron microscope with a magnification scale of $100\mu\text{m}$ and an optical microscope with a zoom factor of 10X. It is observed that when the axial depth of cut is at 0.07mm at a spindle speed of 2200rpm and a feed rate of 20mm/min , there are no chatter marks observed on the workpiece material with the optical microscope as shown in Figure 4.4 (b). The same sample was magnified with SEM, which shows that inside of the work surface is also having the less indentation marks as shown in Figure 4.4(b). Further, if the cutting exceeds the limit of 0.07mm , large sized pits are observed as shown in Figure 4.4(c) and the corresponding microscope image was shown in Figure 4.4(d). It signifies that the machining enters into the chatter prone regions when it exceeds the average stable depth of cut of 0.07mm .



(a) SEM image at 0.07mm



(b) Optical microscope image at 0.7mm



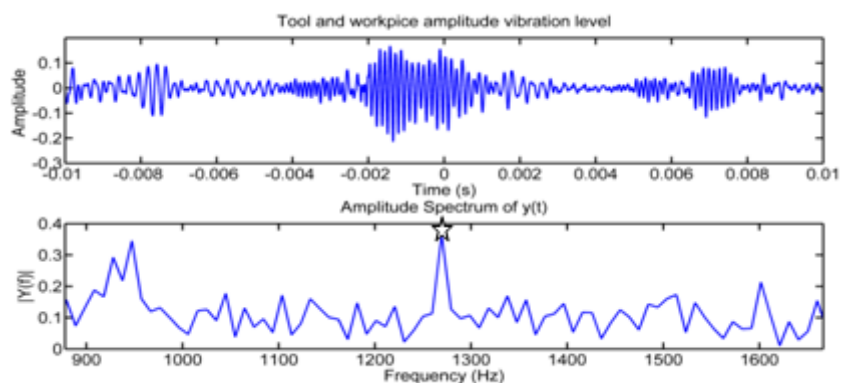
(c) SEM image at 0.17mm



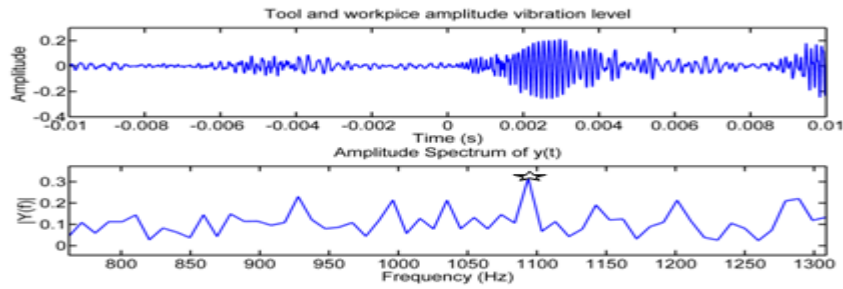
(d) Optical microscope image at 0.17mm

Figure 4.4: Machining areas of workpiece at different depths of cut

Cutting signals recorded in the oscilloscope in the form of time-histories and corresponding FFT plots are shown in Figure 4.5 at two different depths of cut of 0.07mm and 0.17mm respectively.



(a) Depth of cut 0.07mm (Stable)

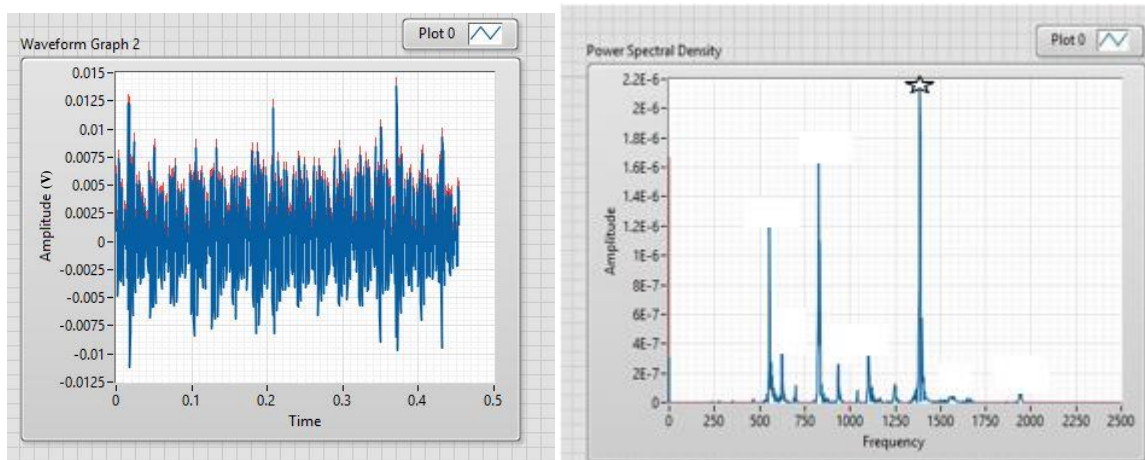


(b) Depth of cut 0.17mm (Unstable)

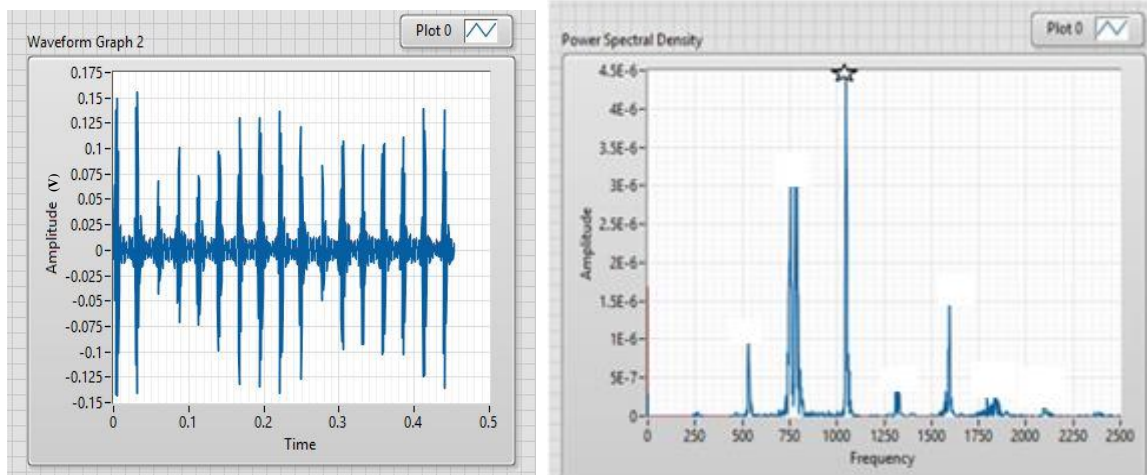
Figure 4.5: Time history and FFT plots for different axial depths of cut.

It is observed from a series of plots that, when there is an increment in the axial depth of cut, the amplitude of tool vibration levels during machining increases which forms the tool chatter marks on the workpiece and there is also a shift in the chatter frequency (seen as star) from 1300Hz to 1100Hz. It signifies that when the depth of cut increases the chatter likely to appear early at the engagement of cutting tool.

For each cutting points, the sound-pressure signal information has been analysed with a microphone (sensitivity of $-73\text{dB}\pm 3\text{dB}$) interfaced with the LabVIEW software to verify the correctness of the stability lobe diagram. Experiments were performed at selected combinations of axial depth of cut and spindle speed from analytical stability lobe diagram. Figure 4.6 shows the amplitude of sound signal(v) in time domain(s) and the corresponding power spectral density(PSD) plots. In initial case, two axial depth of cuts 0.07mm and 0.17 mm at a spindle speed of 2200rpm are considered. The PSD contains the tool chatter frequencies(indicated as stars). It is observed that the chatter frequency occurs at the frequencies of 1350Hz for 0.07mm, 1090Hz for 0.17 mm respectively.



(a) Depth of cut 0.07mm (stable)



(b)Depth of cut 0.17mm (unstable)

Figure 4.6: Amplitude and FFT plots for differnt axial depths of cut

Based on the tool machining vibration levels, sound signal spectrographies and the surface images of corresponding machining areas, the points are superposed in the analytical stability lobe diagram. Figure 4.7 shows the corresponding stability lobe diagram for full immersion down milling process. It is clear that the experimentally tested points are well matching with respect to analytically obtained stability boundary.

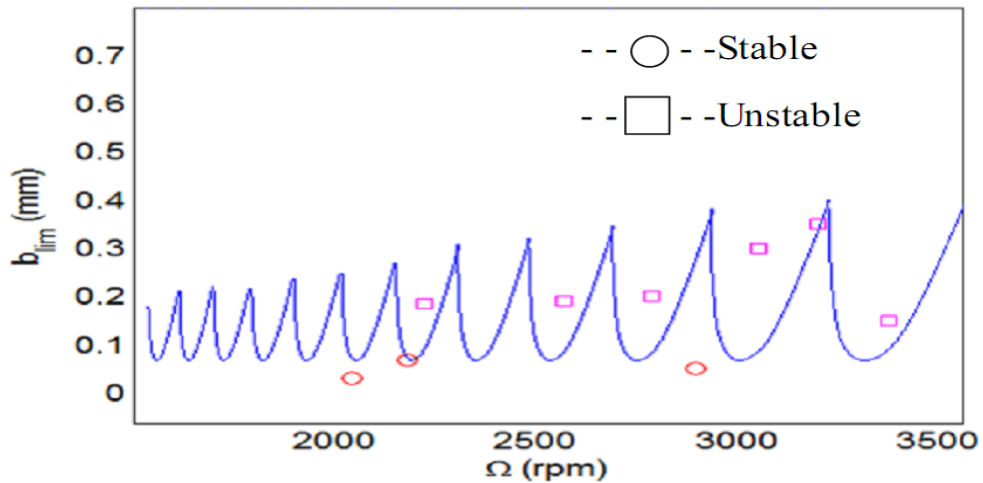


Figure 4.7: Predicted SLD with experimental validation

In practice, stability of the cutting process with the spindle-tool system has to be studied with various practical considerations including process damping, tool run-out, variable

pitch effects etc. A brief study of these effects with the proposed spindle-tool model is presented in the following sections.

4.1.1 Effects of process damping

Process damping can be described as the energy dissipation due to relative velocity and interference between the relief angle of a cutting tool and the existing vibrations on the machined workpiece surface. Many researchers have investigated process damping in turning and milling operations. It occurs when there is a contact between the cutter flank and the vibrations imprinted on the machined surface. It influences the dynamic cutting forces and lead to process damping.

The chatter-free depths of cut are observed to diminish substantially at low spindle speeds, where the stability lobes become more closely spaced. Fortunately, the process damping effect can serve to increase the allowable chip width for low spindle speeds. The process damping force, F_d is characterized as a 90° phase shift relative to the displacement and opposite in sign from the velocity. Given the preceding description, the process damping force is modeled as the viscous damping force as

$$F_d = -C \frac{b}{V} \dot{y} \quad (4.28)$$

Here, the process damping force in the y direction (perpendicular to the cut surface) is expressed as a function of the cutter velocity (\dot{y}), chip width (b), cutting speed (V) and a process damping coefficient (C). A primary difficulty to defining an analytical solution for milling stability is the time dependence of the cutting force direction. To solve this problem the average angle of the tooth in the cut (f_{ave}), is considered in an average force direction. This approach produces an independent (or) time-invariant system. The use of directional orientation factors, μ_x and μ_y , to be first project this force into the x and y mode directions and, second, project these results onto the surface normal. The following equations are used to obtain the stability lobe boundaries for the milling process [168]:

$$b_{lim} = \frac{-1}{2K_s Re(H_{or})N_t^*} \quad (4.29)$$

$$\frac{f_c}{\Omega N_t} = j + \frac{\varepsilon}{2\pi} \quad (4.30)$$

$$N_t^* = \frac{\phi_e - \phi_s}{360 / N_t} \quad (4.31)$$

$$\varepsilon = 2\pi - 2 \tan^{-1} \left(\frac{\text{Re}[H_{or}]}{\text{Im}[H_{or}]} \right) \quad (4.32)$$

$$H_{or} = \mu_x H_x + \mu_y H_y \quad (4.33)$$

Where the N_t^* is the average number of teeth in the cut, ϕ_e and ϕ_s are the exit and start angles of radial immersion, N_t is number of teeth on the cutter, $j=0, 1, 2, \dots$ is lobe number, H_{or} is the oriented frequency response function, β is the force angle in degrees (for Aluminium alloy $\beta=75^\circ$).

The process damping force can be conveniently applied for up and down milling processes. The geometry for the up-milling process shown in the Figure 4.8 where the n is surface normal direction which is defined by ϕ_{avg} .

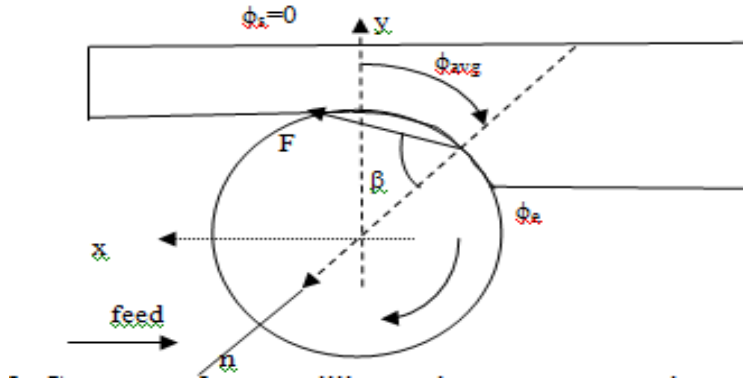


Figure 4.8: Geometry for up-milling using average tooth angle approach

The projection of the process damping force from the n direction onto the x direction is

$$F_x = F_d \cos(90 - \phi_{avg}) = - \left(C \frac{b}{V} \cos(90 - \phi_{avg}) \right) \dot{n} \quad (4.34)$$

Where the new velocity term is $\dot{n} = \cos(90 - \phi_{avg})\dot{x}$. Substituting the velocity term in the F_x expression gives

$$F_x = -\left(C \frac{b}{V} \cos^2(90 - \phi_{avg})\right)\dot{x} \quad (4.35)$$

The new damping for the stability calculations in x and y directions, is therefore:

$$c_{new,x} = c_x + \left(C \frac{b}{V} \cos^2(90 - \phi_{avg})\right) \quad (4.36)$$

$$c_{new,y} = c_y + \left(C \frac{b}{V} \cos^2(180 - \phi_{avg})\right) \quad (4.37)$$

The geometry for the down milling case is shown in Figure 4.9.

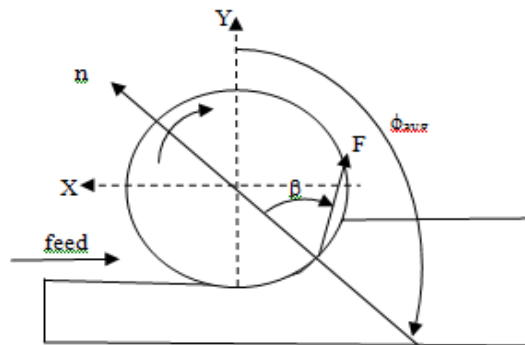


Figure 4.9: Geometry for down-milling using average tooth angle approach

Using the same approach as described in the up milling case, the x and y direction damping values are provided for down milling as [168].

$$c_{new,x} = c_x + \left(C \frac{b}{V} \cos^2(\phi_{avg} - 90)\right) \quad (4.38)$$

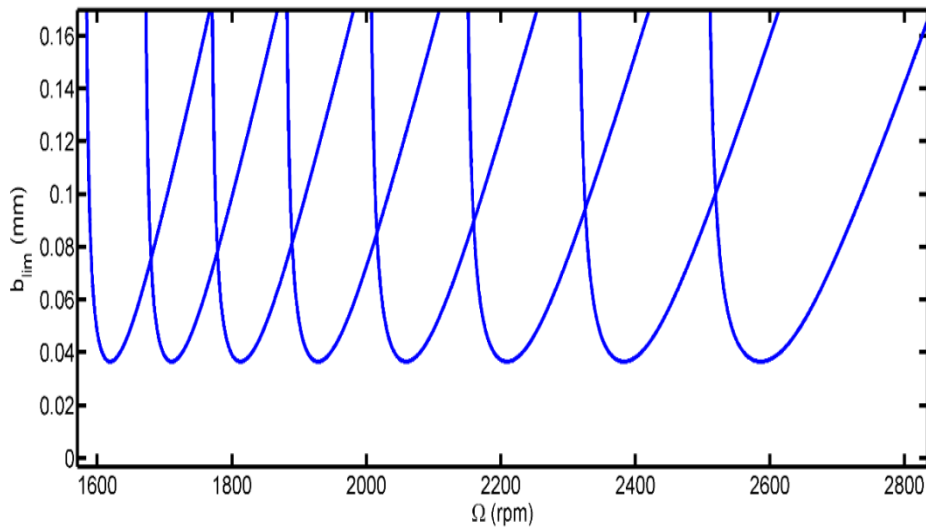
$$c_{new,y} = c_y + \left(C \frac{b}{V} \cos^2(180 - \phi_{avg})\right) \quad (4.39)$$

The expressions for directional orientation factors μ_x and μ_y for up and down milling processes are given in Table 4.2

Table 4.2: Summary of directional orientation factors

Up milling	Down milling
$\mu_x = \cos(\beta - (90 - \phi_{avg}))\cos(90 - \phi_{avg})$	$\mu_x = \cos(\beta + (\phi_{avg} - 90))\cos(\phi_{avg} - 90)$
$\mu_y = \cos(180 - \beta - \phi_{avg})\cos(180 - \phi_{avg})$	$\mu_y = \cos(\beta - (180 - \phi_{avg}))\cos(180 - \phi_{avg})$

A MATLAB program is developed to study the effect of process damping with the above modifications in the classical model. The numerical study is carried out with $\phi_s = 0deg$ and $\phi_e = 90deg$ (50% radial immersion). The stability regions are plotted for the up-milling process using the fundamental frequency response data at tool-tip obtained from the finite element analysis. Figure 4.10 shows the comparison stability plots with process damping constant varied from zero (no process damping) to a maximum value ($C=6.5 \times 10^5 N-s/m$). It is observed that, the process damping increases the average stable depth of cut from 0.04mm to 0.3mm.



(a) Without process damping

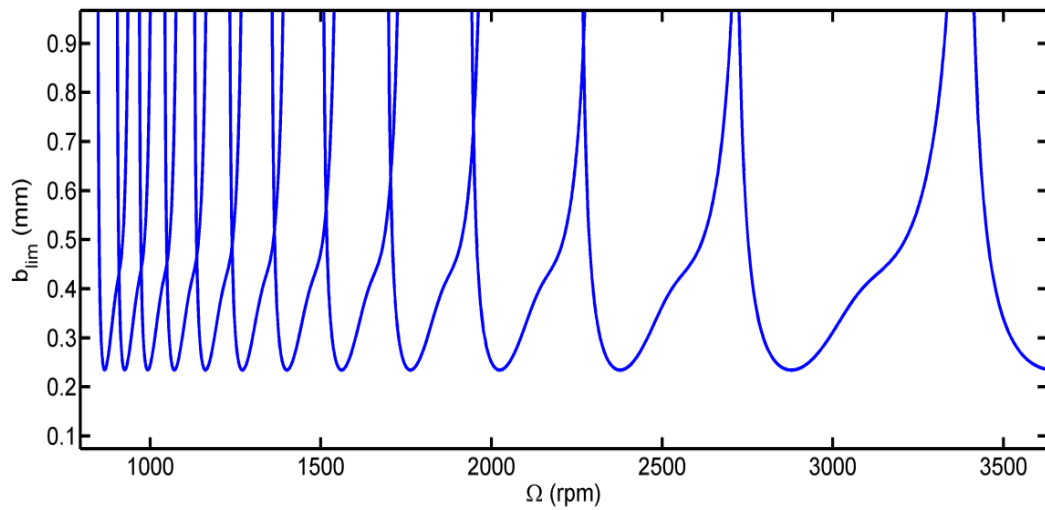
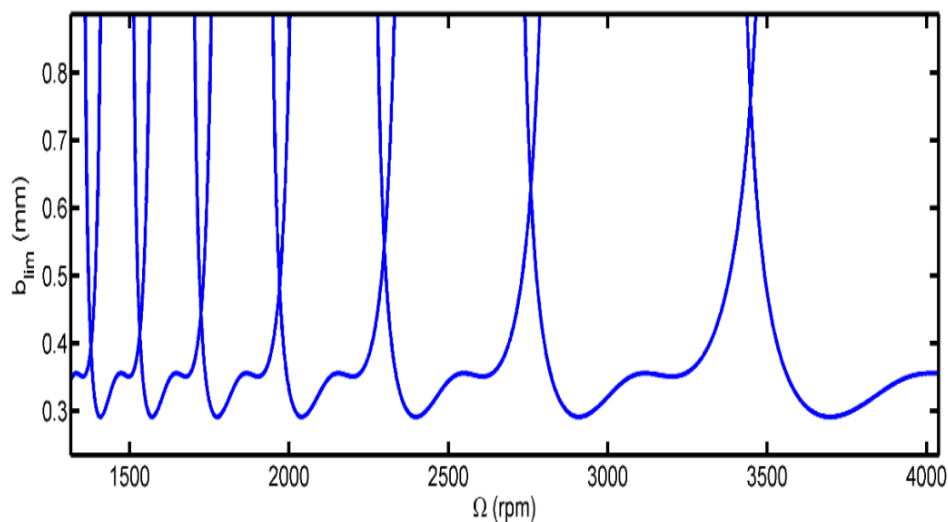
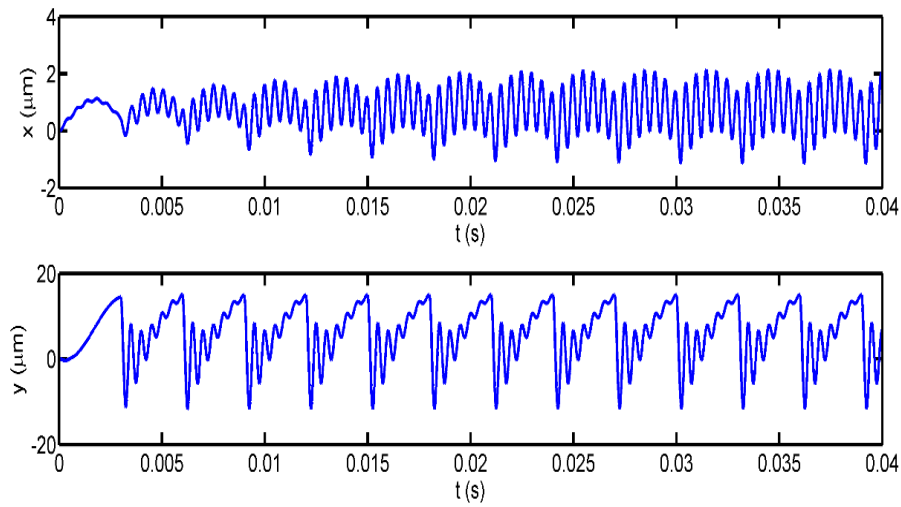
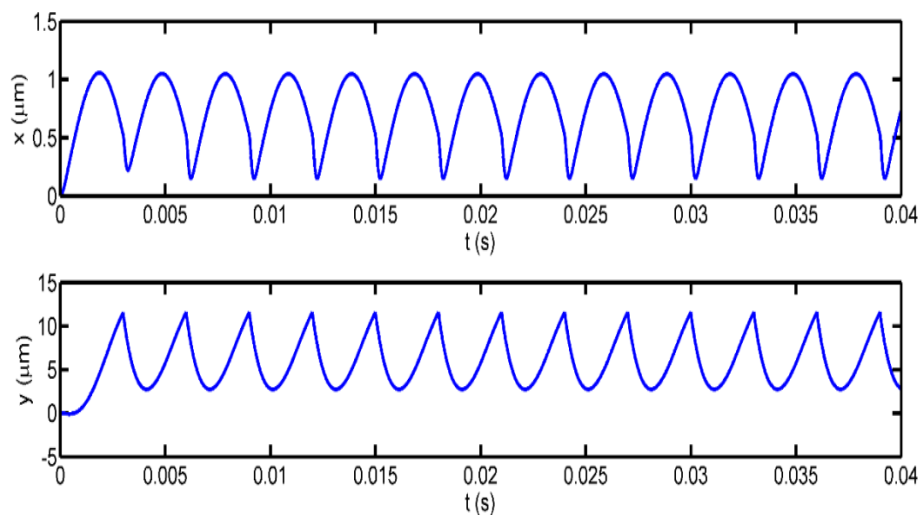
(b) With process damping ($C=6.5 \times 10^4$ N-s/m)(c) With process damping ($C=6.5 \times 10^5$ N-s/m)

Figure 4.10: Analytical stability lobe diagrams

The cutting force simulation requires the input of modal parameters the tool geometry, and machining specifications. The modal parameters include the stiffness, damping ratio and natural frequency for each tool mode in the x and y-directions. Figure 4.11 depicts the time domain simulation results with and without process damping effect for the two degree of freedom milling model. By introducing the process damping effect in the model, it is observed that tool displacements levels reduce in both the x and y directions. Furthermore it provides the steady tool displacements which are essentially required during a stable cut.



(a) without process damping

(b) With process damping ($C=6.5 \times 10^5$ N-s/m)Figure 4.11: Cutting tool vibrations at $\Omega = 3000rpm$ at 1mm depth of cut

Effect of process damping is similar to the internal damping in spindle –tool system where the damping at the interfaces between collet and tool as well as chuck and collet has significant influence on the system stability.

There are various sources of machining errors due to tool run-out, deflection of the tool, work-piece displacements and variable pitch end mills. In spite of an effective spindle-tool design, sometimes the process may be lost due to these sources of errors.

4.1.2 Cutting force simulation with tool run-out

Tool run-out is an inaccuracy of a rotating mechanical system that the tool does not rotate exactly in-line with its rotational axis. There are two types of run-outs (a) radial and (b) axial. Radial run-out is caused tool being rotated off the centre and axial run-out is due to angular offset of the tool from the axis. Tool run-out effect is an important issue in cutting process and it will occur mainly from the errors between positioning of the spindle and tool holder, radial position of teeth on the cutter, tool dimensional errors, thermal deflection of the tool, imbalance between the tool and holder etc. It causes chip thickness to vary over the tool rotation and therefore the tool experiences uneven forces during each cutting tooth period [102]. Cutting forces were calculated based on the cutting geometry engaged into the workpiece and the empirical equations are used to relate the cutting forces with the uncut chip thickness. Radial run-out is defined by run out distance (eccentricity ρ) and the run cut angle (λ). The trajectory of the cutting tool was approximated by a circular path, thus the chip thickness including tool run-out can be calculated as given by the following expression

$$h_j(\phi_j) = f_t \sin(\phi_j) + h_{ro}^j \quad (4.40)$$

Where h_{ro}^j is the variation of the chip thickness due to run-out in cutting edge j and it will be defined as follows

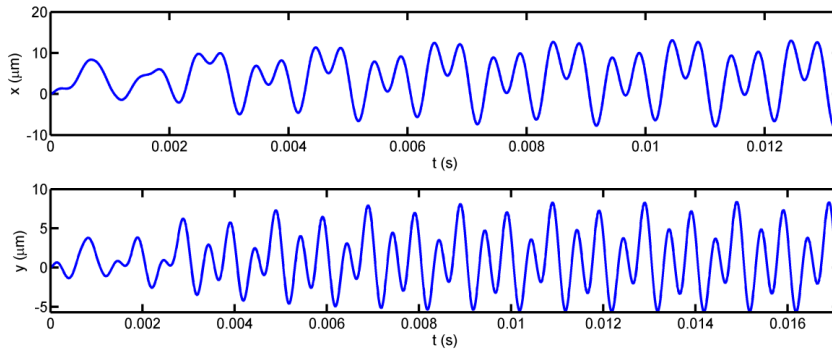
$$h_{ro}^j = \rho_j - \rho_{j-1} \quad (4.41)$$

The run-out of cutting edge, ρ_j , represents the variation of the actual radius of each flute which effects in a variation on cutting forces. The actual radius is the radius of the actual trajectory of the flute, which varies from its nominal radius owing to run-out.

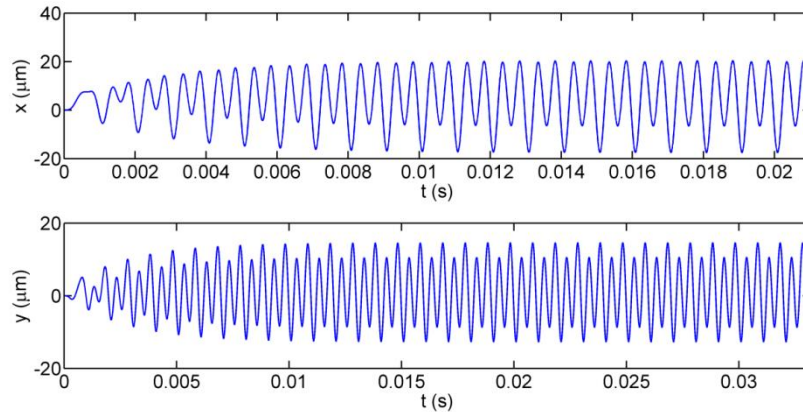
In this study, where small values of depth of cut and helix angles were considered, the variation of the effective radius along the cutting edge may be neglected and then the tool run-out can be adequately defined by means of the difference between the actual and the nominal trajectory for each flute. As the specific cutting force is considered as the function of radial, tangential and axial cutting forces and chip thickness along the cutting edge, the cutting forces in X and Y directions are obtained by resolving the tangential and radial forces as follows

$$\begin{Bmatrix} F_{x,j}(\phi_j) \\ F_{y,j}(\phi_j) \end{Bmatrix} = \begin{bmatrix} -\cos(\phi_j) & -\sin(\phi_j) \\ \sin(\phi_j) & -\cos(\phi_j) \end{bmatrix} \begin{Bmatrix} F_{t,j} \\ F_{r,j} \end{Bmatrix} \quad (4.42)$$

The effect of run-out is illustrated using a 12mm diameter tool. The run-out is measured in the direction of feed. Time domain simulations are carried-out with and without run-out effects for the case of 10 μ m run-out offset as shown in the Figure 4.12. All the parameters of spindle-tool system are considered as per the two dimensional cutting process model.



(a) without run-out



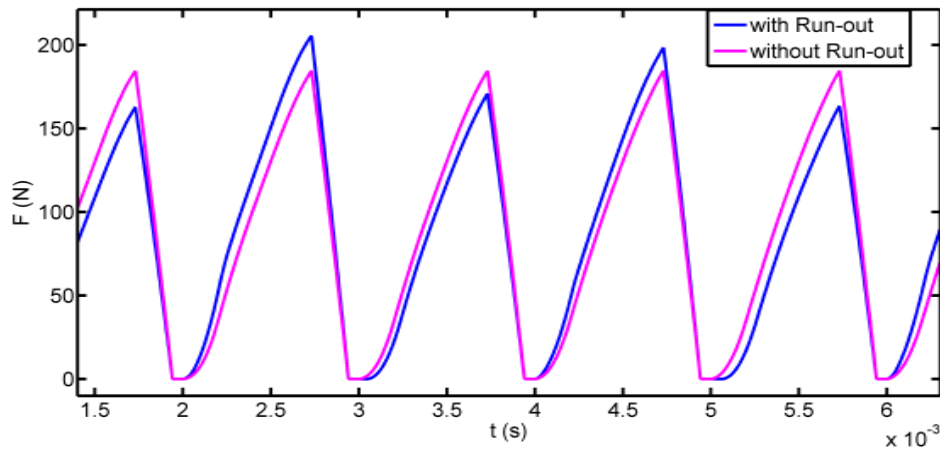
(b) with run-out

Figure 4.12: Tool displacement levels with run-out correction

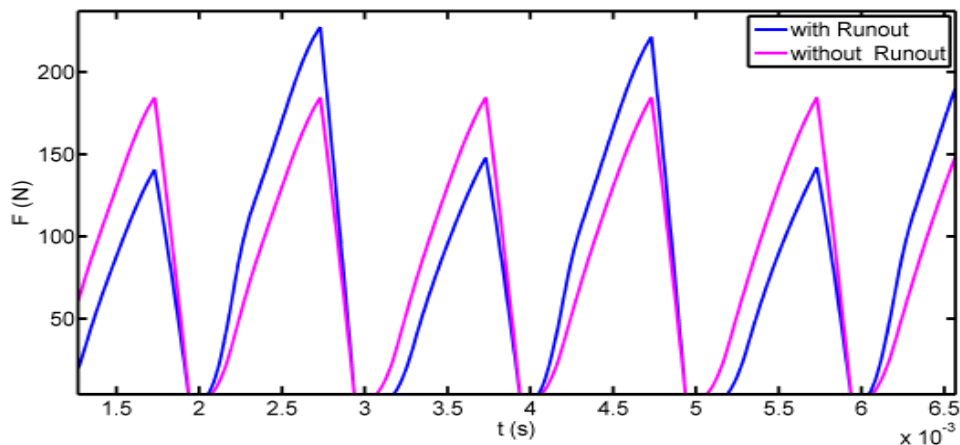
It is observed that run-out in the cutting process causes an increase in the tool displacement levels.

Figure 4.13 shows the simulated cutting forces for the tool with run-out at two values of run-out equal to 10 μ m and 25 μ m. A very less percentage of difference is observed for the change in 10-12 μ m between the cutting forces for each flute as shown in Figure 4.13(a). As it further proceeds, the cutting forces can be seen with high amplitude in the differences

of chip-load on the each tooth as shown in Figure 4.13(b) which leads to undesirable tool vibration levels.



(a) 10 μm



(b) 25 μm

Figure 4.13: Force variations with tooth-to-tooth run-out

4.1.3 Cutting force simulation with variable pitch effect

In normal studies, it is assumed that the teeth are equally spaced around the cutter periphery (i.e., having constant teeth pitch). Variable pitch end mills are often employed in machining hard materials [118]. The variable pitch mills are either having variable helix angle or variable pitch angle. The feed per tooth of a variable pitch tool varies from tooth to tooth as a function of the tooth angle θ_i (deg), as shown in Figure 4.14

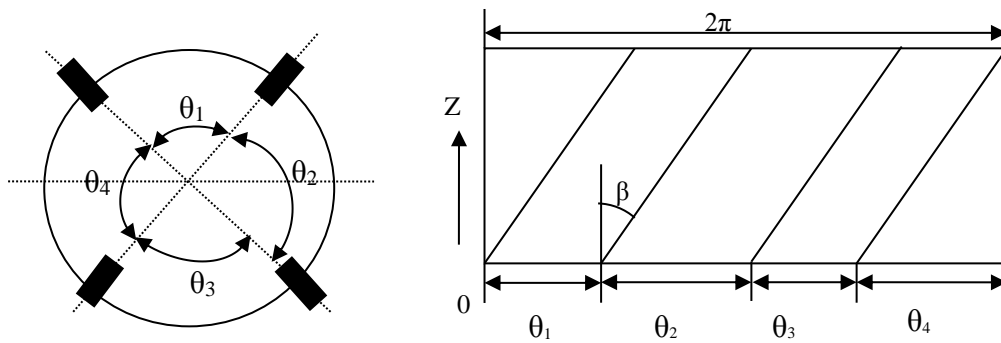


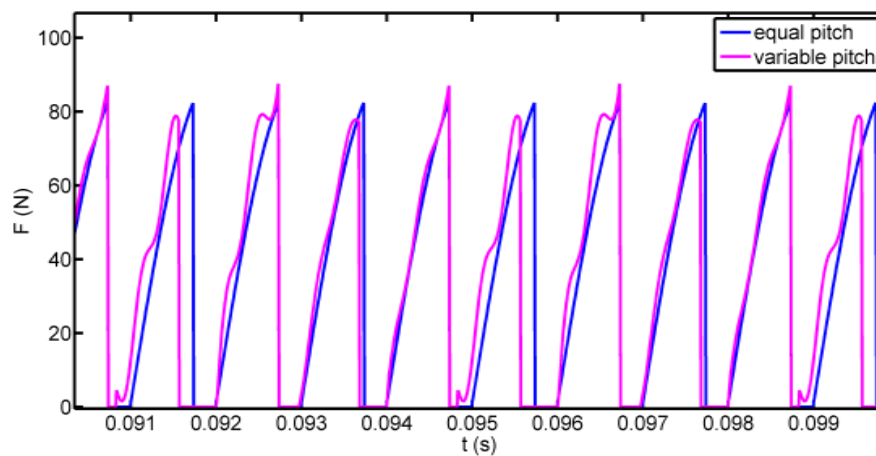
Figure 4.14: Angular position of edges for end mill on cutter circumference

The feed per tooth is described by

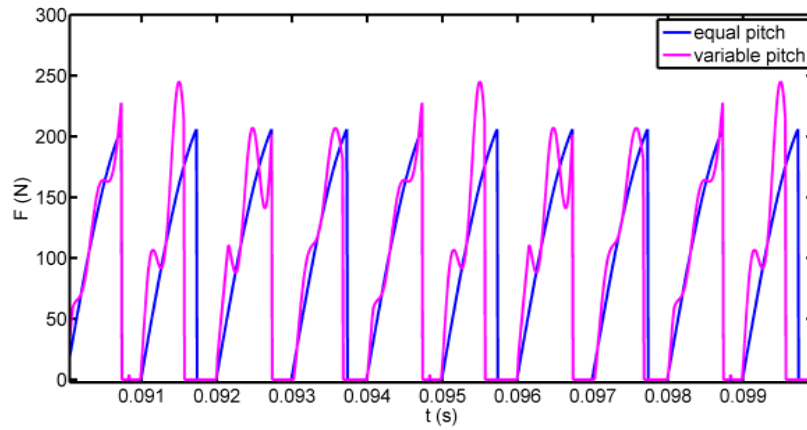
$$f_{t,variable} = \left[\frac{f_{t,mean} \times \theta_i \times N_t}{360^\circ} \right] \quad (4.43)$$

Where $f_{t,mean}$ is the mean feed per tooth and N_t is the number of teeth .

Figure 4.15 shows the resultant forces measured during a 25% radial immersion up-milling cutting of aluminium alloy using the tool with variable pitch spacing $[0^\circ \ 95^\circ \ 180^\circ \ 275^\circ]$ and with equal pitch $[0^\circ \ 90^\circ \ 180^\circ \ 270^\circ]$ for two different axial depths of cut. It is observed that when the depth of cut increases from 1mm to 2.5mm, the variable pitch causes the forces to vary non-linearly. Amplitudes of cutting force components have been also increased considerably.



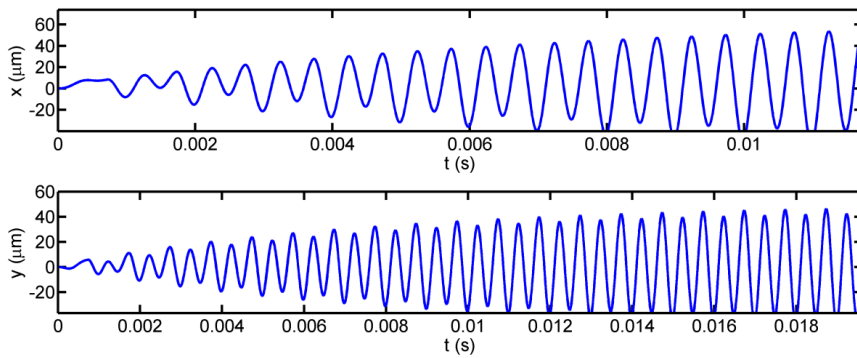
(a) depth of cut=1mm



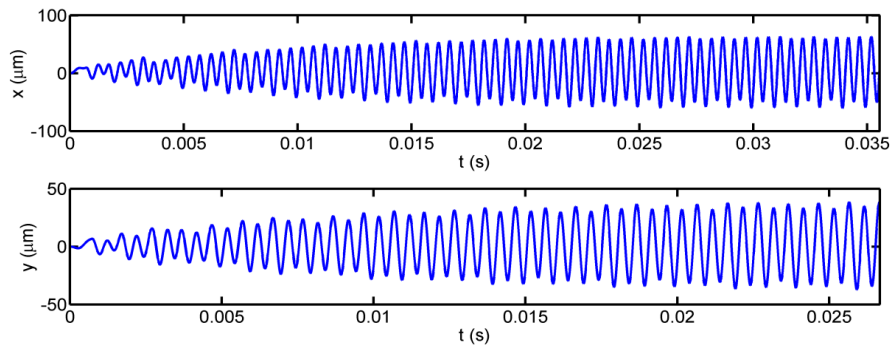
(b) depth of cut=2.5mm

Figure 4.15: Time domain simulation with variable pitch at 25% radial immersion

Cutting tool displacement levels are obtained for the 1mm depth of cut with equal and variable pitch case as shown in Figure 4.16. It is evident that the variable pitch in the cutting tool significantly increases the tool displacement levels drastically.



(a) with equal pitch



(b) with variable pitch

Figure 4.16: Tool vibration levels at 1mm depth of cut

The effect of cutting tool parameters is therefore considerable in assessing the cutting process stability and it requires optimal selection with respect to process parameters. Based on the above results, the permissible limit for the tool run-out may be ascertained with respect to dimensions of the spindle. Also, the tools with variable pitches are allowed during the machining for the higher stable depth of cuts for the proposed spindle-tool design.

4.2 Three-dimensional cutting force model

In practice, spindle-tool system generates three different forces in radial, tangential and axial directions while machining the workpiece. A milling cutter having N_t number of teeth with a lead angle (α) is considered as shown in Figure 4.17. When the cutter engages with the workpiece, the cutting forces cause the systematic vibrations in all the three possible directions [136]. A coordinate system is defined for the end milling process with X direction specifies the feed of cutter, Y defines the normal to feed and Z defines the vertical cutter position with respect to the base plane and i, j and k are the rotating co-ordinate frame. These forces lead to excite the system in all the directions producing the corresponding displacements x, y and z respectively. Generally the chip thickness is measured in radial direction. The total chip thickness is expressed as

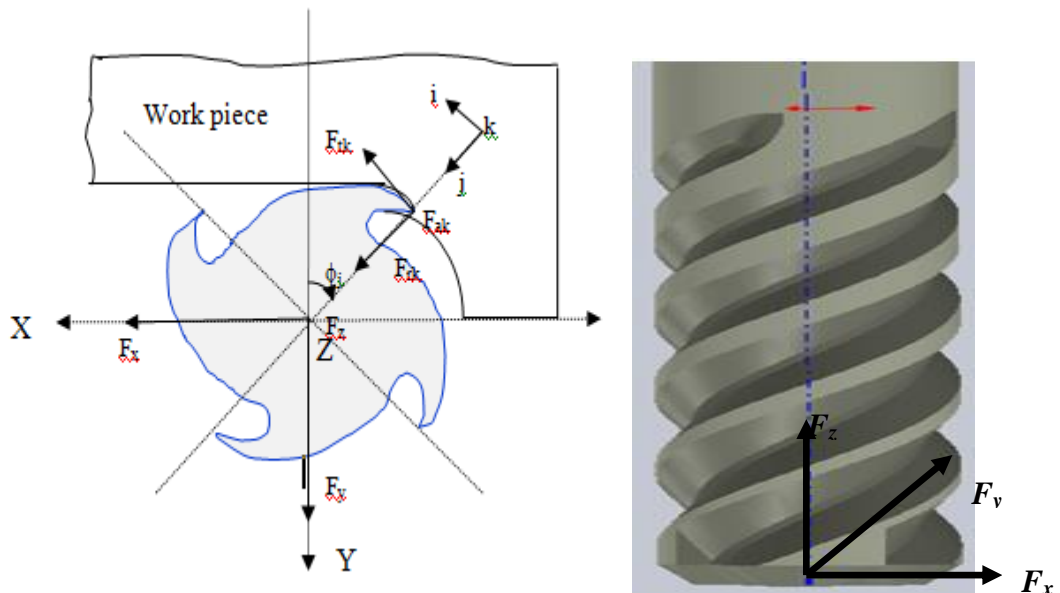


Figure 4.17: Three-degree of freedom cutting force model

$$h(\phi_k) = (h_e + h_d)g(\phi_k) = [f_t \sin \phi_k \sin \alpha + (n_{k,0} - n_k)]g(\phi_k) \quad (4.44)$$

Where (n_{k0}, n_k) are the previous and present positions of the cutter and f_t is feed rate, $g(\phi_k)$ is the step function indicating the in or out of cut. The static component $(f_t \sin \phi_k \sin \alpha)$ in chip thickness has very less contribution in prediction of chatter stability. Generally, it is neglected from the expression. Therefore the final expression in terms of dynamic chip thickness similar to 2-D modeling is given by the following expression

$$h(\phi_k) = [(\Delta x \sin \phi_k + \Delta y \cos \phi_k) \sin \alpha - \Delta z \cos \alpha] g(\phi_k) \quad (4.45)$$

Where $\Delta x = x(t) - x(t - \tau)$, $\Delta y = y(t) - y(t - \tau)$, and $\Delta z = z(t) - z(t - \tau)$, here τ is tooth passing period and t is present time. The tangential (F_{tk}), radial (F_{rk}) and axial (F_{ak}) forces acting on the tooth k is proportional to the dynamic chip thickness and axial depth of cut. If the lead angle (α) is set to 90° , then the x and y projections are identical to the helical square end milling. By resolving all these components on to the three perpendicular directions (X , Y and Z), the final expression is obtained as function of their average cutting force coefficients as [171]

$$\begin{Bmatrix} dF_x \\ dF_y \\ dF_z \end{Bmatrix} = \begin{bmatrix} -\sin(\alpha) \cos(\phi) & -\cos(\phi) & -\cos(\alpha) \sin(\phi) \\ -\sin(\alpha) \cos(\phi) & \sin(\phi) & -\cos(\alpha) \cos(\phi) \\ \cos(\alpha) & 0 & -\sin(\alpha) \end{bmatrix} \times \begin{Bmatrix} dF_r \\ dF_t \\ dF_a \end{Bmatrix} \quad (4.46)$$

The resultant cutting force is obtained by the summation of all individual force components acting on every tooth and is given as follows

$$F_x = \sum_{k=0}^{N_t-1} F_{xk}; F_y = \sum_{k=0}^{N_t-1} F_{yk}; F_z = \sum_{k=0}^{N_t-1} F_{zk} \quad (4.47)$$

The force expressions in x , y and z directions are arranged in matrix form to obtain

$$\begin{Bmatrix} F_x \\ F_y \\ F_z \end{Bmatrix} = bK_t [A(t)] \begin{Bmatrix} \Delta x \\ \Delta y \\ \Delta z \end{Bmatrix} \quad (4.48)$$

where the elements of matrix $[A(t)]$ are the time varying directional dynamic force coefficients which depend on the angular position of the cutter. Thus, the average term in Fourier series expansion of $[A(t)]$ is included to eliminate the periodic time varying

coefficients. The final form is obtained as follows:

$$[A_o] = \frac{1}{\phi_p \phi_s} \int_{\phi_s}^{\phi_e} [A(\phi)] d\phi = \frac{N}{4\pi} [\beta] \quad (4.49)$$

where the matrix $[\beta]$ contains the following directional orientation factors

$$\beta_{xx} = \left[-K_r (\sin^2 \phi \sin^2 \alpha) - \sin^2 \phi \sin \alpha - K_a \left(\frac{-\sin 2\phi}{2} + \phi \right) \left(\frac{\sin 2\alpha}{2} \right) \right]_{\phi_s}^{\phi_e} \quad (4.50)$$

$$\beta_{xy} = \left[-K_r \left(\frac{\sin 2\phi}{2} + \phi \right) \sin^2 \alpha - \left(\frac{\sin 2\phi}{2} + \phi \right) \sin \alpha - K_a \left(\frac{\sin 2\alpha}{2} \right) \sin^2 \phi \right]_{\phi_s}^{\phi_e} \quad (4.51)$$

$$\beta_{xz} = 2 \left[K_r \left(\frac{\sin 2\alpha}{2} \right) \sin \phi - (\sin \phi \cos \alpha) - K_a (\cos^2 \alpha \cos \phi) \right]_{\phi_s}^{\phi_e} \quad (4.52)$$

$$\beta_{yx} = \left[-K_r (\sin^2 \phi \sin^2 \alpha) + \left(\frac{-\sin 2\phi}{2} + \phi \right) \sin \alpha - K_a \left(\frac{\sin 2\alpha}{2} \sin^2 \phi \right) \right]_{\phi_s}^{\phi_e} \quad (4.53)$$

$$\beta_{yy} = \left[-K_r \left(\frac{\sin 2\phi}{2} + \phi \right) \sin^2 \alpha + \sin^2 \phi \sin \alpha - K_a \left(\frac{\sin 2\phi}{2} + \phi \right) \left(\frac{\sin 2\alpha}{2} \right) \right]_{\phi_s}^{\phi_e} \quad (4.54)$$

$$\beta_{yz} = 2 \left[K_r \left(\frac{\sin 2\alpha}{2} \sin \phi \right) + (\cos \phi \cos \alpha) + K_a (\cos^2 \alpha \sin \phi) \right]_{\phi_s}^{\phi_e} \quad (4.55)$$

$$\beta_{zy} = 2 \left[K_r \left(\frac{\sin 2\alpha}{2} \sin \phi \right) + (\cos \phi \cos \alpha) + K_a (\cos^2 \alpha \sin \phi) \right]_{\phi_s}^{\phi_e} \quad (4.56)$$

$$\beta_{zx} = 2 \left[-K_r \left(\frac{\sin 2\alpha}{2} \cos \phi \right) + K_a (\sin^2 \alpha \cos \phi) \right]_{\phi_s}^{\phi_e} \quad (4.57)$$

$$\beta_{zy} = 2 \left[K_r \left(\frac{\sin 2\alpha}{2} \sin \phi \right) - K_a (\sin^2 \alpha \sin \phi) \right]_{\phi_s}^{\phi_e} \quad (4.58)$$

$$\beta_{zx} = 2\phi \left[-K_r (\cos^2 \alpha) + K_a \left(\frac{\sin 2\alpha}{2} \right) \right]_{\phi_s}^{\phi_e} \quad (4.59)$$

The dynamic milling equation with directional orientation factors is obtained as

$$\{F(t)\} = \frac{N_t}{4\pi} bK_t [\beta] \{\Delta(t)\} \quad (4.60)$$

The vibration vector with regeneration effect consists of both delay terms ($e^{-i\omega_c \tau}$) and the frequency response function $[G(i\omega_c)]$ matrix at the tool/workpiece contact region and is given by the expression as

$$\{\Delta(t)\} = [1 - e^{-i\omega_c \tau}] [G(i\omega_c)] \{F(t)\} \quad (4.61)$$

Where the transfer function matrix is given as:

$$[G(i\omega_c)] = \begin{bmatrix} G_{xx}(i\omega_c) & G_{xy}(i\omega_c) & G_{xz}(i\omega_c) \\ G_{yx}(i\omega_c) & G_{yy}(i\omega_c) & G_{yz}(i\omega_c) \\ G_{zx}(i\omega_c) & G_{zy}(i\omega_c) & G_{zz}(i\omega_c) \end{bmatrix} \quad (4.62)$$

The dynamic cutting force system is given by

$$\{F(t)\} = \frac{N_t}{4\pi} bK_t (1 - e^{-i\omega_c \tau}) [\beta] [G(i\omega_c)] \{F(t)\} \quad (4.63)$$

The characteristic equation of the closed loop dynamic milling system is finally expressed as:

$$\det \left\{ [I] - \frac{N_t}{4\pi} bK_t (1 - e^{-i\omega_c \tau}) [\beta] [G(i\omega_c)] \right\} = 0 \quad (4.64)$$

The eigenvalues (Λ) of the above equation can be solved for a given chatter frequency ω_c , static cutting factors (K_t, K_r, K_a), radial immersion angles (ϕ_s and ϕ_e) and frequency response function of the structure. These have real and imaginary components given as follows

$$\Lambda = \Lambda_{Re} + i\Lambda_{Im} = -\frac{N_t}{4\pi} \beta K_t (1 - e^{-i\omega_c \tau}) \quad (4.65)$$

The final expression for the stable depth of cut is obtained as:

$$b_{lim} = -\frac{2\pi}{N_t K_t} \Lambda_{Re} \left(1 + \left(\frac{\sin \omega_c \tau}{1 - \cos \omega_c \tau} \right)^2 \right) \quad (4.66)$$

Where the Λ_{Re} is the real part of the eigen-value and ω_c is the chatter frequency and the corresponding spindle speed (Ω) is

$$\Omega = \frac{60}{N_t \tau} \text{ (rpm)} \quad (4.67)$$

Where N_t is the number of teeth and τ is the tooth passing period, obtained same as in two-dimensional model.

The end milling process requires a cylindrical cutter having cutting edges on the periphery as well as the cutting edges at the base, to provide each successive engagement of cutting edges with appropriate impact on workpiece. The cutting tool is modelled as a series of single point tools having one cutting edge and the cutter is discretized along the Z-direction with 's' slices. To model the cutting forces in all the three directions, a rotating co-ordinate system for each cutting edge segment at the j^{th} slice and k^{th} cutting edge is incorporated. The individual cutting forces at each cutting edge is evaluated in all the radial, tangential and axial directions. Finally, the summation of component forces at every cutting edge with respect to the slices are given by the following expressions

$$F_x(t) = \sum_{j=1}^s \sum_{k=0}^{N-1} (-F_{rk} \cos(\phi) - F_{tk} \cos(\phi)) \quad (4.68)$$

$$F_y(t) = \sum_{j=1}^s \sum_{k=0}^{N-1} (-F_{rk} \cos(\phi) + F_{tk} \sin(\phi)) \quad (4.69)$$

$$F_z(t) = \sum_{j=1}^s \sum_{k=0}^{N-1} (-F_{ak}) \quad (4.70)$$

During helical end milling process, cutter's displacements (vibrations) are determined in the directions: perpendicular to the tool's rotational axis and collinear to the feed motion vector ($y(t)$), perpendicular to the tool's rotational axis and feed motion vector ($x(t)$), parallel to tool's rotational axis ($z(t)$). In order to determine cutter's instantaneous displacements related to cutter's deflections, induced by cutting forces in all the three directions, the following differential motion equations are considered for each mode:

$$\ddot{x}(t) + 2 \times \xi_x \times \omega_x \times \dot{x}(t) + \omega_x^2 \times x(t) = F_x(t) \times \frac{\omega_x^2}{K_{xx}} \quad (4.71)$$

$$\ddot{y}(t) + 2 \times \xi_y \times \omega_y \times \dot{y}(t) + \omega_y^2 \times y(t) = F_y(t) \times \frac{\omega_y^2}{K_{yy}} \quad (4.72)$$

$$\ddot{z}(t) + 2 \times \xi_z \times \omega_z \times \dot{z}(t) + \omega_z^2 \times z(t) = F_z(t) \times \frac{\omega_z^2}{K_{zz}} \quad (4.73)$$

where $(\omega_x, \omega_y, \omega_z)$, (ξ_x, ξ_y, ξ_z) and (K_{xx}, K_{yy}, K_{zz}) are the modal frequencies, damping factors and stiffness coefficients in x , y and z directions, respectively, F_x , F_y , F_z are instantaneous cutting forces in the machine tool coordinates. Table 4.3 depicts the dynamic parameters used in the simulation.

Table 4.3: Directional dynamic parameters for simulation

Cutting stiffness in X, Y and Z directions ($K_{xx}=K_{yy}=K_{zz}$)	2.1×10^8 N/m
Damping ratios($\xi_x=\xi_y=\xi_z$)	0.01
Tool diameter	12mm
Average specific cutting pressure(K_s) (corresponding to Aluminum alloy)	750N/mm^2
number of teeth (N_t)	4

The stability regions are plotted for the up-milling process using the frequency-domain data at tool-tip obtained from the finite element analysis and is shown in Figure 4.18 for 40% depth of immersion. For comparison sake, the stability-lobe using 2-D model is also plotted (blue colour contour). It is clearly observed that the limiting axial depth of cut increases by 55 percent approximately with three dimensional force model (as seen from dotted-black curve) due to consideration of axial cutting force component.

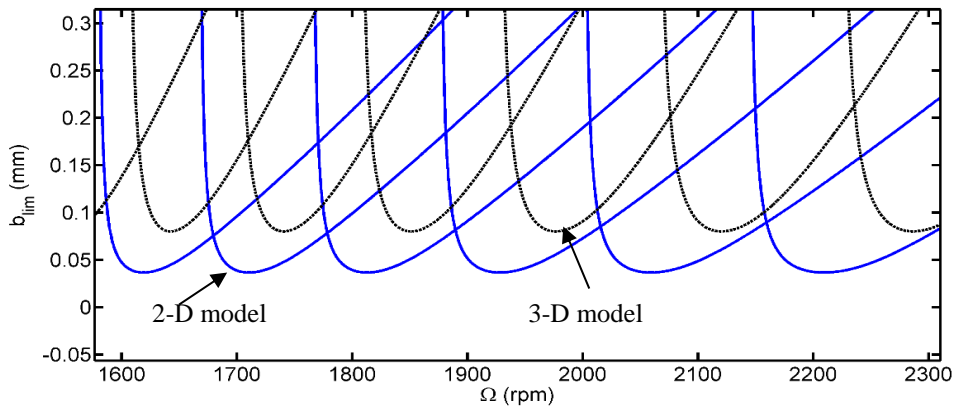
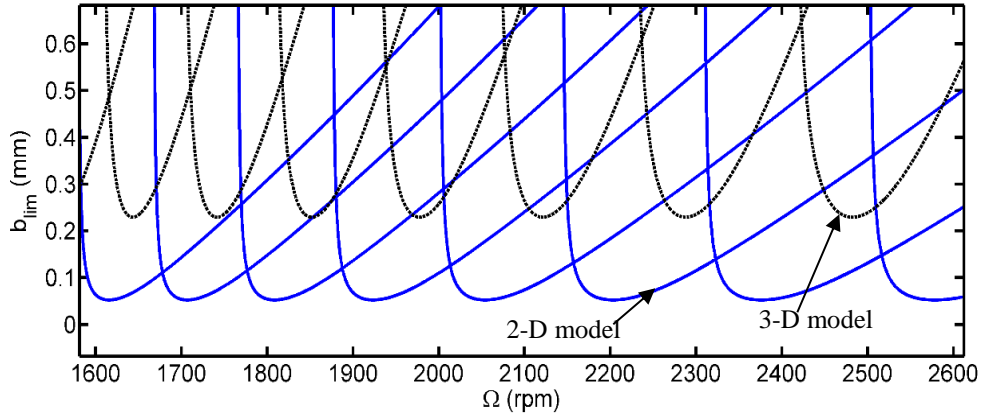


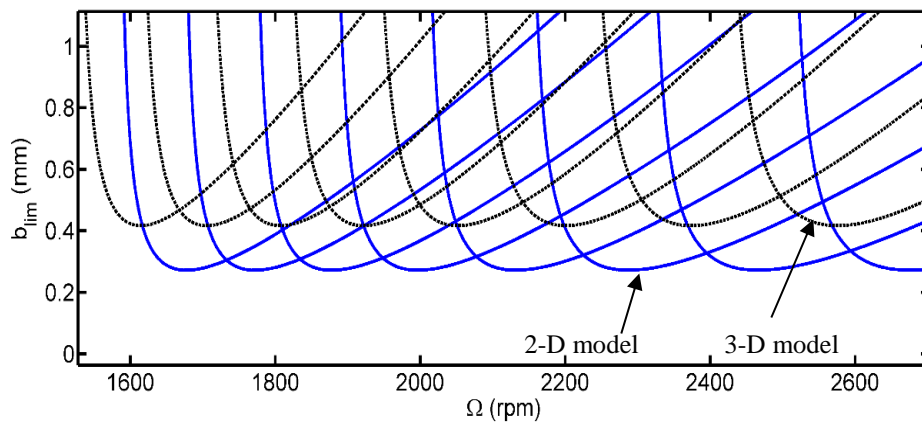
Figure 4.18: Stability lobe diagrams with 40% depth of immersion

Similarly, the two and three dimensional stability plots are obtained for the change in the percentage of damping ratios. It is evident that with a slight enhancement in the damping

ratios, the average stable depth of cut drastically increases in both the cases as shown in Figure 4.19. Here also 40 percent depth of immersion is considered.



(a) $\xi_x = \xi_y = \xi_z = 0.01$



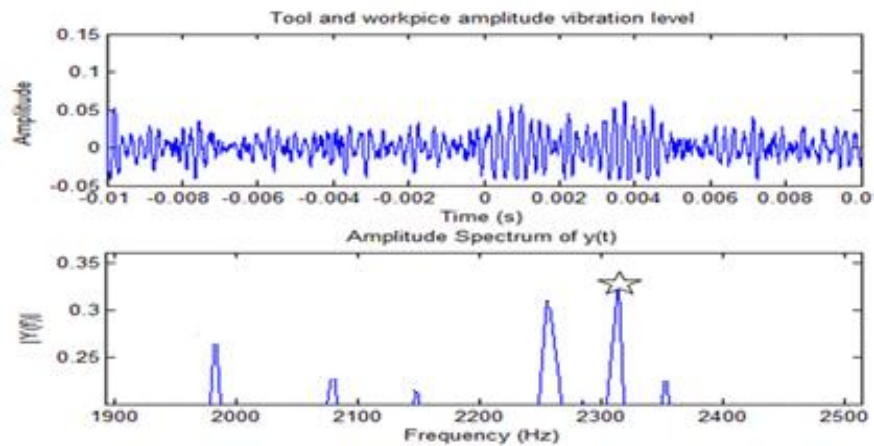
(b) $\xi_x = \xi_y = \xi_z = 0.05$

Figure 4.19: Stability lobe plots for two different damping ratios

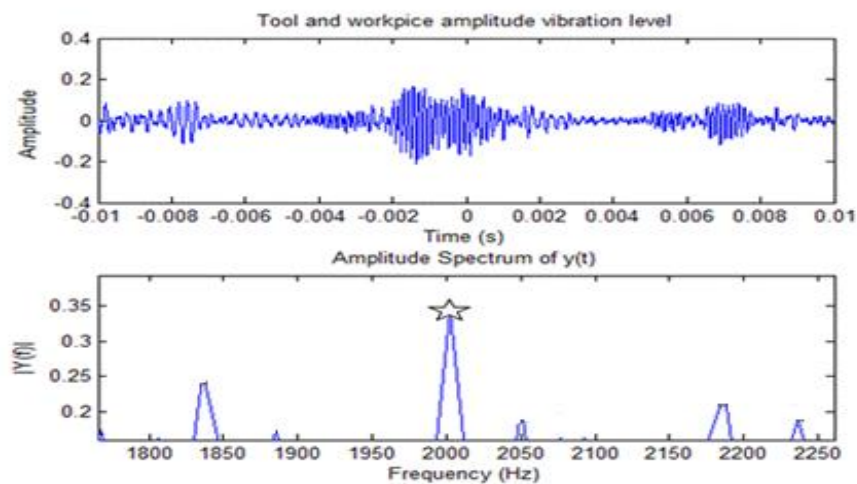
In order to ascertain the reliability of stability boundary, experimental work is conducted on CNC milling centre employing the same spindle. The machine tool has 3-axes with a spindle motor having maximum speed of 4,000 rpm. A High speed steel (HSS) end mill with four flutes having 12mm diameter is inserted in tool-holder. Up-milling with 10 percentage radial immersion in machining is performed on aluminium alloy (Al 3031). Based on analytical stability lobe diagram, a set of experimental tests are conducted at different combination of spindle speeds and axial depth of cut. The output data for analysis of abnormal vibrations during cutting process at specified speeds and depth of cut are recorded using a 4-channel digital oscilloscope (Tektronix-43034), an accelerometer (PG

109 M0, frequency range 1 to 10kHz) with a charge amplifier mounted over the spindle housing.

The time histories and corresponding FFT plots are shown in Figure 4.20 at two different depths of cut 0.196mm and 0.285mm respectively both at 1850 rpm, where the stability of cutting has to be confirmed from analytical lobe diagram. The chatter frequency (indicated in star) occurred at 2380 Hz as its amplitude of vibration level is high as shown in Figure 4.20(b). Similarly, when there is an increment in the axial depth of cut, the amplitude of tool vibration levels during machining increases and there is a shift in the chatter frequency from 2300Hz to 2000Hz. It signifies that when the depth of cut increases the chatter likely to appear early at the engagement of cutting tool.



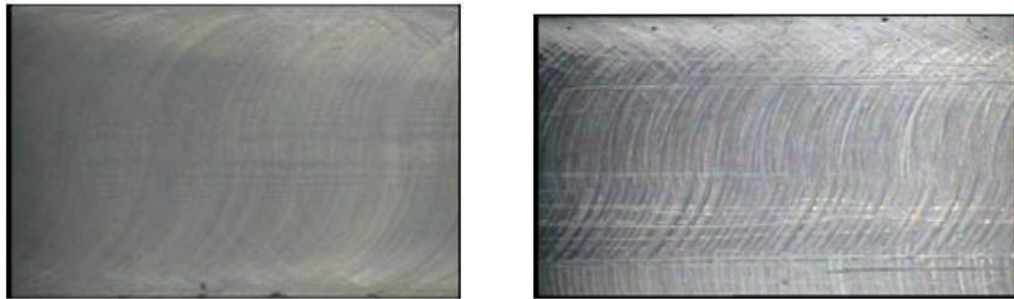
(a) depth of cut=0.196 mm



(b) depth of cut=0.285 mm

Figure 4.20: Experimental response and FFT plots at different axial depths of cut

Further, an optical microscope is used to study the machined surfaces. A relatively rough cut surface is observed from Figure 4.21(b) at an axial depth of cut 0.285mm (spindle speed of 1850 rpm) indicating it as unstable.



(a) Depth of cut=0.196mm

(b) Depth of cut=0.285mm

Figure 4.21: Optical microscope images of workpiece

Based on the tool machining vibration levels and the surface images of corresponding machining areas, the experimental cutting states are super-imposed over the analytical stability lobe diagram as shown in Figure 4.22. It is observed that the analytically predicted lobes from the 3D model provide the correct stability boundaries for the tested conditions.

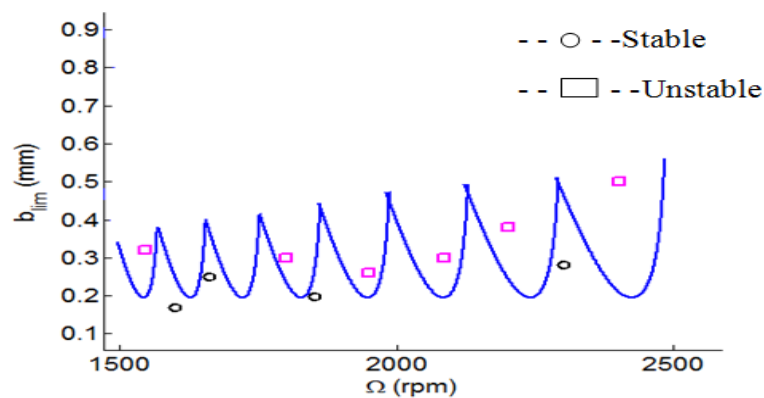
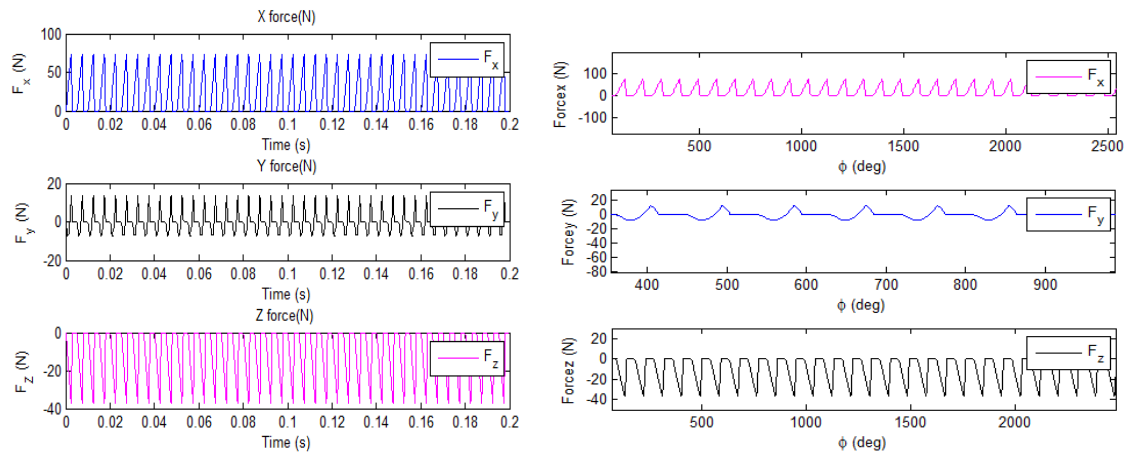


Figure 4.22: Predicted SLD with experimental validation

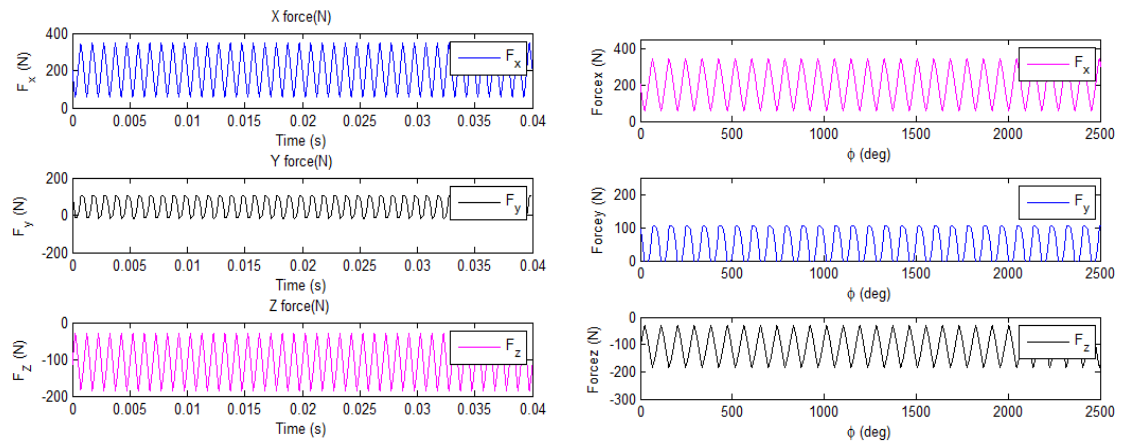
4.2.1 Time-domain simulations

In the proposed method, the spindle speed was selected as 1850 rpm, and tool diameter as 12mm, the axial depth of cut is varied between 1 to 2 mm and feed per tooth is taken as 0.15mm. A 10% radial immersion up-milling process is considered for the cutting force analysis. It is seen that, there is a flatten portion in cutting forces with respect to cutter

rotation angle (ϕ) for an axial depth of cut of 1mm as shown in Figure 4.23(a). As the axial depth of cut increases, sharp waveforms are observed with increase in magnitude of cutting force in all the three directions, as seen from Figure 4.23(b). The modal equations are solved together with zero initial conditions using ode45 function in Matlab. These simulations are obtained from a user interactive computer program.



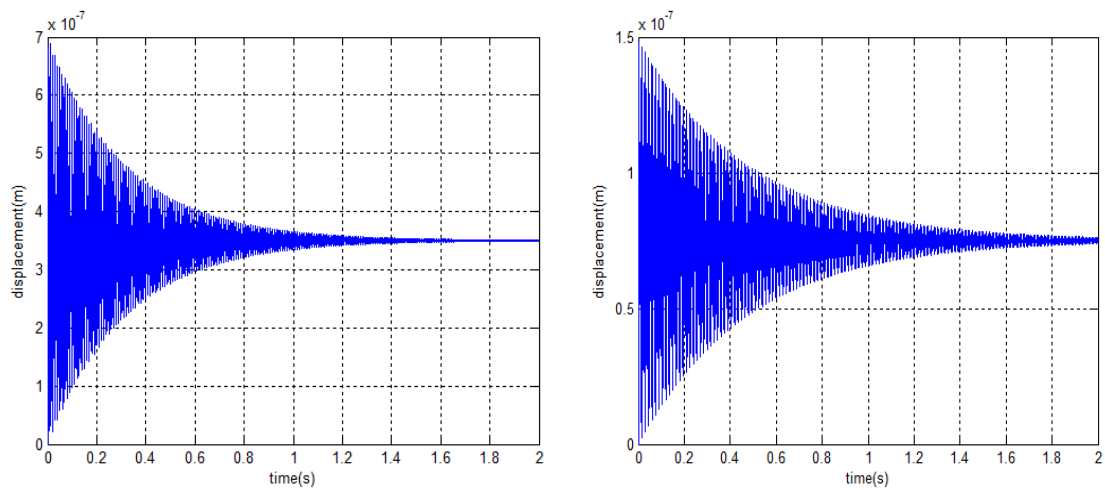
(a) 1mm axial depth of cut



(b) 2mm axial depth of cut

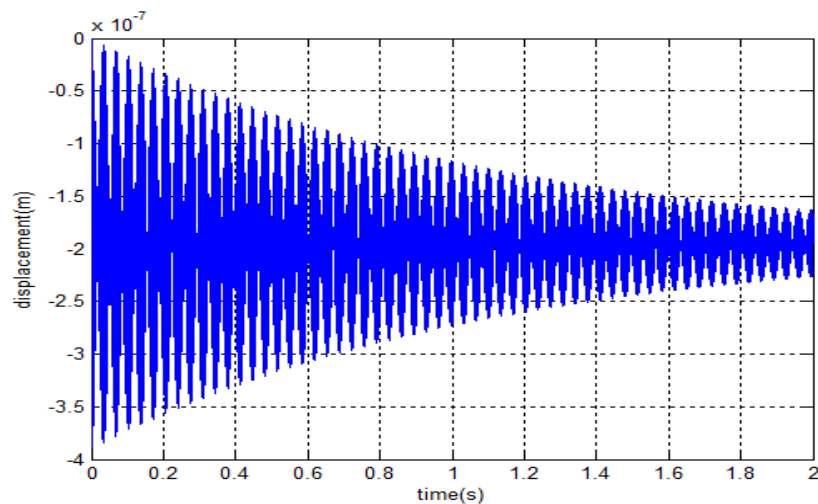
Figure 4.23: Three directional cutting force histories

Cutting displacement components at the cutting tool in the X , Y and Z directions are investigated. The simulation is carried out for an axial depth of cut = 1mm as shown in Figure 4.24. It is seen that the initial transient vibration level was high in the x direction and it dies out approximately at 1.5s compared to the other two directions. Vibrations generated in the z direction signify that it has more influence to produce the chatter in the machining process.



(a) x-direction vibration

(b) y-direction vibration



(c) z-direction vibration

Figure 4.24: Time history plots for an axial depth of cut of 1mm

Similarly the simulation was carried out for an axial depth of cut of 2mm. It is observed that, the vibration level at the engagement of cut at the beginning is higher and the transient vibration dies out at 1.8s in x direction compared to the other two directions as shown in Figure 4.25.

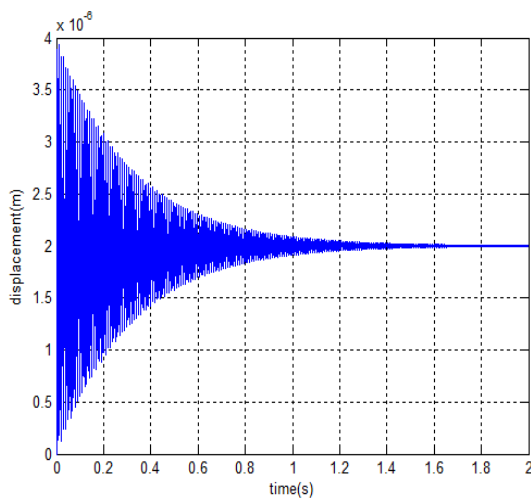
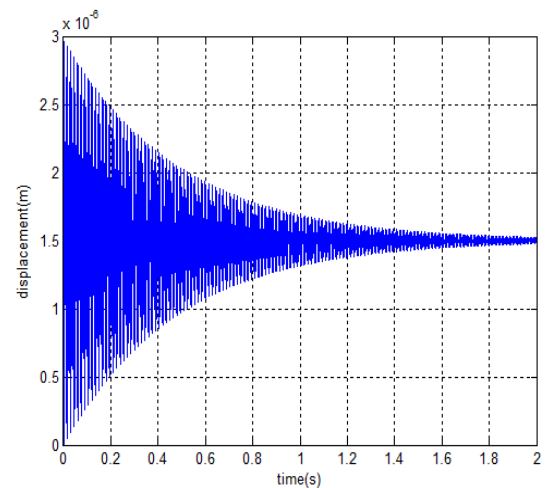
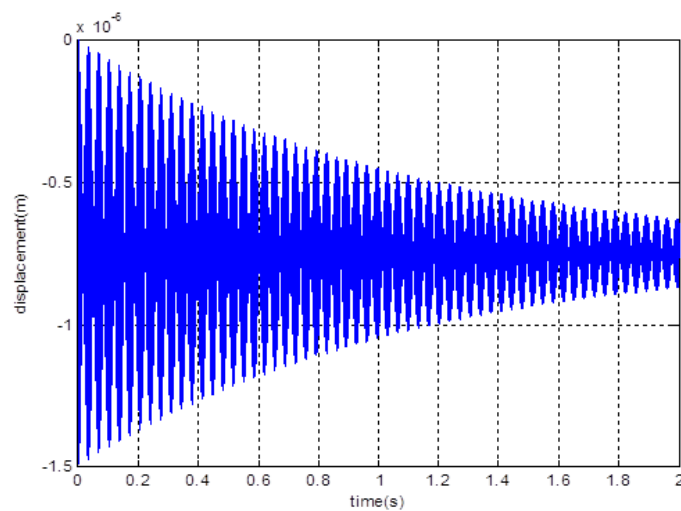
(a) x -direction vibration(b) y -direction vibration(c) z -direction vibration

Figure 4.25: Time history plots for an axial depth of cut of 2 mm

When the axial depth of cut increases the amplitude of vibration levels also increase in all the three directions. For the sake of further understanding the phase plane diagrams at the two depths of cuts are also plotted in X direction. Figure 4.26 shows the phase diagrams in X directions at two different depth of cuts considered. It is seen that in both the cases there exists a stable centre.

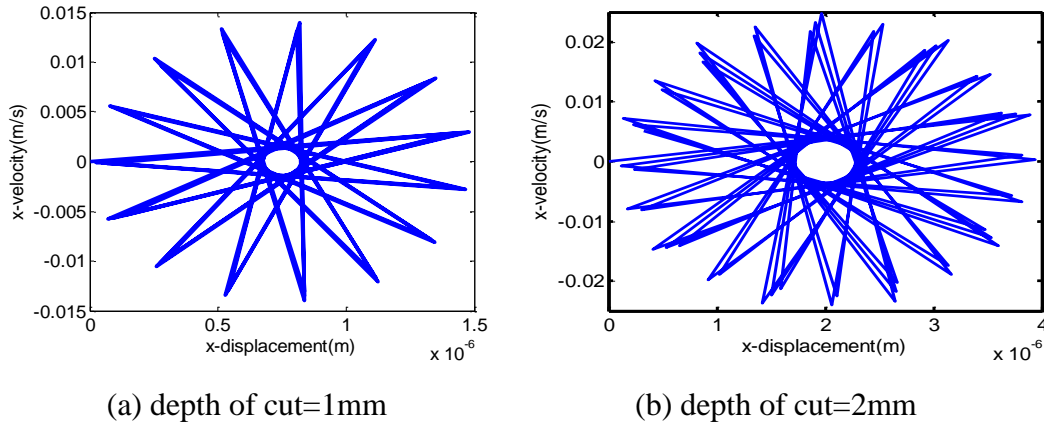


Figure 4.26: Phase plane plots at 1850 rpm

A case with unstable cutting operation for the same spindle-tool system is also studied by varying the helix angle of the tool and depth of cut as shown in Figure 4.27.

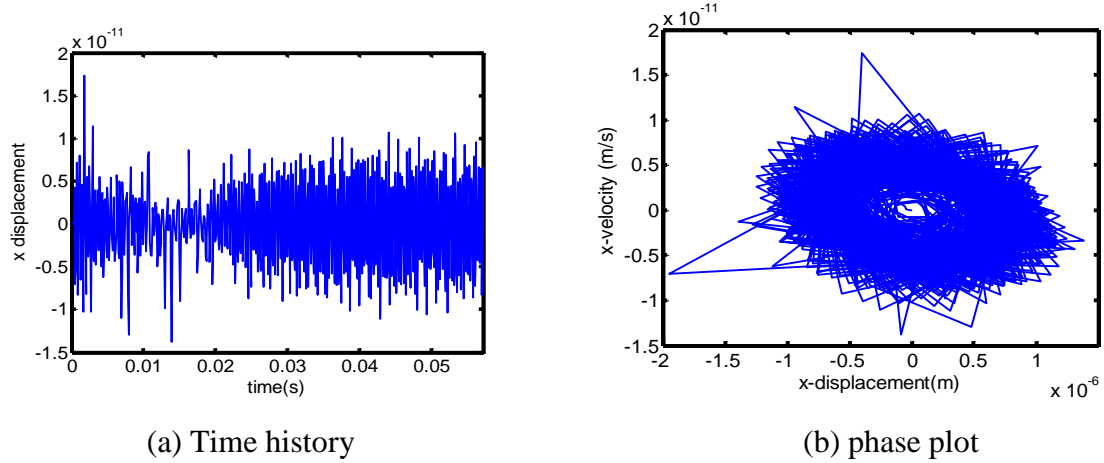


Figure 4.27: Time domain simulation at a depth of 4mm

4.2.2 Nonlinear force feed model

The cutting process stability with a spindle-tool system depends on the cutting force model accounting several practical considerations. Generally in the nonlinear force-feed model, uncut chip thickness (h) is taken to the power a positive constant (γ). The tool immersion angle is varied along the axial direction (Z) in terms of helix angle (β) as [142]:

$$\phi_j(z, t) = \frac{2\pi\omega}{60}t + (j-1)\phi_p - \frac{z}{r} \tan\beta \quad (4.74)$$

Where the pitch angle $\phi_p = \frac{2\pi}{N_t}$, r is the cutting tool radius. The differential milling force expressions is written as:

$$dF_t = g(\phi_j)K_t(h_j(\phi_j))^\gamma dz \quad (4.75)$$

$$dF_r = g(\phi_j)K_r(h_j(\phi_j))^\gamma dz \quad (4.76)$$

$$dF_a = g(\phi_j)K_a(h_j(\phi_j))^\gamma dz \quad (4.77)$$

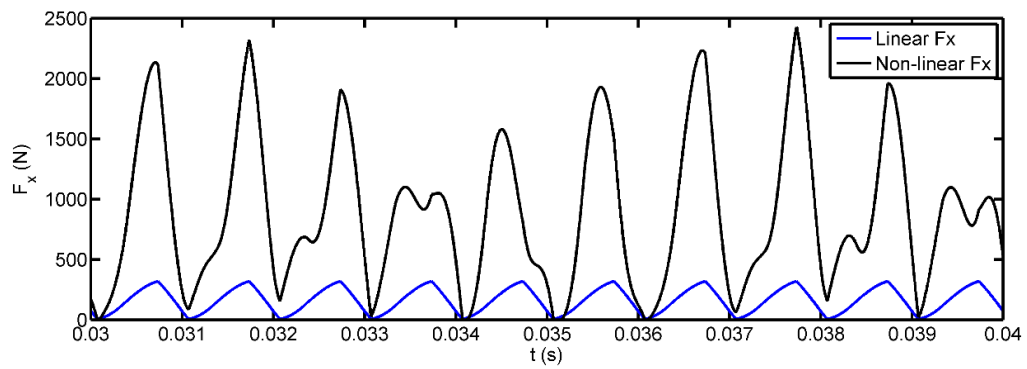
Here, K_t and K_r are the cutting mechanics parameters which characterize the local cutting mechanics of the differential cutting edge and $h_j(\phi_j) = f_t \sin(\phi_j)$ is static chip thickness. The exponents of the chip thickness characterize the size effect in metal cutting are taken same in all three directions. Also, $g(\phi_j)$ is a screen function that is equal to one if j^{th} cutting edge is in cut otherwise equals to zero. When uncut chip thickness is less than zero, dF_t and dF_r are both zero. This situation corresponds to loss of contact between tool and work-piece. The differential forces in the X, Y and Z directions is obtained by coordinate transformation of the differential forces in tangential, radial and axial directions as follows

$$\begin{Bmatrix} dF_x \\ dF_y \\ dF_z \end{Bmatrix} = \begin{bmatrix} -\cos\phi & -\sin\phi & 0 \\ \sin\phi & -\cos\phi & 0 \\ 0 & 0 & 1 \end{bmatrix} \begin{Bmatrix} dF_t \\ dF_r \\ dF_a \end{Bmatrix} \quad (4.78)$$

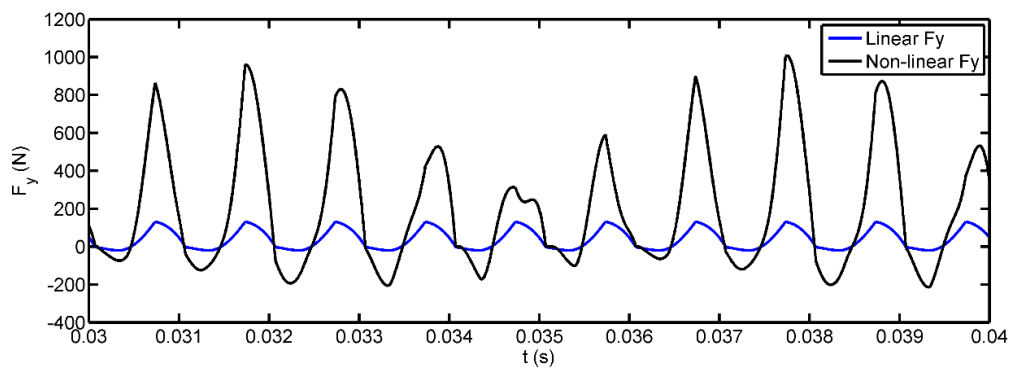
The total cutting force acting on the j^{th} cutting edge can be attained by integrating along the axial depth of cut (b) given by the following expression:

$$F_l = \int_0^z dF_l dz \quad (l = x, y \text{ and } z) \quad (4.79)$$

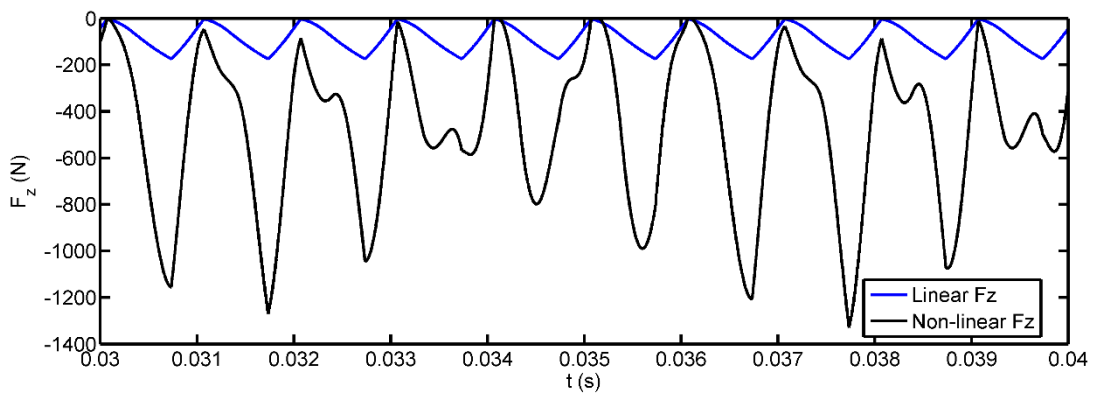
The cutting forces are evaluated for a four-fluted endmillcutter with a helix angle of 65° , feed rate of 2 mm/tooth, $\gamma = 0.83$ and depth of cut = 2 mm. Both the linear and non-linear force models are compared as shown in the Figure 4.28. It is observed that the cutting forces increases drastically by introducing the power index. The maximum cutting forces for the linear model is very low compared to the nonlinear model. In the linear model, cutting forces in all the directions behave in the symmetrical wave form with respect to the time whereas nonlinear model does not represent any harmonic wave form.



(a) Cutting force simulation in x-direction



(b) Cutting force simulation in y-direction



(c) Cutting force simulation in z-direction

Figure 4.28: Effect of non-linear feed rate forces

4.3 Effects of spindle-tool system parameters on stability

The average stable depth of cut (b_{lim}) is directly related to the chatter vibration and milling instability. There are significant number of important design parameters related to spindle-tool system, such as the dimensions of spindle shaft and its housing, bearing locations, preload of the bearings and tool overhang of the cutting tool as studied in earlier chapter. As, the tool-tip frequency response has a significant influence on the cutting process stability, the effects of above parameters on limiting depth of cut are studied by keeping the common cutting parameters as constant.

In this regard, stability of slot milling process for different lengths of the tool overhang, bearing span ratios, diameters of cutting tool, interface stiffness and axial prelaod are considered for the analysis. The cutting conditions considered are as in two-dimensional model namely spindle speed=2200rpm, helix angle(β)=65°, and tool diameter=12mm. An average stable depth of cut is computed in each combination of spindle-tool parameters according to the following equation from stability lobe diagrams

$$\bar{b} = \frac{\int_{j=0}^{N_{max}} b_{lim,j} dN}{N_{max}} \quad (4.80)$$

where N_{max} refers to the maximum speed limit in stability lobe diagram, while $b_{lim,j}$ is the instantaneous limiting depth of cut at particular speed N_j . Figure 4.29 shows the discretization of stability lobe in order to predict the proposed average stable depth of cut.

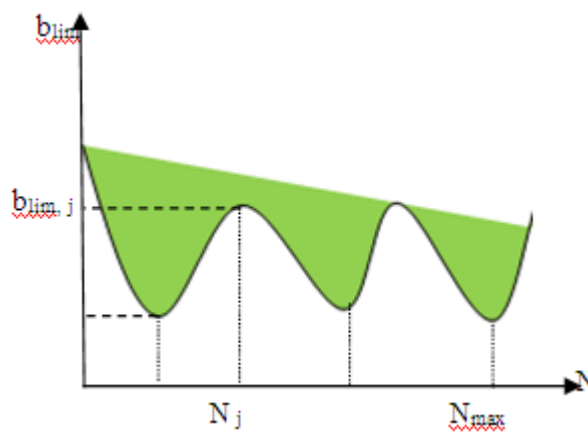
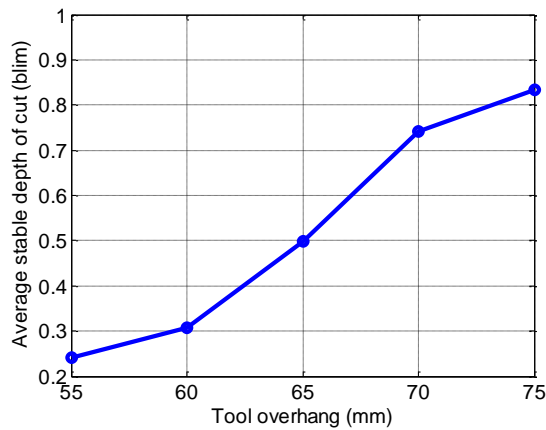
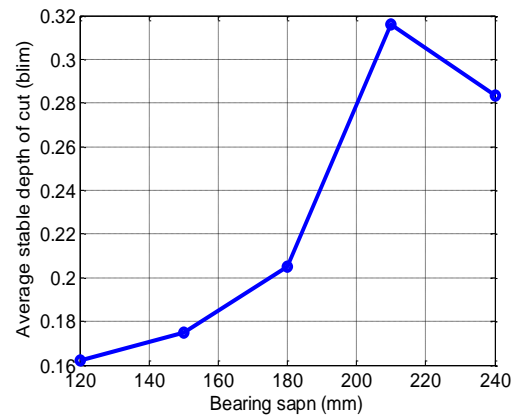


Figure 4.29: Prediction of average stable depth of cut

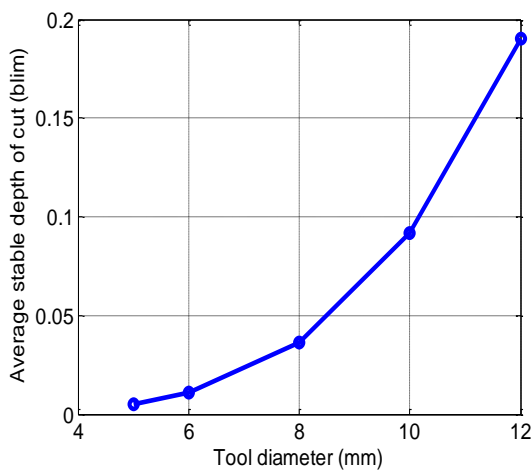
Figure 4.30 shows the variation of simulated data for the different values of tool overhang (TO), bearing span, tool diameter, interface stiffness and axial preload. When there is an increase in bearing span of the spindle machine, there is an increase in the average stable depth of cut as shown in Figure 4.30(b). But after the bearing span of 180mm the average stable depth decreases due to second mode of vibration came into existence which critically influences the dynamic stability of the system. Similarly, it is observed that when there is an increase in the tool overhang length and tool diameter of the cutting tool, there is an increase in the average stable depth of cut (b_{lim}) as shown in Figure 4.30(a) and 4.30(c). While the interface stiffness and axial preload decreases the depth of cut as shown in Figure 4.30(d) and 4.30(e). In each of these graphs one of the parameter is varied with respect to initial set (tool overhang= 65mm, bearing span=90mm, tool diameter=12mm, interface stiffness= 1.5×10^5 and axial preload=1500N) as considered in chapter-3.



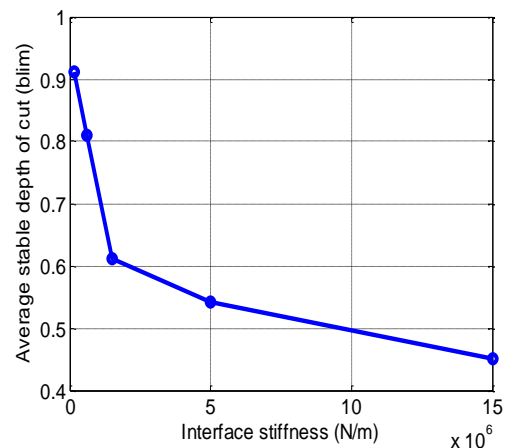
(a) b_{lim} vs tool overhang
bearing span



(b) b_{lim} vs



(c) b_{lim} vs tool diameter



(d) b_{lim} vs interface stiffness

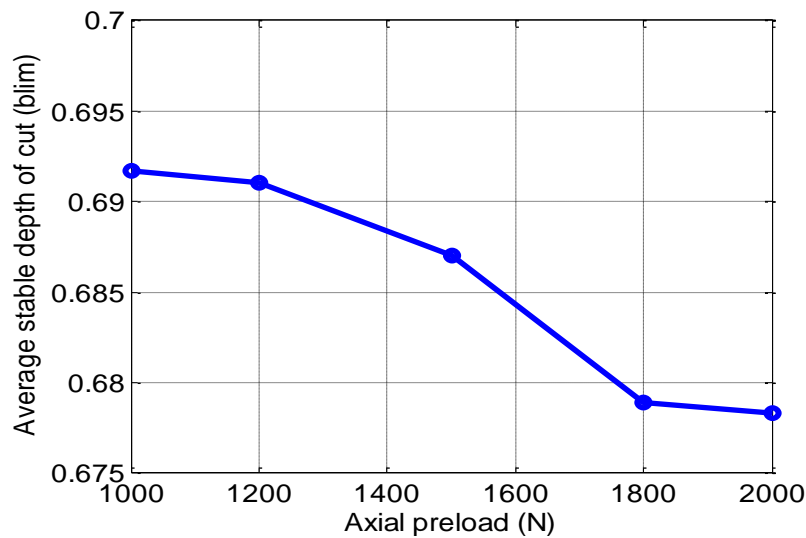
(e) b_{lim} vs axial preload

Figure 4.30: Variation of average depth of cut as a function of spindle tool parameters

Figure 4.31 shows the stability lobe corresponding to a critical value of bearing span=180mm. It is observed from the lobe diagram that the critical depth of cut is 0.312mm.

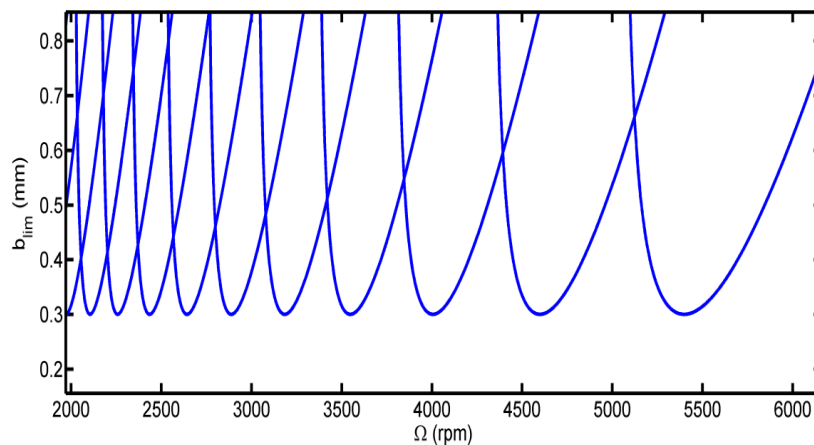


Figure 4.31 Stability lobe diagram at the critical bearing span=180mm

4.4 Cutting dynamics with nonlinear bearing forces

The effects of bearing contact forces supporting the spindle along with the cutting forces at the tool-tip node on overall stability are studied in this section. The solution is obtained as a transient analysis problem first in time domain and then the frequency spectrum is

obtained using fast Fourier transformation (FFT) algorithm. The reduced coupled differential equations were solved by explicit Runge-Kutta solver using MATLAB ode45 function with zero initial conditions. Figure 4.32 shows the time histories and corresponding FFT diagrams at the tool-tip node corresponding to the bearing parameters previously defined in the chapter-3. It is clearly observed from frequency responses that the additional modes due to chatter and tooth passing oscillations are formed apart from spindle resonance modes and ball passing frequencies due to cutting forces and ball contact forces respectively.

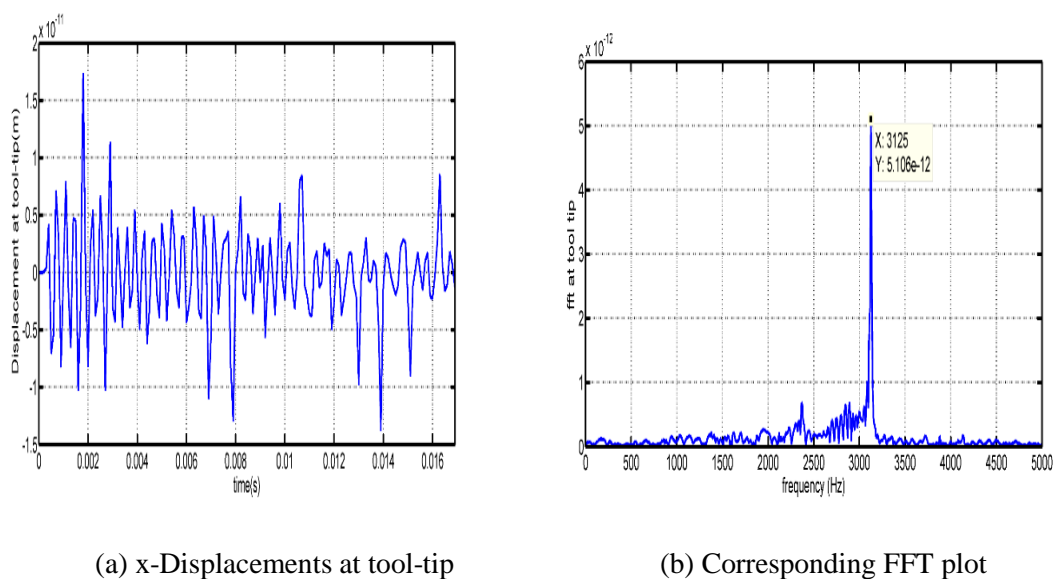
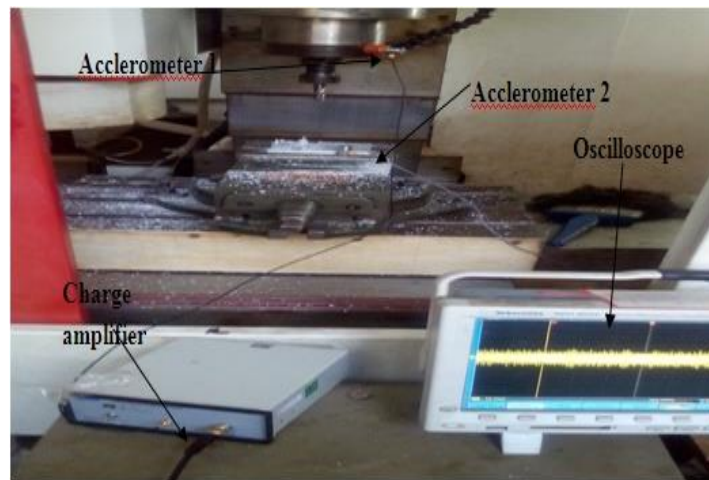
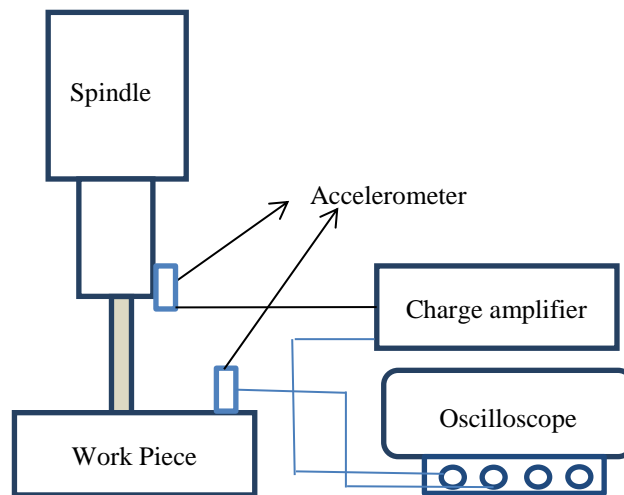


Figure 4.32: Transient response with bearing and cutting forces

In order to ascertain the reliability of dynamic stability of the system, cutting experiments are conducted on CNC milling center. As described earlier, the machine tool has 3-axes with a spindle motor having maximum speed of 4,000 rpm. A HSS end mill cutter with four flutes having 12mm diameter is employed for cutting operation. Down-milling operation is performed on aluminum alloy (Al 6061) work-piece. The output data for analysis of abnormal vibrations during the cutting process at specific speeds, feeds and depths of cut are recorded using a digital oscilloscope (Type: Tektronix-43034), along with two piezoelectric accelerometers and charge amplifier. Figure's 4.33(a) and 4.33 (b) shows the experimental set up and the schematic diagram employed in this regard.



(a) Photograph of the experimental set-up



(b) Schematic view of the experimental set-up

Figure 4.33: Experimental set-up employed

The corresponding FFT plots are shown in Figure 4.34 for an axial depth of cut of 0.5mm, feed of 20mm/min and a spindle speed of 2600 rpm. Using the same cutting parameters analytically FFT is arrived as shown in Figure 4.34(b). It is observed that the multiple peaks are arrived in experimental FFT because of the chatter phenomenon during cutting process as compared to the theoretical frequency response.

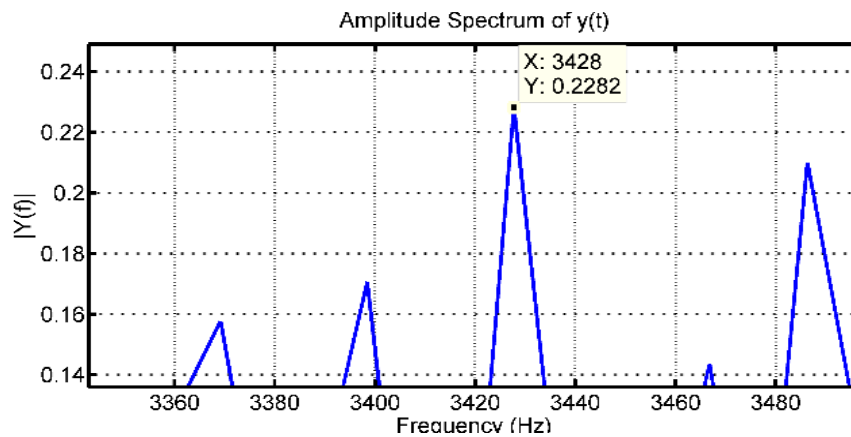
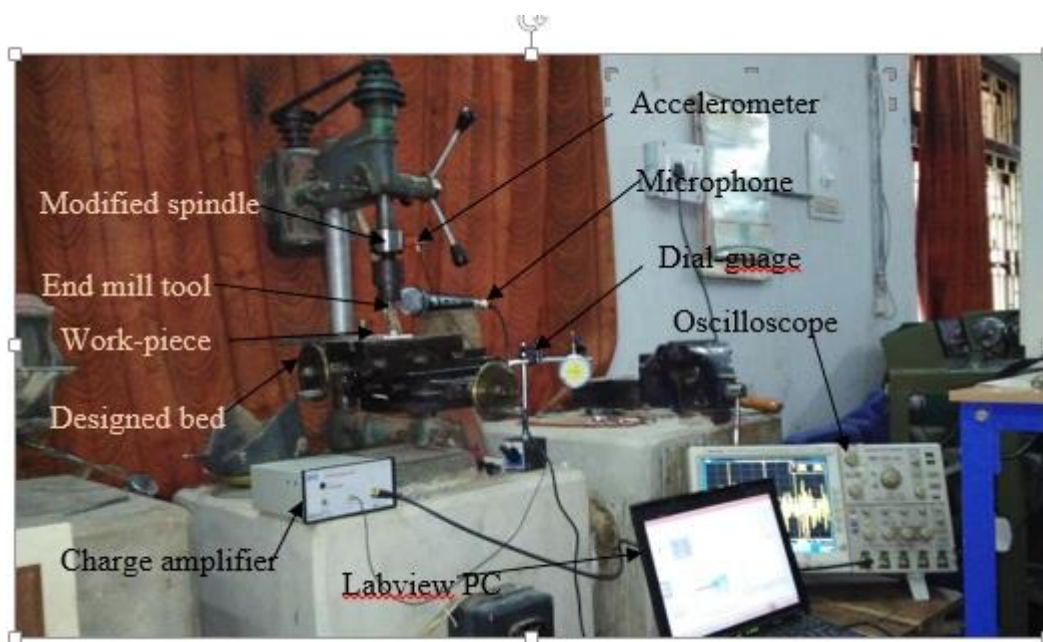


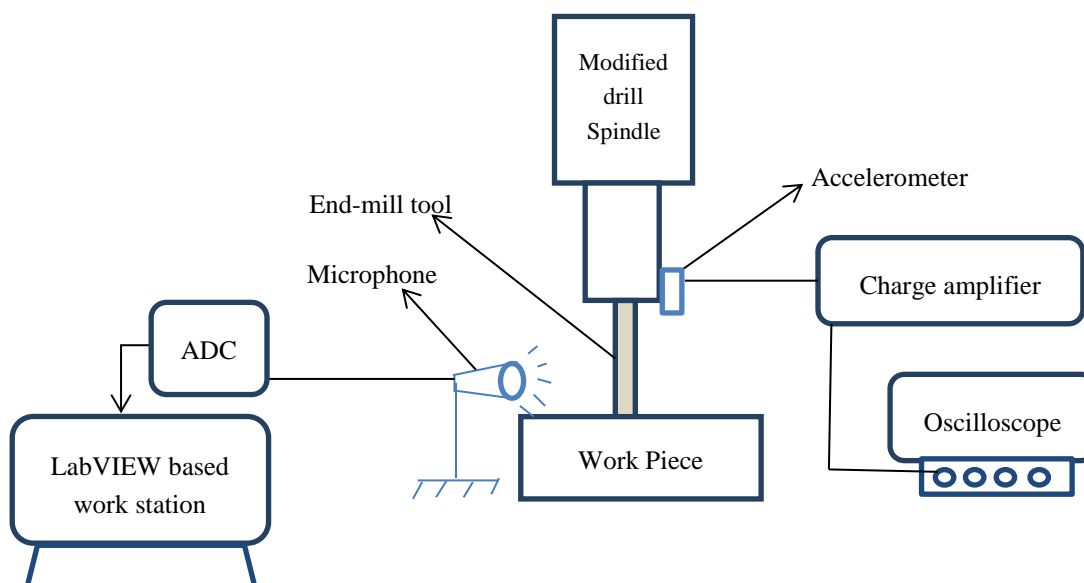
Figure 4.34: Experimental FFT plot

4.5 Stability analysis of a practical drill spindle for milling

The design and analysis procedure of modified drill spindle as described in the chapter-3 has been extended to study the cutting process stability in a slot milling operation. Milling tests are conducted on the manual drilling machine with a designed portable milling work bed with modified spindle according to the specifications. The machine tool has 3-axes with a spindle motor having maximum speed of 1750 rpm. Machining is carried out with a HSS end mill with four cutting edges fitted in the collet has a 12mm diameter. All milling tests are performed on aluminium alloy (Al6061) work pieces of 100mm×8mm×5mm thickness. Figure 4.35 (a) shows the experimental set up for measurement of vibration signals during cutting operation. Similarly, Figure 4.35 (b) shows the schematic diagram of the experimental set-up. The instrumentation employed are (1) 4-channel digital oscilloscope (Tektronix-43034) (2) accelerometer (frequency range 1 Hz to 10 kHz) mounted on the bearing collar of the spindle in radial direction (3) charge amplifier to amplify the signals of accelerometer (4) microphone (frequency range 8 Hz to 12 kHz, sensitivity of $-73\text{dB}\pm 3\text{dB}$) connected with LabVIEW interface (5) Dial-gauge used to measure the depths of cut provided to drilling machine.



(a) Photograph of the experimental set-up



(b) Schematic view of the experimental set-up

Figure 4.35: Experimental set-up employed for the modified drilling machine

During cutting operation, the vibration signals in time-domain are recorded in the oscilloscope at different depths of cut and spindle speeds. Initially an analytical stability lobe diagram is plotted from the frequency responses at the tool tip of modified drill spindle

system in order to approximately know the range of operating speeds and depths of cut. A combination of three speeds and two depths of cut are used in experimental tests. FFT plots are obtained from then time history data from the acclerometer signals. Figure 4.36 represents the time domain and FFT plots at the spindle of 1030 rpm at two axial depths of cut of 0.5mm and 1mm.

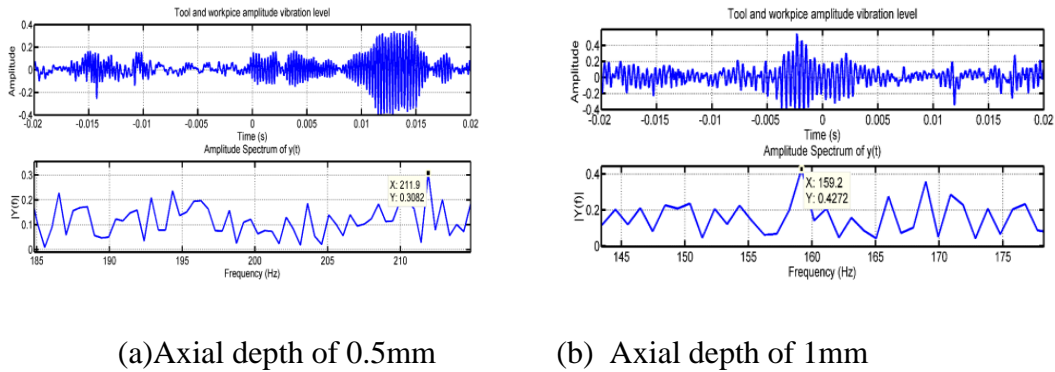


Figure 4.36: Time histories and FFT plots at 1030 rpm

It is observed that, when the depth of cut increases the chatter frequencies are found to be 211.9Hz and 159.2Hz respectively from FFT plots. Similarly, as the spindle speed changes to 1300rpm, Figure 4.37 shows the experimentally acceleration response and its FFT diagrams corresponding to two different depths of cut. At the depth of cut 0.5mm, the amplitude of vibration level grows suddenly which produces the rough chatter marks at the frequency of 125Hz. As the depth of cut increases to 1mm there is almost smooth cutting operation as observed from the time histories.

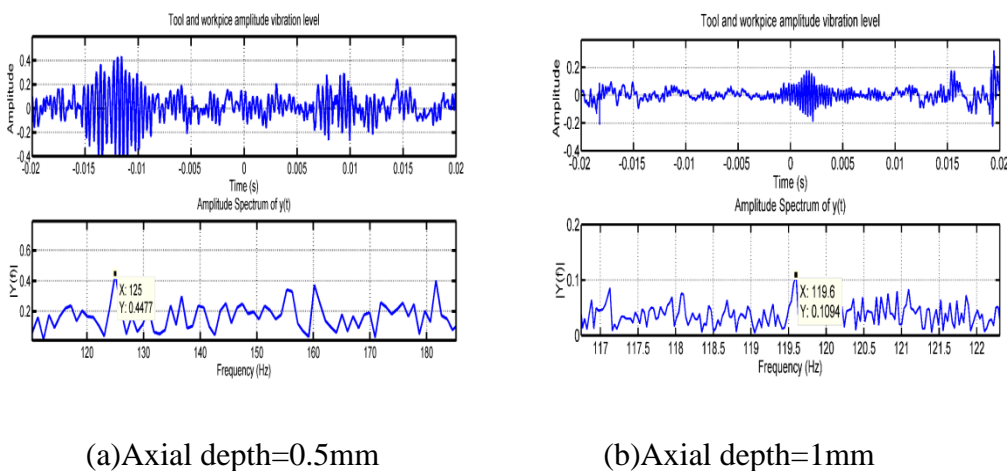


Figure 4.37: Time histories and FFT plots at 1300 rpm

Further, the spindle speed has changed to 1650rpm with same depths of cut of 0.5mm and 1mm respectively as shown in Figure 4.38. The amplitude of the vibration level in time history grows suddenly at the beginning of cut corresponding to the frequency of 68.36Hz in the FFT plot. As the depth of cut increases to 1mm the chatter frequency are observed at a lesser frequency of 35Hz from FFT plot.

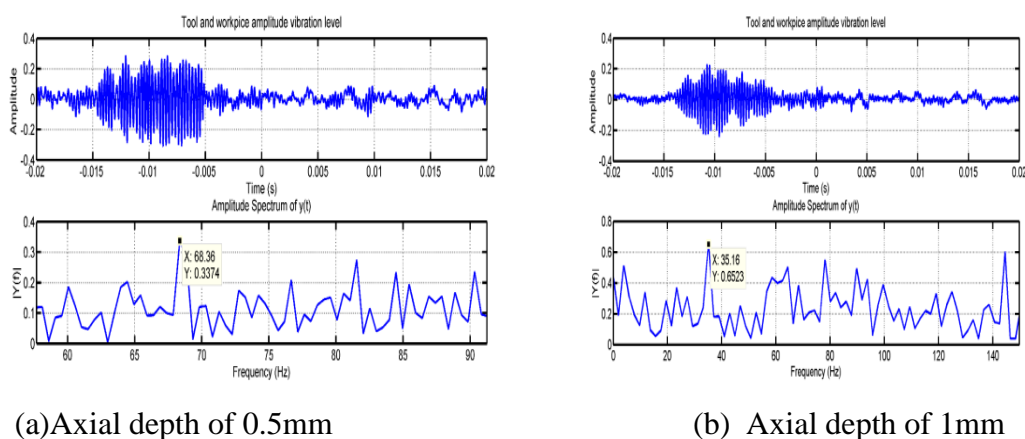


Figure 4.38: Time history and FFT plots at 1650 rpm

4.5.1 Sound spectrum analysis using LabVIEW

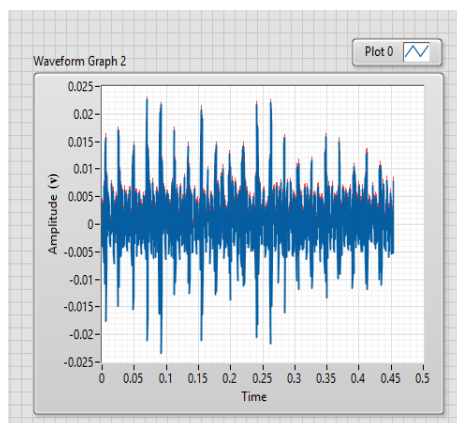
Typically in machine shops and on production floors, chatter can be identified from the noise signals during cutting operations and by using the nature of the chatter marks on the workpiece surface. The periodic impacts of the cutting tooth with the workpiece and the corresponding vibrations levels generate the sound pressures during the machining process. Experienced operators can usually extract information from it and correct or modify the cutting parameters. The sound spectrums are currently elaborated by two simple methods (1) by sampling, through acoustic analyses of sound acquired with microphones or sonometers, which are then power density digitalised or (2) by simulations that simulate the acoustic situation in a certain zone. These spectral measurements are obtained by taking measurements at certain points in the area being evaluated and calculating the rest of the points by interpolation.

In the present work, along with the accelerometer signals, the sound pressure intensity levels are also recorded using a microphone to distinguish unstable cutting conditions from a selected cutting conditions as seen from Figure 4.39. The amplitude of the sound pressure levels are recorded as time domain signals during the cutting operation at different combinations of speed and axial depths of cut and the corresponding power

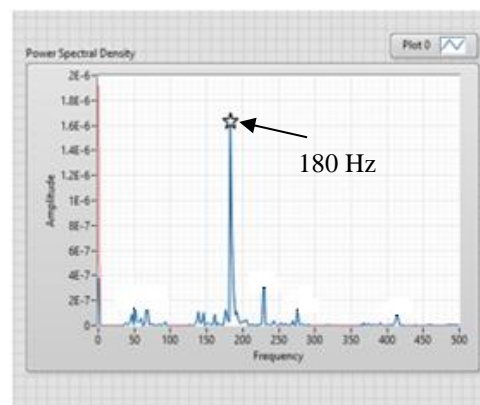
spectral density(PSD) plots are obtained simultaneously using LabVIEW software. From these diagrams, the tooth passing and chatter frequencies are identified.

LabVIEW software was used to develop a data acquisition platform capable of recording the sound emission from the cutting process and collect the data in time domain with a microphone placed inside the machine chamber. The fast fourier transform of the time-based audio signal was calculated on-line to obtain the frequency-domain spectrum of the milling sound signals. The audio signal was displayed on-line on the computer screen in time domain.

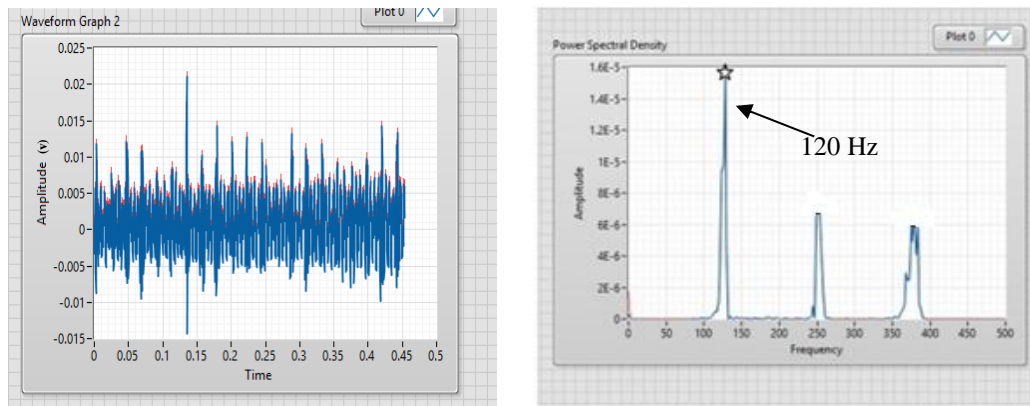
For the full-immersion down milling process considered on the table top modified drilling machine with 12mm diameter end mill tool, the experimental is recorded. Figure 4.39 shows the amplitude of sound signal (in volts) in time domain and the corresponding power spectral density plots corresponding to two depths of cut. Initially the for the axial depth of cuts of 1mm and 2mm for the spindle speed of 1030rpm the PSD contains tool chatter frequencies as shown in Figure 4.39(b) and 4.39(d). It is observed from the plots, the chatter frequency is observed at the frequency of 180Hz for 0.5mm, as the depth of cut increases to 1mm the amplitude of sound signal raised suddenly and the chatter marks are observed on the workpiece at a frequency of 120Hz. It is nearly matching with that obtained from the accelerometer data.



(a) Microphone signal

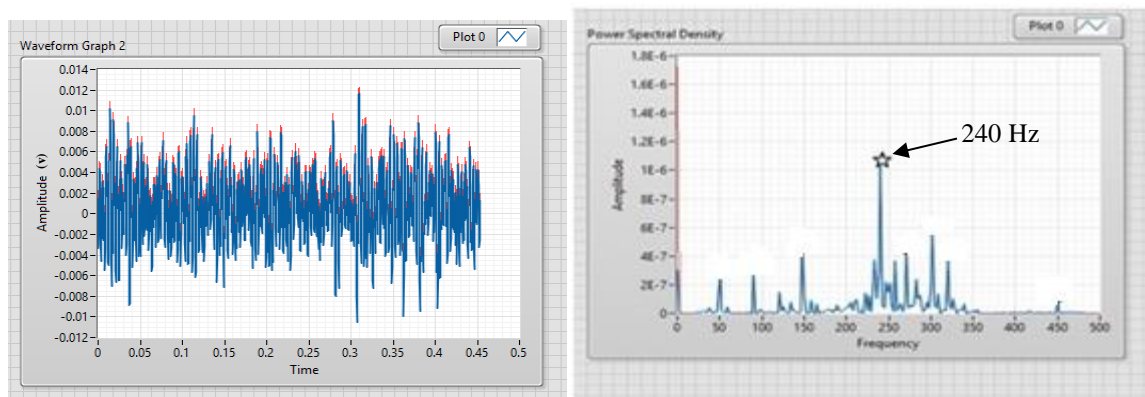


(b) PSD plot at axial depth=0.5mm

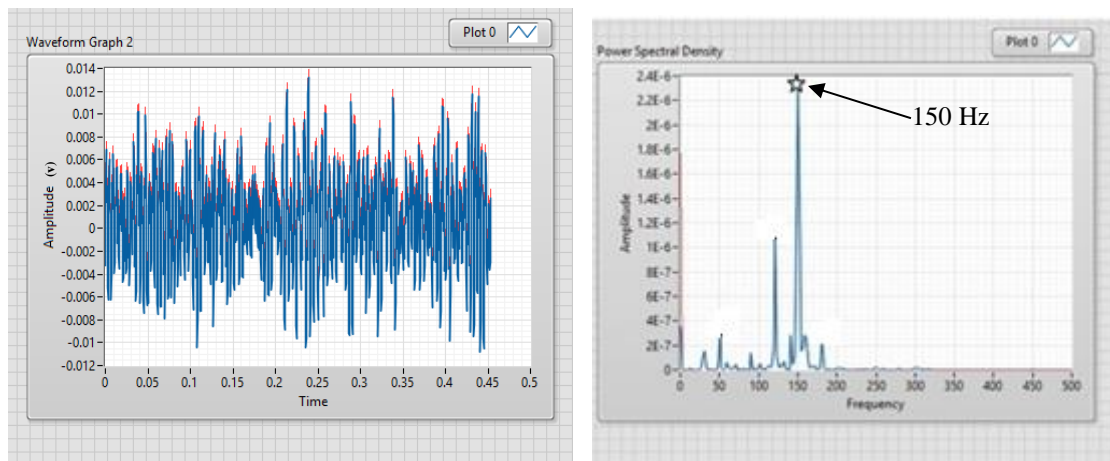


(c) Microphone signal (d) PSD plot at axial depth=1mm
Figure 4.39: Amplitude and FFT plots for different depths of cut at 1030 rpm

Similarly, the cutting tests are carried out at a spindle speed of 1300rpm with the same axial depth of cuts previously taken. It is observed that the cutting sound signals gives the light and sharp signal frequencies nearer to the chatter frequency of 240Hz at a depth of 1mm. Whenever the depth raised to 1mm at the same spindle speed the pattern of the frequencies changed drastically with the amplitude of signals. The chatter frequency hampers the stable cutting process whenever the system reaches the frequency of 150Hz as shown in the Figure 4.40.



(a) Microphone signal (b) PSD plot at axial depth=0.5mm

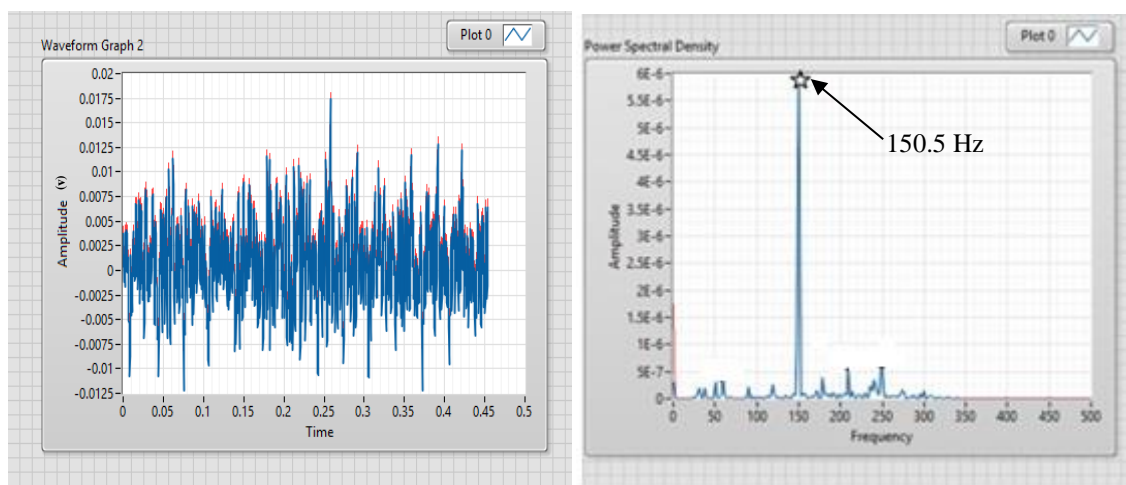


(c) Microphone signal

(d) PSD plot at axial depth=1mm

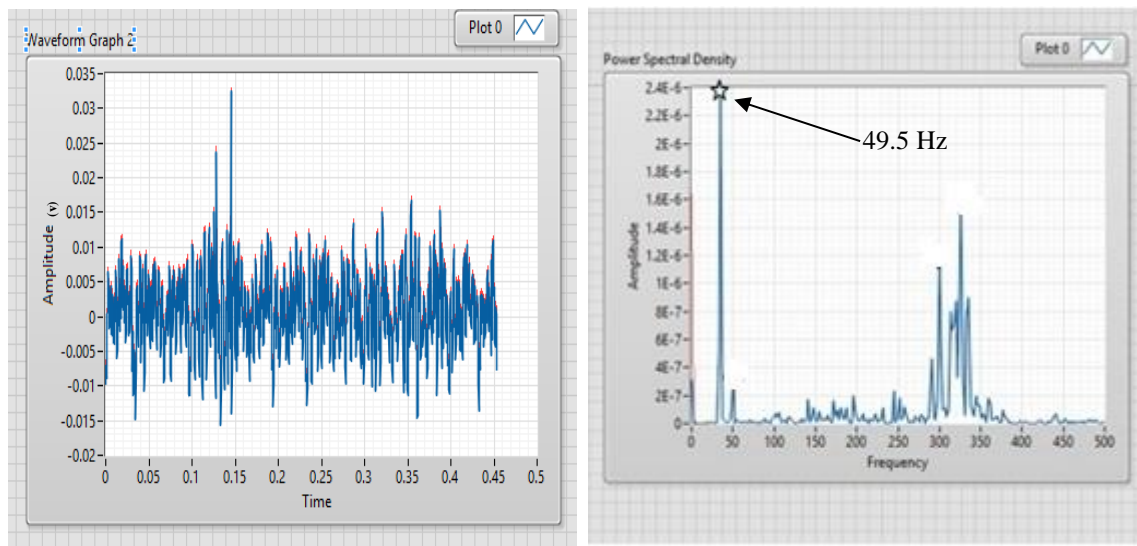
Figure 4.40: Amplitude and FFT plots for different depths of cut at 1300 rpm

Further the cutting process is extended to the spindle speed of 1650rpm. The cutting sound becomes tedious and deep, and low frequency components can be more predominant for the depth of cut 0.5mm. The rise in the depth of cut increases the friction and cutting forces between the cutting tool and work surface which in turn produces the chatter at the start of the cut as shown in the Figure 4. 41.



(a) Microphone signal

(b) PSD plot at axial depth=0.5mm



(c) Microphone signal

(d) PSD plot at axial depth=1mm

Figure 4.41: Amplitude and FFT plots for different depths of cut at 1650 rpm

These time-based audio signals clearly identify the chatter frequencies on-line and to build the proper boundaries of the stability lobe diagram. Milling sound pressure signals analyze the status of the cutting process and it is easy to implement for monitoring. From these data, it is observed that even the chatter frequencies are present in the FFT or PSD diagrams it cannot be concluded that the process is unstable. When the lower chatter frequencies are observed, it may result in cutting process instability. To confirm further, the surface images of the work pieces are examined for chatter marks. The experimentally tested cutting states (as points) are superimposed on the analytical stability lobe diagram obtained earlier. Figure 4.42 shows these points in the lobe diagram and the corresponding work surface images are also illustrated. It is observed from these plots that when the axial depth of cut is 0.5mm there are slight chatter marks on the workpiece. If depth of cut exceeds the limit 1mm, the machining enters into the chatter prone regions. These experimental cutting points are clearly defining the correctness of the boundaries of the analytically predicted stability lobes.

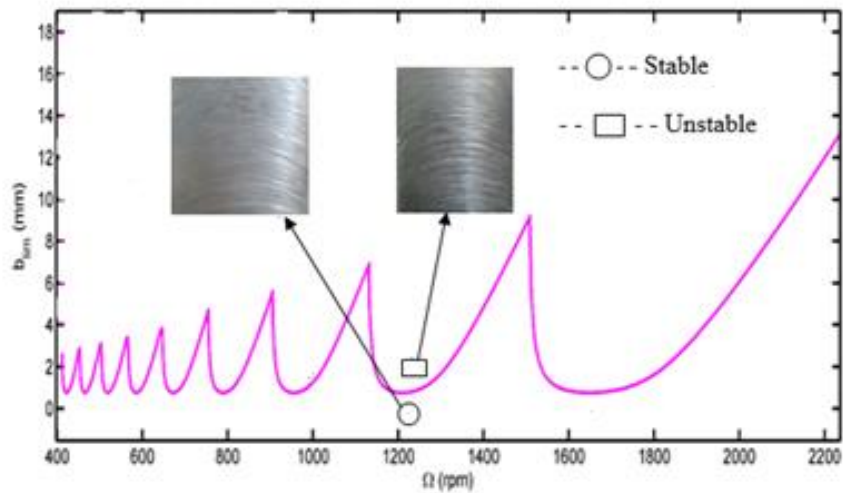
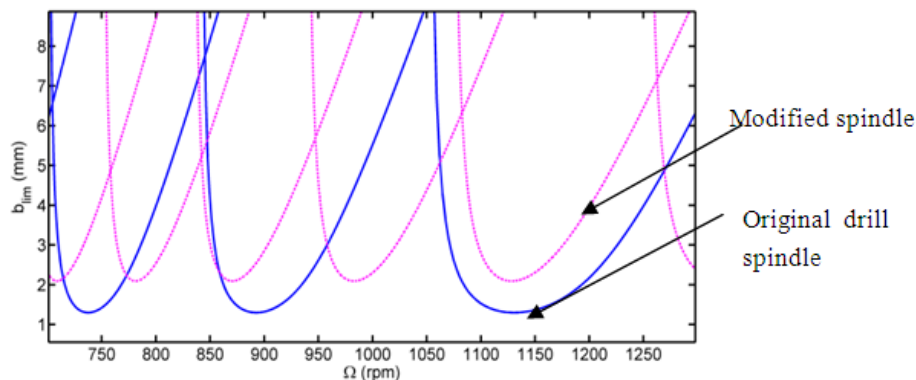


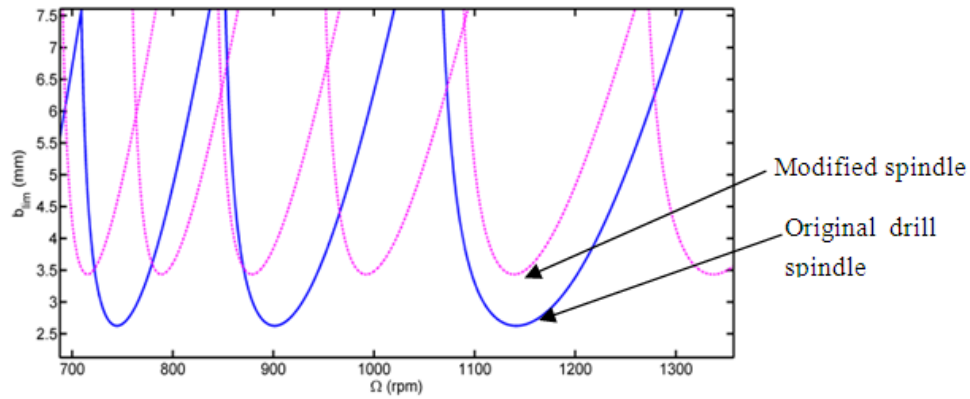
Figure 4.42: Testing of stability boundaries with surface images

4.5.2 Stability charts for modified drill spindle

A study is conducted on the modified and the original drill spindle with the change in the percentage of damping ratios. The directional dynamics are considered as follows: $K_x=K_y=2.1e^7$ N/m, tool diameter=12mm, specific cutting coefficient for aluminium alloy $K_s=750$ N/mm², number of teeth=4. The stability regions are plotted for the down milling process for the slot milling operation. Figure 4.43 shows the analytical stability lobe diagram of modified drill spindle obtained from its tool-tip frequency response using two dimensional cutting model with two different modal damping values. The plots also show the stability lobes for the original single bearing drill spindle system. It is evident that when a slight percentage of enhancements in the damping ratios, the average stable depth of cut drastically increases in both the cases of modified spindle assembly.



(a) $\xi_x=\xi_y=0.02$



$$(b) \xi_x = \xi_y = 0.04$$

Figure 4.43: Stability lobe diagrams for modified spindle

4.6 Conclusions

The development of new spindle designs and their corresponding stability studies provide a guiding technology to reduce the production costs.

- In this chapter, a realistic spindle tool unit of a vertical CNC milling machine is considered for the analysis. Based on the formulation of dynamic milling with regeneration in the chip thickness, the stability lobes are plotted.
- The three dimensional cutting force models were employed to generate the expressions for stable depth of cut and operating speeds during machining operation and these outcomes were compared with those obtained from two-dimensional cutting force model.
- Two practical considerations were taken into account in three dimensional force model such as percentage of immersion and damping to study the stability. Results were found to be very interesting, as the change in damping provides an efficient way in increase the average stable depth of cut.
- Parametric studies were conducted for different cases of bearing span, tool overhang, tool diameter, interface stiffness and axial preload for the spindle system and their influence on the average stable depth of cut has been considered. It was observed that for large bearing span conditions, the second mode of chatter frequencies have the considerable effect on the system dynamics which leads to dynamic instability during cutting conditions.
- In order to obtain the machining stability boundaries, a dynamic milling model is developed by considering the variable pitch effect and permissible run-out effect to

carry out the same chip load for each cutting edge. Furthermore, the non-linear feed forces are studied to identify the allowable permissible limits for the present model.

- In order to ascertain the dynamic stability of the spindle tool unit both the nonlinear bearing forces and the cutting forces were considered at the particular nodes. Later corresponding FFT plots were arrived both from the cutting tests and from the numerical simulations.
- A table top drill spindle model was considered and its improvement for milling applications has been presented. In order to use the drilling machine for milling operations, a portable *X-Y* table was fabricated as per the existing dimensions of the base to ensure a smooth cutting operation.
- The modular computer programs developed in this part facilitate in considering more number of geometric parameters of the spindle-tool system to minimize the chatter vibrations with an accurate picture of cutting stability.

Chapter-5

Control strategies in end milling process

Several aspects of the current trends in production intensify mechanical vibration problems coming from the interaction between the manufacturing process and the machine tool structure. In particular, the dynamical loads generated by the process tend to increase so as to fulfill the demand for productivity. At the same time, the efficiency requirements lead to the production of high rigidity machine tools with low energy consumption. This implies the use of lightweight structures and an explanation of the moving parts inducing low damping properties and thus low dynamical stiffness. Also, the development of novel materials requiring extreme machining conditions as well as the rising complexity of tool or workpiece geometries contribute to the propensity of vibrations to occur. On the other hand, the demand for an increasing accuracy makes such vibration problems in machine tools less tolerable.

Under severe machining conditions, mainly two types of detrimental structural vibrations are susceptible to arise between the tool and the workpiece. These two types are the resonances and the instabilities. Generally, the instabilities, commonly called: chatter, are more critical for the production than resonances, due to the fact that much more energy is induced by the closed-loop interactions formed between the machine and the process. Apart from these, various phenomena may lead to the process instabilities.

In general the occurrence of chatter increases the production costs and it minimizes the productivity. An intuitive way to suppress chatter is to reduce the process load by decreasing the material removal rate and thus the productivity. Active structural control techniques probably present the greatest potential of development. They are characterized by the use of a sensing system delivering information to a controller. Based on a pre-defined control strategy, this controller transmits instructions to an actuating system in order to mitigate the detected vibrations. The main attractiveness of these methods comes from their high degree of adaptivity due to the fact that the controller can be easily reprogrammed. This constitutes a key aspect in modern manufacturing techniques, as a great amount of production costs can be saved using one flexible machine tool instead of several specialized ones. The latest developments in computer technology and numerical simulation techniques will always be more attractive for industrial applications.

This chapter presents the chatter control concept using the semi active and active techniques using the previously analyzed spindle-tool system and the cutting conditions in usual operating ranges.

5.1 Methods for Chatter Mitigation

As the chatter is result of interaction between the cutting conditions and structural dynamics characteristics of spindle-tool system, there exist two methods of chatter mitigation. In the first type of methods, cutting conditions are adjusted, while in the second type the structural dynamic characteristics of the system are modified. The methods based on the process parameters, take advantage of the stability lobes pattern by finding the maxima of stability. In this category, two subdivisions can be identified: offline and on-line methods. The offline or passive methods select suitable machining parameters, i.e. spindle speed and depths of cut, based on the predicted stability lobes diagrams. The on-line or active methods monitor the process and as soon as chatter is detected, the process parameters are adjusted in order to stabilize the cut. So, they need the integration in the machine environment of a monitoring system transmitting information to a decision making device providing new set of machining conditions.

In this approach of process parameter adjustment, there are some limitations with respect to machining operations such as the spindle speed and depth of cut cannot be varied to maintain stable cutting zone [168]. This may halt the cutting process. Also, all required ranges of natural frequencies cannot be achieved due to response limitations of the spindle.

On the other hand, by adjusting the dynamic characteristics of spindle-tool system either passively, actively or semi-actively, the stability of cutting operations can be maintained comfortably. In passive method of chatter mitigation, often (a) dynamic rigidity of spindle-tool system is increased or (b) geometric shape of the cutter can be changed or (c) the vibration absorbers are inserted or (d) dynamic or impact dampers may be used.

In general, high dynamic stiffness and high damping are desirable in avoiding chatter. This is intuitive because a very stiff tool is not free to vibrate and damping removes energy from vibrations, including chatter vibrations. Unfortunately, stiffness and damping are restricted to physically realizable levels. There is no such thing as a perfectly rigid spindle. As technology continues to advance, machining speeds are getting faster, workpiece materials are getting harder, and part geometries are getting more intricate. This makes difficult to increase the dynamic stiffness and damping. The passive systems are simple, but have no intelligence and flexibility which leads to non-optimized performance for various machining conditions.

In the active methods, the vibration is minimized by continuously applying force on the system by using piezoelectric actuators and active dynamic absorbers. The approach is expensive and requires high power sources. The third category is known as semi-active control offering simple and low cost effective adaptable way of vibration reduction. Figure 5.1 represents the proposed classification of the methods dedicated to the mitigation of chatter.

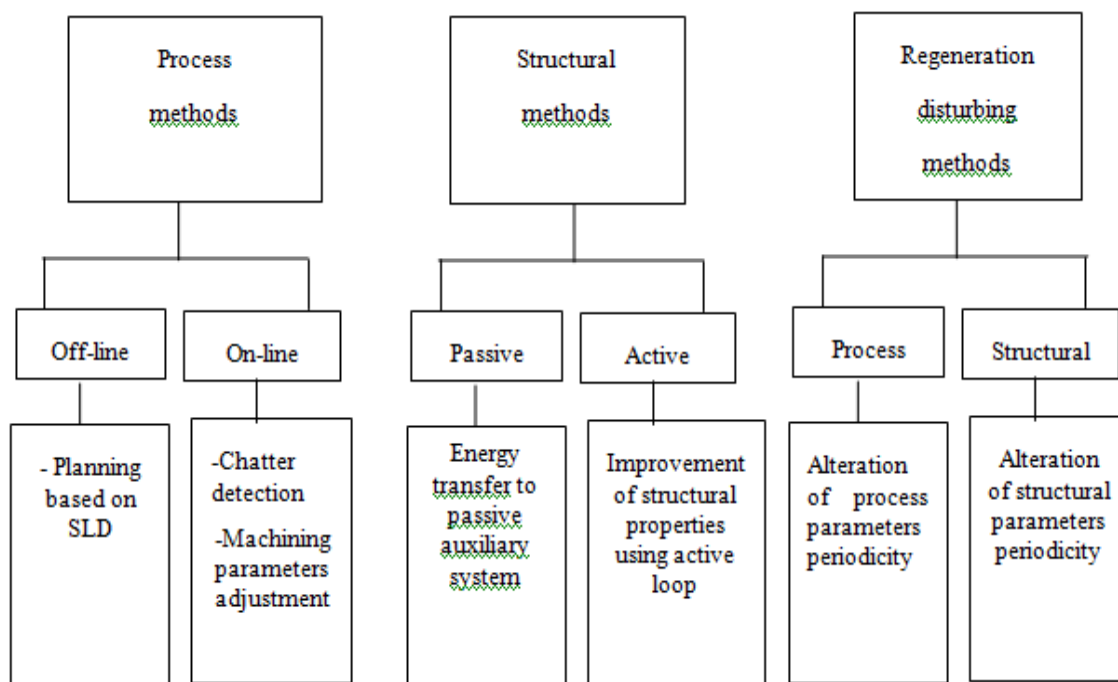


Figure 5.1: Classification of the methods for chatter mitigation

In the above figure, the third category of methods tries to disturb the periodicity of feedback loop between the machine structure and the process. These methods are called regenerative disturbing methods. Among, them a distinction can be made between those employing parameters related to the process and those using structural parameters.

5.2 Semi-active control using secondary system

In machining operations self-excited vibrations or chatter is the most important type of vibration. The machine tool chatter is due to regeneration phenomenon or by mode-coupling. Regenerative type is most common and the phase difference between the inner and outer waves and dynamic gain of the system play an important role in the stability of cutting process. For the chatter suppression in milling process, use of tunable vibration absorbers is quite common. In the present work, the cutting tool and work piece are modeled as flexible and rigid parts respectively.

Figure 5.2(a) shows the spindle-tool system employed earlier with secondary spring mass damper model connected at one of the nodes along the two bending directions. The dynamic behavior of the spindle-tool unit is well established through the modeling of the restricted spindle rotating system on the front and rear bearings.

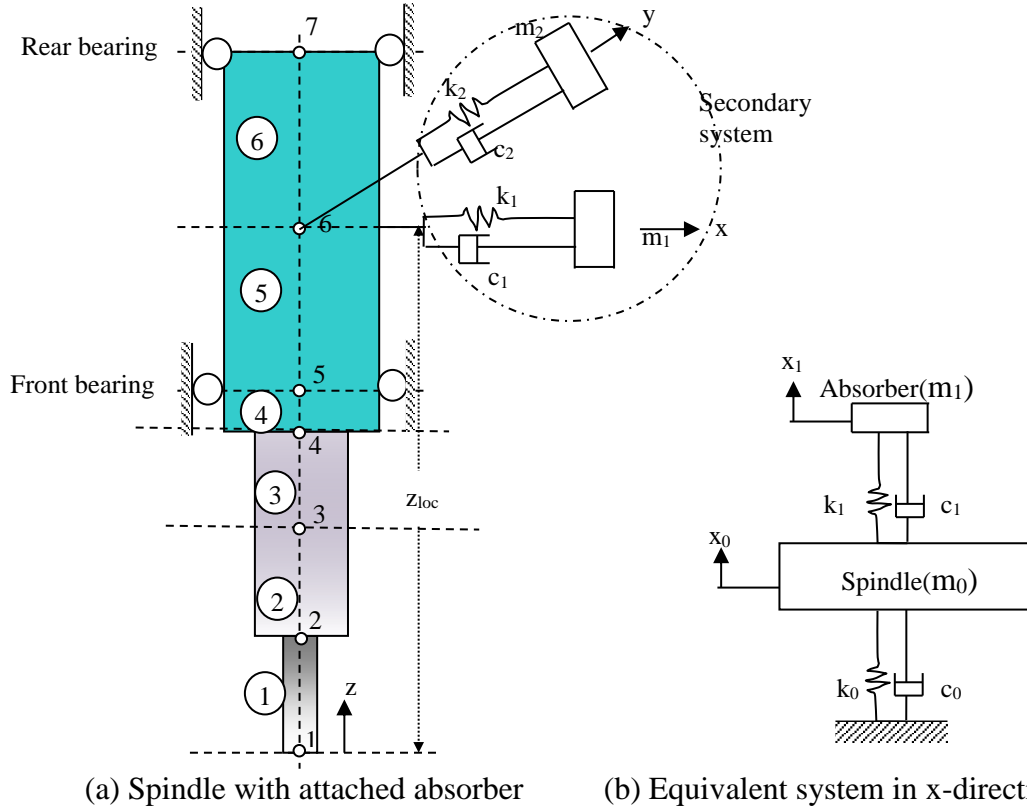


Figure 5.2: Finite element discretization of spindle-tool system with vibration absorber

The two-dof system investigated in this work is depicted in Figure 5.2(b). The movement of the primary spindle system mass (m_0) and the vibration absorber masses (m_1 and m_2) relative to the ground due to a force $P(t)$ acting on the primary mass are represented by $x_0(t)$ and $y_0(t)$. The primary mass is connected to ground by a spring with stiffness k_0 and a viscous damper with constant c_0 . The absorber masses in two bending directions are connected to the primary mass by springs having stiffness (k_1 and k_2) and viscous dampers with constants (c_1 and c_2). The equations of motion in two bending directions are given as [167]

$$m_0 \ddot{x}_0 + c_0 \dot{x}_0 + c_1 (\dot{x}_0 - \dot{x}_1) + k_0 x_0 + k_1 (x_0 - x_1) = P(t) \quad (5.1)$$

$$m_1 \ddot{x}_1 + c_1 (\dot{x}_1 - \dot{x}_0) + k_1 (x_1 - x_0) = 0 \quad (5.2)$$

$$m_0 \ddot{y}_0 + c_0 \dot{y}_0 + c_2 (\dot{y}_0 - \dot{y}_1) + k_0 y_0 + k_2 (y_0 - y_1) = P(t) \quad (5.3)$$

$$m_2 \ddot{y}_1 + c_2 (\dot{y}_1 - \dot{y}_0) + k_2 (y_1 - y_0) = 0 \quad (5.4)$$

The solution for the displacement vector in the frequency domain can be written as

$$x=[H(\omega)]P \quad (5.5)$$

where $[H(\omega)]$ is the frequency response function matrix and is given by

$$[H(\omega)]=(-\omega^2[M]+i\omega[C]+[K])^{-1} \quad (5.6)$$

In the present analysis, spindle-tool system is analyzed as a continuous system discretized into six beam elements with each node having two translations and two rotational degrees of freedom. Two sets of spring mass and damper systems are attached in x and y directions to the spindle at suitable location. The boundary conditions of the spindle-tool system are therefore include

- (1) Forces at the bearing nodes in two bending directions
- (2) The secondary system (absorber) forces at the connected node

The time varying cutting forces are not accounted in this design.

A computer program is developed in MATLAB to analyze the spindle-tool system with vibration absorber. The spindle speed is set at 4000rpm. The coefficients of Rayleigh's damping α and β are obtained as 17.32 and $3.67e-6$ respectively for 1% damping ratio. The stiffness behavior of angular contact bearings relies on the applied loads and the bearing layout. The system is simulated with the following parameters: Diameter of the ball (D_b)=9mm, Axial preload applied (F_a)=1500N, Angular contact of the ball-bearing(θ)=25degrees, Number of balls (N_b) =20. The frequency response at the tool-tip are studied for the following absorber parameters: mass of the damper $m_1=m_2=1$ Kg, absorber stiffness $k_1=k_2=1.5 \times 10^5$ N/m, absorber damper values $c_1=c_2=1.5$ N-s/m.

Figure 5.3 shows the effect of vibration damper on the tool tip FRF. It is seen that absorber affects considerably the amplitude of the vibration and there are two close peaks in the resultant FRF. The FRF simulation results show that the magnitude of maximum amplitude is dropped from $3.2e-5$ m/N to $1.4e-5$ m/N, which is 55.9 percent drop and natural frequency dropped from 2056Hz to 1995Hz with the utilization of the spring damper absorber model.

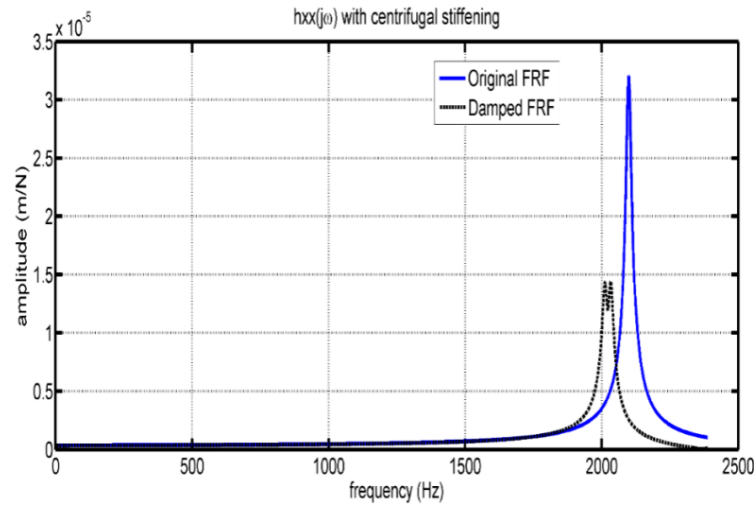


Figure 5.3: Tool tip FRF of the spindle-tool unit

To obtain the stability lobe diagrams, the equivalent modal properties obtained from dynamic analysis namely the modal stiffness and natural frequencies are taken as $K_{xx}=K_{yy}=2.1 \times 10^8$ N/m, $\omega_x=\omega_y=2056$ Hz, and modal damping ratios $\zeta_x=\zeta_y=0.01$. The other parameters are tool diameter=12mm, average specific cutting pressure (corresponding to Aluminum alloy) $K_s=750$ N/mm², the number of teeth (N_t) = 4. The stability regions are plotted for the slot-milling process as shown in Figure 5.4. This is arrived by using frequency response data at tool-tip obtained from the finite element analysis. It is observed that stable depth of cut is improved from to 0.15mm to 0.48 mm for the spindle-tool system embedded with semi-active damper. Semi-active control strategy used for this model is very efficient in reducing the amplitudes of tool-tip frequency responses with good computational accuracy.

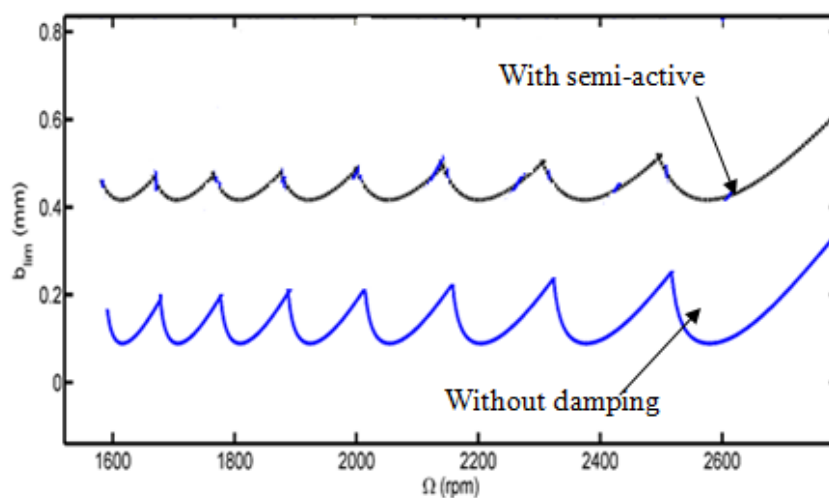


Figure 5.4: Stability lobe plots with and without absorber

However, there are many alternative locations of absorber placement as well as their parametric selection which would give much better improvement in the stable depth of cut. Therefore, it is attempted as a next part.

Optimum absorber parameters

The locations of absorber placement as well as the values of the stiffness and damping values are optimized to minimize the amplitude in the tool-tip frequency response. The problem is formulated as follows.

$$\text{Minimize } f(X) = H_{max}(i\omega) \quad (5.7a)$$

Subjected to the variable constants

$$1.5 \times 10^4 \leq k_{1,2} \leq 1.5 \times 10^6 \text{ N/m} \quad (5.7b)$$

$$1.2 \leq c_{1,2} \leq 1.6 \text{ N-s/m} \quad (5.7c)$$

$$116 \leq z_{loc} \leq 248 \text{ mm (within spindle length)} \quad (5.7d)$$

Here, $X = [k_{1,2}, c_{1,2}, z_{loc}]$ is the design vector to be estimated. Physically the spring-damper model can be realized as a plate mass attached to the primary spindle tool system. Particle swarm optimisation (PSO) approach is implemented to solve the problem. The objective function is the amplitude of tool-tip frequency response that is defined by making use of the finite element model of spindle-tool system with tuned spring-damper system which takes the various inputs such as stiffness and damping constants along with the location of absorber interactively. In the present case, the absorber parameters in both the directions are taken as same. i.e., $k_1 = k_2$ and $c_1 = c_2$.

PSO is basically developed through simulation of bird flocking in n-dimension space. The position of each particle is represented random vector and also the velocity is represented similarly. Modification of the particle position is realized by the position and velocity information. From an initial position, a swarm of particles starts flying in the search space exploring optimal points. Each particle position represents a potential solution. Therefore, the performance of each particle position is evaluated by the fitness function which is to be maximized always. During the flight (iterations), the best experiences (positions) for each particle is stored in its memory and called personal best (P_{best}). The lowest value of all the P_{bests} , determines the global best (G_{best}) of the swarm. Each particle tries to modify its position using the following information: (a) the current positions $X = (x_1, x_2, \dots, x_n)$ (b) the current velocities $V = (v_1, v_2, \dots, v_n)$ (c) the distance between the current position (P_{best} and G_{best}). This modification can be represented by the concept of velocity and it is updated or modified (for each particle) as follows [152]:

$$V_i^{t+1} = WV_i^t + C_1 r_1 (X_i^{Pbest} - X_i^t) + C_2 r_2 (X^{Gbest} - X_i^t) \quad (5.8)$$

where V_i^{t+1} is the particle velocity at new iteration ($t + 1$), W is inertia weight, C_1 , C_2 are the acceleration coefficients called cognitive and social factors, t is the generation, (r_1, r_2) are two separate random numbers between 0 and 1, X_i^{Pbest} is the P_{best} of the particle i (local best position) and X^{Gbest} is the G_{best} of the group (global best position).

Therefore, the new particle position is obtained by:

$$X_i^{t+i} = X_i^t + V_i^{t+i} \quad (5.9)$$

Figure 5.5 shows the general flowchart of PSO strategy.

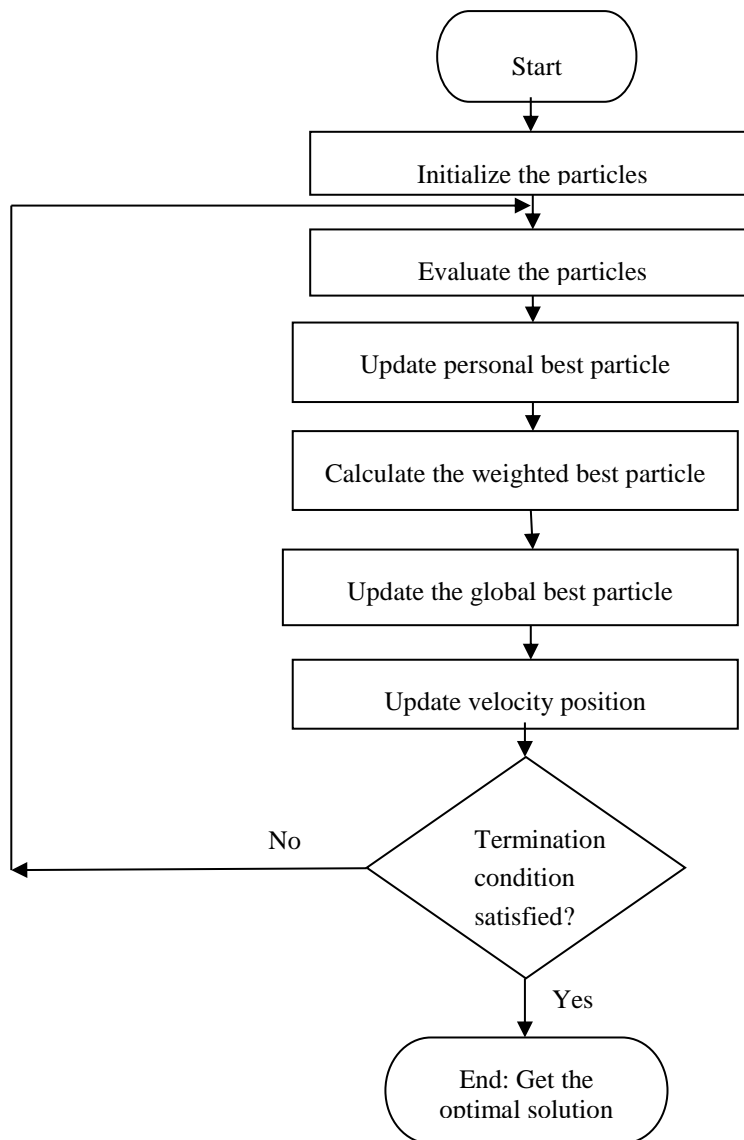


Figure 5.5: Flowchart of PSO algorithm

A MATLAB program is developed for this three variable optimization scheme. The termination criterion employed is the number of generations which is considered as 500. Swarm size in each generation is varied and a size of 30 is found to be optimal. Figure 5.6 shows the convergence trend of the fitness function which in present case is $F=1/(1+f(X))$.

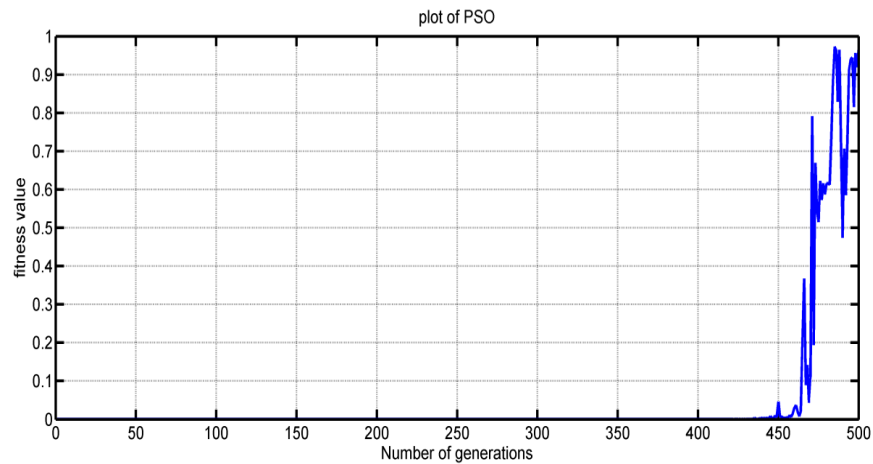


Figure 5.6: Convergence trend corresponding to population size=30

The final best optimized design variables are obtained as $k_1 = k_2 = 194812.965 \text{ N/m}$; $c_1 = c_2 = 1.296 \text{ N-s/m}$; $z_{loc} = 128.875 \text{ mm}$. Figure 5.7 shows the tool-tip frequency response for the system with optimized damper parameters in comparison to the system before optimization. This time, the natural frequencies of the spindle-tool system increase to 2291 Hz and 2315 Hz respectively. The amplitude has reduced from $1.433 \times 10^{-5} \text{ m/N}$ to $1.048 \times 10^{-5} \text{ m/N}$ in comparison with the system attached to unoptimized absorber.

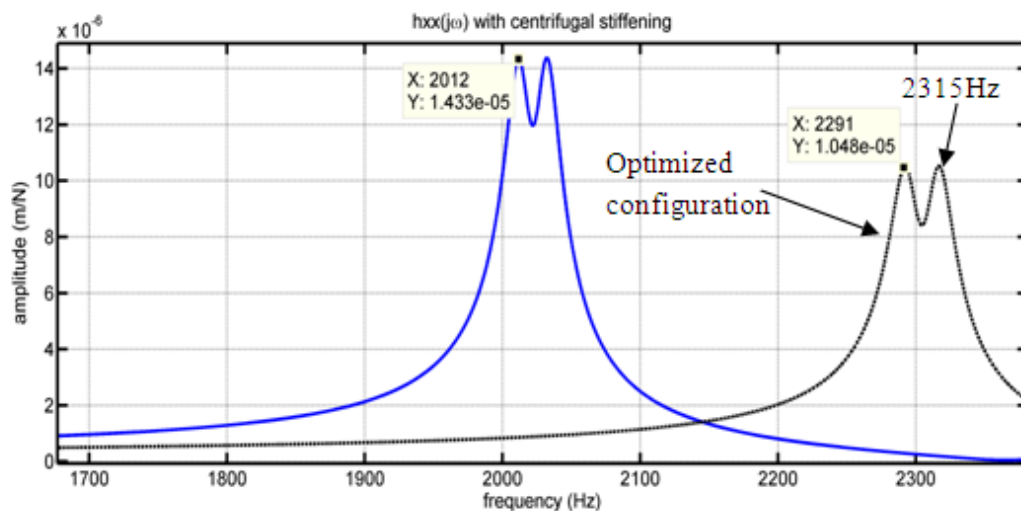


Figure 5.7: Tool tip FRF with optimal vibration absorber parameters

Figure 5.8 shows the corresponding stability lobe diagram of spindle tool system during the up milling process with optimized vibration absorber parameters. It is observed that a stable depth of cut of 0.532 mm has been achieved with improved tool-tip frequency response, which was previously 0.152mm before insertion of the optimized absorber.

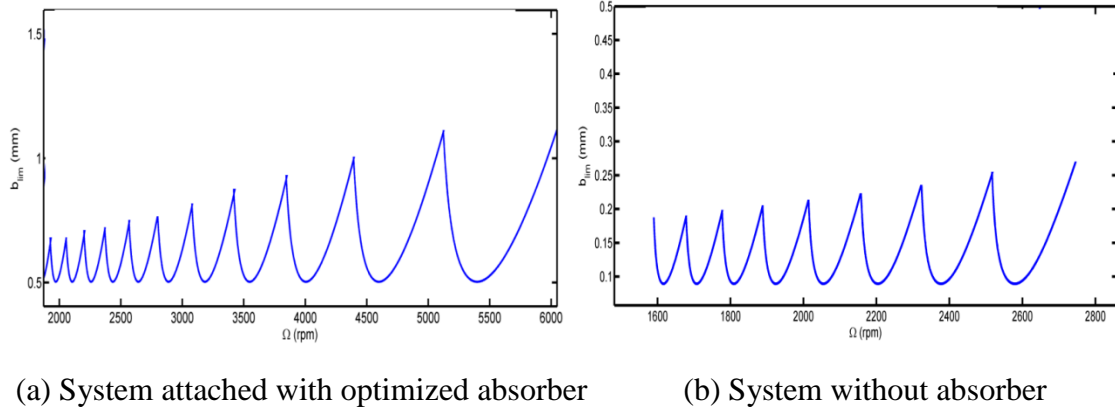


Figure 5.8: Stability lobe diagrams from tool-tip FRF

In above design, the cutting force influences are not considered and also the amplitude in tool-tip FRF reduces only around the first mode. A more realistic control scheme is therefore required.

5.3 Active vibration control

In-process detection of chatter is a quite complex phenomenon. Vibration control is another strategy to suppress chatter instability. The aim of this strategy is to reduce the relative displacements between the tool and the workpiece and thus to suppress chatter. The two DOF model of a milling process is described by

$$[M]\ddot{X}(t) + [C]\dot{X}(t) + [K]X(t) = bH(t)[X(t - \tau) - X(t)] + U(t) \quad (5.10)$$

Here, b is the depth of cut and the first term on the right hand side represents the dynamic cutting force with $H(t)$ representing the cutting force variation matrix. Also $U(t)$ represents the control force. When depth of cut is large, the system becomes unstable and the perturbation $X(t)$ increases resulting in chattering behaviour. By adding an active control $U(t)$ to the perturbation system, the closed loop becomes stable for higher depths of cut. There are different adaptive control optimization methods, where the process parameters are computed and regulated in order to optimize certain index of performance like reduction of vibration, increasing productivity, improvement of surface quality and control of tool wear. Alternatively, without directly changing the process parameters, by employing certain controls which could provide the required force $U(t)$ we can minimize the amplitudes of vibration at the contact region.

Design of PID controller

PID-based control is the major design method in the automatic control industry. These controllers are extensively used in robotics industries, electrical system units, aircrafts, machining industries etc. These methods are popularized because of their robustness in an extensive variety of operational forms, and their structure, in addition to the awareness for designers and machinists with the PID algorithms.

A PID controller is actually a three part system:

(1) Proportional compensation: the main function of the proportional compensator is to introduce a gain (K_P) that is proportional to the error reading which is produced by comparing the systems output and input. (2) Derivative compensation: in a unitary feedback system, the derivative compensator will introduce the derivative of the error signal multiplied by a gain K_D . In other words, the slope of the error signal's waveform is what will introduce to the output. Its main purpose is that of improving the transient response of the overall closed-loop system. (3) Integral compensation: in a unitary feedback system, the integral compensator will introduce the integral of the error signal multiplied by a gain K_I . This means that the area under the error signal's curve will be affecting the output signal. It improves the steady-state error of overall closed-loop system.

Active control system needs information of minimum two basic components of a system: (1) the plant (G), which defines the mathematically modeled behavior of the system, and (2) the output(Y), which is the objective trying to approach. First analyse the components and behavior of a system (uncompensated) and then the individual components of a PID (proportional-integral-derivative) controller. The final step would be to bring these two together and design a PID controller that will compensate the originally observed system [157]. A system can be made up of various components arranged equally in various ways; but it is better to analyse the components and their functionality as a classical closed-loop system shown in Figure 5.9.

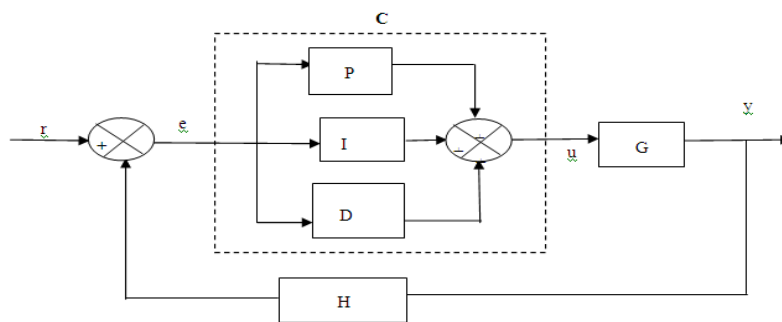


Figure 5.9: Block diagram of a single-input single-output system closed loop system

Here r is input, C is controller, G is plant and is mathematically expressed as a transfer function, y is output, and H is feedback. It is important to note that the transfer function for the complete loop, which could be further simplified into just one block with a single input and single output by the use of the closed loop transfer function

$$C(s) = \frac{G(s)}{1 + C(s) - G(s)H(s)} \tag{5.11}$$

Therefore, a PID controller can be mathematically described in two domains

In time domain the control signal is represented as

$$U(t) = K_p e(t) + K_D \frac{d}{dt} e(t) + K_I \int_0^t e(x) dx \tag{5.12}$$

Here, the tracking error is represented by the variable (e) and the variation among the preferred input (r) and output (y). In particular, the concerned error signal (e) drive, be directed to the controller, which calculates the integral and derivative of the signal.

The error signal will be transferred to the mathematically derived transfer function (G) which produces a new output (y). This output will be processed to the feed-back (H) which again produces the new signal (e) which further proceeds to compute the new derivatives and integral values and the process will continue.

Most of the time, in active control, PD controller is sufficient to improve the transient response while maintaining the stability of the process. This eliminates the steady-state error and compensates for the system nonlinearity (or uncertainty). The control scheme with PD controller is shown in Figure 5.10. The error and its rate are adopted as the two input variables in the system.

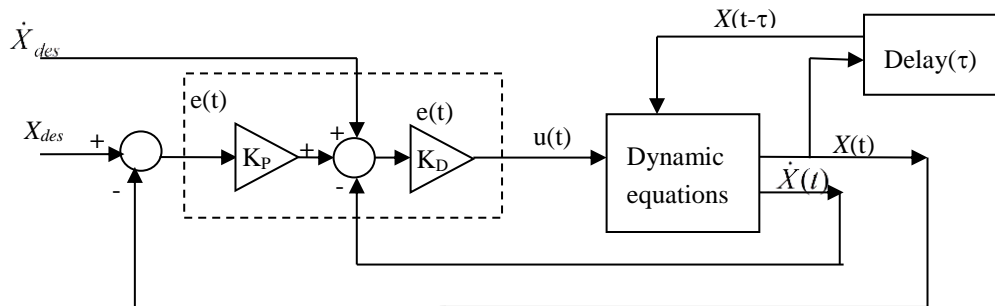


Figure 5.10: Block diagram of control scheme

The error (e) is expressed as deviation of the measured displacement ($X(t)$) from the reference force (X_{des}):

The total regenerative cutting force of the milling dynamics as described previously in the two dimensional cutting force model in chapter-4 are considered for analysis. A considerable reduction in the vibration levels has occurred at $K_P=380$ and $K_D = 2\sqrt{K_P} = 39$ in both x and y directions as shown in Figure 5.12.

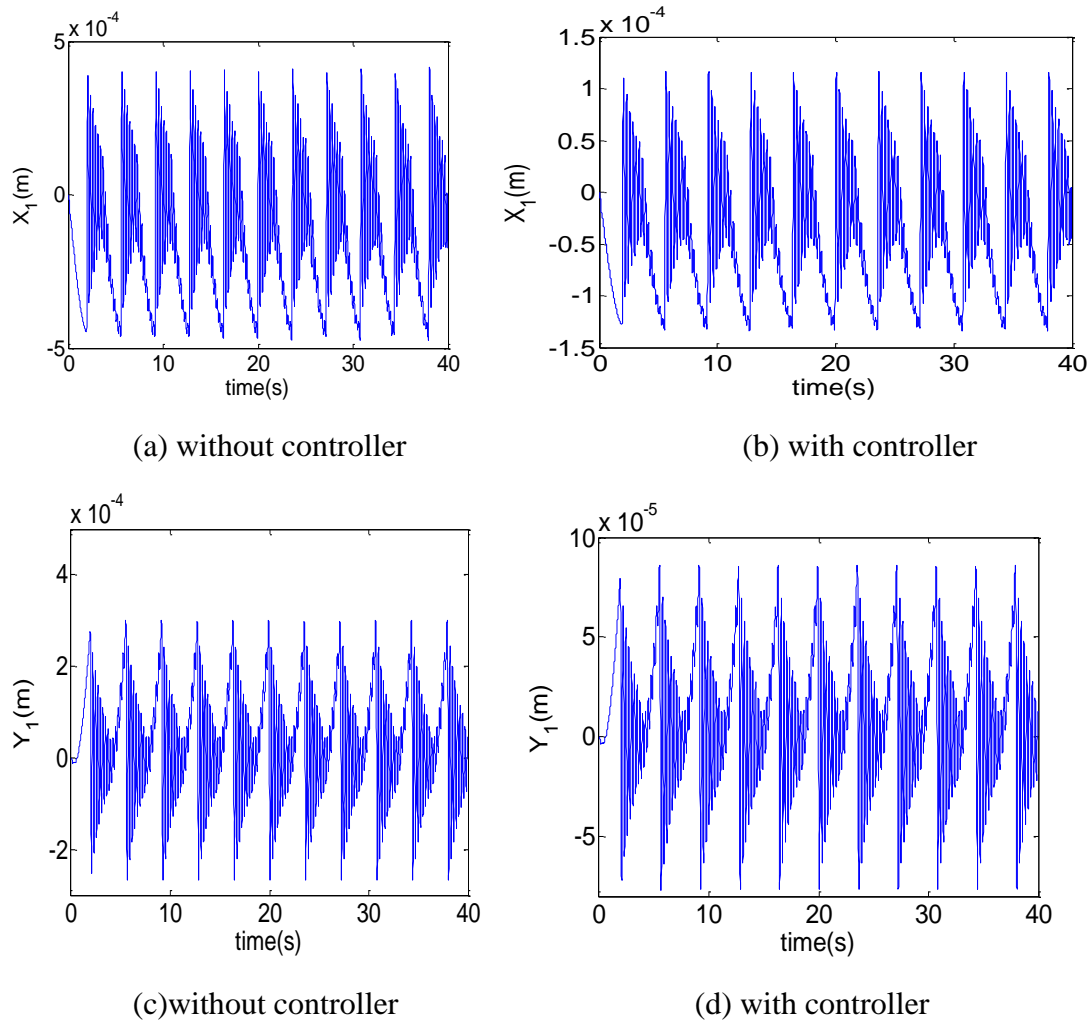


Figure 5.12: Tool tip vibration levels at a depth of 1mm

Similarly, Figure 5.13 shows the corresponding vibration levels obtained for a depth of cut 3mm at the same spindle speed. It is observed that the amplitude of displacement levels is increased when the depth of cut increases. As the controller is applied the vibration levels are reduced in both the directions.

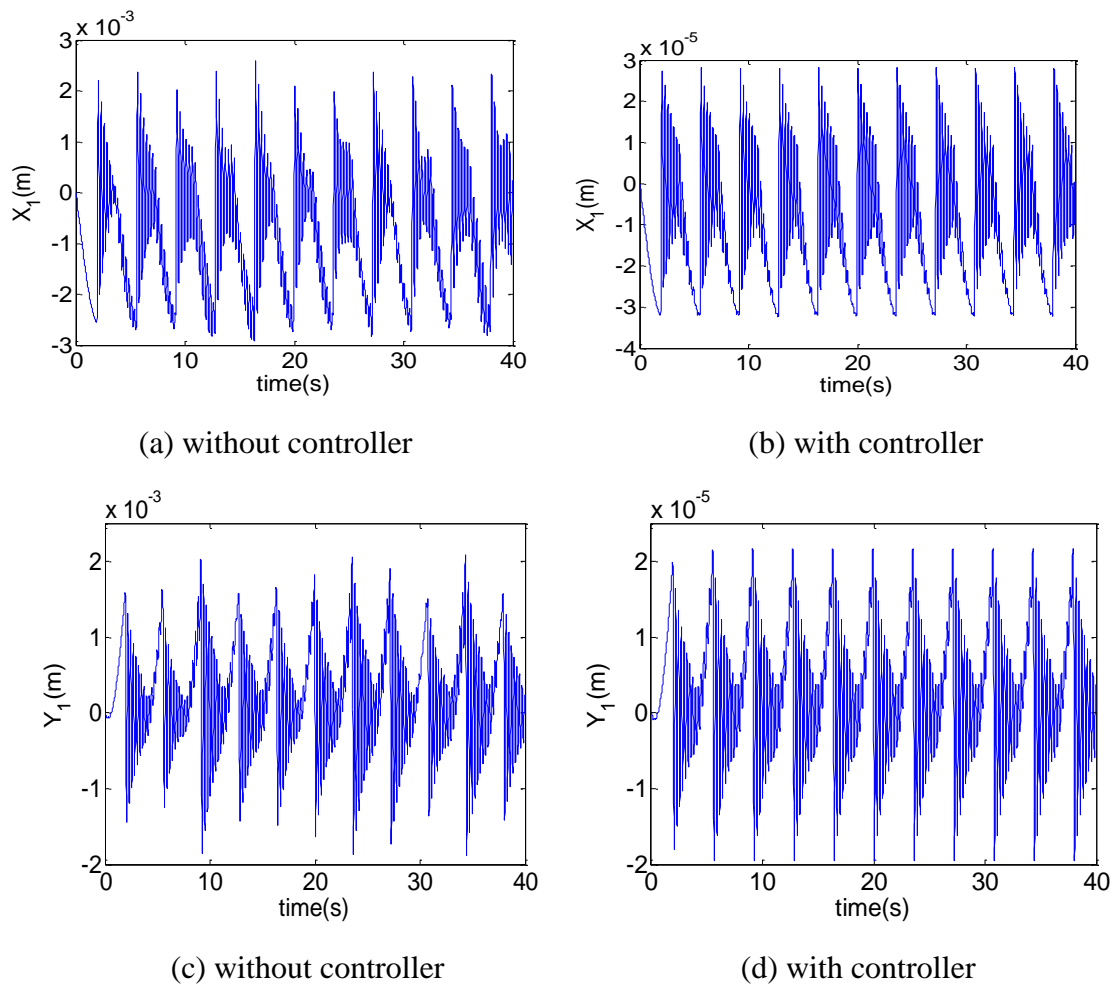
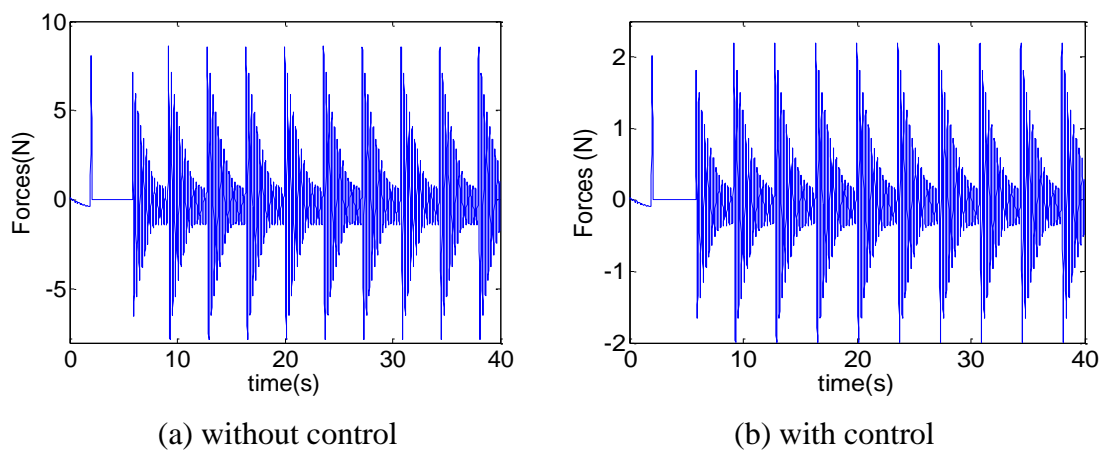


Figure 5.13: Tool tip vibration levels at a depth of 3mm

Figure 5.14 shows the regenerative cutting forces obtained for two different depths of cut at 1mm and 3mm. Initially, it is seen that, when the depth of cut increases the amplitude of the forces also increases. It is also observed that, when the PD control is applied there is a considerable reduction in the amplitude of the cutting forces.



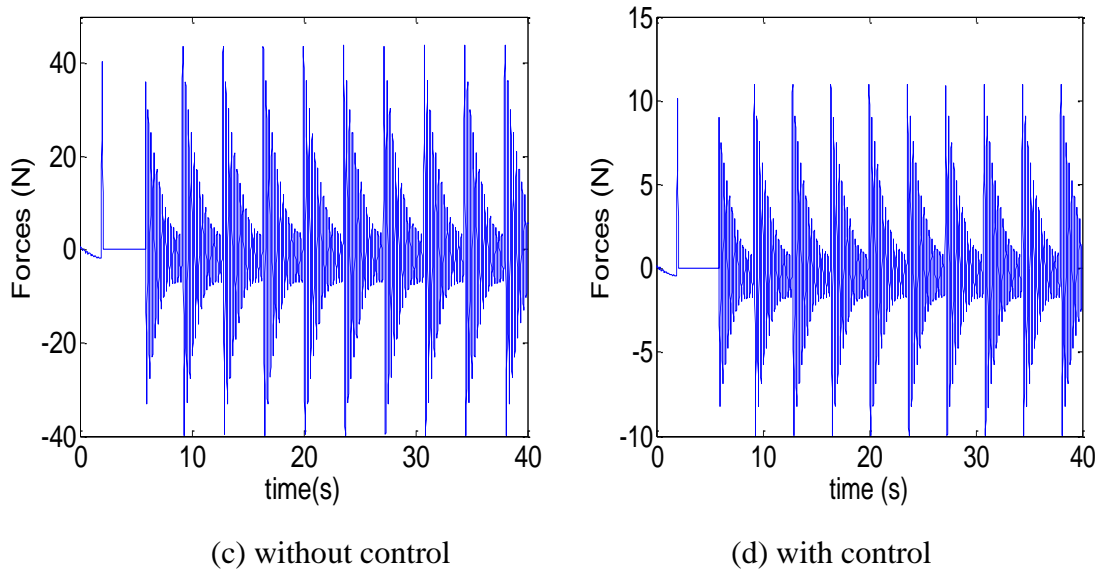
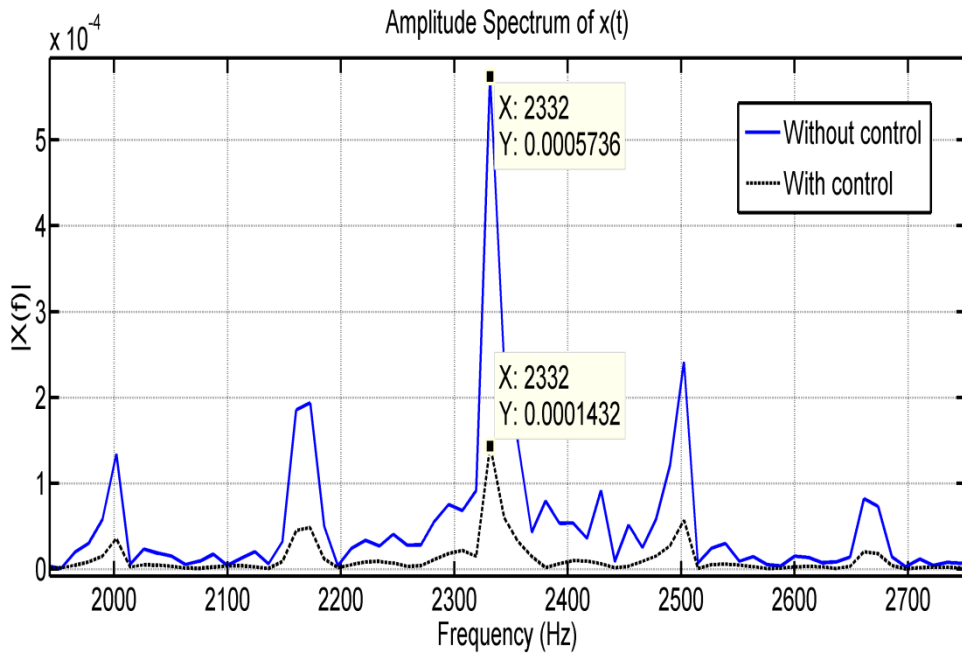
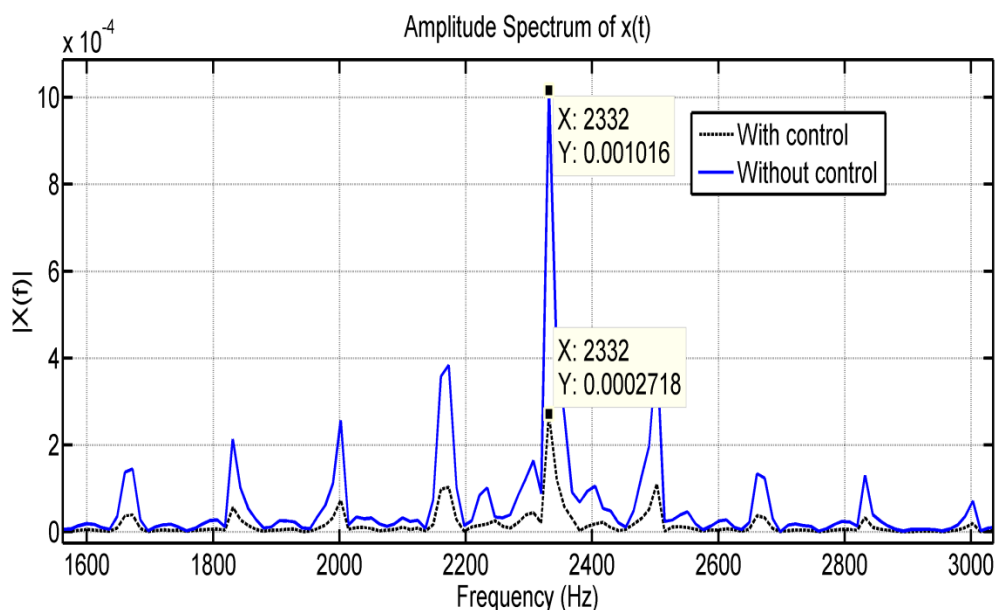


Figure 5.14: Time domain simulation at a depth of 1mm and 3mm

Figure 5.15 shows the FFT plots at the tool-tip node in x direction with and without controller at two different depths of cut. Vibration amplitudes have reduced considerably by applying the control forces at node near to the tool-tip.



(a) Axial depth=1mm



(b) Axial depth=2mm

Figure 5.15: FFT plots at different depths of cut

It is observed that the PD controller is easy to be implemented and gains can be designed based upon the system parameters if they can be achieved or estimated precisely. Moreover, the PD gain can be designed just based on the system tracking error and treats the system to attain the steady state.

5.4 Conclusions

This chapter has presented some control strategies for chatter mitigation due to regenerative phenomenon. The primary structural vibration modes are considered for the entire spindle unit which has the significant role in ascertaining the self-excited vibration. In summary the following are the important issues considered.

- Initially the semi-active methods are introduced for the spindle model by placing the tuned mass dampers. Optimal studies are conducted using the PSO algorithm to identify the location of vibration absorber and its stiffness and damping parameters to maximize the stable depth of cut.
- With this damped FRF's at tool-tip the corresponding stability lobes are plotted. This has increased the average stable depth of cut.
- Active controller design has been presented using PD control scheme and explained with the finite element model of spindle-tool system to reduce the tool-tip vibration levels for the up milling process.
- The PD controller produces the feasible results, by reducing the tool-tip vibration levels at a very less time.

Chapter-6

Conclusions

In this work, a comprehensive study of the spindle-tool system design has been presented with its influences on the machining instability in the end milling process. Prediction of frequency response at the tool tip is of paramount importance in assessing the machining quality at the design stage. A coupled dynamic field approach for prediction of tool-tip frequency response of spindle-housing system has been presented.

6.1 Summary

Dynamics of spindle-tool system of a practical CNC machining center XLMILL has been considered and analyzed by finite element modeling in order to understand its vibrational characteristics and tool-tip frequency response behaviour. Effect of operating speeds, depth of cuts and tool-workpiece combinations on vibration behaviour were studied. The dynamic characteristics of the system were validated with those obtained from three-dimensional finite element model of the system along with receptance coupling approach in which the receptances of spindle tip were assembled with that of the holder-tool system. Experimental modal analysis was conducted on the CNC machining spindle system to obtain the modal characteristics of combined system by using both impact hammer and vibration shaker tests. Interactive programs developed in the work facilitates user to select the required number of elements in the model, alter various spindle-tool parameters or account conveniently any cross-sectional changes such as step/taper portions on spindle. Some studies are carried-out to estimate optimal spindle-tool parameters to maximize the dynamic rigidity of the spindle and hence in improvising the stability of cutting operation. Several experimental cutting studies were conducted on manual bench drilling machine spindle for end milling operations and it was found that modifications of existing spindle by adapting additional bearing system has enhanced the stability regions without appreciable chatter vibrations in the system. Generalized programs were developed for obtaining accurate stability lobe plots from the tool-tip frequency responses. These plots have been validated by conducting the cutting tests using the vibration and sound signals. Once chatter vibrations start due to regeneration, some external control methods need to be employed for achieving normal cutting conditions. Two common control schemes were illustrated with present spindle-tool system. In first method, tuned mass vibration dampers were employed on the spindle, while in other approach; active strategy using model-based control was presented for minimization of vibration amplitudes when chatter begins. Modular programming

approach employed in this work helps in easy changes for considering effects of several variables. Point-wise summary of the work is given below:

- The spindle-holder and tool system of a CNC machine centre has been analysed by finite element modeling and receptance coupling method to obtain the tool-tip frequency response functions.
- The dynamic characteristics of the model were compared with experimental modal analysis on the practical spindle system.
- The generalized computer programs were further used to carry out parametric studies on dynamic stiffness of spindle and optimum spindle system variables were identified to achieve the maximum dynamic stiffness.
- In this regard, the ball bearings were modelled using non-linear Hertzian contact forces with axial preload along with the joint interfaces at spindle, holder and tool idealized as spring damper systems.
- DOE and ANOVA techniques are employed to identify the effective spindle-tool parameters on the tool-tip frequency response. Based on the simulated results, the data was generalized with the help of a neural network model that works as a function estimator for the GA based optimization module. The optimal data obtained from this optimization technique increases the dynamic stiffness of the structure and proposes to design a new modified spindle-tool unit which can be able to bear the dynamic vibrations during the cutting process.
- The modeling methods developed in this work facilitate to us apply to any type spindle-tool assemblies. In view of this, a practical spindle unit of an in-house manual drilling machine is considered for the analysis. Finite element models are applied for the spindle-tool unit of a drill spindle and optimal topology of designs were proposed to improve the dynamic stiffness.
- The fundamental frequency responses arrived from the spindle-tool unit was utilized to plot the two and three dimensional stability lobes. Both these plots were further validated by conducting the cutting tests which shows the correctness of boundaries.
- The time-domain simulation studies were carried for three dimensional helical force model at different depths of cut. These simulations were further extended to study the various effects like variable tool pitches, tool-run outs, process damping, high speed effects and nonlinear feed rates. This virtual scenario developed in this work can be implemented for milling process optimization at the design stage when selecting various parameters of a particular cutting tool and their associated process dynamics.
- In order to utilize a bench drilling machine with its work-bed, the spindle design was modified slightly and a portable X-Y table for mounting of workpiece was fabricated.

Several experimental studies have been carried out on this set up to know the effects of the spindle-tool parameters on overall cutting process stability.

- In order to control the instability and improve the stable depth of cut, two control schemes such as semi-active and active strategies were implemented using the finite element model of the spindle-tool system.

6.2 Future work

The computer simulations and experimental studies carried out in this work have in general applications in stability assessment in different machining operations. In spite of these studies, there are several possible issues considered for future research work. Some these includes

- The thermal expansion of the spindle is an important issue as it changes the dimensions of the spindle-tool unit, bearing and spindle dynamics when the spindle is rotating at high speeds and this may be considered during modeling.
- In the RCSA approach modeling of cutter flutes and the flexible coupling at the interfaces of the joints are the important issues which need to be further studied and analyzed in order to increase the accuracy of the tool-point FRF predictions.
- The process mechanics and dynamic models will be applied to cover various other milling operations such as flank, face and peripheral five axis milling process.
- The workpiece dynamics is an important phenomenon while machining the flexible work pieces and may be considered as the future work.
- The concept of frictional damping can be considered at cutting tool as it increases the cutting depth over the solid tool.
- More robust control techniques such as adaptive control with FUZZY rule base can be considered to improve the stability of the cutting process.
- For the experimental test bed developed on bench drilling machine an electromagnetic actuator system has to be designed so as to reduce the vibrations during higher depths of cut based on proposed PD control module.

References

- [1] A. Bhattacharya. Metal cutting theory and practise, Central book publishers, New-Delhi, 2002.
- [2] J. T. Black and R. A. Kohser. Materials and Processes in manufacturing, Wiley-India, New-Delhi, 2013.
- [3] K. Cheng. Machine Dynamics fundamentals application and practise, Springer-verlag, London, 2009.
- [4] A Palmgren. Ball and Roller Bearing Engineering, Burkbank, 1959.
- [5] A. B Jones. A general theory for elastically constrained ball and radial roller bearings under arbitrary load and speed conditions. *A M S E Journal of Basic Engineering*, 309--320, 1960.
- [6] M. DeMulJ, J. M. Vree, and D. A. Mass. Equilibrium and association load distribution in ball and roller bearings loaded in five degrees. *Tribology*, 11 (1):142--148, 1989.
- [7] I. H Filiz, and G. Gorur. Analysis of preloaded bearings under combined axial and radial loading. *International Journal of Machine Tools and Manufacture*, 34(1):1--11, 1994.
- [8] L. Houpert. A uniform analytical approach for ball and roller bearings calculations. *AS ME J. Tribol*, 119:851--858, 1997.
- [9] X. Hernot, M. Sartor, and J. Guillot. Calculation of the stiffness matrix of angular contact ball bearings by using the analytical approach. *Journal of Mechanical Design, Transactions of the ASME*, 122(1): 83--90, 2000.
- [10] J. A. Harris. *Rolling Bearing Analysis*, 4 ed. John-Wiley, 2001.
- [11] T. L. H. Walford and B. J. Stone. The measurement of the radial stiffness of rolling element bearing under oscillation condition. *Journal of Mechanical Engineering Science*, 22(4):175--181, 1980.
- [12] T. L. H. Walford and B. J. Stone. The sources of damping in rolling element bearing under oscillation condition. *Proc. Instn. Mech. Engrs*, 197:225--232, 1983.
- [13] R. Tiwari and N. S. Vyas. Estimation of non-linear stiffness parameters of rolling element bearings from random response of rotor-bearing systems. *Journal of Sound and Vibration*, 187(2):229--239, 1995.
- [14] E. R. Marsh and D. S. Yantek. Experimental measurement of precision bearing dynamic stiffness," *Journal of Sound and Vibration*, 202(1):55--66, 1997.
- [15] R. Aini, H. Rahnejat and R. Gohar. An experimental investigation into bearing-induced spindle vibration. *Proc Instn Mech Engrs*, 209:107--114, 1995.

-
- [16] J. L. Walter. Design of high speed grease lubricated spindles for machine tool production equipment. *SAE (Society of automotive engineers) Transactions*, 99(5): 1061--1070, 1990.
- [17] W. F. Popoli. Spindle-bearing basics. *Manufacturing Engineering*, 125(5):52--57, 2000.
- [18] S. B. Rao. Metal cutting machine tool design - A Review. *Journal of manufacturing science and engineering, Transactions of the ASME*, 119(4):713--716, 1997.
- [19] Y. Kang, Y. P. Chang, J. W. Tsai, S. C. Chen and L. K. Yang. Integrated CAE strategies for the design of machine tool spindle-bearing systems. *Finite elements in analysis and design*, 37: 485--511, 2001.
- [20] W. F. Popoli. High speed spindle design and construction. *Technical paper society of manufacturing engineers*. 98--146, 1998.
- [21] M. Weck and A. Koch. Spindle- Bearing systems for high speed applications in machine tools. 42(1): 445--448, 1993.
- [22] C. W. Lin, J. F. Tu and J. Kamman. An integrated thermo -mechanical -dynamic model to characterize motorized machine tool spindles during very high speed rotation. *International Journal of Machine Tools & Manufacture*, 43:1035--1050, 2003.
- [23] S. Jiang and H. Mao. Investigation of variable optimum preload for a machine tool spindle. *International Journal of Machine Tools & Manufacture*, 50: 19--28, 2010.
- [24] E. Ozturk, U. Kumar, S. Turner and T. Schmitz. Investigation of spindle bearing preload on dynamics and stability limit in milling. *CIRP Annals-Manufacturing Technology*, 61:343--346,2012.
- [25] H. Cao, T. Holkup and Y. Altintas. A comparative study on the dynamics of high speed spindles with respect to different preload mechanisms. *Int J Adv Manuf Technol*, 57:871--883, 2011.
- [26] J. D. Kim, I. Zverv and K. B. Lee. Model of Rotation Accuracy of High-Speed Spindles on Ball Bearings. *Journal of Sci Res*. 2:477--484, 2010.
- [27] A. Zahedi and M. R. Movahhedy. Thermo-mechanical modeling of high speed spindles. *Scientia Iranica B*, 19(2): 282--293,2012.
- [28] A. Zivkovic, M. Zeljkovic, S. Tabakovic and Z. Milojevic. Mathematical modeling and experimental testing of high-speed spindle behavior. *Int J Adv Manuf Technol*, 77: 1071--1086, 2015.
- [29] S. Yang. A study of the static stiffness of machine tool spindles. *Int. J. Mach. Tool Des. Res*, 21(1):23--40, 1981.
- [30] R. L. Ruhl and J. F. Booker. A finite element model for distributed parameter turbo rotor systems. *A S M E Journal of Engineering for Industry*, 128--132, 1972.

-
- [31] H. D. Nelson and J. M. McVaugh. The dynamics of rotor-bearing systems using finite elements. *A S M E J. Mech. Des.*, 93(2):593--600, 1976.
- [32] H. D. Nelson. A finite rotating shaft element using Timoshenko beam theory. *A S M E J. Mech. Des.*, 102(4):793--803, 1980.
- [33] B.R. Jorgensen and Y. C. Shin. Dynamics of spindle-bearing systems at high speeds including cutting load effects. *Journal of Manufacturing Science and Engineering, Transactions of the A S M E*, 120(2):387--394, 1998.
- [34] B. Bossmanns, J.F.Tu and J. Kamman. Thermal model for high speed motorized spindles. *International J. Mach. Tools Manuf*, 39:1345--1366, 1999.
- [35] C.W. Lin, J. F.Tu and J. Kamman. An integrated thermo-mechanical dynamic model to characterize motorized machine tool spindles during very high speed rotation. *International J. Mach. Tools Manuf*, 43:1035--1050, 2003.
- [36] H. Li and Y. C. Shin. Integrated dynamic thermo-mechanical modeling of high speed spindles, part 1: Model development. *J. Manuf. Sci. and Eng., Transactions of the A S M E*, 126:148--158, 2004.
- [37] H. Li and Y. C. Shin. Integrated dynamic thermo-mechanical modeling of high speed spindles, part 2: Solution Procedure and Validations. *J. Manuf. Sci. and Eng., Transactions of the ASME*, 126:159--168, 2004.
- [38] Y. Cao and Y. Altintas. A general method for the modelling of spindle-bearing systems. *J., Mech. Des., Transactions of the A S M E*, 126:1089--1104, 2004.
- [39] Y. Altintas and Y. Cao. Virtual design and optimization of machine tool spindles. *Annals of CIRP*, 54(1):379--382, 2005.
- [40] N. Suzuki, Y. Kurata, T. Kato, R. Hino and E. Shamoto. Identification of transfer function by inverse analysis of self-excited chatter vibration in milling operations. *Precision Engineering*, 36: 568--575, 2012.
- [41] V. Gagnol, T. Phu Le and P. Ray. Modal identification of spindle-tool unit in high-speed machining. *Mechanical Systems and Signal Processing*, 25: 2388--2398, 2011.
- [42] P. Tandon and Md. Rajik Khan. Three dimensional modeling and finite element simulation of a generic end mill. *Computer-Aided Design*, 41:106--114, 2009.
- [43] M. Rantataloa, J. O. Aidanpaab, B. Goranssonc and P. Normand. Milling machine spindle analysis using FEM and non-contact spindle excitation and response measurement. *International Journal of Machine Tools & Manufacture*, 47:1034--1045, 2007.
- [44] H. Cao, B. Li and Z. He. Finite Element Model Updating of Machine-Tool Spindle Systems. *Journal of Vibration and Acoustics*, 135: 0245031--0245034, 2013.
- [45] W. X. Tanga and Q. H. Songa. Prediction of chatter stability in high-speed finishing end Milling considering multi-mode dynamics. *Int. J. Machine Tools & Manf*, 209:2585--2591, 2009.

-
- [46] V. Gagnola, B. C. Bouzgarrou, P. Raya and C. Barra. Model-based chatter stability prediction for high-speed spindles. *Int. J. Machine Tools & Manf*, 47:1176--1186, 2007.
- [47] U. Bravo, O. Altuzarra, L. N. Lopez de Lacalle, J. A. Sanchez and F. J. Campa. Stability limits of milling considering the flexibility of the workpiece and the machine. *Int. J. Machine Tools & Manf*, 45:1669--1680, 2005.
- [48] W. R. Wang and C. N. Chang. Dynamic Analysis and Design of a Machine Tool Spindle- Bearing System. *ASME J. Vibr. Acoust*, 116: 280--285, 1994.
- [49] C. W. Lin and J. F. Tu. Model-Based Design of Motorized Spindle Systems to Improve Dynamic Performance at High Speeds. *Journal of Manufacturing Process*, 9:94--108, 2007.
- [50] S. Jiang and S. Zheng. Dynamic Design of a High-Speed Motorized Spindle-Bearing System. *Journal of Mechanical Design ASME*, 132:0345011--0345015, 2010.
- [51] J. P. Hung, Y. L. Lai, T. L. Luo and H. C. Su. Analysis of the machining stability of a milling machine considering the effect of machine frame structure and spindle bearings: experimental and finite element approaches. *Int. J. Adv Manf technology*, 68:2393--2405, 2013.
- [52] G. Belforte, F. Colombo, T. Raparelli, A. Trivella and V. Viktorov. High-speed electro spindle running on air bearings: design and experimental verification. *Meccanica*, 43: 591--600, 2008.
- [53] X. Chao, J. Zhang, D. Yu, Z. Wu and J. Feng. Dynamics prediction of spindle system using joint models of spindle tool holder and bearings. *Proc IMechE Part C: J Mechanical Engineering Science*, 229(17): 3084--3095, 2015.
- [54] R. M. Mohammad and P. Mosaddegh. Prediction of chatter in high speed milling including gyroscopic effects. *International Journal of Machine Tools & Manufacture*, 46: 996--1001, 2006.
- [55] S. Jiang and S. Zheng. A modeling approach for analysis and improvement of spindle-drawbar-bearing assembly dynamics. *International Journal of Machine Tools & Manufacture*, 50:131--142, 2010.
- [56] A. D. S. Ahmed and M. Atsushi. Investigation about the characterization of machine tool spindle stiffness for intelligent CNC end milling. *Robotics and Computer-Integrated Manufacturing*, 34:133--139, 2015.
- [57] M. Wang, L. Gao and Y. Zheng. Prediction of regenerative chatter in the high-speed vertical milling of thin-walled workpiece made of titanium alloy. *Int J Adv Manuf Technol*, 72:707--716, 2014.
- [58] M. Chi, M. Xuesong, Y. Jun, Z. Liang and S. Hu. Thermal characteristics analysis and experimental study on the high-speed spindle system. *Int J Adv Manuf Technol*, 79:469--489, 2015.

-
- [59] S. S. Park, Y. Altintas and M. Movahhedy. Receptance coupling for end mills. *Int. J. Machine Tools & Manuf*, 43: 889--896, 2003.
- [60] T. L. Schmitz and G. S. Duncan. Three-Component Receptance Coupling Substructure Analysis for Tool Point Dynamics Prediction. *J. of Manufacturing Science and Engineering*, 127:782--790, 2005.
- [61] M. R. Movahhedy and J. M. Gerami. Prediction of spindle dynamics in milling by sub-structure coupling. *Int. J. Machine Tools & Manuf*, 46: 243--251, 2006.
- [62] A. Erturk, H. N. Ozguven and E. Budak. Analytical modelling of spindle-tool dynamics on machine tools using Timoshenko beam model and receptance coupling for the prediction of tool point FRF. *Int. J. Machine Tools & Manuf*, 46(15):1901--1912, 2006.
- [63] T. L. Schmitz and G. S. Duncan. Receptance coupling for dynamics prediction of assemblies with coincident neutral axes. *J. Sound and Vibration*, 289:1045--1065, 2006.
- [64] T. L. Schmitz, K. P. Won, G. S. Duncan, W. G. Sawyer and J. C. Ziegert. Shrink fit tool holder connection stiffness/damping modelling for frequency response prediction in milling. *Int. J. Machine Tools & Manuf*, 47:1368--1380, 2007.
- [65] E. Ozturk, U. Kumar, S. Turner and T. Schmitz. Investigation of spindle bearing preload on dynamics and stability limit in milling. *CIRP Annals-Manufacturing Technology*, 61(1):343--346, 2012.
- [66] M. Namazi, Y. Altintas, T. Abe and N. Rajapakse. Modeling and identification of tool holder spindle interface dynamics. *Int. J. Machine Tools & Manuf*, 47:1333--1341, 2007.
- [67] Z. Jun, T. Schmitz, Z. Wanhua and L. U. Bingheng. Receptance Coupling for Tool Point Dynamics Prediction on Machine Tools. *Chinese journal of mechanical Engineering*, 24: 340--345, 2011.
- [68] T. L. Schmitz. Torsional and axial frequency response prediction by RCSA. *Precision Engineering*, 34:345--356, 2010.
- [69] U. V. Kumar and T. L. Schmitz. Spindle dynamics identification for Receptance Coupling Substructure Analysis. *Precision Engineering*, 36: 435--443, 2012.
- [70] L. Zhongqun, L. Shuo and C. Yizhuang. Receptance Coupling for End Mill Using 2-section Step Beam Vibration Model. *Second International Conference on Intelligent Computation Technology and Automation*, IEEE: DOI 10.1109/ICICTA.2009.276, 2009.
- [71] M. F. Ghanatim and R. Madoliat. New continuous dynamic coupling for three component modelling of tool-holder-spindle structure of machine tools with modified effected tool damping. *Journal of manufacturing science and engineering*, 134(2):021015, 2012.

-
- [72] S. Filiz, C. H. Cheng, K. Powell, T. Schmitz and O. Ozdoganlar. An improved tool–holder model for RCSA tool point frequency response prediction. *Precision engineering*, 33:26--36, 2009.
- [73] J. Zhang, T. Schmitz, W. Zhao and B. Lu. Receptance coupling for dynamics prediction of a fluted tool. *Chinese journal of mechanical engineering*, 24(3):340--345, 2011.
- [74] M. Mehrpouya, E. Graham and S. S.Park. Frequency response function based joint dynamics modelling and identification, *Mechanical Systems and Signal Processing*, 39:265--279, 2013.
- [75] V. Ganguly and T. L. Schmitz. Spindle dynamics identification using particle swarm optimization. *J. Manufacturing processes*, 15:444--451, 2013.
- [76] P. Albertelli, M. Goletti and M. Monno. A new receptance coupling substructure analysis methodology to improve chatter-free cutting conditions prediction. *Int. J. Machine tools and Manufacture*, 72:16--24, 2013.
- [77] I. Mancisidor, A. Urkiola, R. Barcena, J. Munoa, Z. Dombovan and M Zatarain. Receptance coupling for tool point dynamic prediction by fixed boundaries approach. *Int. J. Machine tools and Manufacture*, 78:18--29, 2014.
- [78] R. D. Bishop, D. C. Johnson. *The Mechanics of Vibration*, Cambridge University Press, Cambridge, UK, 1960.
- [79] D. Liu, H. Zhang, Z. Tao and Y. Su. Finite element analysis of high-speed motorized spindle based on ANSYS. *The open Mechanical Engineering Journal*, 5:1--10, 2011.
- [80] C. Salomon. Die Frasarheit Werkstttstechnik, 20: 469--474, 1926.
- [81] A. J. P. Sabberwal. Chip section and cutting force during the milling operation. *Annals of the CIRP*, 10:197--203, 1961.
- [82] F. Koenigsberger and A. J. P. Sabberwal. An investigation into the cutting force pulsations during milling operations. *International Journal of Machine Tool Design and Research*, 1:15--33, 1961.
- [83] E. J. A. Armarego, N. P. Deshpande. Computerized end-milling force predictions with cutting models allowing eccentricity and cutter deflections. *Annals of the CIRP*, 40(1): 25--29, 1991.
- [84] S. Smith and J. Tlusty. An overview of modeling and simulation of the milling process. *ASME Journal of Engineering for Industry*, 113(2):169--175, 1991.
- [85] J. Tlusty and F. Ismail. Basic nonlinearity in machining chatter. *Annals of the CIRP*, 30:21--25, 1981.
- [86] J. W. Sutherland and R. E. DeVor. A dynamic method for the cutting force system in the end milling process. *Sensors and Controls for Manufacturing, ASME*, 33: 269--279, 1988.

-
- [87] D. Montgomery and Y. Altintas. Mechanism of cutting force and surface generation in dynamic milling. *ASME Journal of Engineering for Industry*, 113:160--168, 1991.
- [88] Y. Altintas and P. Lee. Mechanics and dynamics of ball end milling. *ASME Journal of Manufacturing Science and Engineering*, 120:684--692, 1998.
- [89] S. Smith and J. Tlustý. Efficient simulation programs for chatter in milling. *Annals of the CIRP*, 42:463--466, 1993.
- [90] J. Tlustý and P. McNeil. Dynamics of Cutting Forces in End Milling. *Annals of the CIRP*, 24:21--25, 1970.
- [91] W.A. Kline, R. E. DeVor and W. J. Zdeblick. A mechanistic model for the force system in end milling with application to machining airframe structures. *Manufacturing Engineering Transactions*, 297, 1980.
- [92] Y. Altintas and A. Spence. End Milling Force Algorithms for CAD Systems. *Manufacturing Technology CIRP Annals*, 40:31--34, 1991.
- [93] X.P. Li, A. Y. C. Nee, Y. S. Wong and H. Q. Zheng. Theoretical modelling and simulation of milling forces. *Journal of Materials Processing Technology*, 90: 266-272, 1999.
- [94] Z. Li and Q. Liu. Solution and Analysis of Chatter Stability for End Milling in the Time-domain. *Chinese Journal of Aeronautics*, 21:169--178, 2008.
- [95] S. Khachana and F. Ismail. Machining chatter simulation in multi-axis milling using graphical method. *International Journal of Machine Tools & Manufacture*, 49:163--170, 2009.
- [96] Y. Altintas, G. Stepan, D. Merdol and Z. Dombovari. Chatter stability of milling in frequency and discrete time domain. *CIRP Journal of Manufacturing Science and Technology*, 1:35--44, 2008.
- [97] H.B Lacerda and V. T. Lima. Evaluation of Cutting Forces and Prediction of Chatter Vibrations in Milling. *J. of the Braz. Soc. of Mech. Sci. &Eng*, 26(1), 74--81, 2004.
- [98] H. Li and X. Li. Modelling and simulation of chatter in milling using a predictive force model. *International Journal of Machine Tools & Manufacture*, 40:2047--2071, 2000.
- [99] H. Z. Li, W. B. Zhang and X. P. Li. Modelling of cutting forces in helical end milling using a predictive machining theory. *International Journal of Mechanical Sciences*, 43:1711--1730, 2001.
- [100] C. H. Chiou, M. S. Hong and K. F. Ehmann. Instantaneous shear plane based cutting force model for end milling. *Journal of Materials Processing Technology*, 170:164--180, 2005.
- [101] M. Wan and W. H. Zhang. Systematic study on cutting force modelling methods for peripheral milling. *International Journal of Machine Tools & Manufacture*, 49:424--432, 2009.

-
- [102] M. Wan, W. H. Zhang, J. W. Dang and Y. Yang. A novel cutting force modelling method for cylindrical end mill. *Applied Mathematical Modelling*, 34:823--836, 2010.
- [103] J. W. Dang, W. H. Zhang, Y. Yang and M. Wan. Cutting force modeling for flat end milling including bottom edge cutting effect. *International Journal of Machine Tools & Manufacture*, 50:986--997, 2010.
- [104] X. P. Li and H. Z. Li. Theoretical modelling of cutting forces in helical end milling with cutter run out. *International Journal of Mechanical Sciences*, 46:1399--1414, 2004.
- [105] E. D. Cifuentes, H. P. rezGarcia, M. G. Villasen and A. V. Idoipe. Dynamic analysis of runout correction in milling. *Int. J. Machine Tools & Manf*, 50:709--717, 2010.
- [106] T. L. Schmitz, J. Couey, E. Marsh, N. Mauntler and D. Hughes. Run out effects in milling: Surface finish, surface location error, and stability *International Journal of Machine Tools & Manufacture*, 47:841--851, 2007.
- [107] S. B. Wanga, L. Geng, Y. F. Zhanga, K. Liu and T. ENg. Cutting force prediction for five-axis ball-end milling considering cutter vibrations and run-out. *International Journal of Mechanical Sciences*, 97: 206--215, 2015.
- [108] Y. Sun and Q. Guo. Numerical simulation and prediction of cutting forces in five-axis milling processes with cutter run-out. *International Journal of Machine Tools & Manufacture*, 51:806--815, 2011.
- [109] T. L. Taner, Ö. Ömer and E. Budak. Generalized cutting force model in multi-axis milling using a new engagement boundary determination approach. *Int J Adv Manuf Technol*, 77:341--355, 2015.
- [110] Q. Sheng, Z. Jibin, T. Wang and T. Fengjie. Improved method to predict cutting force in end milling considering cutting process dynamics. *Int J Adv Manuf Technol*, 78:1501--1510, 2015.
- [111] O. Olufayo, K. Hossein. Tool life estimation based on acoustic emission monitoring in end-milling of H13 mould-steel. *Int J Adv Manuf Technol*, 81:39--51, 2015.
- [112] N. D. Sims, G. Manson and M. Brian. Fuzzy stability analysis of regenerative chatter in milling. *Journal of Sound and Vibration*, 329: 1025--1041, 2010.
- [113] C. Ming, W. Ming and X. Zhang. Grade of stability in fuzzy chatter stability lobe model in milling. *Machining Science and Technology: An International Journal*, 15(3):306--323, 2011.
- [114] M. Wan, Y. Chao Ma, W. H. Zhang and Y. Yang. Study on the construction mechanism of stability lobes in milling process with multiple modes. *Int J Adv Manuf Technol*, 79:589--603, 2015.

-
- [115] Y. Altintas, S. Engin and E. Budak. Analytical Stability Prediction and Design of Variable Pitch Cutters. *Journal of Manufacturing Science and Engineering*, 121(2):173--179, 1999.
- [116] E. Budak. An analytical design method for milling cutters with non constant pitch to increase stability, part I: theory. *Journal of Manufacturing Science and Engineering*, 125(1): 29--34, 2003.
- [117] E. Budak. An analytical design method for milling cutters with non constant pitch to increase stability, part 2: application. *Journal of Manufacturing Science and Engineering*, 125(1):35--38, 2003.
- [118] G. Jin, Q. Zhang, S. Hao and Q. Xie. Stability Prediction of Milling Process with Variable Pitch Cutter. *Mathematical Problems in Engineering, Hindawi Publishing Corporation*, Article ID: 932013.
- [119] Q. Song, X. Ai and J. Zhao. Design for variable pitch end mills with high milling stability. *Int J Adv Manuf Technol*, 55:891--903, 2011.
- [120] P. Huang, J. Li, J. Sun and J Zhou. Study on vibration reduction mechanism of variable pitch end mill and cutting performance in milling titanium alloy. *Int J Adv Manuf Technol*, 67:1385—1391, 2013.
- [121] V. Sellmeier and B. Denkena. Stable islands in the stability chart of milling processes due to unequal tooth pitch. *International Journal of Machine Tools & Manufacture*, 51:152--164, 2011.
- [122] N. H. Hanna and S. Tobias. A Theory of Nonlinear Regenerative Chatter. *J. Eng. Ind*, 96(1): 247-255, 1974.
- [123] V. L. Martínez, J. C. Jáuregui-Correa, O. M. González-Brambila, G. Herrera-Ruiz and A. Lozano-Guzmán. Instability conditions due to structural nonlinearities in regenerative chatter. *Journal of Nonlinear Dynamics*, 56:415--427, 2009.
- [124] J. Gradišek, M. Kalveram and K. Weinert. Mechanistic identification of specific force coefficients for a general end mill. *Int J Mach Tools Manuf*, 44(4):401--414, 2004.
- [125] C. L. Tsai. Analysis and prediction of cutting forces in end milling by means of a geometrical model. *Int J Adv Manuf Technol*, 31:888--896, 2007.
- [126] R. G. Landers and A. G. Ulsoy. Nonlinear Feed Effect in Machining Chatter Analysis. *Journal of Manufacturing Science and Engineering*, 130:011017(1--8), 2008.
- [127] H. Moradi, G. Vossoughi, R. M. Mohammad and H. Salarieh. Suppression of nonlinear regenerative chatter in milling process via robust optimal control. *Journal of Process Control*, 23:631--648, 2013.
- [128] A.M. A. Khaled, R. Fales and A. S. Gizawy. Identification of cutting force coefficients for the linear and nonlinear force models in end milling process using

- average forces and optimization technique methods. *Int J AdvManufTechnol*, 79:1671--1687, 2015.
- [129] Y. Altintas and E. Budak. Analytical prediction of stability lobes in milling. *Annals of the CIRP*, 44:357--362, 1995.
- [130] S. H. Gao and G. Meng. Unstable islands and bifurcation analysis in a spindle Milling system supported by ball bearings. *Journal of Multi-body Dynamics*, 2011.
- [131] W. X. Tanga and Q. H. Songa. Prediction of chatter stability in high-speed finishing end milling considering multi-mode dynamics. *Int. J. Machine Tools &Manf*, 209:2585--2591, 2009.
- [132] U. Bravo, O. Altuzarra, L.N. Lopez de Lacalle, J. A. Sanchez and F.J. Campa. Stability limits of milling considering the flexibility of the workpiece and the machine. *Int. J. Machine Tools &Manf*, 45:1669--1680, 2005.
- [133] I. Mane, V. Gagnol, B.C. Bouzgarrou and P. Ray. Stability-based spindle speed control during flexible workpiece high-speed milling. *Int. J. Machine Tools &Manf*, 48:184--194, 2008.
- [134] E. Solis, C.R. Peres, J. E. Jimenez, J.R. Alique and J. C. Monje. A new analytical--experimental method for the identification of stability lobes in high-speed milling. *Int. J. Machine Tools &Manf*, 44:1591--1597, 2004.
- [135] G. Quintana, J. Ciurana, I. Ferrer and C. A. Rodriguez. Sound mapping for identification of stability lobe diagrams in milling processes. *Int. J. Machine Tools &Manf*, 49:203--211, 2009.
- [136] T. Surmann and D. Biermann. The effect of tool vibrations on the flank surface created by peripheral milling. *CIRP- Annals Manufacturing Technology*, 57:375--378, 2008.
- [137] S. Seguy, T. Insperger, L. Arnaud, G. Desein and G. Peigne. On the stability of high-speed milling with spindle modal identification of spindle-tool unit in high-speed machining speed variation. *Int J Adv Manuf Technol*, 48:883--895, 2012.
- [138] G. S. Raphael and T.C. Reginaldo. A Contribution to Improve the Accuracy of Chatter Prediction in Machine Tools Using the Stability Lobe Diagram. *J. of Manf Science and Engg, ASME*, 136:021005--021007, 2014.
- [139] Z. K. Penga, M .R. Jackson, L. Z. Guo, R. M. Parkin and G. Meng. Effects of bearing clearance on the chatter stability of milling process. *Nonlinear Analysis: Real World Applications*, 11: 3577--3589, 2010.
- [140] J. Munoa, Z. Dombovari, I. Mancisidor, Y. Yang and M. Zatarain. Interaction between Multiple Modes in Milling processes. *Machining Science and Technology: An International Journal*, 17(2):165--180, 2013.
- [141] J. Liu and X. Chen. Dynamic design for motorized spindles based on an integrated model. *Int J Adv Manuf Technol*, 71:1961--1974, 2014.

-
- [142] K. Kecik, R. Rusinek and J. Warminski. Modeling of high-speed milling process with frictional effect. *Proc IMechE Part K: J Multi-body Dynamics*, 227(1):3--11.
- [143] T. Y. Fonga and J. Mingder. Dimensional quality optimisation of high-speed CNC milling process with dynamic quality characteristic. *Robotics and Computer-Integrated Manufacturing*, 21:506--517, 2005.
- [144] H. Mounayri, H. Kishawy and J. Bricenoa. Optimization of CNC ball end milling: a neural network -based model. *Journal of Materials Processing Technology*, 166:50--62, 2005.
- [145] H. Mounayri, J. F. Briceno and M. Gadallah. A new artificial neural network approach to modelling ball-end milling. *Int J Adv Manuf Technol*, 47:527--534, 2010.
- [146] U. Zuperl, F. Cus and M. Reibenschuh. Neural control strategy of constant cutting force system in end milling. *Robotics and Computer-Integrated Manufacturing*, 27:485--493, 2011.
- [147] J. F. Briceno, H. Mounayri and S. Mukhopadhyay. Selecting an artificial neural network for efficient modelling and accurate simulation of the milling process. *International Journal of Machine Tool and Manufacture*, 42:663--674, 2002.
- [148] P. Palanisamy and S. Kalidass. Prediction of Surface Roughness for AISI 304 Steel with Solid Carbide Tools in End Milling Process Using Regression and ANN Models. *Arab J SciEng*, 39:8065--8075, 2014.
- [149] A. M. Zain, H. Haron and S. Sharif. Integration of simulated annealing and genetic algorithm to estimate optimal solutions for minimising surface roughness in end milling Ti-6AL-4V. *International Journal of Computer Integrated Manufacturing*, 24:574--592, 2011.
- [150] R. J. Saffar and M. R. Razfar. Simulation of end milling operation for Predicting cutting forces to minimize tool deflection by Genetic Algorithm. *Machining Science and Technology: An International Journal*, 14:81--101, 2010.
- [151] P. Palanisamy, I. Rajendran, S. Shanmugasundaram. Optimization of machining parameters using genetic algorithm and experimental validation for end-milling operations. *Int J Adv Manuf Technol*, 32:644--655, 2007.
- [152] H. T. Hsieh, C.H. Chu. Improving optimization of tool path planning in 5-axis flank milling using advanced PSO algorithms. *Robotics and Computer-Integrated Manufacturing*, 29, 3--11, 2013.
- [153] M. Jaberipour and E. Khorrarn. Two improved harmony search algorithms for solving engineering optimization problems. *Commun Nonlinear Sci Numer Simulat*, 15, 3316--3331, 2010.

-
- [154] O. Zareia, M. Fesanghary, B. Farshi, J. Saffar and R. M. R. Razfar. Optimization of multi-pass face-milling via harmony search algorithm. *Journal of materials processing technology*, 209: 2386--2392, 2009.
- [155] A. Albrecht, S. S. Park, Y. Altintas, G. Prichstow. High frequency bandwidth cutting force measurements in milling using capacitance displacement sensors. *Int. J. Machine Tool and Manufacture*, 45:993--1008, 2005.
- [156] S. S. Park and Y. Altintas. Dynamic Compensation of Spindle Integrated Force Sensors with Kalman Filter. *Journal of Dynamic Systems, Measurement, and Control*, 126:443--451, 2004.
- [157] J. L. Jang and Y. S. Tarng. A study of the active vibration control of a cutting tool, *Journal of Materials Processing Technology*, 95:78--82, 1999.
- [158] G. S. Duncan, M. F. Tummond and T. L. Schmitz. An investigation of the dynamic absorber effect in high-speed machining. *International Journal of Machine Tools & Manufacture*, 45:497--507, 2005.
- [159] R. Madoliat, S. Hayati and A. G. Ghalebahman. Investigation of chatter suppression in slender end mill via a frictional damper. *ScientiaIranica B*, 18(5):1069--1077, 2011.
- [160] A. Parus, B. Powalka, K. Marchelek, S. Domek and M. Hoffmann. Active vibration control in milling flexible workpieces. *Journal of Vibration and Control*, 19(7):1103--1120, 2013.
- [161] R. Madoliat, S. Hayati, G. G. Ahmad. Modeling and Analysis of Frictional Damper Effect on Chatter Suppression in a Slender Endmill Tool. *Journal of Advanced Mechanical Design, Systems, and Manufacturing*, 5(2):115--128, 2011.
- [162] E. A. Regib, J. Ni and S. H. Lee. Programming spindle speed variation for machine tool chatter suppression. *International Journal of Machine Tools & Manufacture*, 43:1229--1240, 2003.
- [163] S. A. Sulaiman, A. K. M Nurul Amin and M. D. Arif. Application of Permanent Magnets for Chatter Control in End Milling of Titanium Alloy Ti-6Al-4V. *Advanced Materials Research*, 576:15--18, 2012.
- [164] J. Monnin, F. Kuster and K. Wegener. Optimal control for chatter mitigation in milling-Part1: Modeling and control design. *Control Engineering Practice*, 24:156--166, 2014.
- [165] J. Monnin, F. Kuster and K. Wegener. Optimal control for chatter mitigation in milling-Part2: Experimental validation, *Control Engineering Practice*, 24:167--175, 2014.
- [166] E. Graham, M. Mehrpouya and S. S. Park. Robust prediction of chatter stability in milling based on the analytical chatter stability. *Journal of Manufacturing Processes*, 15:508--517, 2013.

- [167] H. Moradi, G. Vossoughi, M. Behzad and R. M. Mohammad. Vibration absorber design to suppress regenerative chatter in non linear milling process: Application for machining of cantilever plates. *Applied Mathematical Modelling*, 39:600--620, 2015.
- [168] H. T. Zhang, Y. Wu, D. He and H. Zhao. Model predictive control to mitigate chatters in milling processes with input constraints. *International Journal of Machine Tools & Manufacture*, 91:54--61, 2015.
- [169] R. Rafal, L. Pawel, K. Krzysztof, K. Bogdan and W. Jerzy. Chatter identification methods on the basis of time series measured during titanium super alloy milling. *International Journal of Mechanical Sciences*, 99:196--207, 2015.
- [170] H. Wu, Y. Wang, M. Li, M. Al-Saedi and H. Handroos. Chatter suppression methods of a robot machine for ITER vacuum vessel assembly and maintenance. *Fusion Engineering and Design*, 89:2357--2362, 2014.
- [171] T. L Schmitz and K.S Smith. *Machining dynamics- Frequency response to improve productivity*, Springer science, NY, 2009.

APPENDIX-A

Finite element matrices

A.1 Shape Functions

For consideration of axial preload effects, a ten degree beam element is considered according to following field variables.

$$u = a_0 + a_1x$$

$$v = b_0 + b_1x + b_2x^2 + b_3x^3 \quad (A1)$$

$$w = c_0 + c_1x + c_2x^2 + c_3x^3$$

$$\theta_y = d_0 + d_1x + d_2x^2$$

$$\theta_z = e_0 + e_1x + e_2x^2$$

The displacements u , v , w , θ_y and θ_z are expressed in terms of element nodal displacements u_i , v_i , w_i , θ_{yi} , θ_{zi} and u_j , v_j , w_j , θ_{yj} and θ_{zj} . There are 16 unknowns in equations which satisfy both homogeneous equations and element boundary conditions.

$$\begin{bmatrix} u & v & w & \theta_y & \theta_z \end{bmatrix}^T = [N]\{q\} \quad (A2)$$

[N] is a matrix formed by shape functions, and {q} is nodal displacement.

$$[N] = \begin{bmatrix} [N_u] \\ [N_v] \\ [N_w] \\ [N_{\theta_y}] \\ [N_{\theta_z}] \end{bmatrix} = \begin{bmatrix} N_{u1} & 0 & 0 & 0 & 0 & N_{u1} & 0 & 0 & 0 & 0 \\ 0 & N_{t1} & 0 & 0 & N_{t2} & 0 & N_{t3} & 0 & 0 & N_{t4} \\ 0 & 0 & N_{t1} & -N_{t2} & 0 & 0 & 0 & N_{t3} & -N_{t4} & 0 \\ 0 & 0 & -N_{\theta 1} & N_{\theta 2} & 0 & 0 & 0 & -N_{\theta 3} & N_{\theta 4} & 0 \\ 0 & N_{\theta 1} & 0 & 0 & N_{\theta 2} & 0 & N_{\theta 3} & 0 & 0 & N_{\theta 4} \end{bmatrix} \quad (A3)$$

$$\{q\} = \begin{bmatrix} u_i & v_i & w_i & \theta_{yi} & \theta_{zi} & u_j & v_j & w_j & \theta_{yj} & \theta_{zj} \end{bmatrix}^T \quad (A4)$$

Shape functions defined as:

$$\begin{aligned}
N_{t1} &= \frac{1}{1+\Phi} \left[2s^3 - 3s^2 - \Phi s + (1+\Phi) \right]; N_{\theta1} = \frac{6}{(1+\Phi)L} (s^2 - s); \\
N_{t2} &= \frac{L}{1+\Phi} \left[s^3 - \left[2 + \frac{\Phi}{2} \right] s^2 + \left[1 + \frac{\Phi}{2} \right] s \right]; N_{\theta2} = \frac{1}{(1+\Phi)} \left[3s^2 - (4+\Phi)s + (1+\Phi) \right]; \\
N_{t3} &= -\frac{1}{1+\Phi} \left[2s^3 - 3s^2 - \Phi s \right]; N_{\theta3} = -\frac{6}{(1+\Phi)L} (s^2 - s); \\
N_{t4} &= \frac{L}{1+\Phi} \left[s^3 - \left[1 - \frac{\Phi}{2} \right] s^2 - \left[\frac{\Phi}{2} \right] s \right]; N_{\theta4} = \frac{1}{(1+\Phi)} \left[3s^2 - (2-\Phi)s \right];
\end{aligned} \tag{A5}$$

where $\Phi = \frac{12EI}{k_s AGL^2}$, $s = \frac{x}{L}$

Set the weighted functions as

$$\begin{aligned}
\begin{bmatrix} W_1 \\ W_2 \\ W_3 \\ W_4 \\ W_5 \end{bmatrix} &= \begin{bmatrix} [N_u]^T \\ [N_v]^T \\ [N_w]^T \\ [N_{\theta_y}]^T \\ [N_{\theta_z}]^T \end{bmatrix}
\end{aligned} \tag{A6}$$

From equations (A.5) and (A.6) the following equations can be obtained:

$$\begin{bmatrix} \frac{\partial u}{\partial x} & \frac{\partial v}{\partial x} & \frac{\partial w}{\partial x} & \frac{\partial \theta_y}{\partial x} & \frac{\partial \theta_z}{\partial x} \end{bmatrix}^T = \begin{bmatrix} \frac{\partial N}{\partial x} \end{bmatrix} \{q\} = [N'] \{q\} \tag{A7}$$

$$\begin{bmatrix} \frac{du}{dt} & \frac{dv}{dt} & \frac{dw}{dt} & \frac{d\theta_y}{dt} & \frac{d\theta_z}{dt} \end{bmatrix}^T = [N] \{\dot{q}\} \tag{A8}$$

$$\begin{bmatrix} \frac{d^2 u}{dt^2} & \frac{d^2 v}{dt^2} & \frac{d^2 w}{dt^2} & \frac{d^2 \theta_y}{dt^2} & \frac{d^2 \theta_z}{dt^2} \end{bmatrix}^T = [N] \{\ddot{q}\} \tag{A9}$$

$$\begin{bmatrix} \frac{\partial W_1}{\partial x} & \frac{\partial W_2}{\partial x} & \frac{\partial W_3}{\partial x} & \frac{\partial W_4}{\partial x} & \frac{\partial W_5}{\partial x} \end{bmatrix}^T = \begin{bmatrix} \left[\frac{\partial N_u}{\partial x} \right]^T & \left[\frac{\partial N_v}{\partial x} \right]^T & \left[\frac{\partial N_w}{\partial x} \right]^T & \left[\frac{\partial N_{\theta_y}}{\partial x} \right]^T & \left[\frac{\partial N_{\theta_z}}{\partial x} \right]^T \end{bmatrix}^T$$

$$= \begin{bmatrix} [N_u']^T & [N_v']^T & [N_w']^T & [N_{\theta_y}']^T & [N_{\theta_z}']^T \end{bmatrix}^T \tag{A10}$$

$[M] = [M]_T + [M]_R$ where $[M]_T$ and $[M]_R$ are the translational and rotational mass matrices.

$$[M]_T = \frac{\rho AL}{420(1+\Phi)^2} \begin{bmatrix} m_{a1} & 0 & 0 & 0 & 0 & m_{a2} & 0 & 0 & 0 & 0 \\ 0 & m_1 & 0 & 0 & m_2 & 0 & m_3 & 0 & 0 & m_4 \\ 0 & 0 & m_1 & -m_2 & 0 & 0 & 0 & m_3 & -m_4 & 0 \\ 0 & 0 & -m_2 & m_5 & 0 & 0 & 0 & m_4 & m_6 & 0 \\ 0 & m_2 & 0 & 0 & m_5 & 0 & -m_4 & 0 & 0 & m_6 \\ m_{a2} & 0 & 0 & 0 & 0 & m_{a1} & 0 & 0 & 0 & 0 \\ 0 & m_3 & 0 & 0 & -m_4 & 0 & m_1 & 0 & 0 & -m_2 \\ 0 & 0 & m_3 & m_4 & 0 & 0 & 0 & m_1 & m_2 & 0 \\ 0 & 0 & -m_4 & m_6 & 0 & 0 & 0 & m_2 & m_5 & 0 \\ 0 & m_4 & 0 & 0 & m_6 & 0 & -m_2 & 0 & 0 & m_5 \end{bmatrix} \quad (A11)$$

$$[M]_R = \frac{\rho I}{30(1+\Phi)^2 L} \begin{bmatrix} 0 & 0 & 0 & 0 & 0 & 0 & 0 & 0 & 0 & 0 \\ 0 & 36 & 0 & 0 & m_7 & 0 & -36 & 0 & 0 & m_7 \\ 0 & 0 & 36 & -m_7 & 0 & 0 & 0 & -36 & -m_7 & 0 \\ 0 & 0 & -m_7 & m_8 & 0 & 0 & 0 & m_7 & m_9 & 0 \\ 0 & m_7 & 0 & 0 & m_8 & 0 & -m_7 & 0 & 0 & m_9 \\ 0 & 0 & 0 & 0 & 0 & 0 & 0 & 0 & 0 & 0 \\ 0 & -36 & 0 & 0 & -m_7 & 0 & 36 & 0 & 0 & -m_7 \\ 0 & 0 & -36 & m_7 & 0 & 0 & 0 & 36 & m_7 & 0 \\ 0 & 0 & -m_7 & m_9 & 0 & 0 & 0 & m_7 & m_8 & 0 \\ 0 & m_7 & 0 & 0 & m_9 & 0 & -m_7 & 0 & 0 & m_8 \end{bmatrix} \quad (A12)$$

The mass matrix $[M_c]$ is used to compute the centrifugal force is given by

$$[M_c] = \frac{\rho AL}{420(1+\Phi)^2} \begin{bmatrix} 0 & 0 & 0 & 0 & 0 & 0 & 0 & 0 & 0 & 0 \\ 0 & m_1 & 0 & 0 & m_2 & 0 & m_3 & 0 & 0 & m_4 \\ 0 & 0 & m_1 & -m_2 & 0 & 0 & 0 & m_3 & -m_4 & 0 \\ 0 & 0 & -m_2 & m_5 & 0 & 0 & 0 & m_4 & m_6 & 0 \\ 0 & m_2 & 0 & 0 & m_5 & 0 & -m_4 & 0 & 0 & m_6 \\ 0 & 0 & 0 & 0 & 0 & 0 & 0 & 0 & 0 & 0 \\ 0 & m_3 & 0 & 0 & -m_4 & 0 & m_1 & 0 & 0 & -m_2 \\ 0 & 0 & m_3 & m_4 & 0 & 0 & 0 & m_1 & m_2 & 0 \\ 0 & 0 & -m_4 & m_6 & 0 & 0 & 0 & m_2 & m_5 & 0 \\ 0 & m_4 & 0 & 0 & m_6 & 0 & -m_2 & 0 & 0 & m_5 \end{bmatrix} \quad (A13)$$

$$m_1 = 156 + 294\Phi + 140\Phi^2; m_2 = (22 + 38.5\Phi + 17.5\Phi^2)L; m_3 = 54 + 126\Phi + 70\Phi^2;$$

$$m_4 = -(13 + 31.5\Phi + 17.5\Phi^2)L; m_5 = (4 + 7\Phi + 3.5\Phi^2)L^2; m_6 = -(3 + 7\Phi + 3.5\Phi^2)L^2;$$

$$m_7 = (3 - 15\Phi)L; m_8 = (4 + 5\Phi + 10\Phi^2)L^2; m_9 = (-1 - 5\Phi + 5\Phi^2)L^2; \Phi = \frac{12EI}{vAGL^2}$$

$$m_{a1} = 140(1 + \Phi)^2; m_{a2} = 70(1 + \Phi)^2$$

The gyroscopic matrix $[G]$ is:

$$[G] = \frac{\rho J}{30(1+\Phi)^2 L} \begin{bmatrix} 0 & 0 & 0 & 0 & 0 & 0 & 0 & 0 & 0 & 0 \\ 0 & 0 & -36 & m_7 & 0 & 0 & 0 & 36 & m_7 & 0 \\ 0 & 36 & 0 & 0 & m_7 & 0 & -36 & 0 & 0 & m_7 \\ 0 & -m_7 & 0 & 0 & -m_8 & 0 & m_7 & 0 & 0 & -m_9 \\ 0 & 0 & -m_7 & m_8 & 0 & 0 & 0 & m_7 & m_9 & 0 \\ 0 & 0 & 0 & 0 & 0 & 0 & 0 & 0 & 0 & 0 \\ 0 & 0 & 36 & -m_7 & 0 & 0 & 0 & -36 & -m_7 & 0 \\ 0 & -36 & 0 & 0 & -m_7 & 0 & 36 & 0 & 0 & -m_7 \\ 0 & -m_7 & 0 & 0 & -m_9 & 0 & m_7 & 0 & 0 & -m_8 \\ 0 & 0 & -m_7 & m_9 & 0 & 0 & 0 & m_7 & m_8 & 0 \end{bmatrix} \quad (A14)$$

The stiffness matrix $[K]$ is given by

$$[K] = \frac{EI}{(1+\Phi)L^3} \begin{bmatrix} k_1 & 0 & 0 & 0 & 0 & -k_1 & 0 & 0 & 0 & 0 \\ 0 & 12 & 0 & 0 & 6L & 0 & -12 & 0 & 0 & 6L \\ 0 & 0 & 12 & -6L & 0 & 0 & 0 & -12 & -6L & 0 \\ 0 & 0 & -6L & k_2 & 0 & 0 & 0 & 6L & k_3 & 0 \\ 0 & 6L & 0 & 0 & k_2 & 0 & -6L & 0 & 0 & k_3 \\ -k_1 & 0 & 0 & 0 & 0 & k_1 & 0 & 0 & 0 & 0 \\ 0 & -12 & 0 & 0 & -6L & 0 & 12 & 0 & 0 & -6L \\ 0 & 0 & -12 & 6L & 0 & 0 & 0 & 12 & 6L & 0 \\ 0 & 0 & -6L & k_3 & 0 & 0 & 0 & 6L & k_2 & 0 \\ 0 & 6L & 0 & 0 & k_3 & 0 & -6L & 0 & 0 & k_2 \end{bmatrix} \quad (\text{A15})$$

$$k_2 = (4+\Phi)L^2; k_3 = (2-\Phi)L^2$$

$$[K] = \frac{P}{30(1+\Phi)L} \begin{bmatrix} 0 & 0 & 0 & 0 & 0 & -k_1 & 0 & 0 & 0 & 0 \\ 0 & 0 & 0 & 0 & 6L & 0 & -12 & 0 & 0 & 6L \\ 0 & 0 & 12 & -6L & 0 & 0 & 0 & -12 & -6L & 0 \\ 0 & 0 & -6L & k_2 & 0 & 0 & 0 & 6L & k_3 & 0 \\ 0 & 6L & 0 & 0 & k_2 & 0 & -6L & 0 & 0 & k_3 \\ 0 & 0 & 0 & 0 & 0 & k_1 & 0 & 0 & 0 & 0 \\ 0 & -12 & 0 & 0 & -6L & 0 & 12 & 0 & 0 & -6L \\ 0 & 0 & -12 & 6L & 0 & 0 & 0 & 12 & 6L & 0 \\ 0 & 0 & -6L & k_3 & 0 & 0 & 0 & 6L & k_2 & 0 \\ 0 & 6L & 0 & 0 & k_3 & 0 & -6L & 0 & 0 & k_2 \end{bmatrix} \quad (\text{A16})$$

APPENDIX-B

Fourth order Runge-Kutta time integration method

This method is used to find X_{i+1} from X_i upto terms of order $(\Delta t)^4$. All second order differential equations are converted to state space form before beginning the method.

From matrix eq. of motion, acceleration vector can be expressed as:

$$\ddot{\vec{x}}(t) = [M]^{-1}(\vec{F}(t) - [C]\dot{\vec{x}}(t) - [K]\vec{x}(t)) \quad (\text{B1})$$

In this method a new vector, $\vec{X}(t)$, is defined which contains the unknown displacements and velocities as:

$$\vec{X}(t) = \begin{Bmatrix} \vec{x}(t) \\ \dot{\vec{x}}(t) \end{Bmatrix} \quad (\text{B2})$$

$$\dot{\vec{X}} = \begin{Bmatrix} \dot{\vec{x}} \\ \ddot{\vec{x}} \end{Bmatrix} = \begin{Bmatrix} \dot{\vec{x}} \\ [M]^{-1}(\vec{F} - [C]\dot{\vec{x}} - [K]\vec{x}) \end{Bmatrix} \quad (\text{B3})$$

Rearranging above the equations to get displacement and velocity terms as:

$$\dot{\vec{X}}(t) = \begin{bmatrix} [0] & [I] \\ -[M]^{-1}[K] & -[M]^{-1}[C] \end{bmatrix} \begin{Bmatrix} \vec{x}(t) \\ \dot{\vec{x}}(t) \end{Bmatrix} + \begin{Bmatrix} 0 \\ [M]^{-1}\vec{F}(t) \end{Bmatrix} \quad (\text{B4})$$

$$\dot{\vec{X}}(t) = \vec{f}(\vec{X}, t)$$

Where,

$$\vec{f}(\vec{X}, t) = [A]\vec{X}(t) + \vec{F}'(t) \quad (\text{B5})$$

$$[A] = \begin{bmatrix} [0] & [I] \\ -[M]^{-1}[K] & -[M]^{-1}[C] \end{bmatrix} \quad \text{and} \quad \vec{F}'(t) = \begin{Bmatrix} \vec{0} \\ [M]^{-1}\vec{F}(t) \end{Bmatrix} \quad (\text{B6})$$

Now, $\vec{X}(t)$ can be obtained from the recurrence formula as:

$$\vec{X}_{i+1} = \vec{X}_i + \frac{1}{6}[\vec{K}_1 + 2\vec{K}_2 + 2\vec{K}_3 + \vec{K}_4] \quad (\text{B7})$$

$$\vec{K}_1 = h\vec{f}(\vec{X}_i, t_i) \quad (\text{B8})$$

$$\vec{K}_2 = h\vec{f}(\vec{X}_i + \frac{1}{2}\vec{K}_1, t_i + \frac{1}{2}h) \quad (\text{B9})$$

$$\vec{K}_3 = h\vec{f}(\vec{X}_i + \frac{1}{2}\vec{K}_2, t_i + \frac{1}{2}h) \quad (\text{B10})$$

$$\vec{K}_4 = h\vec{f}(\vec{X}_i + \vec{K}_3, t_{i+1}) \quad (\text{B11})$$

APPENDIX-C

Static condensation technique

In the structural dynamics area, model order reduction techniques have been widely used in global-local analysis, eigen-value problem, structural vibration and buckling, sensitivity studies and control parameters design and model update. For all model reduction/expansion techniques, there is a relationship between the master dof (adof) and the deleted dof (ddof) which can be written in general terms as

$$\{X_n\} = \begin{Bmatrix} X_a \\ X_d \end{Bmatrix} = [T] \{X_a\} \quad (C1)$$

Where 'n' denotes all degrees of freedom, 'a' denotes master or tested dof, 'd' denotes deleted or omitted dof

$$\{X_1\} = [T_{12}] \{X_2\} \quad (C2)$$

Since the energy of the system needs to be conserved, a balance can be written between the energy at state 1 and state 2 as

$$U = \frac{1}{2} \{X_1\}^T [K_1] \{X_1\} = \frac{1}{2} \{X_2\}^T [K_2] \{X_2\} \quad (C3)$$

Substituting the transformation gives

$$U = \frac{1}{2} \{[T_{12}] \{X_2\}\}^T [K_1] \{[T_{12}] \{X_2\}\} = \frac{1}{2} \{X_2\}^T [K_2] \{X_2\} \quad (C4)$$

Rearranging some terms then yields

$$U = \frac{1}{2} \{X_2\}^T [T_{12}]^T [K_1] [T_{12}] \{X_2\} = \frac{1}{2} \{X_2\}^T [K_2] \{X_2\} \quad (C5)$$

Then the reduced stiffness is related to the original stiffness by

$$[K_2] = [T_{12}]^T [K_1] [T_{12}] \quad \text{or} \quad [K_a] = [T]^T [K_n] [T] \quad (C6)$$

The mass is reduced in a similar fashion

$$[M_a] = [T]^T [M_n] [T] \quad (C7)$$

$$[K_a] = [T]^T [K_n] [T] \quad (C8)$$

Using the reduced mass and stiffness matrices, the eigen-solution produces frequencies that are higher than those of the original system (for most of the reduction schemes).

The eigen-solution of the reduced matrices

$$[[K_a] - \lambda [M_a]] \{X_a\} = \{0\} \quad (C9)$$

The stiffness equation becomes

$$[K_n] \{X_n\} = \{F_n\} \quad (C10)$$

can be partitioned into the ‘a’ active DOF and the ‘d’ deleted or omitted DOF to form two equations given as

$$\begin{bmatrix} [K_{aa}] & [K_{ad}] \\ [K_{da}] & [K_{dd}] \end{bmatrix} \begin{Bmatrix} X_a \\ X_d \end{Bmatrix} = \begin{Bmatrix} F_a \\ F_d \end{Bmatrix} \quad (C11)$$

Assuming that the forces on the deleted DOF are zero, then the second equation can be written as

$$[K_{da}] \{X_a\} + [K_{dd}] \{X_d\} = \{0\} \quad (C12)$$

which can be solved for the displacement at the deleted DOF as

$$\{X_d\} = -[K_{dd}]^{-1} [K_{da}] \{X_a\} \quad (C13)$$

The first equation can be written as

$$[K_{aa}] \{X_a\} + [K_{ad}] \{X_d\} = \{F_a\} \quad (C14)$$

and upon substituting for the ‘d’ deleted DOF gives the equation becomes

$$[K_{aa}] \{X_a\} + [K_{ad}] [K_{dd}]^{-1} [K_{da}] \{X_a\} = \{F_a\} \quad (C15)$$

This can be manipulated to yield the desired transformation to be

$$[T_s] = \begin{bmatrix} [I] \\ [t_s] \end{bmatrix} = \begin{bmatrix} [I] \\ -[K_{dd}]^{-1} [K_{da}] \end{bmatrix} \quad (C16)$$

Using this transformation, the reduced stiffness and mass matrices can be written as

$$[K_a^G] = [T_s]^T [K_n] [T_s] \quad (C17)$$

$$[M_a^G] = [T_s]^T [M_n] [T_s] \quad (C18)$$

APPENDIX-D

Training algorithm for MLP neural network

D.1 Neuron model

The simple model of an artificial neuron is shown in Figure B.1, where O_1, O_2, \dots, O_n are the inputs to the artificial neuron and W_{1B}, W_{2B}, W_{nB} are the weights attached to the input links. The weights are multiplicative factors of the inputs to account for the strength of the synapse. Hence the total input I_B received by the soma of the artificial neuron is

$$\begin{aligned} I_B &= W_{1B}O_1 + W_{2B}O_2 + \dots + W_{nB}O_n \\ &= \sum_{i=1}^n W_{iB}O_i \end{aligned} \tag{D1}$$

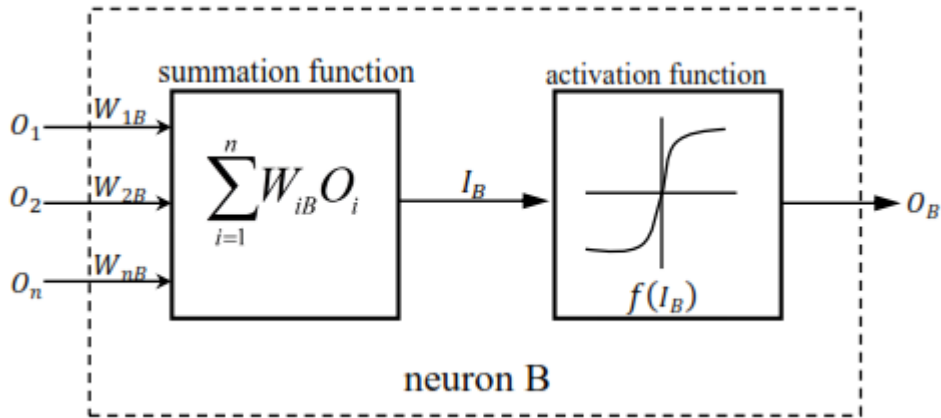


Figure B.1: Mathematical model of neuron

To generate the final output O_B , the sum is passed to a non-linear filter ' f ' called activation function or transfer function or Squash function which releases the output.

$$O_B = f(I_B) \tag{D2}$$

Following sigmoidal functions are used as activation functions for approximating non-linear data;

$$\text{Logarithmic sigmoid function } f(x) = \frac{1}{1 + e^{-x}}; \tag{D3}$$

$$\text{Hyperbolic tangent sigmoid function } f(x) = \tanh(x) = \frac{e^x - e^{-x}}{e^x + e^{-x}} \tag{D4}$$

D.2 Learning in Multi-Layer Perceptron

The notations followed are W_1, W_2, W_3, \dots are the weight matrices, (θ_j, ϕ_j) are the bias terms and (β, α) are learning and momentum factors. The following steps are followed.

1. Output at the j^{th} hidden layer neuron

$$h_j = f\left(\sum_i x_i W_1(i, j) + \theta_j\right) \quad (\text{D5})$$

2. Output of j^{th} output layer neuron

$$O_j = f\left(\sum_i h_i W_2(i, j) + \phi_j\right) \quad (\text{D6})$$

3. i^{th} component of output error at output layer

$$e_i = T_i - O_i \quad (\text{D7})$$

4. i^{th} component of output error at hidden layer

$$\delta_i = h_i(1-h_i)\left(\sum_j W_2(i, j) \cdot e_j\right) \quad (\text{D8})$$

5. Adjustment of weights between i^{th} neuron in hidden layer and j^{th} neuron in output layer in cycle t is

$$\Delta W_2(i, j)(t) = \beta \cdot h_i \cdot e_j + \alpha \cdot \Delta W_2(i, j) \cdot (t-1) \quad (\text{D9})$$

6. Adjustment of weights between i^{th} neuron in input layer and j^{th} neuron in hidden layer is

$$\Delta W_1(i, j)(t) = \beta \cdot x_i \cdot \delta_j + \alpha \cdot \Delta W_1(i, j) \cdot (t-1) \quad (\text{D10})$$

7. Adjustment of threshold/bias

$$j^{\text{th}} \text{ output neuron: } \Delta \phi_j = \beta \cdot e_j \quad (\text{D11})$$

$$j^{\text{th}} \text{ hidden neuron: } \Delta \theta_j = \beta \cdot e_j \quad (\text{D12})$$

APPENDIX-E

LabVIEW programs for sound spectrum analysis

E.1 Read the sound spectrum data

The following program is used for receiving the signals from micro-phon into LabVIEW software. LabVIEW 2015 is used.

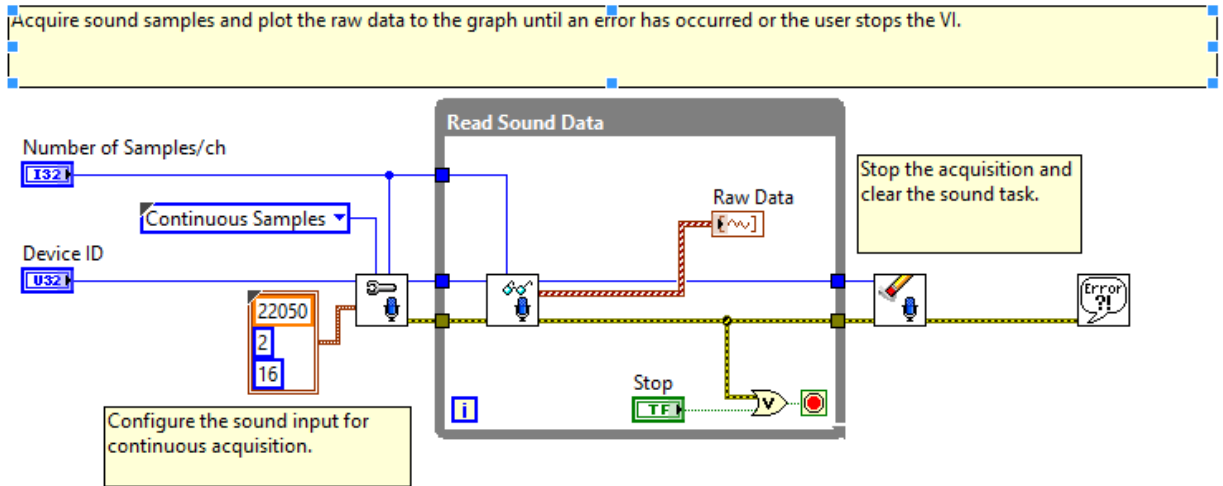


Figure E.1: Block diagram to read the sound data

E.2 Save the sound spectrum data

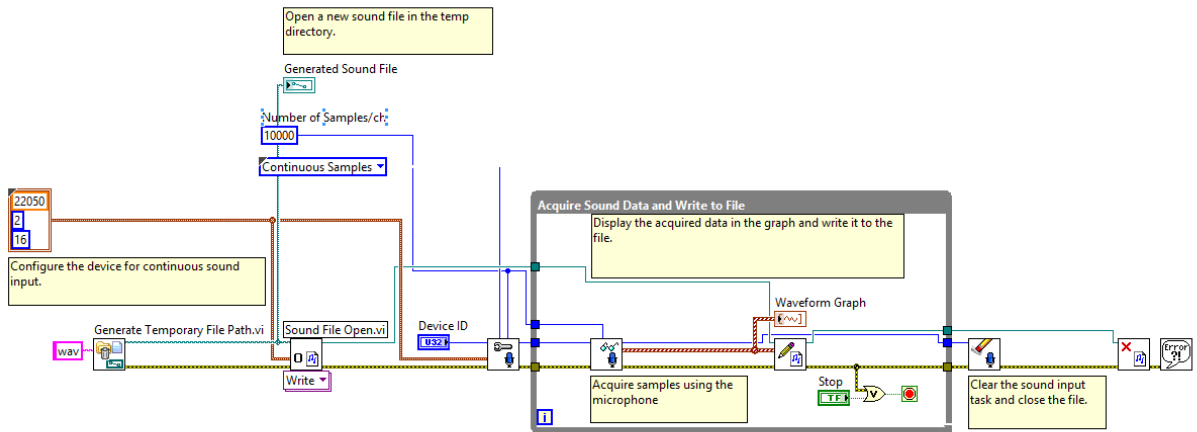


Figure E.2: Block diagram to save the sound data

E.3 Power spectral density of the cutting signal

Using signal analysis express VI, Fourier transforms are taken to display the frequency domain plots. Figure C3 shows the block diagram employed to convert time domain to frequency domain.

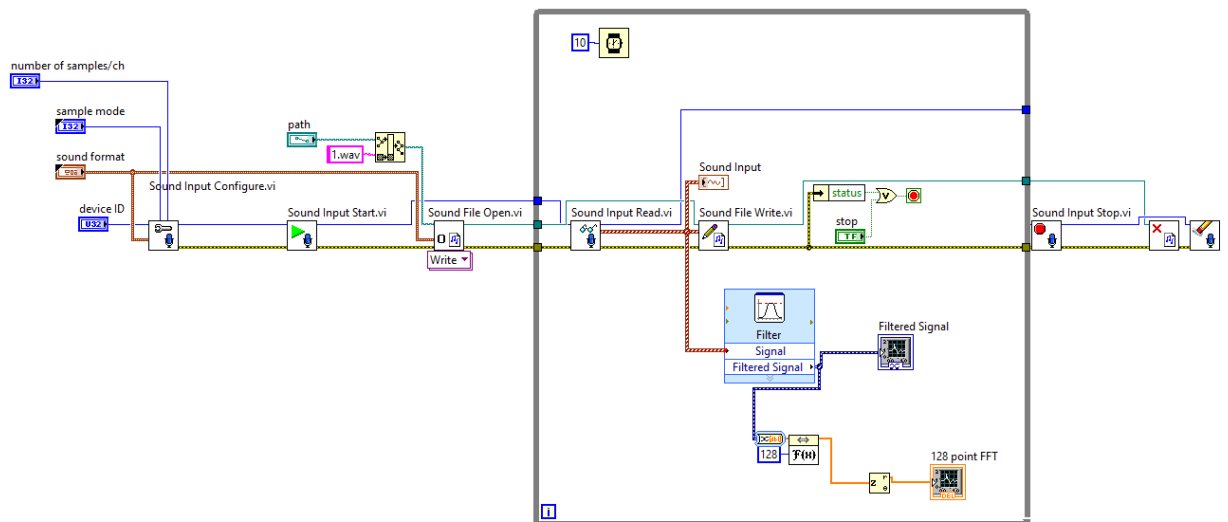


Figure E.3: Block diagram for the spectral sound

APPENDIX-F

Computer programs

A list of partial codes for important programs developed in the work is summarized below. All the codes are developed in MATLAB.

F.1 Finite element method to obtain the matrices

```
=====
% Initializing global matrices as null matrices
K=zeros(4*n+4,4*n+4);
M=zeros(4*n+4,4*n+4);
Gr=zeros(4*n+4,4*n+4);
speed=15000;
omega=speed*2*pi/60;

fid=fopen('sample.m','r');
for k=1:n %elements
    for p=1:8 % dof
        ne(p)=fscanf(fid,'%f',1);
    end
    switch k
    case 1

le=L1;A=A1;G=G1;RA=R1*A1;RI=R1*I1;YI=E1*I1*(1+1i*eta);r=sqrt(I1/A1);
    case 2

le=L2;A=A2;G=G2;RA=R2*A2;RI=R2*I2;YI=E2*I2*(1+1i*eta);r=sqrt(I2/A2);
    case 3

le=L3;A=A3;G=G2;RA=R2*A3;RI=R2*I3;YI=E2*I3*(1+1i*eta);r=sqrt(I3/A3);
    case 4

le=L4;A=A4;G=G2;RA=R2*A4;RI=R2*I4;YI=E2*I4*(1+1i*eta);r=sqrt(I4/A4);
    case 5

le=L5;A=A5;G=G2;RA=R2*A5;RI=R2*I5;YI=E2*I5*(1+1i*eta);r=sqrt(I5/A5);
    end

    ks=0.9;

% BOUNDARY CONDITIONS
theta=25*pi/180;Db=0.009;Z=20;F=1500;
K(7,7)=1.77236*10^7*(Z^2*Db)*(cos(theta)^2/sin(theta)^0.333)*F^0.333;
K(8,8)=1.77236*10^7*(Z^2*Db)*(cos(theta)^2/sin(theta)^0.333)*F^0.333;
K(9,9)=1.77236*10^7*(Z^2*Db)*(cos(theta)^2/sin(theta)^0.333)*F^0.333;
K(10,10)=1.77236*10^7*(Z^2*Db)*(cos(theta)^2/sin(theta)^0.333)*F^0.333;

% ASSEMBLING OF ELEMENTS
for ii=1:8
    p=ne(ii);
    for jj=1:8
        q=ne(jj);
        K(p,q)=K(p,q)+kef(ii,jj);
    end
end
=====
```

```

        M(p,q)=M(p,q)+me(ii,jj);
        Gr(p,q)=Gr(p,q)+ge(ii,jj);
    end
end
end
fclose(fid);

Gq=- (omega*Gr);
Cr=Gq; % Total damping
t1=1;
for om=0:1:15000 %rad/sec
    A1=K-M*om^2+1i*om*Cr;
    Hg=inv(A1);
    tfrf(t1)=Hg(1,1);
    t1=t1+1;

end

```

F.2 Program for receptance coupling

```

=====
% four bending receptances form FINITE ELEMENT METHOD

h3b3breal=xlsread('soliddamping.xlsx',1,'A1:A4000');
h3b3bimg=xlsread('soliddamping.xlsx',1,'B1:B4000');
h3b3b=(h3b3breal+1i*h3b3bimg)';
l3b3breal=xlsread('soliddamping.xlsx',1,'D1:D4000');
l3b3bimg=xlsread('soliddamping.xlsx',1,'E1:E4000');
l3b3b=(l3b3breal+1i*l3b3bimg)';
n3b3breal=xlsread('soliddamping.xlsx',1,'G1:G4000');
n3b3bimg=xlsread('soliddamping.xlsx',1,'H1:H4000');
n3b3b=(n3b3breal+1i*n3b3bimg)';
p3b3breal=xlsread('soliddamping.xlsx',1,'J1:J4000');
p3b3bimg=xlsread('soliddamping.xlsx',1,'K1:K4000');
p3b3b=(p3b3breal+1i*p3b3bimg)';

% Calculate assembly receptances
for cnt = 1:length(w)
    % Define generalized receptance matrices
    % Free-free cylinder
    R11 = [h11(cnt) l11(cnt); n11(cnt) p11(cnt)];
    R2b3a=[h2b3a(cnt) l2b3a(cnt); n2b3a(cnt) p2b3a(cnt)];
    R2b2b=[h2b2b(cnt) l2b2b(cnt); n2b2b(cnt) p2b2b(cnt)];
    R2a2a=[h2a2a(cnt) l2a2a(cnt); n2a2a(cnt) p2a2a(cnt)];
    R12a=[h12a(cnt) l12a(cnt); n12a(cnt) p12a(cnt)];
    R3a2b=R2b3a;
    R2a1=R12a;
    R3b3b=[h3b3b(cnt) l3b3b(cnt); n3b3b(cnt) p3b3b(cnt)];

    R13a= R12a*inv(R2a2a+R2b2b)*R2b3a;
    R3a3a = [h3a3a(cnt) l3a3a(cnt); n3a3a(cnt) p3a3a(cnt)];

    R3a1=R3a2b*inv(R2a2a+R2b2b)*R2a1;
    G11 = R11 - R13a/(R3a3a + R3b3b)*R3a1;

    % Individual terms in G11

```

```

H11(cnt) = G11(1,1);
L11(cnt) = G11(1,2);
N11(cnt) = G11(2,1);
P11(cnt) = G11(2,2);

```

F.3 Programs for Stability Computations

```

=====
alphaxx = 0.5*((cos(2*phie)-2*Kn*phie+Kn*sin(2*phie))-(cos(2*phis)-
2*Kn*phis+Kn*sin(2*phis)));
alphaxy = 0.5*((-sin(2*phie)-2*phie+Kn*cos(2*phie))-(-sin(2*phis)-
2*phis+Kn*cos(2*phis)));
alphayx = 0.5*((-sin(2*phie)+2*phie+Kn*cos(2*phie))-(-
sin(2*phis)+2*phis+Kn*cos(2*phis)));
alphayy = 0.5*((-cos(2*phie)-2*Kn*phie-Kn*sin(2*phie))-(-cos(2*phis)-
2*Kn*phis-Kn*sin(2*phis)));

wnmax = max([wnx wny]);
w = (0:0.1:2*wnmax/2/pi)'*2*pi; % frequency, rad/s
FRFxx = (wnx^2/kx)./(wnx^2 - w.^2 + li*2*zetax*wnx.*w); % m/N
FRFyy = (wny^2/ky)./(wny^2 - w.^2 + li*2*zetay*wny.*w);

for cnt = 1:length(w)
    % Oriented FRF
    FRF_or = [alphaxx*FRFxx(cnt) alphaxy*FRFyy(cnt); alphayx*FRFxx(cnt)
alphayy*FRFyy(cnt)]; % m/N
    % Calculate two eigenvalues
    E = eig(FRF_or);
    temp = E(1);
    lambda1(cnt) = temp;
    temp = E(2);
    lambda2(cnt) = temp;
    if (cnt > 1)
        dot_prod1 = real(lambda2(cnt))*real(lambda2(cnt-1)) +
imag(lambda2(cnt))*imag(lambda2(cnt-1));
        dot_prod2 = real(lambda2(cnt))*real(lambda1(cnt-1)) +
imag(lambda2(cnt))*imag(lambda1(cnt-1));
        if (dot_prod2 > dot_prod1)
            temp = lambda2(cnt);
            lambda2(cnt) = lambda1(cnt);
            lambda1(cnt) = temp;
        end
    end
end
end

lambda1 = lambda1';
lambda2 = lambda2';

alim1 = (2*pi/Nt/Kt)./((real(lambda1)).^2 + (imag(lambda1)).^2) .*
(real(lambda1) .* (1 + (imag(lambda1))./real(lambda1)).^2)); % m
alim2 = (2*pi/Nt/Kt)./((real(lambda2)).^2 + (imag(lambda2)).^2) .*
(real(lambda2) .* (1 + (imag(lambda2))./real(lambda2)).^2));

[index1] = find(alim1 > 0);
alim1 = alim1(index1);
alim1 = alim1*1e3; % mm
w1 = w(index1);

```

```

epsilon1 = pi - 2*psi1;
omega11 = (60/Nt)*w1./(epsilon1 + 2*0*pi);      % rpm
omega12 = (60/Nt)*w1./(epsilon1 + 2*1*pi);
omega13 = (60/Nt)*w1./(epsilon1 + 2*2*pi);
omega14 = (60/Nt)*w1./(epsilon1 + 2*3*pi);

[index2] = find(alim2 > 0);
alim2 =
psi2 = atan2(imag(lambda2), real(lambda2));
psi2 = psi2(index2);
epsilon2 = pi - 2*psi2;
omega21 = (60/Nt)*w2./(epsilon2 + 2*0*pi);
omega22 = (60/Nt)*w2./(epsilon2 + 2*1*pi);
omega23 = (60/Nt)*w2./(epsilon2 + 2*2*pi);
omega24 = (60/Nt)*w2./(epsilon2 + 2*3*pi);

```

F.4 Programs for time domain computations

```

=====
for cnt1 = 1:steps

    for cnt2 = 1:Nt
        teeth(cnt2) = teeth(cnt2) + 1;
        if teeth(cnt2) > steps_rev
            teeth(cnt2) = 1;
        end
    end

    Fx = 0;
    Fy = 0;
    Fz = 0;

    for cnt3 = 1:Nt
        for cnt4 = 1:steps_axial
            phi_counter = teeth(cnt3) - (cnt4-1);
            if phi_counter < 1      % helix has wrapped through phi = 0
                phi_counter = phi_counter + steps_rev;
            end
            phia = phi(phi_counter); % angle for given axial disk, deg
            z = cnt4*dz;
            if z <= d/2
                kappa_p = acos(1-2*z/d); % force projection angle,
            else
                kappa_p = pi/2;
            end

            if (phia >= phis) & (phia <= phie)
                if z <= d/2
                    theta = kappa_p - acos(1 - 2*(z-dz)/d);
                else
                    db = d/2*theta;
                    db = dz;
                end
                n = x*sin(phia*pi/180) - y*cos(phia*pi/180);
            h = (ft*sin(phia*pi/180) + surf(cnt4, phi_counter) -
            n)*sin(kappa_p)^beta; % m

```

```

        if h < 0
            Ft = 0;
            Fn = 0;
            Fa = 0;
            surf(cnt4, phi_counter) = surf(cnt4, phi_counter) +
ft*sin(phia*pi/180);
        else
            Ft = kt*db*h;
            Fn = kn*db*h;
            Fa = ka*db*h;
            surf(cnt4, phi_counter) = n;
        end
    else
        Ft = 0;
        Fn = 0;
        Fa = 0;
    end
end

    Fx = Fx + Ft*cos(phia*pi/180) +
Fn*sin(phia*pi/180)*sin(kappa_p) - Fa*sin(phia*pi/180)*cos(kappa_p);
    Fy = Fy + Ft*sin(phia*pi/180) -
Fn*cos(phia*pi/180)*sin(kappa_p) + Fa*cos(phia*pi/180)*cos(kappa_p);
    Fz = Fz -Fa;
end
end

    Forcex(cnt1) = Fx;
    Forcey(cnt1) = Fy;
    Forcez(cnt1) = Fz;

```

F.5 Programs FFT and amplitude spectrum

```

=====
t=xlsread('FFT1.xlsx',2,'Q1:Q10000');
A=xlsread('FFT1.xlsx',2,'R1:R10000');
Fs = 5000; % Sampling frequency
T = 1/Fs; % Sample time
L = 3000; % Length of signal
%t = (0:L-1)*T; % Time vector
% Sum of a 50 Hz sinusoid and a 120 Hz sinusoid
t=xlsread('FFT1.xlsx',2,'Q1:Q10000');
y = 2*randn(size(t)); % Sinusoids plus noise
NFFT = 2^nextpow2(L); % Next power of 2 from length of y

% Plot single-sided amplitude spectrum.
figure(1)
subplot(2,1,1)
plot(t,A,'b')
xlabel('Time (s)');
ylabel('Amplitude ');
title('Tool and workpice amplitude vibration level')
subplot(2,1,2)
plot(f,2*abs(Y(1:NFFT/2+1)))
title('Amplitude Spectrum of y(t)')
xlabel('Frequency (Hz)')
ylabel('|Y(f)|')

```


F.6 Programs for process damping

```
zetax=(Cx1+(C*b*cos(90-phiavg).^2)/V)/(2*wnx*mx);
zetay=(Cy1+(C*b*cos(180-phiavg).^2)/V)/(2*wnx*mx);

FRF_real_x = FRF_real_x*1e3;
FRF_imag_x = FRF_imag_x*1e3;
FRF_real_y = FRF_real_y*1e3;
FRF_imag_y = FRF_imag_y*1e3;
% Directional orientation up milling factors
mux = cos((beta - (90- phiavg)*pi/180)*cos(90-phiavg)*pi/180);
muy = cos((180-phiavg-beta)*pi/180)*cos((180-phiavg)*pi/180);
% Oriented FRF
FRF_real_orient = mux*FRF_real_x + muy*FRF_real_y;
FRF_imag_orient = mux*FRF_imag_x + muy*FRF_imag_y;
% Define average number of teeth in cut, Nt_star
Nt = 4;
phis = 0;          % deg
phie = 60;
Nt_star = (phie - phis)*Nt/360;

% Calculate blim
blim = -1./(2*Ks*FRF_real_orient*Nt_star); % mm

% Calculate epsilon
for cnt = 1:length(FRF_imag_orient)
    if FRF_imag_orient(cnt) < 0
        epsilon(cnt) = 2*pi -
2*atan(abs(FRF_real_orient(cnt)/FRF_imag_orient(cnt)));
    else
        epsilon(cnt) = pi -
2*atan(abs(FRF_imag_orient(cnt)/FRF_real_orient(cnt)));
    end
end
end
```

Dissemination

International journals

1. Jakeer Hussain Shaik, Srinivas J. (2016) Analytical prediction of chatter stability of end milling process using three dimensional cutting force model, Journal of the Brazilian Society of Mechanical Sciences and Engineering, DOI 10.1007/s40430-016-0567-x.
2. Jakeer Hussain S, Srinivas J (2015) A modelling approach for the design and study of stability issues in end milling with variable tool parameters. Manufacturing technology today, ISSN: 0972-7396.
3. Jakeer Hussain S, Srinivas J (2014) Influence of Secondary Factors of Spindle Geometry on the Dynamic Stability in End-milling Operation, Journal of Mechanical Design and Vibration vol. 2: 35-46.
4. Jakeer Hussain Shaik, Srinivas J. (2014) Dynamic stability of a motorized high speed machine tool spindle supported on bearings, Applied Mechanics and Materials, vol. 612: 29-34.
5. Jakeer Hussain Shaik, Srinivas J. (2013) Identification of dynamic rigidity for high speed spindles supported on ball bearings, International Journal of Research in Engineering and Technology(IJRET), ISSN: 2319 -1163: 146-150.
6. Jakeer Hussain Shaik, Srinivas J. (2015) Optimal design of high speed precise machine tool spindles for improving the dynamic stability in end-milling process, Sadhana - Academy Proceedings in Engineering Sciences (Under review)
7. Jakeer Hussain Shaik, Srinivas J. (2016) Optimal design of spindles with the joint interface effects and tool parameters using neuro-genetic approach, Sains Malaysiana (Under review)
8. Jakeer Hussain Shaik, Srinivas J. (2015) Semi-analytical prediction approach of frequency response in high speed machine tool spindle units, Chinese journal of mechanical engineering, (Under review)

9. Jakeer Hussain Shaik, Srinivas J. (2016) Dynamic modelling and stability studies of end-milling process using a retrofitted drill-spindle system, Measurements (Under review)

International conferences

1. Jakeer Hussain Shaik, Srinivas J. (2012) Dynamic behaviour of high speed spindles, International National Conference on Recent Advances in Material Processing Technology, National Engineering College, Kovilpatti, Tamilnadu.
2. Jakeer Hussain Shaik, Srinivas J. (2013) Analysis and Dynamic Stability of Integrated Micro End Mill Spindles, International Conference on Computer Aided Engineering (CAE-2013), Department of Mechanical Engineering, IIT Madras.
3. Jakeer Hussain Shaik, Srinivas J. (2014) Dynamic stability of a motorized high speed machine tool spindle supported on bearings, International Conference on Design, Manufacturing and Mechatronics (ISET-2014), KJ Institute of technology, PUNE.
4. Jakeer Hussain Shaik, Srinivas J. (2014) Investigation of the cutting edge radius size effect on dynamic forces in micro end milling, IDMC-2014, NIT Rourkela.
5. Jakeer Hussain Shaik, Srinivas J. (2015) Morphological studies to predict the chatter vibrations in end milling of Aluminum (Al6061). NCPCM-2015, NIT ROURKELA.
6. Jakeer Hussain Shaik, Srinivas J. (2016) Analysis and Optimal modeling of end-mill spindles for improvising dynamic stiffness using neuro-genetic approach, National symposium on rotor dynamics-2016, NIT ROURKELA.

Curriculum Vitae

Mr. Jakeer Hussain Shaik

Ph. D scholar,

Dept. of Mechanical Engineering

National Institute of Technology, Rourkela

Odisha, India 769008.

Email : jakeershaik786@yahoo.co.in

Mobile:08596957456

ACADEMIC PROJECT DETAILS

Ph.D: Investigation of dynamic modelling and stability issues in end milling operation.

M.Tech: Analysis of adhesively bonded double lap joints in FRP Laminated composites

EXPERIENCE

Five years teaching experience at K. L UNIVERSITY

Four years Research and teaching experience during Ph.D at NIT ROURKELA.

SUBJECTS TAUGHT

Strength of materials

Engineering Drawing

Fluid Mechanics & hydraulic Machines

Design of machine elements

Engineering Vibrations

Finite Element modeling

Manufacturing Technology

LABS DEALLED

Strength of materials Lab.

Fluid Mechanics and Hydraulic Machines lab.

Machine drawing using CAD lab.

Manufacturing Technology Lab

Machine tools Laboratory

IC engines Lab.

COMPUTER SKILLS

MATLAB (Matrix Laboratory)

CAD

ANSYS WORKBENCH

SOLIDWORKS

STRENGTHS

Hardworking

My determination to learn

Commitment at work

Self Learning

PERSONAL PROFILE

Name : Jakeer Hussain Shaik

Father's Name : Abdul Gafoor Shaik

Mother's Name : Irshad Begum Shaik

Languages Known : English, Telugu & Hindi

Date of Birth : 13-04-1985

Gender : Male

Marital Status : Married

Permanent Address : S/o. Abdul Gafoor Shaik,

Door no. 36-8-44/50,

Nehru nagar, wood pet,

Vijayawada, Krishna Dist, Andhra Pradesh, India.